

**Physical properties and transport mechanisms in  
natural crystalline phases under high pressure and  
temperature environments: A first-principles approach**

**Thesis submitted for the degree of  
Doctor of Philosophy (Science) of  
Jadavpur University**



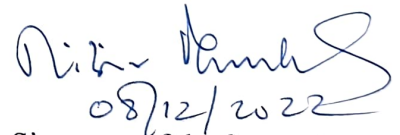
**Sudip Kumar Mondal  
Department of Physics  
Index Number: 162/16/Phys./25  
Jadavpur University  
Kolkata-700032  
November 2022**





## CERTIFICATE FROM THE SUPERVISOR

This is to certify that the thesis entitled “**Physical properties and transport mechanisms in natural crystalline phases under high pressure and temperature environments: A first-principles approach**” submitted by **Sri Sudip Kumar Mondal** who got his name registered on **26.08.2016** for the award of Ph. D. (Science) Degree of Jadavpur University, is absolutely based upon his own work under the supervision of **Professor Nibir Mandal** and that neither this thesis nor any part of it has been submitted for either any degree / diploma or any other academic award anywhere before.



Signature of the Supervisor

with date and official seal

NIBIR MANDAL  
Professor  
Dept. of Geological Sciences  
Jadavpur University  
Kolkata - 700 032



*To my family,  
I give it all,  
including this.*



## **ACKNOWLEDGEMENTS**

Rome ne fut pas faite toute en un jour. Rome wasn't built in a day. Speaking strictly and only about the time, neither was the compilation of this doctoral thesis! Here, I like to seize the opportunity to express my sincere gratitude to everyone who encouraged and assisted me throughout my doctoral study. I am thankful for their continuous guidance, positive criticism and insightful advice during this decisive period of my career.

I am forever grateful to my advisor, Professor Nibir Mandal for his unwavering support and belief in me at every stage of my doctoral study. He has been an ideal mentor and teacher, offering suggestions and encouragement with a perfect blend of vision and humour. He introduced me to the realm of the earth sciences and always inspired me to explore intriguing research connecting the bridge between geology and physics which undoubtedly widened my domain of research. Every conversation we had has led to a constant improvement of my knowledge and wisdom, be it academic or quality of being. I cherish these wonderful instances of learning, and I'm proud of my time working under his supervision.

I am especially thankful to Professor Ashok K Arya of Bhava Atomic Research Centre, Mumbai for his continuous support and motivation in my research. He taught me the profound essence of density functional theory and its practice. It was Professor Arya who first introduced me to high-performance computing. In fact, computers have done the majority of the work in this thesis (they never receive their due credit!). I have benefited greatly from his wealth of knowledge and meticulous editing. My sincere acknowledgement goes to Prof. Dipak Chandra Paul, Prof. Sukhen Das, Prof. Sanjay Kumar, Prof. Debashish Biswas, Prof. Partha Pratim Roy, and Prof. Shantanu Maitra for their words of encouragement.

I am fortunate to have been a part of the jugeotodynamics research group. I gratefully recognize the support of my group mates and colleagues in JU. I had an exciting period to work with my then colleague, now Prof. Pratik Kumar Das, who has carefully taught me the working principles and knowhow of several DFT packages. My sincere thanks to Dr. Shamik Sarkar, Dr. Sujoy Dasgupta, Dr. Puspendu Saha, Dr. Rwiti Basu for being always present and helping me. I also had the pleasure of sharing my routine academic duties and achievements in jugeotodynamics lab with Dr. Ritabrata Dasgupta, Dr. Giridas Maiti, Manaska Mukhopadhyay, Dip Ghosh, Arnab, Nandan, Gourishankar,

Pramit and Ayan. Dr. Amiya Baruah and Dr. Koustav Chatterjee merits special mention for their extensive support. Finally, Joyjeet, for I would like to thank you not only for academic helps but also in financial camaraderie.

It is very important to strike a balance between the hectic lab works and the life outside of it. I am privileged that I never had to walk on a tight rope for I have such a group of amazing friends, the enjoyments of the weekly retreats with them can't be stressed enough. My special thanks to Debarshi, Souradeep, Sayan, Nur, Titas, Sourav, Adak, Abuda, Atanuda, Debuda, Bidisha, Swarnali, Krittish, Tanmoy, Supradip, Chinmoyee, Suman, Priyanka, Neel, Firoz, Baitan, Tatoon, Joy, Suman (Again!), Soumik, Tanmoy (again!), Kaushik, Pritha, Sampurna and the list go on. Thank you for constantly listening to my poor jokes and lectures and smiling when things become serious. Carpe diem- they say. But I couldn't have carped a single diem without you guys!

I am thankful to DST, Govt. of India for supporting my thesis work through the INSPIRE programme. I am also grateful to HPC-Europa3 programme to provide me with project fellowships to work with Prof. Andreas Hermann at the University of Edinburgh and Prof. Lidunka Vocadlo at University College London, UK. I acknowledge the sincere guidance and suggestions of Prof. Hermann in working with ammonia-water mixture. My sincere thanks to Prof. Vocadlo for teaching me the method of solid-liquid phase coexistence melting.

I am forever indebted to my parents. You are the source of relentless encouragement and motivation. Maa, thank you for tackling a ridiculous number of phone calls and for comforting me. Baba, thank you for your love and for always reminding me that there is light at the end of the tunnel. My brothers and sisters, Subham, Santu, Riddhi, Pinididi, Anushree (still baffled why her nickname is Mom!) and Sneha demand special mention for their faith in their 'Dada'/'Bhai' over the years. Immense gratitude as always to you for your patience and support.

I am blessed with a beautiful daughter who is a better person than I am even though she is a cat. Thank you, Scandium aka Pengu for continuously judging me and craving for food! Hopefully our tragicomic bustle can go on forever.

*Sudip Kumar Mondal*



# CONTENTS

	<b>Abstract</b>	<b>i-ii</b>
<b>Chapter 1</b>	<b>Introduction</b>	<b>1</b>
	1.1 First principles material physics	3
	1.2 Natural atomic and molecular crystalline solids	6
	1.3 First principles calculations in extreme environments	12
	1.4 Thesis Outline	16
<b>Chapter 2</b>	<b>First principles techniques: A theoretical background</b>	<b>29</b>
	2.1 Preamble	31
	2.2 Born-Oppenheimer approximation	34
	2.3 Thomas-Fermi model	35
	2.4 Density functional theory	37
	2.4.1 Hohenberg-Kohn theorems	37
	2.5 Exchange-correlation functionals	41
	2.5.1 Local density approximation (LDA)	42
	2.5.2 Generalised gradient approximation (GGA)	43
	2.5.3 Hybrid exchange-correlation functionals	44
	2.6 Pseudopotential formalism	44
	2.6.1 Norm-conserving pseudopotentials	46
	2.6.2 Ultrasoft pseudopotentials	47
	2.7 Ab-initio molecular dynamics	48
<b>Chapter 3</b>	<b>Computational methodologies</b>	<b>55</b>
	3.1 Foreword	57
	3.2 The equation of state for solid	58
	3.3 Phase transition	61
	3.4 Electronic properties	62
	3.4.1 Band structure	62
	3.4.2 Density of states (DOS)	64

3.5	Quasi-harmonic approximation	66
3.6	Vibrational frequencies (phonons)	68
3.7	Diffusion coefficient	70
3.8	Electrical conductivity	72
3.9	Radial and pair distribution function	73
<b>Chapter 4</b>	<b>Silicates-I: <math>U_{1-x}Th_xSiO_4</math> solid solution</b>	<b>79</b>
4.1	Introductory notes	81
4.2	Computational methods	85
4.3	Structural parameters	87
4.4	Characteristics of the phase transition	92
4.5	Polyhedral geometry and distortion	96
	4.5.1 Theoretical framework for polyhedral distortion	97
4.6	U/ThO <sub>8</sub> polyhedral distortion	100
4.7	Highlights of the results	109
<b>Chapter 5</b>	<b>Silicates-II: Titanite (CaTiSiO<sub>5</sub>)</b>	<b>117</b>
5.1	Introduction	119
5.2	Computational approach	121
5.3	Structural analysis	122
5.4	Elastic constants tensor	126
5.5	Negative elasticity	131
	5.5.1 Elastic moduli	136
5.6	Electronic and optical properties	139
5.7	Concluding notes	143
<b>Chapter 6</b>	<b>Dense hydroxide Brucite [Mg(OH)<sub>2</sub>]</b>	<b>147</b>
6.1	Overture	149
6.2	Computational methodology	152
6.3	Crystal structure and equation of state	153
6.4	Proton transport mechanisms	155

6.5	Proton diffusion coefficients	160
6.5.1	Anisotropy in proton diffusion	166
6.6	Electrical conductivity	168
6.7	Highlights of the outcomes	171
<b>Chapter 7</b>	<b>Molecular crystalline NH<sub>3</sub>-H<sub>2</sub>S mixture</b>	<b>179</b>
7.1	Motivation	181
7.2	Computational details	185
7.3	AIMD Phase diagram	186
7.4	Plastic and superionic phases	191
7.5	Diffusivity of H, N and S	197
7.6	Analysis of local structures	201
7.7	Combined P-T effects on band gap	205
7.8	Concluding notes	207
<b>Chapter 8</b>	<b>Summary and conclusions</b>	<b>215</b>
8.1	U <sub>1-x</sub> Th <sub>x</sub> SiO <sub>4</sub> : Phase transition & mechanical property	217
8.2	Effect of polyhedral distortion on phase transition	219
8.3	Elastic property of titanite	220
8.4	Electronic and optical property of titanite	221
8.5	H-diffusion in brucite under high pressure	222
8.6	Electrical conductivity of brucite	224
8.7	Plastic, superionic and melting behaviour of AMS	225
8.8	Local structure and band gap of AMS	226
8.9	Future scope	227
	<b>List of publications</b>	<b>231</b>



## Abstract

The present thesis explores the physical and chemical behaviour of naturally occurring atomic and molecular crystalline solids in the interior of the earth and other extra-terrestrial planets. Understanding their physical and chemical properties under extreme thermodynamic conditions, e.g., ultra-high pressures and/or temperatures is of vital significance, especially to interpret the phase stability, elastic properties, chemical compositions of planetary materials as well as their microscale transport properties, e.g., diffusion. This study adopts two major computational approaches: electronic structure calculations in the framework of Density functional theory (DFT) and ab-initio molecular dynamics (AIMD) simulations, to elucidate the role of the underlying atomic scale mechanisms in governing the macrophysical behaviour relevant to planetary processes and natural materials development.

A direction of this thesis work focuses on two important nesosilicates: zircon [ $\text{ZrSiO}_4$ ] and titanite [ $\text{CaTiSiO}_5$ ] present in Earth's crust and mantle. Tetragonal zircon is known as the most potential mineral phase to host heavy elements (U, Th, Pu) in their crystal structures, and this mineral phase is an outstanding material for nuclear waste immobilization and U-Zr-Pb geochronology. Zircon structured coffinite [ $\text{USiO}_4$ ] and thorite [ $\text{ThSiO}_4$ ] are detected to form solid solutions. Using DFT simulations this thesis provides a comprehensive analysis of the pressure induced zircon- to reidite-type phase transition of  $\text{U}_{1-x}\text{Th}_x\text{SiO}_4$  ( $x = 0$  to  $1$  in steps of  $0.25$ ) solid solution. The phase transition pressure ( $P_T$ ) is shown to vary nonlinearly with increasing Th content in the solid solution and attain a minimum value of  $6.82$  GPa for  $x = 0.5$ . The calculated maximum compressibility of zircon type  $\text{U}_{0.5}\text{Th}_{0.5}\text{SiO}_4$  supports this finding, implying that the phase becomes most pressure sensitive (i.e., soft) at this specific U/Th ratio. The thesis also presents a novel approach to the analysis of the polyhedral distortions of triangular dodecahedra (snub-disphenoids). Two parameters ( $\delta$  and  $\sigma^2$ ) have been defined to quantify the longitudinal and angular distortions of highly irregular U/ThO<sub>8</sub>-triangular dodecahedra. The distortion analysis indicates that the difference in angular distortions ( $\sigma_{\text{U}}^2$  and  $\sigma_{\text{Th}}^2$ ) between the zircon- and reidite-type phases ( $\Delta\sigma^2$ ) becomes minimum when U and Th occur equally in the solid solution. The concurrence of  $P_T$  and  $\Delta\sigma^2$  minima indicates that the polyhedral distortion plays a critical role in dictating the zircon- to reidite-type transition. The distortions parameters,  $\delta$  and  $\sigma^2$  are independent of the elements occupying the snub-disphenoid space. Also, they are defined without any attribute to external parameters. This study hypothesizes that the parameters:  $\delta$  and  $\sigma^2$  can be used to calculate the distortion of similar AB<sub>8</sub>-type snub-disphenoids in other crystalline phases.

The thesis presents a completely new theoretical data set on the mechanical properties of monoclinic titanite phase. The theoretical calculations reveal unusual negative values of the elastic constant:  $C_{36}$  for C2/c phase and negative pressure gradients of the shear elastic constants,  $C_{44}$ ,  $C_{55}$  and  $C_{36}$  for both titanite phases. This study predicts the necessary condition for an elastic constant to have a negative pressure gradient. Furthermore, a novel atomic scale mechanism for such negative elasticity is reported; the rotational bond kinematics, driven by valence charge accumulation on (001) plane during the lattice deformation which causes structural collapse in a direction orthogonal to the applied shear strain, resulting in the negative elastic behaviour. Dielectric-function analysis predicts an exceptionally strong opacity of the wide band-gap ( $3.2$  eV) titanite in the UV region, indicating this crystalline phase as a shield material for UV radiation. It is also demonstrated from the theoretical calculations that titanite can be used to develop optical devices, such as filters and polarizers.

Brucite [ $\text{Mg}(\text{OH})_2$ ] is a hydrogen-rich naturally occurring hydroxide phase, especially encountered abundantly in subduction zones of Earth's plates. The presence of two-dimensional wells between layers of  $\text{MgO}_6$ -octahedra in  $\text{P}\bar{3}$ -type brucite provides large interstitial space for the

hydrogen atoms to diffuse in the lattice framework. A part of this thesis investigates the hydrogen or proton diffusion in crystalline  $P\bar{3}$ -type trigonal brucite in the pressure range 10-85 GPa and in the temperature range 1250-2000K using AIMD simulation. The diffusion coefficients of H, mediated by the amorphization of the H-sublattice, show an anomalous variation with pressure along different isotherm. The diffusion of H is observed to attain maxima in the pressure range 73-76 GPa before decreasing in magnitude on further increment of pressure. The present study reveals that proton diffusion is highly anisotropic in brucite, with virtually no proton diffusion occurring along the crystallographic *c*-axis. The protonic conductivities are also evaluated and compared with the geophysical magnetic satellite observations. The conductivity analysis suggests that brucite can occur in appreciable amounts in the lower mantle and mantle transition zone. The finding explains the occurrence of high conductivity zones in deep earth, widely reported in solid earth geophysics.

Another direction of this thesis deals with the major constituents of the ice giants Uranus and Neptune, such as molecular mixtures of methane, water and ammonia. At combined high pressure-high temperature conditions these molecular mixtures can contribute to electrical conductivity of planetary interiors through superionicity, where protons diffuse through stationary heavy atoms in the lattices. Atmospheric abundances of nitrogen and sulphur inferred from microwave absorption experiments are found to be anomalous with reference to the solar ratios, implying the presence of substantial amounts of H<sub>2</sub>S in these planets. Using AIMD simulation, a line of the thesis work explores the plastic and superionic natures of the ammonia monosulphide [NH<sub>3</sub>:H<sub>2</sub>S -1:1] phases. The calculated phase diagram from AIMD simulations shows that the ambient phase (Space Group-P4/nmm) preferentially melts from the solid state at 500K, where the rest high-pressure phases undergo plastic deformation (or rotational states), followed by superionic states before the onset of melting at higher temperatures. The simulations also reveal a sharp increase of the melting points from the P4/nmm phase at 500K in ambient condition to Cc phase at 2250K and 20 GPa, which reaches a maximum of 2500K at 40 GPa. For the high-pressure P2<sub>1</sub>/m and Abm<sub>2</sub> phase the melting point remains fixed at 2500K and then drops to 2250K for the Cmma phase at 167 GPa. The thermal corrections to pressure for the phases beyond 40 GPa decrease following melting. The melts are thus denser than their solid counterparts at the elevated pressures mentioned above. The steep slope in the melting curve at lower pressure has potential implications for planetary science and points towards the possible existence of solid NH<sub>3</sub>-H<sub>2</sub>S mixture in the shallow mantle region of Uranus and Neptune. Barring the ambient phase, the phase diagram demarcates a zone of fast hydrogen diffusion, in the presence of stable sulphur and nitrogen sublattice. This fast proton transport results in superionicity in ammonia monosulphide. An analysis of the pair distribution function is presented to identify the formation of short-lived H<sub>2</sub>, S<sub>2</sub> molecules and other chemical motifs like H<sub>2</sub>NS and HSNH at elevated pressure and temperature, triggered by rapid movement of constituting atoms. The density of states calculation confirms the low-pressure phases as wide band-gap semiconductor (1.0 to 3.5 eV), apart from the Abm<sub>2</sub> and Cmma phase. The band-gap is reduced on increasing temperatures, and the reduction is most prominent for the Cc phase at 20 GPa, 2.86 eV at 500K to 0.8 eV at 2250K.

Overall, this present thesis provides a distinctive description of the effect of elevated pressure and/or temperature as well as of the ultra-active chemical environment on the physical and microscale transport properties of crystalline solids from an atomistic point of view. These key properties are pertinent for the composition of planetary interiors together with an outlook on novel characteristics of materials.

# Introduction

---

1

*First principles material physics*

*Natural atomic and molecular crystalline solids*

*First principles calculations in extreme environments*

*Thesis outline*





## 1.1 First principles material physics

The phrase '*First principles*' refer to those calculations based on the fundamental laws of nature, where no empirically adjustable parameter is invoked. The only parameters that are allowed are the fundamental constants of physics. To be exact, since the aim is to investigate the properties of matter, the pertinent basic laws of physics are those describing the interactions between nuclei and electrons, that is, those of the quantum mechanics. The major objective of first principles calculations is to explore the structure-composition-physical property correlation, that are often hidden in plain sight, by employing computational techniques. Majority of these techniques are formulated in the framework of Density Functional Theory (DFT). Way back in 1964-1965, Hohenberg and Kohn[1] and, Kohn and Sham[2] realized the difficulty in tackling the complex wave function of a many-particle system containing  $N$  particles, which is a function of  $3N$  spatial variables and  $N$  spin variables. Thus, they conceptualized the DFT approach to solve quantum mechanical equation in an attempt to calculate the ground state properties of

## ***Chapter 1***

a system which later proved by Mermin [3] to be useful for finite temperature properties, too. In their revolutionary and efficient methodology, Hohenberg and Kohn proposed the use of electron density as the principal quantity, capable of fully describing the properties of a system, in place of the complicated many-body electronic wave function. However, implementation of DFT is not straight forward. The cost to pay for this enormous simplification is a modification of the basic equations of quantum mechanics with introducing a few new terms, one of which, is called exchange-correlation (XC) energy. The principal limitation in DFT can be attributed to the choice of the exact functional for XC energy owing to their unknown description for many-body systems. To overcome this limitation, this theoretical approach evokes a number of approximations, e.g., *local density approximation* (LDA) which was put forward by Kohn and Sham [2] themselves, and *generalized gradient approximation* (GGA) [4,5] , providing sufficient accuracy in calculated physical properties. The accuracy of DFT driven results can vary from nominal to considerable upon changing the preferred approximations. The LDA formalism assumes a uniform density everywhere which in turn overestimates the correlation energy and undervalues the exchange one. Since the errors rising out from the exchange and the correlation parts are antipodal in nature, they tend to compensate each other to a reasonable extent. To rectify this bias of LDA, the inhomogeneous distribution of the actual electron density is addressed by considering a gradient dependent form of the density. This incorporates the spatial variation of electron density, which is tackled by GGA to enumerate the ground state energies with better accuracy.

## *Introduction*

The past few decades have witnessed an overwhelming popularity of the increasing application of DFT, as this efficient tool is successfully employed to predict the electronic structures of atoms, molecules and later expanded to crystalline solids and clusters [6–9]. This growing popularity owes mainly to its advantage over computation with high accuracy, as compared to other methods, e.g., many-particle methods. Furthermore, the first principles method can also be implemented to handle systems containing large number of atoms, as generally required in several fields of research, ranging from condensed matter system, nanotechnology to pharmaceutical science and biological systems. This has inspired several researchers to employ the recently developed ab-initio or first principles structure searching method such as USPEX [10,11], AIRSS [12] and CALYPSO [13] to investigate the evolution of novel material phases under ultra-high pressure which were previously unknown [14–22]. The unique application of DFT in the field of new materials research has enabled scientists to identify materials demonstrating industrially demanding physical properties, such as super conductivity, superionic behaviour, high corrosion and thermal resistance and exciting opto-electronic behavior.

Understanding physical as well as chemical behavior of solids under extreme conditions is one of the major challenges in physics and, particularly, in materials sciences. Creating such extreme physical conditions in laboratory is often hindered by the requirement of expensive technological devices. Furthermore, direct measurements of targeted physical properties are not always straight forward and rely on other parameters of interest, the values of

## ***Chapter 1***

which are mostly unknown at those corresponding high-pressure and - temperature regime. To overcome this hurdle, scientists have adopted the electronic structure calculation DFT and ab-initio molecular dynamics (AIMD) method, which is comparatively less expensive and convenient. Motivated by the application of first principles calculations, geoscientists in the early 90's and 2000's have adapted the electronic structure based first principles approach to explore different physical properties of the major constituent mineral phases of the Earth at exceptionally high pressure and temperature conditions expected in the mantle and core [23–31]. Following the same line of research other ab initio studies have later predicted the high-pressure phase transitions and elasticity of several crust, mantle and core forming mineral phases as function of pressure, temperature and chemical environment, e.g., compositions and defects[32–41].

### **1.2 Natural atomic and molecular crystalline solids**

Naturally occurring atomic and molecular crystalline phases have attracted the attention as they can be engineered to attain desired physical and chemical performance making them industrially demanding. A range of silicates are observed to find significant utility in novel material development. Silicates and oxides are the most dominant mineral phases of the Earth. They constitute almost 95% the crust and more than 80% of the mantle[42–45]. Their resistance to ultra-high pressure and temperature and appropriate physical properties makes them suitable candidates for applications in extreme conditions. The typical crystal structures of different silicates are dictated by specific arrangement of  $SiO_4^{4-}$  tetrahedra, which can appear either in isolation

## Introduction

or polymerize by sharing their corners or edges or faces[45]. This polymerization phenomena leads to the formation of numerous silicate structures, e.g., chain silicates, ring silicates and three-dimensional framework silicates or sheet silicates. Oxygen atoms occurring at the corners of  $SiO_4^{4-}$  tetrahedra play a major role in these silicates to coordinate between different cations. Nesosilicates are the most common silicate that features  $SiO_4$  tetrahedral polymerization. Here the isolated tetrahedra leaves the octahedral

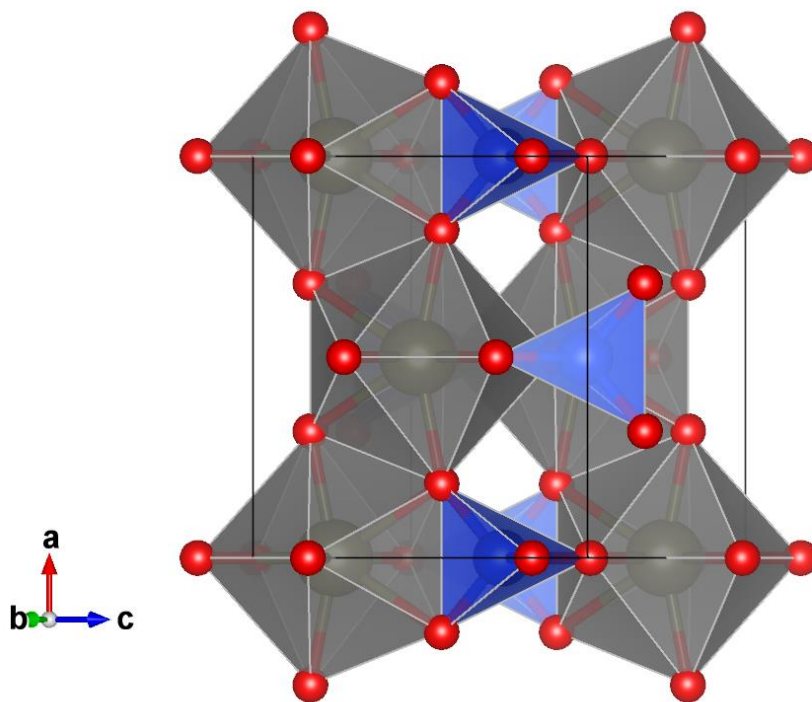


**Figure 1.1:** Crystalline structure of tetragonal zircon representative of the nesosilicate class. The grey and blue polyhedra are  $ZrO_8$  and  $SiO_4$  polyhedra respectively. The red spheres are oxygen atoms.

interstitial spaces to be occupied generally by bivalent cations e.g.,  $Fe^{2+}$ ,  $Mg^{2+}$  and  $Cr^{2+}$  etc. Some examples of naturally occurring nesosilicates are olivine [ $(Mg,Fe)_2SiO_4$ ]; zircon [ $ZrSiO_4$ ] (Figure 1.1); coffinite [ $USiO_4$ ]; thorite [ $ThSiO_4$ ]; titanite [ $CaTiSiO_5$ ] and garnet [ $X_3Y_2(SiO_4)_3$ ]. Here,  $X$  and  $Y$  sites are usually occupied by divalent and trivalent cations in octahedral/tetrahedral framework. As the degree of polymerization increases, the number of corner

## Chapter 1

sharing oxygen also multiplies ranging from 1 to 4. Ring or single chain silicate structures are formed when two oxygen atoms belonging to two neighboring

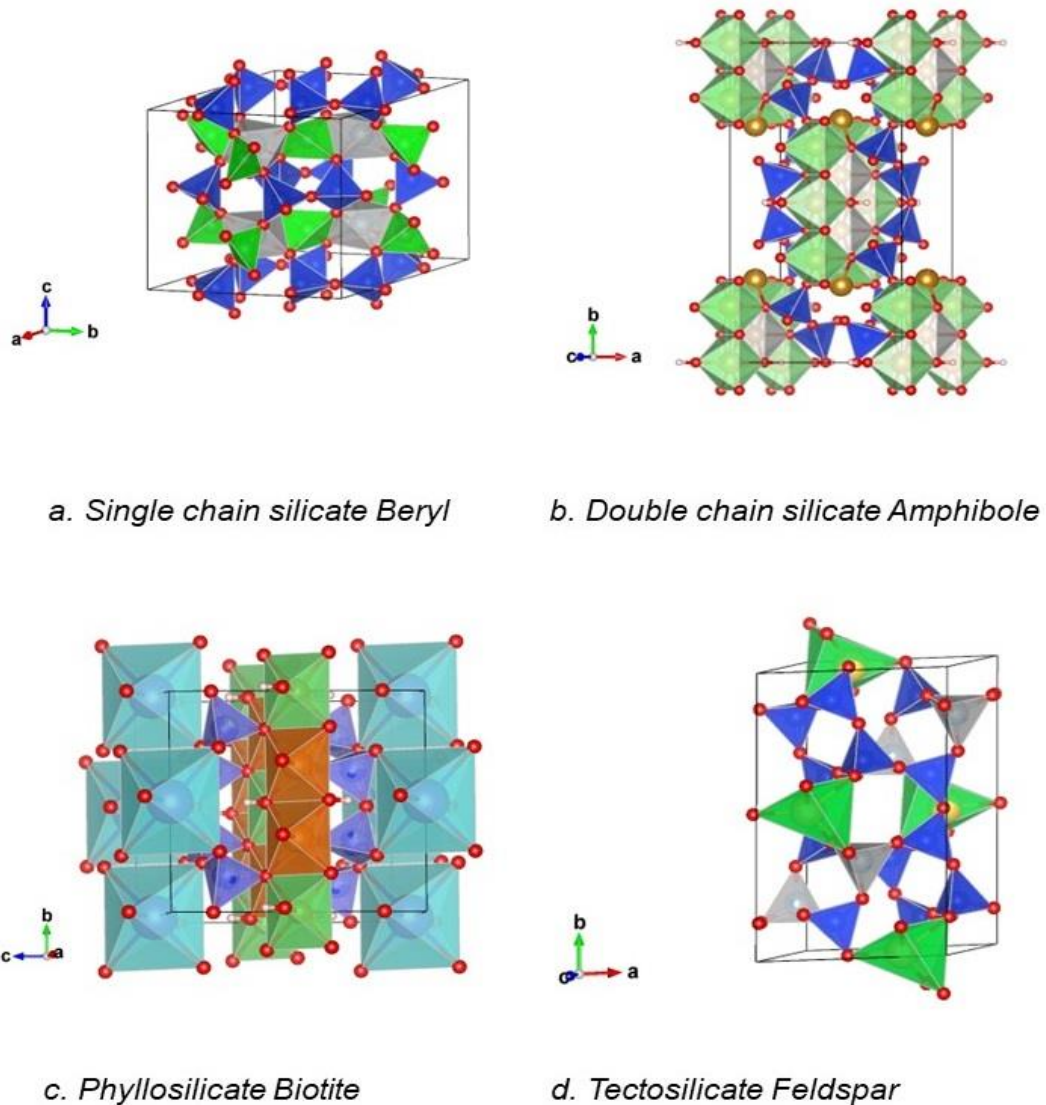


**Figure 1.2:** Crystalline structures of silicate mineral phases in ascending order of polymerization of the  $\text{SiO}_4$  tetrahedral units (shown in blue).

$\text{SiO}_4$  tetrahedra are shared. Pyroxene  $[(\text{Mg},\text{Fe})_2\text{Si}_2\text{O}_6]$  and Beryl  $[\text{Be}_3\text{Al}_2\text{Si}_6\text{O}_{18}]$  (Figure 1.2a) are common chain and ring silicates, respectively, which are found in abundance in the Earth's crust. The chain structures often show their polymerization by sharing three oxygen atoms and constitute a double chain silicate structure which are termed as inosilicates. Amphibole

## ***Introduction***

$[(Mg,Fe)_7Si_8O_{22}(OH)_2]$  (Figure 1.2b) is one of the most notable silicates demonstrating double chain structure. Silicates can also polymerize to form ring structures called cyclosilicates. Often these ring structures coordinate via oxygen atoms to give rise to adjoining rings on a plane resulting in sheet-like polymerization. They are termed as phyllosilicate or sheet silicate. Muscovite  $[KAl_3Si_3O_{10}(OH)_2]$  and biotite  $[K(Mg,Fe)_3AlSi_3O_{10}(F,OH)_2]$  (Figure 1.2c) are the most abundant phyllosilicates in crustal rocks. Sometimes all the four oxygen atoms of  $SiO_4$  tetrahedra are shared leading to the extreme polymerization to form a framework structure, which is called tectosilicate. Quartz  $[SiO_2]$  and feldspar  $[KAlSi_3O_8 - NaAlSi_3O_8 - CaAl_2Si_2O_8]$  (Figure 1.2d) are some of the notable silicates belonging to the class of tectosilicates.

Olivine and its high-pressure polymorphs viz. wadsleyite and ringwoodite are often observed to house nominal amount of water. Their stability in mantle of the Earth establishes them as phases to cycle water from crust to mantle. Two other classes of mineral phases called the dense hydrous mineral silicates (DHMS)[46–51] and nominally anhydrous minerals (NAMs)[52–56] also contribute to this recycling of water and light elements in the mantle. This housing of nominal amount of water or light elements bring forth drastic alteration in their physical properties. Dense hydroxides are another important class of minerals which are observed to be capable of recycling appreciable amount of water through their crystalline structures. Portlandite  $[Ca(OH)_2]$  (Figure 1.3) and brucite  $[Mg(OH)_2]$  are the most notable among them. Contrary to the silicates, these phases are characterised by layered structures where hydrogen atoms reside between planes formed by

## Chapter 1

cationic octahedra. Together with recycling of water, these phases also show pressure induced dynamic/static proton disorder. This proton disorder forces

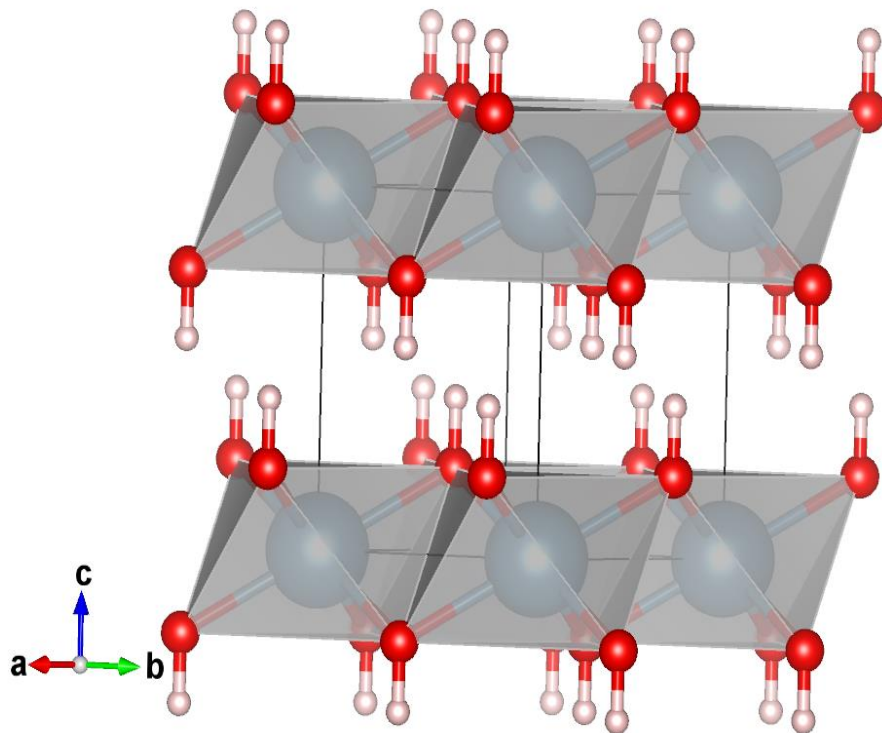


**Figure 1.3:** Crystal structure of ambient phase of portlandite  $[\text{Ca}(\text{OH})_2]$ . The grey polyhedra is the  $\text{CaO}_6$  polyhedra. Red and pink spheres are oxygen and hydrogen atom respectively.

the generation of free protons and enhances their mobility under high pressure temperature condition. Increasing number of mobile hydrogens lead to a significant rise in their electrical conductivity contributing towards the observed conductivity of the mantle.

The crystalline structure discussed so far are covalent and atomic in type where each atom is covalently bonded with its nearest neighbour. However, molecular crystalline structures are also prevalent in nature. Solid methane, hot ices of water, dense crystalline hydrogen sulphide, pressurized metallic hydrogen, Ammonia-water, ammonia-hydrogen sulphide molecular



crystals (Figure 1.4) are a few to name which are abundant in extraterrestrial gas giant and ice giant planets. Under extreme condition they show exotic new physics and chemistry and are often associated with unexpected superionic and

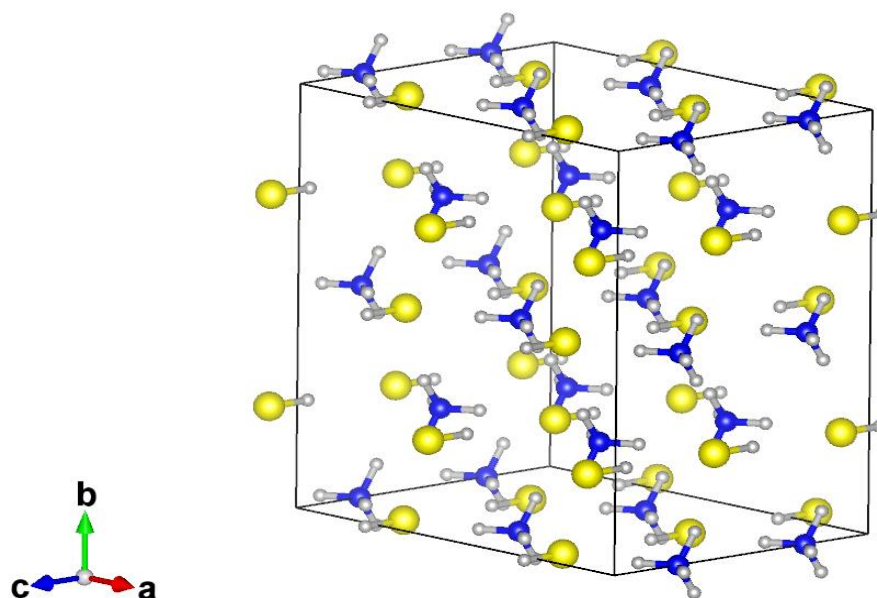


**Figure 1.4:** Ammonia mono sulphide in ambient P4/nmm phase. Blue, Yellow and grey spheres are N, S and H atoms respectively.

superconducting behavior. They generally consist of a central atom belonging to a molecule or ligand at the lattice sites of the crystal which are organized together by relatively weak intermolecular forces. For polar crystals this force may be dipole-dipole force whereas in case of non-polar crystals it can dispersion forces. There is another range of molecular crystals, such as molecular ices where the molecules are held together by hydrogen bonds. They also demonstrate a range of structural transitions in response to elevated pressure. Being held together by weak bonds, in ambient condition the melting point of these crystalline phases are observed to be low compared to covalent crystals. Nevertheless, the melting point increases with pressure and in ultra-

## ***Chapter 1***

high pressure regime often surpasses the melting points of their covalent counterpart.

First principles calculations have been fruitfully employed to explore various facets of the physical properties of the silicates, hydroxides and molecular ices described above. A branch of recent materials research focused upon their morphology and behavior under extreme thermodynamic conditions and ultra-active chemical environments. An atomic level understanding of their material properties is thus necessary to predict a range of their macroscopic applications, e.g., structural transition, band gap modulation, variation in magnetic moments, elasticity, mechanical strength, diffusive behaviour and electrical conductivity etc. The next section highlights some of the major first-principles studies under extreme environment to establish my motivation for studying material properties under such conditions and the eminence of DFT and AIMD in predicting the responses of materials in elevated pressure-temperature regime.

### **1.3 First principles calculations in extreme environments**

Pressure and temperature are regarded as the set of crucial thermodynamic parameters that can transform matter, leading to the evolution of atomic structures and the formation of high-pressure materials with different physical properties to their low-pressure phases. Perhaps the most prolific practitioner of high-pressure and -temperature is the nature herself. Gaseous hydrogen becoming metallic liquid in Jupiter's core and the physico-chemically heterogeneous interior of the Earth are a few of the manifestations of such extreme pressure-temperature conditions. This section

## ***Introduction***

provides a synoptic description of the application of the previously mentioned quantum chemical DFT and AIMD tool in mineral physics to portray the computational proficiency of these computational approaches.

A comprehensive understanding of the response of materials under extreme environments has profound implications in mineral physics. For example, the core of our planet consists of a solid sphere i.e., the inner core, separated at the inner core boundary (ICB) from a surrounding molten spherical shell, called the outer core. The pressure at the Earth's core ranges from 136 GPa at the core-mantle boundary to 364 GPa at the heart of the inner core. Reproducing such a pressure in laboratory set-up is daunting as well as expensive. Iron is the main constituent of the core or more specifically Fe-Ni alloy [57–59]. At ICB solid and liquid iron coexist in equilibrium. Convection of molten Fe in outer core is crucial for generating the Earth's magnetic field. Several geoscientists thus attempt to investigate the possible physical state of iron under such exceptionally high pressure [28,60–63]. First principles studies based on DFT have been extensively employed to predict how pressure can affect spin transition and the phase transitions of BCC to HCP Fe [64–66]. Using the solid-liquid phase coexistence approach Alfe et al. [67] Belonoshko et al. [68] and Wu et al. [69] has determined the melting point of pure Fe at ICB pressure. Subsequent first principles studies have also determined the melting curve of other pure metals like Copper [70], Nickel [71] and Molybdenum [72] etc. at exceptionally high pressures. Ab-initio simulations [61,73] and experimental studies reveal that assuming a pure Fe or Fe-Ni alloy core results in an overestimation of core density ( $\rho$ ) and a deficit in the speed of

## *Chapter 1*

compressional ( $V_p$ ) and shear waves ( $V_s$ ). Several DFT studies have predicted the presence of small amount light elements in Earth's core, such as S ( $\sim 1.7$  wt%), O (1-2.5 wt%) and Si ( $\sim 6$  wt%), to account for the overestimation of core density [57,59,74–77]. First-principles study of Alfe et al. [78] reveals that O favours strong partitioning from solid to liquid Fe at ICB conditions whereas Si exhibits no such preference. A similar study on carbon indicates that, at core conditions, substitutional C in hcp-Fe is thermodynamically more stable than interstitial C[41]. The incorporation of light elements induces changes in transport properties of iron which are computationally investigated by Pozzo et al. [77,79] and Ritterbax and Tsuchiya [80].

The mantle of the Earth is characterized by two consecutive seismic discontinuity at the depths of  $\sim 410$  km and  $\sim 520$  km. Seismic studies have showed discontinuous jumps in seismic velocities at those depths. Over the last few decades earth sciences have witnessed significant growth in the application of DFT, especially to characterize the silicates and their phase transitions at varying depth. The studies reveal consecutive structural transitions in silicates e.g. olivine  $\rightarrow$  wadsleyite at 410 km and wadsleyite  $\rightarrow$  ringwoodite at 520 km which explained the discontinuity in seismic profile[35,81,82]. A further transition to a perovskite structure at 670 km depth in Earth's mantle has also been reported [83–85]. Several geoscientists have employed DFT calculations to unravel intriguing geophysical phenomena like pressure dependent electronic spin transition in ferropericlase [(Mg,Fe)O][86,87] and the micro physics of water in silicates. DHMS, NAMs and transition zone silicates like wadsleyite and ringwoodite often host nominal to appreciable amount of water.

## ***Introduction***

Presence of H<sub>2</sub>O, even in nominal amount, can drastically alter their chemical interaction [88,89] seismic velocities [90], atomic diffusivity [91], electrical conductivity [92–94]. It also drastically reduces the elastic moduli of olivine[95]. While olivine and pyroxene and their high-pressure polymorphs accommodate light elements like H and C, and take part in their recycling into the subduction zones and further deep interior of the Earth, zircon, titanite and beryl type silicates are observed to host large radionuclides. Natural zircon often contains radionuclides and lead as impurities. The superior hydrothermal[96] and chemical resistance of zircon is widely utilized in nuclear energy sector for safe disposal of nuclear waste[97–99] as well as titanite[100]. Zircon based U-Th-Pb geochronology is also extensively used to date the time signature of crust and mantle forming rocks[101–103].

The present thesis focus also on Jovian planets of the solar system where extreme environment exposes unusual and intriguing physics and chemistry of materials. Elements like H and He[104–106] together with individual and mixtures[107] of several high-pressure phases of molecular ices of water[108], ammonia[109], and methane[110] are the major constituents of the mantle regions of ice giant planets where the pressure can reach up to several Mbar. First principles based structure searching algorithm have successfully predicted the stability of ammonia rich hydrate (NH<sub>3</sub>:H<sub>2</sub>O – from 1:2 to 4:1) in the mantle region of those planets and also in large icy moons [111]. In a parallel first-principles study Li et al. [112] has demonstrated the transition and stabilization of novel phases of metallic nitric sulphur hydrides under extreme pressure. These phases are also observed to demonstrate superionic

## ***Chapter 1***

behavior in elevated p-T condition. DFT study of Teerachandran and Hermann [113] have explored novel phases of gas hydrates at around 100GPa and computed their structural transitions and phase diagram. The high-pressure phases of water ice have always been the ‘holy grail’ for high pressure research. First principles study of Takii et al. [114] has shown that hydrogen bonded water ice can also exhibit a plastic phase. From first principles based evolutionary structures, Hermann et al. [115] recognized a sequence of new stable and meta-stable structures of the ground state of water ice in the 1–5 TPa pressure. Previously, it was postulated that an orthorhombic Pbcm structure is stable near 1 TPa. However, according to Hermann et al., it is superseded by a Pmc2<sub>1</sub> phase 930 GPa, followed by a transition to a P2<sub>1</sub> crystal structure at 1.3 TPa. This phase characteristically shows a higher coordination of H with O, and remains stable even at 4.8 TPa pressure.

### **1.4 Thesis outline**

The present doctoral thesis employs two major computational approaches: 1) first-principles electronic structure calculations in the framework of DFT and 2) ab-initio molecular dynamics simulations, to investigate the following issues on natural crystalline materials: mechanical and electronic properties; effects of doping and characterization of pressure and temperature induced phase transitions; diffusion behavior of elements in crystalline lattice and the diffusion mediated electrical conductivities. The thesis is systematically organized in eight chapters. The next chapter is dedicated to present a theoretical premises of density functional theory starting from the many-body Schrödinger equation. Here, I have described the

## *Introduction*

Born-Oppenheimer approximation and its application to decouple the nuclear degrees of freedom from the electronic degrees of freedom. This is followed by a detailed description of the density function theory and several other approximations rendering excellent simplification towards its practical implementation across different computational methods. Different types of exchange-correlation functionals are discussed with their limitations along with their connection to pseudopotential description of elements. Then, the thesis introduces the fundamentals of Ab-initio Molecular Dynamics (AIMD) simulation where the previously decoupled electronic and nuclear degrees of freedom are treated simultaneously to study the evolution of atomic and molecular systems over time. A major direction of this thesis work aims to calculate crucial physical properties of planetary materials using static DFT as well as AIMD simulations. Chapter 3 first provides a detailed description of the theoretical foundations of the computational methods for the calculations. The computational results are then systematically presented in the remaining chapters. Chapter 4 deals with the DFT calculations for radioactive Uranothorite [ $U_{1-x}Th_xSiO_4$ ] solid solutions, providing a comprehensive analysis of the pressure induced zircon-to reidite-type phase transition of  $U_{1-x}Th_xSiO_4$  ( $x = 0$  to  $1$  in steps of  $0.25$ ) solid solution. The phase transition pressure is shown to vary nonlinearly with increasing Th content in the solid solution to attain a minimum value of  $6.82$  GPa for  $x = 0.5$ . A major focus of this chapter is to present a novel approach to the analysis of the polyhedral distortions of triangular dodecahedra (snub-disphenoids). Two geometrical parameters ( $\delta$  and  $\sigma^2$ ) have been introduced to quantify the longitudinal and angular

## *Chapter 1*

distortions of highly irregular U/ThO<sub>8</sub>-triangular dodecahedra. These parameters are then correlated with the anomalous phase transition pressures. A number of crystalline phases are observed to display negative elasticity. However, an atomistic explanation for such unusual remained unexplored in literature. Chapter 5 is dedicated to address the problem of negative elasticity of monoclinic titanite [CaTiSiO<sub>5</sub>], which is an important nesosilicate mineral phase in Earth. A novel atomic scale mechanism is provided to explain such exceptional elastic behaviour. This study also shows its opto-electronic properties, and suggests that the mineral phase can be utilized as a shield material for UV radiation. Chapter 6 comprises AIMD simulation results to discuss the modes of proton diffusion in dense hydroxide brucite [Mg(OH)<sub>2</sub>]. This study addresses the high-pressure proton frustration in brucite and its effect on protonic conductivity at temperatures 1250-2000K and pressures 10-85 GPa. The diffusion of H in brucite demonstrates an anomalous behavior reaching a maximum at ~70 GPa. The calculated proton diffusion constants are utilized to enumerate the electrical conductivities at elevated pressures and temperatures, relevant to the Earth's mantle. Chapter 7 describes the findings on the superionic nature of the molecular mixture of NH<sub>3</sub>-H<sub>2</sub>S phases and their impact on ionic conductivities in extra-terrestrial planetary interior. In addition, a p-T phase diagram of the ammonia mono sulphide mixture is constructed from the AIMD simulations to show the plastic and superionic states along with their melting curve. Different chemical motifs are also identified at different pressure-temperature conditions. This investigation is extended to demonstrate the band gaps as a function of pressure and



## ***Introduction***

temperature. The final chapter (Chapter 8) synthesizes the main outcomes of my thesis work, highlighting the principal conclusions.

## Chapter 1

### References

- [1] Hohenberg P and Kohn W 1964 Inhomogeneous Electron Gas\* *Phys. Rev.* **136** 864–971
- [2] Kohn W and Sham L J 1965 Self-Consistent Equations Including Exchange and Correlation Effects\* *Phys. Rev.* **140** 1133–8
- [3] Mermin N D 1965 Thermal Properties of the Inhomogeneous Electron Gas *Phys. Rev.* **137** A1441–3
- [4] Perdew J P, Jackson K A, Pederson M R, Singh D J and Fiolhais C 1992 Atoms, molecules, solids and surfaces: Applications of the GGA for exchange correlation *Phys. Rev. B* **46**
- [5] Perdew J P, Burke K and Ernzerhof M 1996 Generalized Gradient Approximation Made Simple *Phys. Rev. Lett.* **77** 3865–8
- [6] Parr R G and Yang W 1989 *Density-Functional Theory of Atoms and Molecules* (Oxford University Press)
- [7] Koch W and Holthausen M C 2001 *A Chemist's Guide to Density Functional Theory* (Wiley-VCH Verlag GmbH)
- [8] Sholl D S and Janice S A 2009 *Density Functional Theory: A Practical Introduction* (John Wiley & Sons, Ltd)
- [9] Payne M C, Teter M P, Allan D C, Arias T A and Joannopoulos J D 1992 Iterative minimization techniques for ab initio total-energy calculations: molecular dynamics and conjugate gradients *Rev. Mod. Phys.* **64** 1045–97
- [10] Glass C W, Oganov A R and Hansen N 2006 USPEX-Evolutionary crystal structure prediction *Comput. Phys. Commun.* **175** 713–20
- [11] Oganov A R and Glass C W 2006 Crystal structure prediction using ab initio evolutionary techniques: Principles and applications *J. Chem. Phys.* **124** 1–15
- [12] Pickard C J and Needs R J 2011 Ab initio random structure searching *J. Phys. Condens. Matter* **23** 53201
- [13] Wang Y, Lv J, Zhu L and Ma Y 2010 Crystal structure prediction via particle-swarm optimization *Phys. Rev. B* **82** 94116
- [14] Xia Y, Li Q and Ma Y 2010 Novel superhard polymorphs of Be<sub>3</sub>N<sub>2</sub> predicted by first-principles *Comput. Mater. Sci.* **49** S76–9
- [15] Duan D, Liu Y, Tian F, Li D, Huang X, Zhao Z, Yu H, Liu B, Tian W and Cui T 2014 Pressure-induced metallization of dense (H<sub>2</sub>S)<sub>2</sub>H<sub>2</sub> with high-T<sub>c</sub> superconductivity *Sci. Rep.* **4** 30–2
- [16] Bilić A, Gale J D, Gibson M A, Wilson N and McGregor K 2015 Prediction of novel alloy phases of Al with Sc or Ta *Sci. Rep.* **5** 9909
- [17] Steele B A and Oleynik I I 2016 Sodium pentazolate: A nitrogen rich high energy density material *Chem. Phys. Lett.* **643** 21–6

- [18] Monserrat B, Drummond N D, Dalladay-Simpson P, Howie R T, López Ríos P, Gregoryanz E, Pickard C J and Needs R J 2018 Structure and Metallicity of Phase v of Hydrogen *Phys. Rev. Lett.* **120** 255701
- [19] Monserrat B, Needs R J, Gregoryanz E and Pickard C J 2016 Hexagonal structure of phase III of solid hydrogen *Phys. Rev. B* **94** 1–7
- [20] Monserrat B, Martinez-Canales M, Needs R J and Pickard C J 2018 Helium-Iron Compounds at Terapascal Pressures *Phys. Rev. Lett.* **121** 15301
- [21] Song X, Yin K, Wang Y, Hermann A, Liu H, Lv J, Li Q, Chen C and Ma Y 2019 Exotic Hydrogen Bonding in Compressed Ammonia Hydrides *J. Phys. Chem. Lett.* **10** 2761–6
- [22] Song Z, Mi G, Ma H, Wang Y, Xu L and Li C 2019 First principles calculation on the newly superhard materials of W-B-C ternary system *Solid State Commun.* **301** 113705
- [23] Hemley R J and Cohen R E 1992 SILICATE PEROVSKITE *Annu. Rev. Earth Planet. Sci.* **20** 553–600
- [24] Brodholt J 1997 Ab initio calculations on point defects in forsterite ( $\text{Mg}_2\text{SiO}_4$ ) and implications for diffusion and creep *Am. Mineral.* **82** 1049–53
- [25] Karki B B, Stixrude L, Clark S J, Warren M C, Ackland G J and Crain J 1997 Structure and elasticity of MgO at high pressure *Am. Mineral.* **82** 51–60
- [26] Oganov A R, Brodholt J P and Price G D 2001 Ab initio elasticity and thermal equation of state of  $\text{MgSiO}_3$  perovskite *Earth Planet. Sci. Lett.* **184** 555–60
- [27] Steinle-Neumann G, Stixrude L, Cohen R E and Gülseren O 2001 Elasticity of iron at the temperature of the Earth's inner core *Nature* **413** 57–60
- [28] Alfè D, Gillan M J and Price G D 2002 Composition and temperature of the earth's core constrained by combining ab initio calculations and seismic data *Earth Planet. Sci. Lett.* **195** 91–8
- [29] Alfè D, Price G D and Gillan M J 2002 Iron under Earth's core conditions: Liquid-state thermodynamics and high-pressure melting curve from ab initio calculations *Phys. Rev. B - Condens. Matter Mater. Phys.* **65** 1–11
- [30] Vočadlo L, Alfè D, Gillan M J and Price G D 2003 The properties of iron under core conditions from first principles calculations *Phys. Earth Planet. Inter.* **140** 101–25
- [31] Caracas R, Wentzcovitch R, Price G D and Brodholt J 2005  $\text{CaSiO}_3$  perovskite at lower mantle pressures *Geophys. Res. Lett.* **32** 1–5
- [32] Vočadlo L 2007 Ab initio calculations of the elasticity of iron and iron alloys at inner core conditions: Evidence for a partially molten inner core? *Earth Planet. Sci. Lett.* **254** 227–32
- [33] Mookherjee M and Steinle-Neumann G 2009 Structure and elasticity of hollandite at high pressures *Geochim. Cosmochim. Acta* **73** A898–A898

## Chapter 1

- [34] Caracas R 2010 Elasticity of  $\text{AlFeO}_3$  and  $\text{FeAlO}_3$  perovskite and post-perovskite from first-principles calculations *Geophys. Res. Lett.* **37**
- [35] Hernández E R, Alfè D and Brodholt J 2013 The incorporation of water into lower-mantle perovskites: A first-principles study *Earth Planet. Sci. Lett.* **364** 37–43
- [36] Rebecca A. Fischer, Andrew J. Campbell, Razvan Caracas, Daniel M. Reaman, Dion L. Heinz, Przemyslaw Dera and V B P 2014 Equation of state in the Fe-FeSi system at high pressure and temperatures *J. Geophys. Res. Solid Earth* 2810–27
- [37] Hernández E R, Brodholt J and Alfè D 2015 Structural, vibrational and thermodynamic properties of  $\text{Mg}_2\text{SiO}_4$  and  $\text{MgSiO}_3$  minerals from first-principles simulations *Phys. Earth Planet. Inter.* **240** 1–24
- [38] Shahar A, Schauble E A, Caracas R, Gleason A E, Reagan M, Xiao Y, Shu J and Mao W 2016 Pressure-dependent isotopic composition of iron alloys *Science (80-. )*. **352** 580–2
- [39] Brodholt J and Badro J 2017 Composition of the low seismic velocity  $E'$  layer at the top of Earth's core *Geophys. Res. Lett.* **44** 8303–10
- [40] Li Y, Vočadlo L, Alfè D and Brodholt J 2018 Mg partitioning between solid and liquid iron under the Earth's core conditions *Phys. Earth Planet. Inter.* **274** 218–21
- [41] Li Y, Vočadlo L, Alfè D and Brodholt J 2019 Carbon Partitioning Between the Earth's Inner and Outer Core *J. Geophys. Res. Solid Earth* **124** 12812–24
- [42] Newsom H E, Sims K W W, Noll P D, Jaeger W L, Maehr S A and Beserra T B 1996 The depletion of tungsten in the bulk silicate earth: Constraints on core formation *Geochim. Cosmochim. Acta* **60** 1155–69
- [43] Korenaga J 2009 A method to estimate the composition of the bulk silicate Earth in the presence of a hidden geochemical reservoir *Geochim. Cosmochim. Acta* **73** 6952–64
- [44] Wang X-C, Li Z-X and Li X-H 2013 Early differentiation of the bulk silicate Earth as recorded by the oldest mantle reservoir *Precambrian Res.* **238** 52–60
- [45] Deer FRS W A, Howie R A and Zussman J 2013 An Introduction to the Rock-Forming Minerals
- [46] Frost D J and Fei Y 1998 Stability of phase D at high pressure and high temperature *J. Geophys. Res. Solid Earth* **103** 7463–74
- [47] Komabayashi T and Omori S 2006 Internally consistent thermodynamic data set for dense hydrous magnesium silicates up to 35 GPa, 1600 °C: Implications for water circulation in the Earth's deep mantle *Phys. Earth Planet. Inter.* **156** 89–107
- [48] Guo X and Yoshino T 2013 Electrical conductivity of dense hydrous magnesium silicates with implication for conductivity in the stagnant slab *Earth Planet. Sci. Lett.* **369–370** 239–47
- [49] Liu L 1987 Effects of  $\text{H}_2\text{O}$  on the phase behaviour of the forsterite-enstatite system at high pressures and temperatures and implications for the Earth *Phys. Earth Planet.*

*Inter.* **49** 142–67

- [50] Shieh S R, Mao H K, Hemley R J and Ming L C 1998 Decomposition of phase D in the lower mantle and the fate of dense hydrous silicates in subducting slabs *Earth Planet. Sci. Lett.* **159** 13–23
- [51] Nishi M, Irifune T, Tsuchiya J, Tange Y, Nishihara Y, Fujino K and Higo Y 2014 Stability of hydrous silicate at high pressures and water transport to the deep lower mantle *Nat. Geosci.* **7** 224–7
- [52] Demouchy S and Mackwell S 2006 Mechanisms of hydrogen incorporation and diffusion in iron-bearing olivine *Phys. Chem. Miner.* **33** 347–55
- [53] Denis C M M, Demouchy S and Alard O 2018 Heterogeneous hydrogen distribution in orthopyroxene from veined mantle peridotite (San Carlos, Arizona): Impact of melt-rock interactions *Lithos* **302–303** 298–311
- [54] Thoraval C, Demouchy S and Padrón-Navarta J A 2019 Relative diffusivities of hydrous defects from a partially dehydrated natural olivine *Phys. Chem. Miner.* **46** 0
- [55] Demouchy S, Shcheka S, Denis C M M and Thoraval C 2017 Subsolidus hydrogen partitioning between nominally anhydrous minerals in garnet-bearing peridotite *Am. Mineral.* **102** 1822–31
- [56] Demouchy S, Thoraval C, Bolfan-Casanova N and Manthilake G 2016 Diffusivity of hydrogen in iron-bearing olivine at 3 GPa *Phys. Earth Planet. Inter.* **260** 1–13
- [57] Poirier J P 1994 Light elements in the Earth’s outer core: A critical review *Phys. Earth Planet. Inter.* **85** 319–37
- [58] Allègre C J, Poirier J P, Humler E and Hofmann A W 1995 The chemical composition of the Earth *Earth Planet. Sci. Lett.* **134** 515–26
- [59] Hirose K, Wood B and Vočadlo L 2021 Light elements in the Earth’s core *Nat. Rev. Earth Environ.*
- [60] Stixrude L, Wasserman E and Cohen R E 1997 Composition and temperature of Earth’s inner core *J. Geophys. Res. Solid Earth* **102** 24729–39
- [61] Belonoshko A B, Skorodumova N V, Rosengren A and Johansson B 2008 Elastic Anisotropy of Earth’s Inner Core *Science (80-. )*. **319** 797–800
- [62] Belonoshko A B, Ahuja R and Johansson B 2003 Stability of the body-centred-cubic phase of iron in the Earth’s inner core *Nature* **424** 1032–4
- [63] Belonoshko A B, Lukinov T, Fu J, Zhao J, Davis S and Simak S I 2017 Stabilization of body-centred cubic iron under inner-core conditions *Nat. Geosci.* **10** 312–6
- [64] Mankovsky S, Polesya S, Ebert H, Bensch W, Mathon O, Pascarelli S and Minár J 2013 Pressure-induced bcc to hcp transition in Fe: Magnetism-driven structure transformation *Phys. Rev. B* **88** 184108
- [65] Friák M and Šob M 2008 Ab initio study of the bcc-hcp transformation in iron *Phys.*

## Chapter 1

- Rev. B - Condens. Matter Mater. Phys.* **77** 5296–304
- [66] Ono S, Kikegawa T, Hirao N and Mibe K 2010 High-pressure magnetic transition in hcp-Fe *Am. Mineral.* **95** 880–3
- [67] Alfè D 2009 Temperature of the inner-core boundary of the Earth: Melting of iron at high pressure from first-principles coexistence simulations *Phys. Rev. B - Condens. Matter Mater. Phys.* **79** 1–4
- [68] Belonoshko A B, Ahuja R and Johansson B 2000 Quasi--Ab Initio Molecular Dynamic Study of Fe Melting *Phys. Rev. Lett.* **84** 3638–41
- [69] Wu Y N, Wang D M and Huang Y S 2011 Melting of iron at the earths core conditions by molecular dynamics simulation *AIP Adv.* **1** 1–7
- [70] Vočadlo L, Alfè D, Price G D and Gillan M J 2004 Ab initio melting curve of copper by the phase coexistence approach *J. Chem. Phys.* **120** 2872–8
- [71] Pozzo M and Alfè D 2013 Melting curve of face-centered-cubic nickel from first-principles calculations *Phys. Rev. B - Condens. Matter Mater. Phys.* **88** 1–5
- [72] Cazorla C, Gillan M J, Taioli S and Alfè D 2008 Melting curve and Hugoniot of molybdenum up to 400 GPa by ab initio simulations *J. Phys. Conf. Ser.* **121**
- [73] Belonoshko A B, Simak S I, Olovsson W and Vekilova O Y 2022 Elastic properties of body-centered cubic iron in Earth’s inner core *Phys. Rev. B* **105** L180102
- [74] Zhang Y and Yin Q-Z 2012 Carbon and other light element contents in the Earth’s core based on first-principles molecular dynamics *Proc. Natl. Acad. Sci.* **109** 19579–83
- [75] Côté A S, Vočadlo L and Brodholt J P 2012 Ab initio simulations of iron-nickel alloys at Earth’s core conditions *Earth Planet. Sci. Lett.* **345–348** 126–30
- [76] Wann E T H, Vočadlo L and Wood I G 2017 High-temperature ab initio calculations on FeSi and NiSi at conditions relevant to small planetary cores *Phys. Chem. Miner.* **44** 477–84
- [77] Pozzo M, Davies C, Gubbins D and Alfè D 2014 Thermal and electrical conductivity of solid iron and iron-silicon mixtures at Earth’s core conditions *Earth Planet. Sci. Lett.* **393** 159–64
- [78] Alfè D, Gillan M J and Price G D 2002 Ab initio chemical potentials of solid and liquids solutions and the chemistry of the Earth’s core *J. Chem. Phys.* **116** 7127–37
- [79] Pozzo M, Davies C, Gubbins D and Alfè D 2013 Transport properties for liquid silicon-oxygen-iron mixtures at Earth’s core conditions *Phys. Rev. B - Condens. Matter Mater. Phys.* **87** 1–10
- [80] Ritterbex S and Tsuchiya T 2020 Viscosity of hcp iron at Earth’s inner core conditions from density functional theory *Sci. Rep.* **10** 6311
- [81] Wu Z, Huang F and Huang S 2015 Isotope fractionation induced by phase transformation: First-principles investigation for Mg<sub>2</sub>SiO<sub>4</sub> *Earth Planet. Sci. Lett.*

**409** 339–47

- [82] Yu Y G, Vinograd V L, Winkler B and Wentzcovitch R M 2013 Phase equilibria of  $(\text{Mg,Fe})_2\text{SiO}_4$  at the Earth's upper mantle conditions from first-principles studies *Phys. Earth Planet. Inter.* **217** 36–47
- [83] Tokár K, Jochym P T, Parlinski K, Łażewski J, Piekarczyk P and Sternik M 2010 DFT study of structure stability and elasticity of wadsleyite II *J. Phys. Condens. Matter* **22** 145402
- [84] Parisi F, Sciascia L, Princivalle F and Merli M 2012 The pressure-induced ringwoodite to Mg-perovskite and periclase post-spinel phase transition: a Bader's topological analysis of the ab initio electron densities *Phys. Chem. Miner.* **39** 103–13
- [85] Yu Y G, Wentzcovitch R M, Vinograd V L and Angel R J 2011 Thermodynamic properties of  $\text{MgSiO}_3$  majorite and phase transitions near 660 km depth in  $\text{MgSiO}_3$  and  $\text{Mg}_2\text{SiO}_4$ : A first principles study *J. Geophys. Res. Solid Earth* **116**
- [86] Tsuchiya T, Wentzcovitch R M, da Silva C R S and de Gironcoli S 2006 Spin Transition in Magnesiowüstite in Earth's Lower Mantle *Phys. Rev. Lett.* **96** 198501
- [87] Lin J-F and Tsuchiya T 2008 Spin transition of iron in the Earth's lower mantle *Phys. Earth Planet. Inter.* **170** 248–59
- [88] Prigiobbe V, Negreira A S, Lim D-H and Wilcox J 2013 Density Functional Theory Calculations of the Interaction of Olivine with Water *Energy Procedia* **37** 5875–83
- [89] Padrón-Navarta J A and Hermann J 2017 A Subsolvus Olivine Water Solubility Equation for the Earth's Upper Mantle *J. Geophys. Res. Solid Earth* **122** 9862–80
- [90] Inoue T 1994 Effect of water on melting phase relations and melt composition in the system  $\text{Mg}_2\text{SiO}_4$ - $\text{MgSiO}_3$ - $\text{H}_2\text{O}$  up to 15 GPa *Phys. Earth Planet. Inter.* **85** 237–63
- [91] Caracas R and Panero W R 2017 Hydrogen mobility in transition zone silicates *Prog. Earth Planet. Sci.* **4**
- [92] Panero W R, Smyth J R, Pigott J S, Liu Z and Frost D J 2013 Hydrous ringwoodite to 5 K and 35 GPa: Multiple hydrogen bonding sites resolved with FTIR spectroscopy *Am. Mineral.* **98** 637–42
- [93] Wang D, Mookherjee M, Xu Y and Karato S I 2006 The effect of water on the electrical conductivity of olivine *Nature* **443** 977–80
- [94] Tsuchiya J 2013 First principles prediction of a new high-pressure phase of dense hydrous magnesium silicates in the lower mantle 4570–3
- [95] Liu L, Du J, Zhao J, Liu H, Gao H and Chen Y 2009 Elastic properties of hydrous forsterites under high pressure: First-principle calculations *Phys. Earth Planet. Inter.* **176** 89–97
- [96] Dutta R and Mandal N 2012 Structure, elasticity and stability of reidite ( $\text{ZrSiO}_4$ ) under hydrostatic pressure: A density functional study *Mater. Chem. Phys.* **135** 322–

## Chapter 1

9

- [97] Ewing R C and Lutze W 1995 Zircon: A host-phase for the disposal of weapons plutonium *J. Mater. Res.* **10** 243–6
- [98] Ewing R C, Chakoumakos B C, Lumpkin G R and Murakami T 1987 The Metamict State *MRS Bull.* **12** 58–66
- [99] Geisler T, Pidgeon R T, Van Bronswijk W and Kurtz R 2002 Transport of uranium, thorium, and lead in metamict zircon under low-temperature hydrothermal conditions *Chem. Geol.* **191** 141–54
- [100] Pan Y, Fleet M E and MacRae N D 1993 Late alteration in titanite (CaTiSiO<sub>5</sub>): Redistribution and remobilization of rare earth elements and implications for U/Pb and Th/Pb geochronology and nuclear waste disposal *Geochim. Cosmochim. Acta* **57** 355–67
- [101] Cocherie A and Legendre O 2007 Potential minerals for determining U-Th-Pb chemical age using electron microprobe *Lithos* **93** 288–309
- [102] White L T and Ireland T R 2012 High-uranium matrix effect in zircon and its implications for SHRIMP U-Pb age determinations *Chem. Geol.* **306–307** 78–91
- [103] Reiners P W 2005 Zircon (U-TH)/He thermochronometry *Rev. Mineral. Geochemistry* **58** 151–79
- [104] Atreya S K, Hofstadter M H, In J H, Mousis O, Reh K and Wong M H 2020 Deep Atmosphere Composition, Structure, Origin, and Exploration, with Particular Focus on Critical in situ Science at the Icy Giants *Space Sci. Rev.* **216**
- [105] Helled R, Anderson J D, Podolak M and Schubert G 2011 Interior models of Uranus and Neptune *Astrophys. J.* **726**
- [106] Hubbard W B and Macfarlane J J 1980 Structure and Evolution of Uranus and Neptune *J. Geophys. Res.* **85**
- [107] Bethkenhagen M, Meyer E R, Hamel S, Nettelmann N, French M, Scheibe L, Ticknor C, Collins L A, Kress J D, Fortney J J and Redmer R 2017 Planetary Ices and the Linear Mixing Approximation *Astrophys. J.* **848** 67
- [108] Fortes A D and Choukroun M 2010 Phase behaviour of ices and hydrates *Space Sci. Rev.* **153** 185–218
- [109] Bethkenhagen M, French M and Redmer R 2013 Equation of state and phase diagram of ammonia at high pressures from ab initio simulations *J. Chem. Phys.* **138**
- [110] Benedetti L R, Nguyen J H, Caldwell W A, Liu H, Kruger M and Jeanloz R 1999 Dissociation of CH<sub>4</sub> at high pressures and temperatures: Diamond formation in giant planet interiors? *Science (80-. )*. **286** 100–2
- [111] Naden Robinson V, Marqués M, Wang Y, Ma Y and Hermann A 2018 Novel phases in ammonia-water mixtures under pressure *J. Chem. Phys.* **149**
- [112] Li X, Lowe A, Conway L, Miao M and Hermann A 2021 First principles study of



- dense and metallic nitric sulfur hydrides *Commun. Chem.* **4** 1–10
- [113] Teeratchanan P and Hermann A 2015 Computational phase diagrams of noble gas hydrates under pressure *J. Chem. Phys.* **143**
- [114] Takii Y, Koga K and Tanaka H 2008 A plastic phase of water from computer simulation *J. Chem. Phys.* **128** 204501
- [115] Hermann A, Ashcroft N W and Hoffmann R 2012 High pressure ices *Proc. Natl. Acad. Sci.* **109** 745–50



# First principles approach: A theoretical background

---

# 2

*Preamble*

*Born-Oppenheimer approximation*

*Thomas-Fermi model*

*Density functional theory*

*Hohenberg-Kohn theorems*

*Exchange-correlation functionals*

*Pseudopotential formalism*

*Ab-initio molecular dynamics*



## 2.1 Preamble

The theoretical discussions in this chapter need to begin with the most fundamental equation in quantum mechanics, the Schrödinger equation. The single particle Schrödinger equation in its time dependent form is

$$-\frac{\hbar^2}{2m}\nabla^2\psi(\vec{r},t)+V(r)\psi(\vec{r},t)=i\hbar\frac{\partial\psi(\vec{r},t)}{\partial t}, \quad (2.1)$$

where  $\psi(\vec{r},t)$  is the wave function for the particle and  $V(r)$  is the effective potential experienced by the particle. Contrary to the classical mechanics, the solution to Eq. 2.1 gives us the wave function which reveals only the probability of finding the particle in a particular interval of space, rather than the accurate position and momentum of the particle. The quantum description of a particle owes its peculiarity to the uncertainty in simultaneously determining non-commutative physical

## Chapter 2

observables. In essence, this uncertainty is fundamental, inherent, and irremovable characteristic of quantum mechanics. By invoking the separation of variables technique, the spatio-temporal nature of this equation can be further simplified. The decoupling of the space and time coordinates leads to the formation of two independent partial differential equations: one in 3-D space and the other in time. The time-independent equation involving the spatial wave function  $\psi(\vec{r})$  reads as:

$$\hat{H}\psi(\vec{r}) = E\psi(\vec{r}) \quad (2.2)$$

where  $\hat{H}$  is the well-known Hamiltonian Operator expressed as:

$$\hat{H} = -\frac{\hbar^2}{2m}\nabla^2 + V(r) \quad (2.3)$$

The eigen value of the Hamiltonian obtained by solving Eq. 2.3 represents the energy of the system. The final solution appears as a product of  $\psi(\vec{r})$  and  $\psi(t)$ , the later of which is the solution of the time dependent part, represented by an imaginary exponential function of time.

However, it is very unlikely to encounter a single particle system in real scenario. Most of the real-world systems consists of multiple atom or molecules. Thus, an extension of the single particle to many-body systems are often required. The time independent Schrödinger equation for an isolated N-electron many-body quantum system is represented by

$$\hat{H}\psi_i(\vec{x}_1, \vec{x}_2, \dots, \vec{x}_N, \vec{R}_1, \vec{R}_2, \dots, \vec{R}_M) = E_i\psi_i(\vec{x}_1, \vec{x}_2, \dots, \vec{x}_N, \vec{R}_1, \vec{R}_2, \dots, \vec{R}_M) \quad (2.4)$$

where,  $\psi_i$  depicts the wave function of the  $i^{th}$  state of the system, which in turn is a function of  $3N$  spatial coordinates and the  $N$  spin coordinates of the

## *First principles approach*

electrons, which are collectively termed as  $\{\vec{x}_i\}$  and the 3M spatial coordinates of the nuclei  $\{\vec{R}_A\}$ . For such an isolated system in the absence of any external force field, in the non-relativistic approximation, the Hamiltonian is expressed as:

$$\begin{aligned} \hat{H} = & -\frac{1}{2} \sum_{i=1}^N \nabla_i^2 - \frac{1}{2} \sum_{A=1}^M \frac{1}{M_A} \nabla_A^2 - \frac{1}{2} \sum_{i=1}^N \sum_{A=1}^M \frac{Z_A}{r_i - R_A} \\ & + \sum_{i=1}^N \sum_{j>1}^N \frac{1}{r_i - r_j} + \sum_{A=1}^M \sum_{B>1}^M \frac{Z_A Z_B}{R_A - R_B} \end{aligned} \quad (2.5)$$

For clarity Eqn. 2.5 is written by adapting the so-called system of atomic units, which allows us to drop the mass, charge etc. of the electron along with the Planck's constant and dielectric constant of the free space by setting them to unity.  $i, j$  run over the  $N$  electrons and  $A, B$  run over the  $M$  nuclei respectively with  $M_A$  being the mass of  $A^{th}$  nuclei. The first two terms represent the kinetic energy of the electrons and the nuclei, respectively. The last three terms signify the potential energy arising from the electrostatic interaction between electron-nucleus; repulsive interactions between electron-electron and nucleus-nucleus interactions separately.  $Z_A$  and  $Z_B$  are the charges of the  $A^{th}$  and  $B^{th}$  nuclei.

In order to gain an insight about the system under consideration, it is mandatory to solve the Schrödinger equation. But solving the Schrödinger equation is cumbersome for real system larger than the hydrogen or helium atom themselves, let alone any system which contains two or more electrons. Nevertheless, the condition is not as desolate as it appears to be. Realistic

## Chapter 2

physical intuitions enable one to put forward a few assumptions and approximations aimed at simplifying the Hamiltonian.

### 2.2 Born-Oppenheimer approximation

One of the first approximation made in the endeavor to reduce the Schrödinger equation to a tractable form is the Born-Oppenheimer approximation, also frequently called the adiabatic or the clamped nuclei approximation. Here we recognize that the masses of the nuclei exceed the mass of the electron by a large amount; even for the lightest atom hydrogen, its nucleus is almost 2000 times heavier than the electron. Being lighter, the electrons move on a faster timescale compared to the nucleus. Born and Oppenheimer utilized this significant mass differences into practical implementation. They postulated that the time required for changes to take effect at the electronic degrees of freedom are much lower than that of those nuclei, in a sense that the nuclei can be considered stationary, and the electrons can be essentially thought of moving through the swarm of fixed nuclei. This means that in Eq. 2.5 the kinetic energy of the nuclei reduces to null and the energy of interaction of various nuclei becomes essentially constant. Thus, without much loss of scientific precision, Eq. 2.5 can be replaced by an all-electron Hamiltonian as:

$$\begin{aligned}\widehat{H}_{elec} &= -\frac{1}{2} \sum_{i=1}^N \nabla_i^2 - \sum_{i=1}^N \sum_{A=1}^M \frac{Z_A}{r_i - R_A} + \sum_{i=1}^N \sum_{j>1}^N \frac{1}{r_i - r_j} \\ &= \widehat{T}_e + \widehat{V}_{Ne} + \widehat{V}_{ee}\end{aligned}\tag{2.6}$$



## *First principles approach*

The solution to the Schrödinger equation with all-electron hamiltonian  $\widehat{H}_{elec}$  is the electronic wave function  $\Psi_{elec}$  with corresponding electronic energy eigenvalue of  $E_{elec}$ .  $\Psi_{elec}$  is a function of the electron coordinates, while the nuclear coordinates do not explicitly appear in  $\Psi_{elec}$  and it depends on the positions of the nuclei only parametrically. The total energy of this all-electron system  $E_{tot}$  is thus expressed as the sum of  $E_{elec}$  and nuclear repulsion term, the latter of which is constant.

## **2.3 Thomas-Fermi Model**

The most notable among the conventional methods to solve the all-electron Schrödinger equation is the Hartree and the Hartree-Fock approximations. The latter approximation is essentially based on variational method to solve differential equations. The criticality here lies in the substitution of the wave function by a single Slater determinant, which takes into account the prerequisite of the orthonormality of the wave functions by default. Minimization of the Hartree-Fock energy then yields orthonormal single electron orbitals. But like the previous ones the Hartree-Fock method is also based on mathematically theorizing the wave function itself, which depends on  $3N$  spatial and  $N$  spin variables. Extending this method to study real world system where the number of electrons is very large becomes unmanageable very quickly. Mathematical operations on a wave function to extract physical observables thus outstretch to an astronomically large dimension, and they become computationally extravagant. Theoretical

## Chapter 2

physicists and chemists thus always strived to find an alternative route which can reduce the intricate and complex nature of wave function formalism.

The pioneering work of Thomas and Fermi [1], published in 1927, is regarded as the first attempt to hypothesize a physical quantity leaving out the wave function itself. They proved that the electron density is just as competent as the wave function to fully characterize a system of electrons. They considered a fictitious statistical quantum system of interacting electrons with a constant electron density  $\rho(\vec{r})$ . Their model accounts for only the kinetic energy with a quantum mechanics approach, considering the electron-electron and nuclear-electron interactions in the framework of classical mechanics. According to these considerations, their model arrived at the following approximated energy of an atom:

$$E_{TF}[\rho(\vec{r})] = \frac{3}{10}(3\pi^2)^{2/3} \int \rho^{5/3}(\vec{r}) d\vec{r} - Z \int \frac{\rho(\vec{r})}{r} + \frac{1}{2} \iint \frac{\rho(\vec{r}_1)\rho(\vec{r}_2)}{r_{12}} d\vec{r}_1 d\vec{r}_2 \quad (2.7)$$

Despite the brute-force simplification and crude approximation of the Thomas-Fermi model, which does not incorporate the exchange and correlation energies, its significance can be appreciated by perceiving that the energy is totally quantifiable in terms of electron density, without any additional physical attributes. The expression of total energy in this form has stimulated further introspection along this direction and reinforced the pathway for the development of the density functional theory with time.

## 2.4 Density Functional Theory

In the last five decades the density functional theory (DFT) has paved its own way from the fringe to the podium in each of the major science disciplines- quantum chemistry, solid state physics and material science. Furthermore, the computationally less expensive method of DFT has enabled researchers to corroborate experimental outcomes with theoretical calculations. It is a remarkable success of DFT to explore phenomena of macroscopic importance from the viewpoint of an atomistic description.

The section and the following sections provide an outline of the conceptual framework of DFT. DFT is a popular quantum chemical modelling method extensively used in computational study of real systems in diverse fields of scientific research. This method is specifically aimed to study the electronic structures at the ground state of many-particle systems employing only the electron density  $\rho(\vec{r})$  of single electron system together with the correlation and exchange energy of the electrons. Hohenberg and Kohn [2] first conceptualized the fundamental theorems of density functional theory, which was later proved by Kohn and Sham[3]. These two theorems laid the foundation of DFT.

### 2.4.1 Hohenberg and Kohn theorems

*Theorem #1: The external potential  $v_{ext}(r)$ , hence the total energy is a unique functional of the ground state electron density  $\rho(\vec{r})$ .*

## Chapter 2

The many-body wave function for the ground as well as excited states can be determined once the Hamiltonian of the system is fully known. Since the number of electrons  $N$  is determined by  $\rho(\vec{r})$ , and since  $N$  and the external potential  $v_{ext}(r)$  constitute the fix Hamiltonian of the system, it turns out that the electron density is capable alone to completely determine all the ground-state electronic properties of the system. Later, it was proved by Mermin[4] that not only the properties of ground state but finite temperature properties can also be determined from  $\rho(\vec{r})$ .

**Theorem #2:** *A universal functional of the energy,  $E[\rho]$ , can be defined in terms of the density alone. The exact ground state is the global minima of the functional.*

This theorem states that ground state electron density of the system is the one that minimizes  $E[\rho]$ , and the minimum of  $E[\rho]$  is equal to the ground-state energy. In essence, DFT is effectively a ground state theory.

Hohenberg and Kohn proved that the ground state electron density  $\rho_0(x, y, z) = \rho_0(r)$  uniquely determines the wave function, energy of the ground state and all other ground state electronic properties for systems having non-degenerate ground state. Theorem #1 states that the ground state energy  $E_0$  is a functional of  $\rho_0$ . The non-degenerate ground-state wave function can be represented as a unique functional of the ground-state density,

$$\psi_0(r_1, r_2, \dots, r_n) = \psi[\rho_0(r)]. \quad (2.8)$$

## *First principles approach*

Let us assume  $P$  to be a physical observable. Then as a consequence of Theorem #1 the expectation value of  $P$  will also be a functional of the electron density of the system under study in its ground state. Mathematically,

$$P_0 = P[\rho_0] = \langle \psi[\rho_0(r)] | P | \psi[\rho_0(r)] \rangle \equiv \langle \psi[\rho_0] | P | \psi[\rho_0] \rangle. \quad (2.9)$$

Thus, the energy eigenvalue of a system in its ground state can be expressed as an expectation value of the ground state Hamiltonian of the system.

$$E_{v,0} = E_v[\rho_0] = \langle \psi[\rho_0(r)] | H_e | \psi[\rho_0(r)] \rangle, \quad (2.10)$$

$H_e$  obeys the variational property, i.e.,

$$E_v[\rho_0] \leq E_v[\rho']. \quad (2.11)$$

where  $\rho_0$  is the ground state density in effect of the external potential  $V_{ext}$ , and  $\rho'$  is some arbitrary density other than that of the ground state one. The expectation value of the Hamiltonian with respect to some random wave function different from the wave function of the ground state will always lead to a higher energy than the exact ground state energy itself. Thus, mathematical representation of Theorem 2 confirms that

$$E_{v,0} = E_v[\psi_0] = \langle \psi_0 | H_e | \psi_0 \rangle \leq \langle \psi' | H_e | \psi' \rangle = E_v[\psi']. \quad (2.12)$$

The density functional expression of energy is given by

$$E_{DFT}[\rho_0(r)] = T_s[\rho_0(r)] + E_{ne}[\rho_0(r)] + E_{xc}[\rho_0(r)]J[\rho_0(r)], \quad (2.13)$$

where the first term on the right-hand side is the kinetic energy of the non-interacting electron of identical density,  $E_{ne}[\rho_0(r)]$  is the energy rising from the

## Chapter 2

interaction of electrons and ionic cores and  $E_{xc}[\rho_0(r)]$  represents the exchange and correlation energy. If we equate the exact energy of the system with the one obtained from DFT, the part that remains after subtraction gives an estimate of the exchange-correlation energy expressed as

$$E_{xc}[\rho_0(r)] = (T[\rho_0(r)] - T_s[\rho_0(r)]) + (E_{ee}[\rho_0(r)] - J[\rho_0(r)]) \quad (2.14)$$

Here, the bracketed term appearing first on the right-hand side is the kinetic correlation energy followed by the potential exchange and correlation energy.

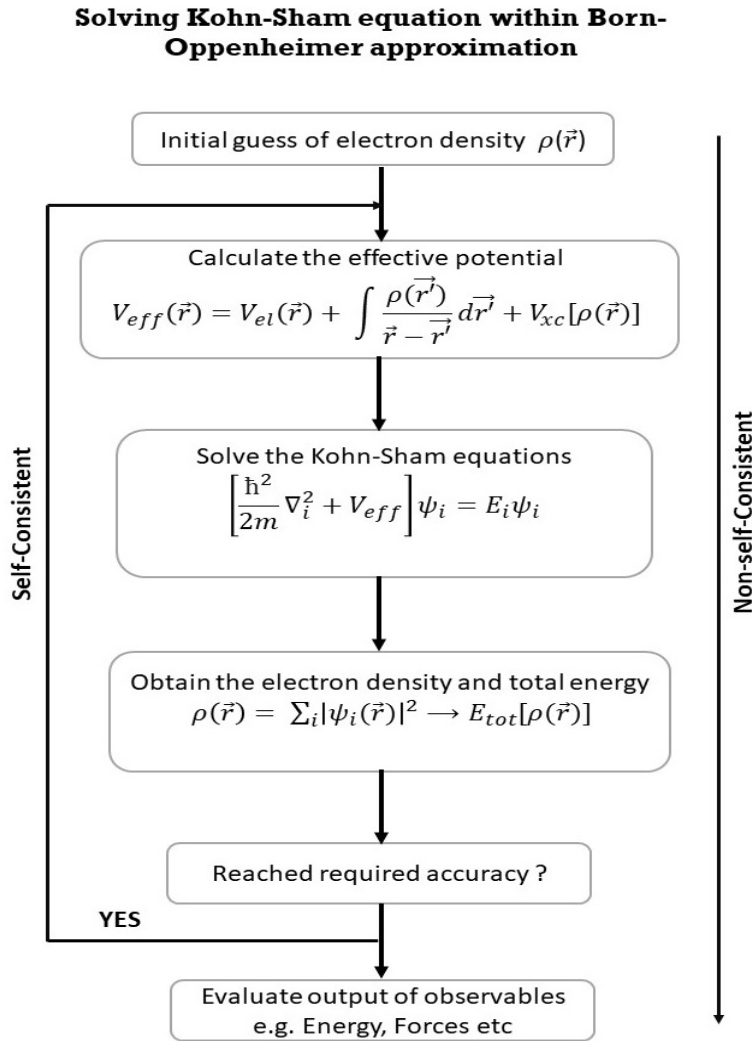


**Figure 2.1:** Self-consistent and non-self-consistent cycle as practically implemented in DFT simulation.

Hohenberg-Kohn theorems assert that, it is possible to calculate all the ground state properties of the many-particle system if the ground state electron density  $\rho_0(r)$  is known. Kohn and Sham also suggested a practical method for implementation of the DFT by finding the ground-state density of electrons,  $\rho_0(r)$ , and the energy  $E_0$  as a functional of  $\rho_0(r)$ . Figure 2.1 illustrates a schematic diagram of the series of steps, cumulatively known as the self-consistent cycle, to consistently approach the ground state electron density and further to calculate the desired physical properties from DFT simulation.

## **2.5 Exchange-correlation functionals**

In principle, the density functional theory is exact. If we know  $E_{xc}[\rho_0(r)]$ , the energy of the system will turn out to be exact electronic free energy. Unfortunately, the exact form of the exchange-correlation energy is not yet known. Since the Kohn-Sham equation contains this unknown functional, one needs to find some approximate approach to define  $E_{xc}[\rho_0(r)]$ .

A major branch, dedicated to the refinement of DFT involves constructing approximate empirical or semi-empirical functional forms of the exchange-correlation energy. By definition, these functional must be able to account for the kinetic correlation energy, which is the difference between the kinetic energy of the fictitious system of non-interacting electrons and the real one as well as the exchange energy associated with the anti-symmetry. The Kohn-Sham total energy also incorporates the correction to self-interaction energy and the Coulombic correlation term. A well-defined exchange

## Chapter 2

correlation functional is capable of determining all these energies with a minimum uncertainty.

### 2.5.1 Local density approximation (LDA)

Kohn and Sham (1965) also provided an approximate functional expression for the exchange correlation, called the local density approximation or LDA. Inspired by Thomas-Fermi model, in LDA the exchange correlation energy per electron at a point  $\mathbf{r}$  is considered the same as that for a homogeneous electron gas that has the same electron density at the point  $\mathbf{r}$ . Here, the dependence of the functional on the electron density has the mathematical form

$$E_{xc}^{LDA}[\rho(r)] = \int \rho(r) \varepsilon_{xc}[\rho(r)] \, dr. \quad (2.15)$$

$\varepsilon_{xc}$  is the exchange correlation energy per electron of a uniform electron gas with electron density  $\rho(r)$ . This has been precisely enumerated using Monte Carlo simulations by Ceperley and Alder [5]. In order to express it in analytic form, the parameterization has been done by Perdew and Zunger [6], and Perdew and Wang [7]. The functional  $E_{xc}^{LDA}$  is expressed as the sum of exchange energy and a correlation energy as,

$$E_{xc}^{LDA} = E_x^{LDA} + E_c^{LDA} \quad (2.16)$$

By construction, this approximation gives accurate results if the electron density of the system is homogeneous and does not vary rapidly in space to yield strong inhomogeneity in density. However, this approximation is found



to be effective in theoretical calculations for a wide range of materials, albeit with some limitations. For example, in molecules, LDA calculations usually yield excellent results for vibrational frequencies and equilibrium distances, but they somewhat overestimate the binding energies.

## 2.5.2 Generalized gradient approximation (GGA)

The exchange-correlation energy of inhomogeneous density differs substantially from the homogeneous distribution of density. Such a system is better tackled with generalized-gradient approximations (GGA). In this approximation the exchange-correlation energy,  $E_{xc}^{GGA}[\rho(r)]$  also contains the gradient of electron density to compensate for its inhomogeneous variation. Mathematically,

$$E_{xc}^{GGA}[\rho(r)] = \int f[\rho(r)]\nabla(\rho) \, dr, \quad (2.17)$$

where  $f$  is some empirical or semi empirical functional of electron density. Like LDA,  $E_{xc}^{GGA}[\rho(r)]$  can also be represented as the sum of an exchange and a correlation part, which are individually handled.

$$E_{xc}^{GGA} = E_x^{GGA} + E_c^{GGA}. \quad (2.18)$$

GGA are more physically consistent as the true electron density is expected to show some gradient dependent variation. The most popular parameterized analytic form of GGA was given by Perdew-Becke-Ernzerhof [8]. However, the choice of the exchange-correlation is not obvious. It depends entirely on the

## Chapter 2

system under study and, also on the physical properties that one is interested to explore.

### 2.5.3 Hybrid exchange-correlation functionals

Nowadays, a new class of sophisticated functionals is extensively used in DFT simulations due to its higher level of accuracy, compared to other functionals mentioned earlier in the discussion. These hybrid functionals consists of a portion which is the exact exchange from Hartree-Fock calculations; the rest of the exchange-correlation functional is sought from other sources, like *ab-initio*. The exchange energy functional is expressed in terms of Kohn-Sham orbitals,

$$E_{xc}^{Hybrid} [n(r)] = E_x^{GGA} + E_c^{GGA} + bE_x^{HF}. \quad (2.19)$$

Here  $E_x^{GGA}$  and  $E_c^{GGA}$  are the exchange and correlation energies.  $E_x^{HF}$  is the exact exchange energy from Hartree-Fock controlled by an empirical parameter  $b$ . The most popular hybrid functional was proposed by Becke et al.[9].

It is important to note that, irrespective of functionals being used, these types of calculations are put in the category of first-principles calculations, in the sense that they do not involve experimental inputs are, other than the fundamental physical constants.

## 2.6 Pseudopotential formalism

Solutions to the Kohn-Sham equations effectively involve the expansion

## *First principles approach*

of the auxiliary Kohn-Sham orbitals in terms of some known basis functions. There exist a range of the basis functions that can be chosen for calculations. Most of the conventional quantum chemistry tools often utilize Gaussian functions. For highly localized orbitals, these functions are found to be an excellent choice. In the course of flourishing research, theoretical chemists have developed basis sets that are well suited for a wide range of materials. The major downside of the Gaussian functions is that the superiority of the basis sets depends on the preference of the user. However, their transferability and the reproducibility of computational results become a serious issue when one deals with diverse systems.

Plane waves are regarded as an alternative set of functions without any undue bias and can also be improved systematically. Plane waves adapted naturally to systems with periodic boundary conditions make their use advantageous over the Gaussian basis functions. Calculations employing plane waves are relatively straightforward, where the forces and the stress tensors can be readily evaluated like energy. However, if any system contains well localized core orbitals or valence orbitals within the core region of the atom, which require to oscillate widely in order to maintain orthogonality with the core orbitals, then a substantial number of plane waves is required to describe the rapidly varying nature of the orbitals. For this reason, to deal with a real system, it is often crucial to bring forth an extra approximation, known as the pseudopotential approximation, to speed up the calculations. Most of the plane wave calculations are thus implemented by using pseudopotentials.

## *Chapter 2*

### **2.6.1 Norm-conserving pseudopotentials**

The prime objective of pseudopotential approximation is to eliminate the electrons near the core from explicit calculations since they do not take part in bond formation and correspondingly in determining the physical properties of material, at least to the limit where their binding energy exceeds the energy involved in the chemical property under study. So, the core electrons are assumed to freeze around the nuclei and the system is then reformulated as an assembly of valence electrons surrounding a non-polarizable rigid ionic core. In this way, theoretically the all-electron atomic potential is replaced by an effective approximate potential where pseudo wave functions consisting of very few nodes are utilized to describe the valence electrons. The only matter that one must be careful about now is the oscillation of the valence wave functions in the core since they must be orthogonal to the wave functions representing the core electrons. This is achieved by the introduction of a pseudopotential which can effectively replace the ionic Coulomb potential in a manner that the eigenvalues of the pseudo wave function match the all-electron ones in some reference configuration of the atom. The pseudo-wave functions are modelled to coincide with the all-electron wave functions beyond a well-defined core radius, keeping them as smooth as feasible within the core radius. However, the only constraint in this modelling is concerned with the orthogonality of wavefunctions. Furthermore they must be normalized to obtain the construction of Norm-conserving pseudopotentials[10]. To satisfy this specific condition, the pseudo wave functions must incorporate the angular momentum.

## *First principles approach*

Different angular momenta for different pseudo wave functions have different eigen values, i.e., they are eigen functions of distinct potentials. But, the difference of the pseudo wave functions is limited within the core region as the pseudo wave functions beyond the core radius replicate the all-electron wave functions. Based on this argument Hamman et al. [11] and Kerker [12] arrived at the following form of the pseudopotential:

$$V_a(\mathbf{r}, \mathbf{r}') = V_a^{loc}(r)\delta(\mathbf{r} - \mathbf{r}') + \sum_{l=0}^{l_{max}} V_{a,l}(r) P_l(\hat{\mathbf{r}}, \hat{\mathbf{r}}')\delta(\mathbf{r} - \mathbf{r}') \quad (2.20)$$

where  $a$  refers to the atom.  $V_a^{loc}(r)$  is the long-range local part and  $V_{a,l}(r)$  is the short-range part depending on angular momentum.  $P_l(\hat{\mathbf{r}}, \hat{\mathbf{r}}')$  i.e., the projection operator on the angular momenta  $l$  is given by

$$P_l(\hat{\mathbf{r}}, \hat{\mathbf{r}}') = \sum_{m=-l}^l Y_{l,m}(\theta, \phi) Y_{l,m}^*(\theta', \phi') \quad (2.21)$$

here  $Y_{l,m}$  are the spherical harmonics.

### **2.6.2 Ultrasoft pseudopotentials**

In case of the first-row element carbon, the second-row element oxygen and nitrogen, the valence orbitals are well localized as shallow core states that are even more dominant in the d-orbitals of transition metal elements. The principle of norm conservation thus can be a very limiting factor for these elements. Since the extraction energies of the shallow lying orbitals are comparable to the valence energies, they must be accounted for in calculations. In these cases, the norm conservation requirement of pseudopotentials demands a huge number of pseudo plane waves to reach acceptable accuracy. Vanderbilt [13] provided a general prescription in which the constraint of norm

## *Chapter 2*

conservation can be removed by constructing smoothly varying wavefunction which match with the all-electron one beyond cut-off radius. However, one has to compensate for the charge density since the pseudo wave functions are not orthonormal anymore. This is achieved by adding an augmentation part. These much softer Vanderbilt pseudopotentials or the ultrasoft pseudopotentials have much lower cut-off energy than the norm conserving ones and thus yield better transferability and reproducibility. Blochl, in 1994, proposed a method to reconstruct the all-electron wave function within the core region[14]. This particular method, viz. the projected augmented wave (PAW), is closely related to the Vanderbilt's soft pseudopotential formalism, and has been observed to be efficient in reproducing effectively identical results of all electron calculations.

### **2.7 Ab-initio molecular dynamics**

Standard DFT has become de facto the method of preference to probe the static or ground state of matter. Over the years the success enjoyed by DFT can largely be attributed to its scalability across different system size and its excellent accuracy in reproducing the microscopic ground state properties. One can then pose a question- is it possible to combine this electronic-structure method with molecular dynamics to obtain an equally accurate description of time averaged thermodynamic properties of systems if it features ergodicity? This question has been addressed! This section lays out a brief account of the ab-initio molecular dynamics method which has been successfully implemented to study high-temperature (beyond debye temperature, even beyond melting

## *First principles approach*

point) properties of atomic and molecular systems, to explore the dynamics of chemical reactions, and also to accurately identify characteristic features of a potential energy surface.

In classical molecular dynamics the system is assumed to be made up of point-like rigid and massive nuclei. These nuclei move under the influence of forces acting between them which are derived from effective potentials albeit empirically devised. Then, it is simply the integration of Newton's equation of motion that provides one with the microscopic trajectory of each individual atom of the system under study. Ab-initio molecular dynamics (AIMD) modelling is motivated by the same consideration, treating the nuclei of atoms as classical point-like particles. The only exception in this approach is that the forces acting on the atomic nuclei are quantum mechanical in nature, and hence they are calculated within the framework of electronic-structure or more specifically the DFT method. However, for the application of this method in practice, the Born-Oppenheimer approximation is still imposed, ensuring that individual treatments of the electronic subsystem remains appropriate.

Standard DFT enables us to self-consistently arrive at the ground state of any chosen ionic configuration and , the forces acting on the individual ions can be calculated by Hellmann-Feynman's [15] theorem. Once a full account of the ionic forces is available, their effect on the evolution of the nuclear trajectories in time can be obtained. The first AIMD simulations was performed by Car and Parrinello[16] back in 1985. There are various algorithms

## Chapter 2

developed in the domain of classical mechanics based on finite-differences approach to solve Newton's equation of motion, the most notable among them

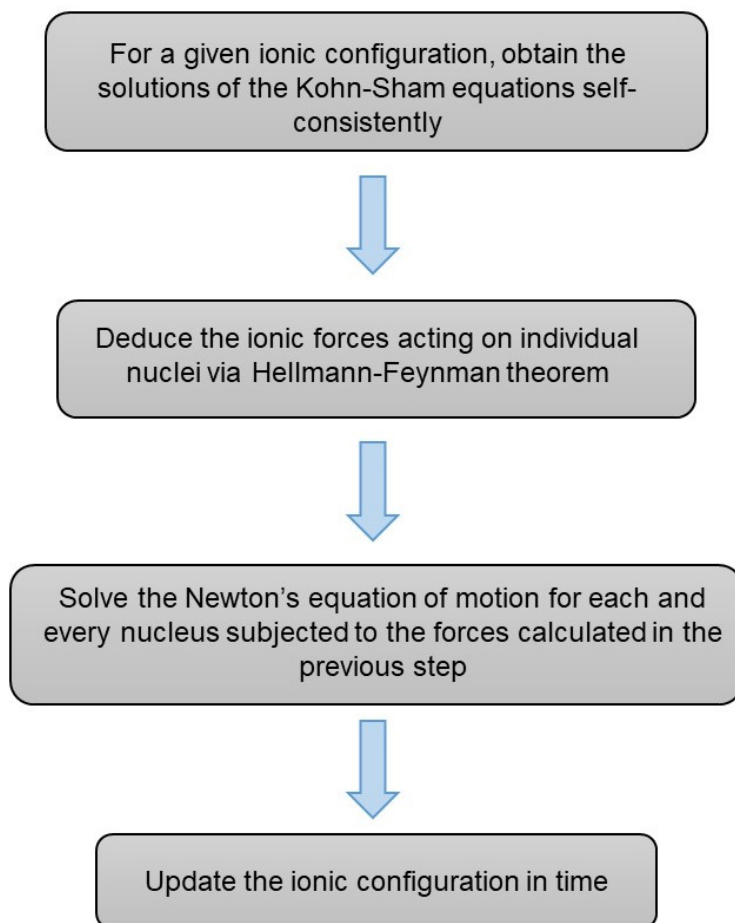


**Figure 2.2:** Flow chart of the steps as implemented in ab-initio molecular dynamics.

is the Verlet algorithm[17]. Figure 2.2 represents the schematic of the systematic method to implement AIMD in practice.

In this way, all the nuclei move along different trajectories on the much strived Born–Oppenheimer surface, i.e., at any instant configuration of the nuclei the electrons are guaranteed to be in the ground state. The first two steps are taken care by the DFT method. The third step involves iterative solution of the classical equation of motion, where Verlet algorithm plays an



## *First principles approach*

important role. The first and foremost practice to solve the Newton's equation of motion for a swarm of nuclei is to discretize it which is represented by:

$$m_i \frac{\partial v_i}{\partial t} = F_i \quad (2.22)$$

where  $m_i$  is the mass of  $i^{\text{th}}$  nuclei, with  $v_i$  and  $F_i$  being its velocity and the force acting on it respectively. Next the time is divided into several equal time steps  $\Delta t$  and the approximate solution to the Newton's equation of motions of the nuclei are obtained using the Verlet algorithm. The positions and velocities of the nuclei in the spatio-temporal phase space are updated following this algorithm as:

$$r_i(t + \Delta t) = r_i(t) + v_i(t)\Delta t + \frac{1}{2m_i} F_i(t)\Delta t^2 \quad (2.23)$$

$$v_i(t + \Delta t) = v_i(t) + \frac{1}{2m_i} (F_i(t) + F_i(t + \Delta t))\Delta t \quad (2.24)$$

If the time steps in Verlet algorithm are chosen small enough compared to the vibrational time period of the system, it conserves the energy to an excellent accuracy in both short- and long-time scale.

In statistical mechanics, the average of any physical observable is calculated as an ensemble average. It is a standard result of statistical mechanics that for an ergodic system the time average and ensemble average converge to a common magnitude as shown by Gibson et al.[18]. There are two major ensembles employed in AIMD simulation. However, the choice of ensemble depends on the problem itself and on the physical property under observation. If the number of atoms,  $N$  and volume of the simulation cell,  $V$

## *Chapter 2*

are kept fixed and the system is allowed to evolve in time, the simulation generates configurations in the constant energy hypersurface that are spread across the phase space according to the microcanonical ensemble or  $(N, V, E)$  ensemble. Sometimes it is mandatory to resort to ensemble other than the microcanonical one, for example the canonical ensemble or the  $(N, V, T)$  ensemble. In canonical ensemble the thermal averages are calculated at constant temperature,  $T$ . The numerical prescription to achieve this is to couple the system under study to an external heat bath (the degree of freedom of the heat bath far exceeds that of the system, so that its temperature remains essentially constant), as proposed by Andersen [19] or Nose' [20] and Hoover [21]. In simulation they are termed as Anderson thermostat or Nose'-Hoover thermostat. I conclude this chapter by recalling another crucial result of statistical mechanics. Irrespective of which ensemble is employed, the thermal averages calculated either in the microcanonical or in the canonical ensemble converges to each other for a sufficiently large system. The next chapter introduces the theoretical premises useful for calculating several physical properties of interest.

**References:**

- [1] Thomas L H 1927 The calculation of atomic fields *Math. Proc. Cambridge Philos. Soc.* **23** 542–8
- [2] Hohenberg P and Kohn W 1964 Inhomogeneous Electron Gas\* *Phys. Rev.* **136** 864–971
- [3] Kohn W and Sham L J 1965 Self-Consistent Equations Including Exchange and Correlation Effects\* *Phys. Rev.* **140** 1133–8
- [4] Mermin N D 1965 Thermal Properties of the Inhomogeneous Electron Gas *Phys. Rev.* **137** A1441–3
- [5] Ceperley D M and Alder B J 1980 Ground state of the electron gas by a stochastic method *Phys. Rev. Lett.* **45** 566–9
- [6] Perdew J P and Zunger A 1981 Self-interaction correction to density-functional approximations for many-electron systems *Phys. Rev. B* **23** 5048–79
- [7] Perdew J P and Wang Y 1992 Accurate and simple analytic representation of the electron-gas correlation energy *Phys. Rev. B* **45** 13244–9
- [8] Perdew J P, Burke K and Ernzerhof M 1996 Generalized Gradient Approximation Made Simple *Phys. Rev. Lett.* **77** 3865–8
- [9] Becke A D 1993 Density-functional thermochemistry. III. The role of exact exchange *J. Chem. Phys.* **98** 5648–52
- [10] Troullier N and Martins J L 1991 Efficient pseudopotentials for plane-wave calculations *Phys. Rev. B* **43** 1993–2006
- [11] Hamann D R, Schlüter M and Chiang C 1979 Norm-Conserving Pseudopotentials *Phys. Rev. Lett.* **43** 1494–7
- [12] Kerker G P 1980 Non-singular atomic pseudopotentials for solid state applications *J. Phys. C Solid State Phys.* **13**
- [13] Vanderbilt D 1990 Soft self-consistent pseudopotentials in a generalized eigenvalue formalism *Phys. Rev. B* **41** 7892–5
- [14] Blöchl P E 1994 Projector augmented-wave method *Phys. Rev. B* **50** 17953–79
- [15] Feynman R P 1939 Forces in Molecules *Phys. Rev.* **56** 340–3
- [16] Car R and Parrinello M 1985 Unified Approach for Molecular Dynamics and Density-Functional Theory *Phys. Rev. Lett.* **55** 2471–4
- [17] Verlet L 1967 Computational “Experiments” on Classical Fluids. I. Thermodynamical Properties of Lennard-Jones Molecules *J. Phys. D. Appl. Phys.* **159** 98–103
- [18] Gibson J B, Goland A N, Milgram M and Vineyard G H 1960 Dynamics of Radiation Damage *Phys. Rev.* **120** 1229–53

## ***Chapter 2***

- [19] Anderson H C 1980 Molecular Dynamics Simulations at Constant Temperature and Pressure *J. Chem. Phys.* **72** 2384–93
- [20] Nosé S 1984 A unified formulation of the constant temperature molecular dynamics methods *J. Chem. Phys.* **81** 511–9
- [21] Hoover W G 1985 Canonical dynamics: Equilibrium phase-space distributions *Phys. Rev. A* **31** 1695–7

## Computational methodologies

---

*Foreword*

*Equation of states of solid*

*Phase transition*

*Electronic properties*

*Quasi-harmonic approximation*

*Vibrational frequencies (phonons)*

*Diffusion coefficient*

*Electrical conductivity*

*Radial and pair distribution function*



### 3.1 Foreward

The fundamentals of density functional theory (DFT) and ab-initio molecular dynamics (AIMD) have been laid out in the previous chapter. In the framework of DFT, the total energy of an atomic/molecular system or clusters is calculated from the charge density of electrons. The energy arising from the motion of the nuclei, treated in a classical manner, are then brought together within the domain of Born-Oppenheimer approximation. The total energy from the DFT and the kinematic variables from the AIMD are consequently utilized to enumerate several static and finite temperature properties of the system under study. This chapter provides the theoretical method used to calculate such properties. The following table categorically lists a set of the important physical properties, however, some of them have been evaluated from the first-principles calculations mentioned in Chapter 2.

**Table 3.1:** Static and finite-temperature properties calculated in the domain of both DFT and AIMD simulations.

## Chapter 3

<b>Static properties from DFT</b>	<b>Finite-Temperature properties from DFT</b>	<b>Finite-Temperature properties from AIMD</b>
<i>Bulk Moduli</i>	<i>Thermoelastic constants</i>	<i>Diffusion coefficients</i>
<i>Elastic constants</i>	<i>Chemical potentials</i>	<i>Electrical conductivity</i>
<i>Band gap</i>	<i>Partitioning Coefficients</i>	<i>Viscosity</i>
<i>Density of states</i>	<i>Superconducting temperature</i>	<i>Melting points</i>
<i>Phonon frequencies</i>	<i>Thermal Expansivity</i>	<i>Superionicity</i>

### 3.2 The equation of state for solids

At zero temperature, the internal energy is the most basic thermodynamic variable associated with a system. The preliminary step of a DFT calculation is to utilize these internal energies to evaluate the equation of state of the system of interest. To begin with, the ionic degrees of freedom for a given set of unit cell parameters defining the crystal symmetry of the system, must undergo full relaxation. This relaxation procedure considers both the atomic positions and the lattice parameters. This allows one to identify the most stable configuration of the atoms i.e., the equilibrium structure by simply minimizing the total energy with respect to the ionic positions as well as lattice parameters. The relaxation of the latter ensures that no external stress/pressure is acting on the system. A similar procedure is repeated for a set of lattice parameters chosen around the equilibrated one. We are then left with a list of different total energies accounting for distinct lattice parameters, and the global minimum of the volume is obtained by plotting the total energies against the systems' volumes. This minimum volume corresponds to the system



optimized at temperature,  $T = 0\text{K}$  and pressure,  $P = 0\text{ GPa}$ . There are several equations of state of solids that elucidate the energy-volume or pressure-volume relations. The most extensively used equation of state is the 3<sup>rd</sup> order Birch-Murnaghan equation of state[1,2],

$$P(V) = \frac{3B_0}{2} \left[ \left( \frac{V_0}{V} \right)^{\frac{7}{3}} + \left( \frac{V_0}{V} \right)^{\frac{5}{3}} \right] \left\{ 1 + \frac{3}{4} (B'_0 - 4) \left[ \left( \frac{V_0}{V} \right)^{\frac{2}{3}} - 1 \right] \right\}. \quad (3.1)$$

where  $V_0$  and  $V$  are the equilibrium and distorted volumes,  $P$  is the deformed pressure. The slope of the pressure-volume fit to Eq. 3.1 yields the zero-pressure bulk modulus which can be expressed as

$$B_0 = -V \left( \frac{\partial P}{\partial V} \right)_{P=0}. \quad (3.2)$$

The pressure-derivative of the bulk modulus can also be calculated from

$$B'_0 = \left( \frac{\partial B}{\partial P} \right)_{P=0}. \quad (3.3)$$

Figure 3.1 illustrates such a Birch-Murnaghan equation of state for thorite [ThSiO<sub>4</sub>].

The Birch-Murnaghan equation considers the variation of volume up to 3<sup>rd</sup> order. Rose and Vinet[3] proposed a modified version of the Birch-Murnaghan equation of state, which is exponential in nature and thus contains higher order terms of volume. The Rose-Vinet equation of state is represented by

$$P = 3B_0 \left( \frac{1-\eta}{\eta^2} \right) \exp \left[ \frac{3}{2} (B'_0 - 1)(1 - \eta) \right], \quad (3.4)$$

where  $\eta$  is the cubic root of the specific volume,

### Chapter 3

$$\eta = \left(\frac{V}{V_0}\right)^{\frac{1}{3}}. \quad (3.5)$$

These equations of state are frequently used to determine high-pressure structures of the crystalline phases.

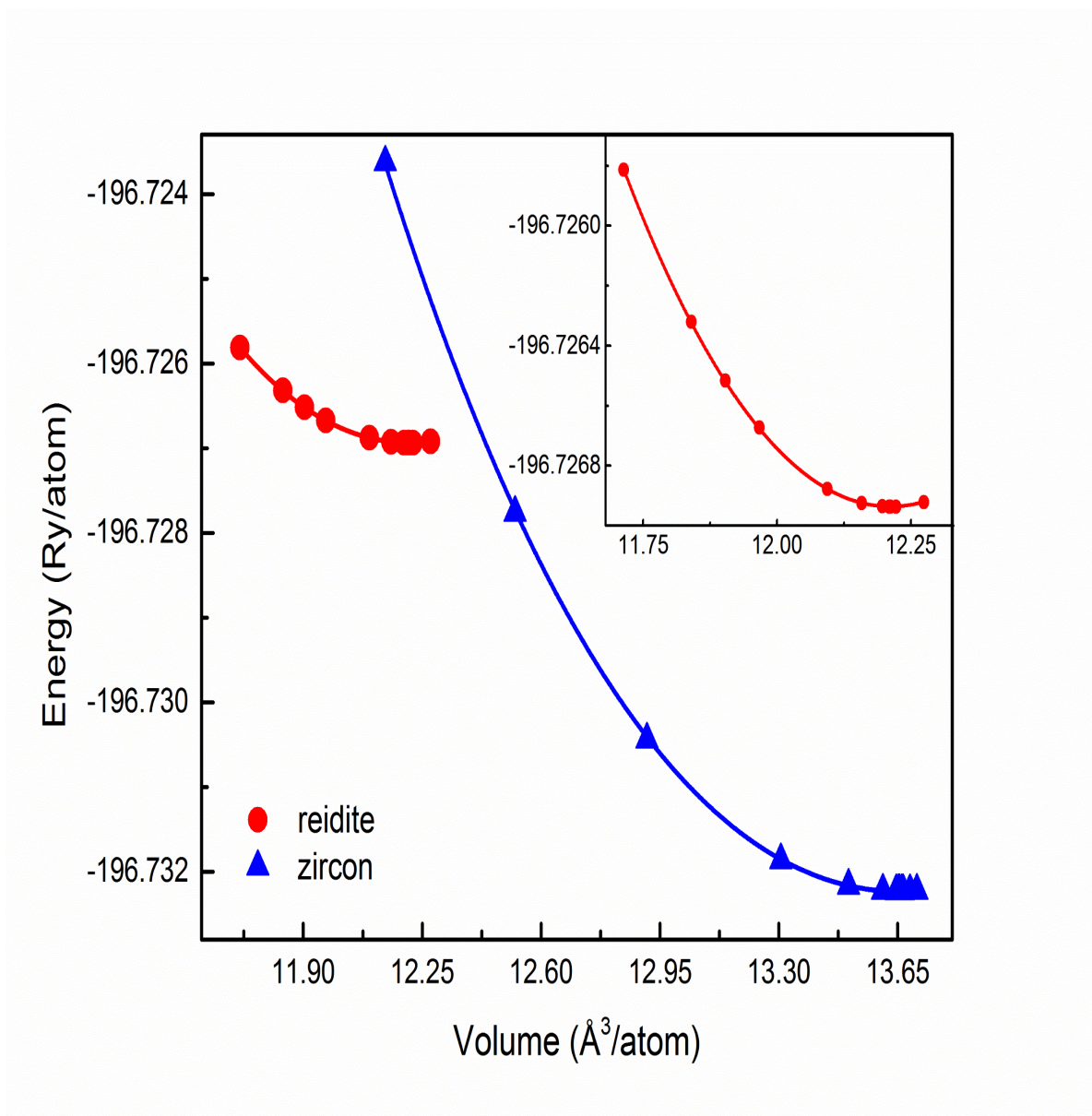


**Figure 3.1:** The Birch-Murnaghan equation of states of zircon- and reidite-type phases of ThSiO<sub>4</sub>. The inset represents the enlarged equation of state of the reidite-type ThSiO<sub>4</sub>.

### 3.3 Phase transition

Crystalline solid phases can undergo structural transitions to new ones[4–8] with increasing external pressure. The new structures often belong to the same class of Bravais lattice but differing in space group. They can also transform to a whole new class of Bravais lattice with lower or higher symmetry. Since the atomic configurations of crystalline phases change, the corresponding energies also differ from each other. The pressure at which the transition occurs can be determined from the slope of the common tangent to the energy-volume curves of the parent and daughter structures. However, if the system under study demonstrates several consecutive transitions at different pressures e.g. as observed in molecular ice of water[9] ammonia-water

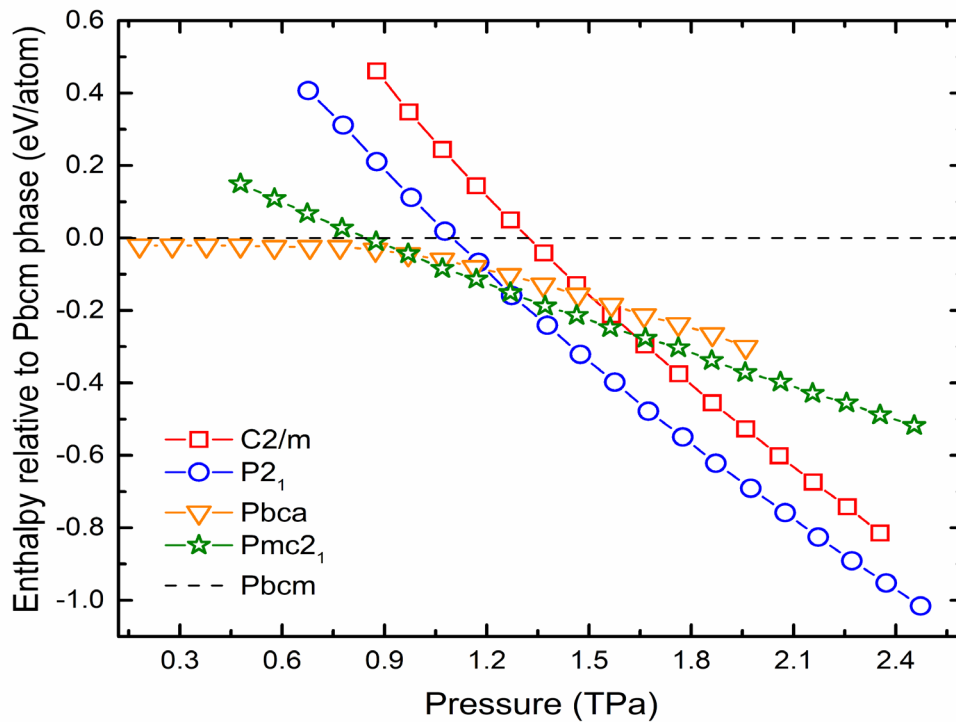


**Figure 3.2:** Ground state enthalpies of different crystalline phases of water ice relative to the Pbcm phase in the pressure range 0.15-2.5 TPa (after Hermann et. al., PNAS, ref. [9]).

## Chapter 3

mixture[10] etc. , an alternative approach, called the ‘Enthalpy crossover’ method becomes much easier to employ. The second method has been utilized in all the present calculations as the method yields a better accuracy. In this method, the point of intersection of the enthalpy-pressure curves for two corresponding crystal structures marks the transition pressure. The enthalpy of the system can be calculated using first-principles technique by computing the internal energy  $U$  and pressure  $P$  as a function of volume  $V$  and then by following the relation

$$H = U + PV \quad (3.6)$$

Calculated enthalpies of two (or more) structures are then plotted against pressure to find their point of intersection(s) to identify the transition pressure(s). The phase with the lowest enthalpy in a chosen pressure range confirms that it is energetically stable, as compared to the others. Figure 3.2 demonstrates the high-pressure structural transition in crystalline water. In the pressure range 0.9-1.3 TPa Pmc2<sub>1</sub> phase is the most stable one. Beyond 1.3 TPa, it is succeeded by the P2<sub>1</sub> phase, which shows its stability up to 2.5 TPa. Apart from the structural transition, the enthalpy-crossover method can also be used to study pressure induced spin transitions[11–13], often observed in mineralogical phases

## 3.4 Electronic properties

### 3.4.1 Band structures

DFT is essentially an electronic-structure method, where the electronic

## *Computational methodologies*

degrees of freedom and its charge density are of prime concern. The charge density derived from DFT can further be exploited to compute several other electronic properties of interest, e.g., the band structures and density of states (DOS). The band structure of a solid is a description of the electronic energy levels subjected to a periodic potential in terms of a set of continuous energy functions. For band structure calculations, a series of successive k-points are chosen to define a path in the first Brillouin zone of the reciprocal space of the crystal. The Kohn-Sham equations are then solved at each chosen k-point along the k-path. It should be noted that the choice of the k-points greatly influences the band structure calculation, since the positions of the k-points in the reciprocal space are dictated by crystal symmetry. The present study followed the systematic steps mentioned below to calculate the band structures of a number of mineral phases:

- First, a self-consistent (scf) calculation is performed, followed by the iterative diagonalization of the Hamiltonian of the system using the wave functions generated in the previous scf step until one reaches the user-defined convergence criteria on energy and force. This step of calculation follows the evaluation of Fermi energy, focusing exclusively on the occupied bands.
- In the second step, a non-self-consistent (nscf) calculation is performed by setting a very tight convergence criteria to implement superposition of the atomic orbitals. Unlike the previous step, the Hamiltonian is diagonalized only on the chosen k-point defining the k-path as mentioned in the nscf input file. The number of bands to calculate are

## **Chapter 3**

set in this step to a higher number than the occupied bands since the nscf calculation takes into account the empty bands also.

- Next, the eigen values of the Hamiltonian, i.e., the energies are calculated at the neighboring k-points by virtue of the overlapping eigen vectors, i.e., wave functions. The results are collected to generate the band-structure plot.

The advantage of the band structure calculation is that apart from the energy eigen values, it also assesses the eigen vectors at the given k-points of the Brillouin zone.

### **3.4.2 Density of states (DOS)**

The band structure of a solid has generally electronic states spread along a line of chosen high-symmetry points. There are several electronic properties that rely on the distribution of electronic states across the entire Brillouin zone. The density of states (DOS) provides a full account of this distribution. The method used to calculate DOS is similar to that for band structures, but we need a dense k-point grid, instead of a predefined k-path. For an accurate description of the DOS, the user needs to employ the improved tetrahedron method[14] in order to sample the Brillouin zone, which demands a gamma point centered k-point grid. Here also a nscf step follows a scf calculation. The number of electronic states vs energy data is then captured in a file for a graphical plot. The band structure and DOS calculations can be used further to determine a number of electronic and optical properties, such as band gap, defect and surface states, dielectric functions, and refractive index. Based on

the band gap, materials are categorized into conductor, semi-conductor or insulator. Additionally, DOS offers the information about the dominant orbitals near Fermi level and the state of hybridization of the different chemical bonds [15–18]. The density of states of pure zircon ( $\text{ZrSiO}_4$ ) with space group: I41/amd in ambient condition is illustrated in Figure 3.3 that shows the total density of states as well as the orbital decomposed contribution of each

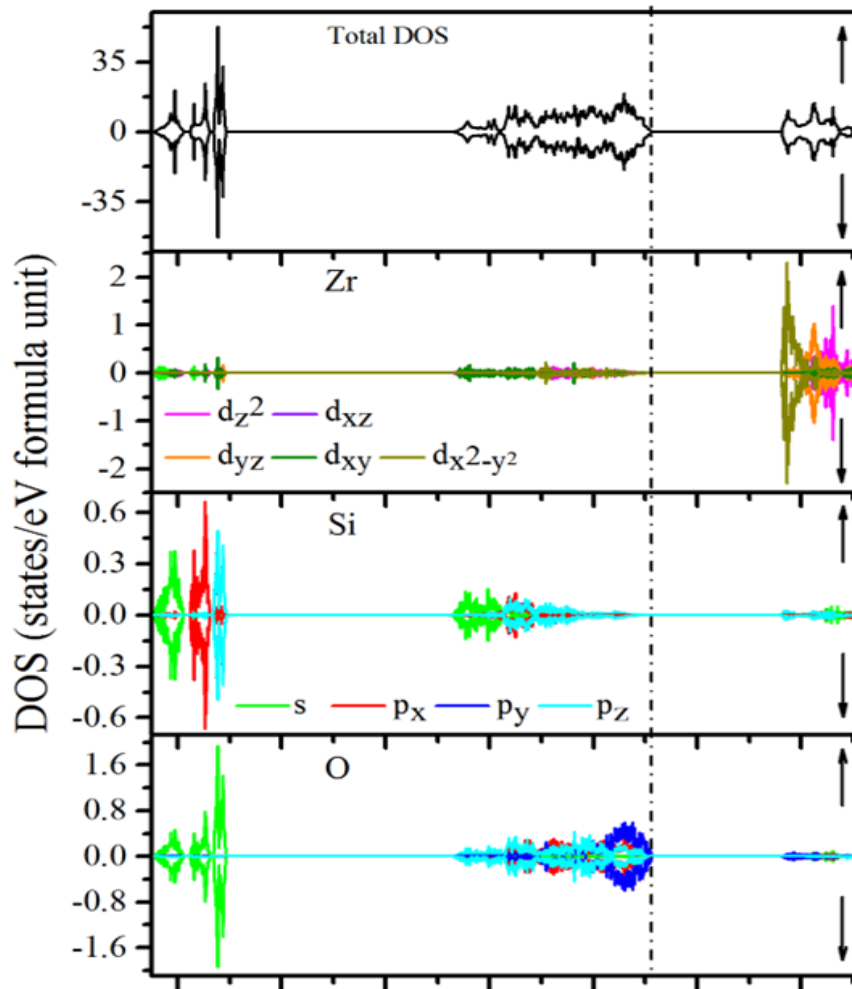


**Figure 3.3:** Total and partial density of states of pure zircon. The up and down arrow represents the up and down spin configurations of the electrons. The vertical dashed line denotes the Fermi level.

atomic species. It is clear that the states near the Fermi level are predominantly occupied by the p-orbital of O and d-orbital of Zr. The valence

## Chapter 3

bands at low energy levels are mostly populated by the s-orbitals of O and s- and p-orbitals of Si. The difference in energy between the valence and conduction bands ( $\sim 3.5$  eV) suggests that  $\text{ZrSiO}_4$  is an insulator.

### 3.5 Quasi harmonic approximation

The previous sections covered an account of the physical properties evaluated at zero temperature. This section is extended to include the description of physical properties at finite, albeit low temperatures. For a given finite temperature the Helmholtz free energy  $F$  gives a relatively more accurate account of energy of the system compared to the internal energy  $U$ . The Helmholtz free energy of the system can be calculated in the regime of so-called ‘Quasi-harmonic approximation’. First, the free energy of a system,  $U$  is expanded around positions of the nuclei which are already equilibrated. The first term so obtained represents the energy of the system, where the ions are located in their equilibrium position,  $E_{perf}(V, T)$ . This energy depends on both  $V$  and  $T$  as the temperature is finite. The linear term appearing in the expansion reduces to zero when the system remains in the minimum-energy configuration. If we neglect the 3<sup>rd</sup> and higher order terms in displacements of the nuclei, the quasi-harmonic energy is given by:

$$U_{harm} = E_{perf} + \frac{1}{2} \sum_{ls\alpha, lt\beta} \phi_{ls\alpha, lt\beta} u_{ls\alpha} u_{lt\beta} \quad (3.7)$$

where,  $\phi_{ls\alpha, lt\beta}$  is the force constant matrix,  $u_{ls}$  is the displacement of the  $s$  atom in the  $l$  unit cell.  $\alpha \beta$  denotes the cartesian components. Thus, the quasi-



harmonic approximation yields the following expression of Helmholtz free energy

$$F(V, T) = E_{perf}(V, T) + F_{harm}(V, T) \quad (3.8)$$

In particular, the 2<sup>nd</sup> term on the right-hand side of Eq. 3.8 can be explicitly written as,

$$F_{harm} = k_B T \sum_n \ln(2 \sinh(\hbar \omega_n / 2k_B T)), \quad (3.9)$$

the summation runs over the  $n$  vibrational modes with frequency  $\omega_n$ . The periodicity of crystal allows us to define vibrational frequencies associated with wave vectors denoted by  $\mathbf{k}$  where each wave vector possess three independent vibrational modes corresponding to each atom constituting the crystal. If  $\omega_{\mathbf{k}i}$  denotes the  $i^{\text{th}}$  mode's frequency with wave vector  $\mathbf{k}$ , Eq. 3.9 can be rewritten in terms of wave vectors as

$$F_{harm} = k_B T \sum_n \ln(2 \sinh(\hbar \omega_{\mathbf{k}i} / 2k_B T)). \quad (3.10)$$

Once the quasi-harmonic Helmholtz free energy is available, physical conditions, e.g., pressure at different temperatures can be readily calculated from the following equation.,

$$P = - \left( \frac{\partial F}{\partial V} \right)_T = - \left( \frac{\partial E_{perf}}{\partial V} \right)_T - \left( \frac{\partial F_{harm}}{\partial V} \right)_T \quad (3.11)$$

The last term of Eq. 3.11 is the ionic part of the thermal pressure, which is always nonzero since the vibrational frequencies depend on the volume. Eq. 3.10 indicates that even at zero temperature the harmonic part of the quasi-

## Chapter 3

harmonic Helmholtz free energy retains a finite value, called the *zero-point energy*, which indirectly contributes to the thermal pressure. Usually, when the volume of a system shrinks,  $\omega_{ki}$  increase and results in larger contributions to thermal pressure, which is responsible for the thermal expansion of solids.

### 3.6 Vibrational frequencies (Phonons)

Calculations of vibrational or phonon frequencies and lattice dynamical properties in the framework of DFT are implemented in two different ways: a. linear response method, involving finite displacement of atoms [19–21] and b. density functional perturbation theory or DFPT [22–24]. The implementation relies on the fact that if atomic displacements are small enough, the displacements and the forces on the atoms maintain a linear relationship. The force constant matrix of Eq. 3.7 is utilized to express this proportionality. The force constant matrix  $\phi_{ls\alpha,lt\beta}$  is mathematically represented by the double-derivative of the free energy  $U$  of the system with respect to atomic displacement,  $\partial^2 U / \partial u_{ls\alpha} \partial u_{lt\beta}$ . In practice, it is achieved by displacing a single atom  $t$  in the unit cell designated by  $l'$  in the cartesian direction, denoted by  $\beta$  while the rest of the atoms are kept fixed at their equilibrium positions. The forces acting on all the atoms thus constitute the elements of  $\phi_{ls\alpha,lt\beta}$  for a particular set of  $(l't\beta)$ . A repetition of the process to cover the rest of the  $l't\beta$  thus generates the total force constant matrix.

The displacements of the atoms bring forth changes in the external potential and in the plane-wave solutions of the Kohn-Sham equation and

## *Computational methodologies*

consequently alters the charge density. In practice, the 2<sup>nd</sup> order perturbation in free energy is thus calculated by expanding the free energy with respect to the variation in Kohn-Sham orbitals to 1<sup>st</sup> order and with respect to the variation in external potential up to 2<sup>nd</sup> order. Thus, the phonon frequencies can be calculated by constructing the dynamical matrix for each atom and then summing over all the atoms of the system. The dynamical matrix forms an eigen equation whose eigenvalues represent the phonon frequencies. The eigen equation can be written as

$$D(k)\varepsilon = M\omega_k^2\varepsilon \quad (3.11)$$

Here  $D$  is the dynamical matrix and  $M$  is the diagonal matrix containing the mass of the atoms. Finite displacement method yields phonon frequencies with good accuracies for a wide class of systems. However, crystalline solids inherently possess periodic boundary conditions, and one must ensure that the elements of the force constant matrix must reduce to negligible values at the boundary. For metals this is readily achieved, but for ionic materials convergence can be slow and tricky. Moreover, for polar materials, vibrational modes are observed to split parallel and perpendicular to the electric field termed as LO-TO splitting. For these materials DFPT is a better choice as it considers the Born effective charge tensor of atoms and static dielectric tensor at high frequencies to compensate the error.

The previous sections discussed the computational methods to calculate various static and finite temperature properties of crystalline materials. But the kinematical properties of an atomic/molecular system, are beyond the

## ***Chapter 3***

regime of standard electronic structure methods. In these scenarios AIMD simulations are employed to statistically determine time-averaged kinematical properties. A description the AIMD simulations is presented in the previous chapter. In the following sections, I will discuss the computational methods for evaluating such properties.

### **3.7 Diffusion coefficients**

As discussed in the previous chapter, for the systems featuring ergodicity, the thermal averages converge to the time averages for the physical properties that shows stochastic variation. Mathematically, both the ergodic theory and the diffusion theory describe microscopic phenomena that are intrinsically stochastic in nature[25]. Diffusion in crystalline phases is a subject of great interest in solid state and condensed matter physics as well as in material sciences as the process can result in microstructural transformations in solids. Interstitial and vacancy defects are mostly responsible for diffusion in lattice structures. Line and surface defects, such as dislocations, grain boundaries and inner and outer surfaces also induce a different kind of diffusion, which are much faster in time scale compared to the lattice diffusion. Often, diffusion in crystalline lattice also manifests as an effect of the ionic frustrations confined in channels in place of point or line defects. However, it is important to note that the phenomenon of diffusion occurs due to the random motions of atoms or ions i.e., they are essentially statistical in nature without any explicit dependence on the force. For any reasonable diffusion of any species to be realized, the diffusing species must

overcome the activation energy barrier. In static cases ( $T=0K$ ), this activation enthalpy can be determined by climbing image nudged elastic band (CI-NEB) method [26] or its more improvised version viz. the generalized solid state nudged elastic band (G-SS-NEB) method [27] proposed by Henkelmann. However, the above methods leave out the effects of finite temperature from the calculation accounting only for the hydrostatic pressure. In order to evaluate the diffusivity under varying  $P$ - $T$  conditions, one must employ AIMD.

The change in diffusivity of the  $i^{th}$  species in a solid with temperature at a specific external pressure can be modelled by the equation

$$D_i = D_{0,i} \exp(-G_i/RT) \quad (3.12)$$

with  $D_{0,i}$  as the pre-factor and  $G_i$  being the Gibb's free energy of activation.  $R$  is the universal gas constant. In practice, the  $D_i$ 's are first evaluated from the

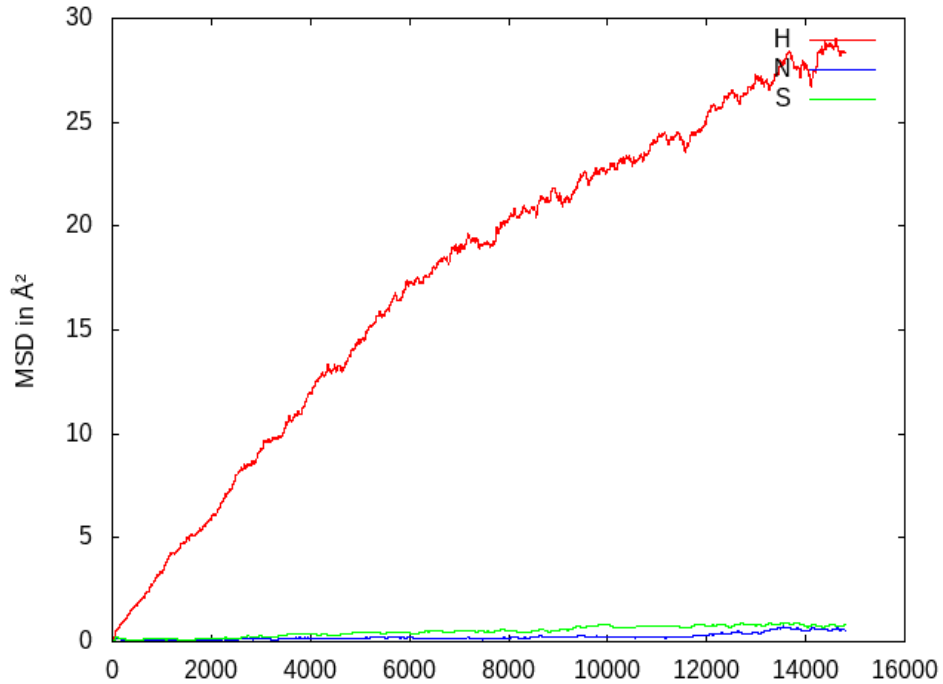


**Figure 3.4:** Mean square displacements of H, N and S at 1750K of the P4/nmm  $NH_3+H_2S$  mixture at 10 GPa.

### Chapter 3

mean square displacement (MSD) of the  $i^{th}$  species of atoms. The MSD of the diffusing species is calculated as a time average as

$$MSD = \langle \sum_i |r_i(t_0 + t) - r_i(t)|^2 \rangle \quad (3.13)$$

Here,  $r_i(t)$  is the vector position of the  $i^{th}$  species of atom at time  $t$ ,  $\langle . \rangle$  represent the time average at  $t_0$ . The MSD (Figure 3.4) are calculated over a sufficiently long time, typically much larger than the vibrational time period of the system.

The calculated MSD's are plotted against the time to determine its slope to find the diffusion coefficient  $D_i$ . However, care must be taken in this operation, allowing adequate time to the system to thermalize so that the initial ballistic collisions between the atoms die out and the system reaches an equilibrium state. The diffusion coefficient  $D_i$  can be then obtained from Einstein's relation,

$$D_i = \frac{MSD}{2nt} \quad (3.14)$$

with  $n = 1, 2, 3$  depending on the dimension of the system under study. These  $D_i$ 's are evaluated at a particular pressure for a set of temperatures. Finally, they are fitted with Eq. 3.12 to find approximate values of the pre-factor  $D_{0,i}$  and the Gibb's free energy of activation  $G_i$ .

## 3.8 Electrical conductivity

Once the diffusion coefficients are evaluated, the calculation of electrical conductivity becomes straight-forward. To estimate the contribution of

conductivity of the  $i^{th}$  species of atom,  $\sigma_i$  to the apparent bulk conductivity of the system, this study uses the Nernst-Einstein equation, ,

$$\sigma_i = \frac{F^2}{RT} D_i q_i^2 c_i, \quad (3.15)$$

where  $q_i$  is the charge of each individual diffusing atom of  $i^{th}$  species and  $c_i$  is its concentration i.e., number of atoms/unit volume.  $F$  is the well-known Faraday's constant. An alternative form of Eq. 3.15, given below is also often utilized.

$$\sigma_i = \frac{1}{k_B T} D_i z_i^2 e^2 c_i, \quad (3.16)$$

where  $z_i$  and  $e$  are the valence of the diffusing species and charge of an electron respectively.  $k_B$  is the thermodynamic Boltzman constant.

### **3.9 Radial and pair distribution function**

Extreme physical conditions, such as high pressures and/or temperatures may result in structural amorphization. This amorphization may be total or partial in a sense that it can occur across the entire crystalline system under study resulting in melting or on a sublattice of it. The latter of which is often called sublattice melting. Whereas melting leads to a loss of long-range order in a crystalline substance retaining only the short-range ones, sublattice melting eliminates the long-range periodic configuration of one or more lattice components mostly in weakly bound ionic binary or ternary crystals upon rise in temperature. Sublattice melting sets in motion of charged ions in system which is the central phenomena behind superionic nature of

### Chapter 3

materials. The amorphization, sublattice melting or more generally melting of materials are not captured within the application regime of only electronic structure methods as the plane-wave pseudopotential method of DFT is limited to crystalline materials with definite periodic boundary conditions. The radial distribution function (RDF) and pair distribution function (PDF) calculated from AIMD simulations are capable of successfully characterizing the change of order due to amorphization or melting ranging up to the nearest, subnearest coordination of atoms and further.

RDF represent the so-called ‘structure’ of a system, i.e., the positioning and ordering of atoms. In general, the RDF exploits the local variation in particle densities with respect to some reference particle, averaged over its local environment in a statistical sense. The RDF is expressed as,

$$g(r) = \frac{\langle \rho(r) \rangle}{\rho}, \quad (3.17)$$

where  $\rho(r)$  is the local density of particles around some reference particle and  $\rho$  is the bulk density. Since it leaves counting the reference atom,  $g(r)$  starts at a value of zero and shows a first peak at a distance where the first shell of atoms is located with respect to the reference atom. This shell is called the 1<sup>st</sup> solvation shell.  $g(r)$  converges to 1 for large distances in an isotropic material. The probability of finding an atom at a distance  $r$  in a shell of thickness  $dr$  is given by

$$p(r) = g(r)4\pi r^2 dr \quad (3.18).$$



Thus, the product  $\rho g(r)$  on integration over the first peak of the RDF gives the total number of atoms within the 1<sup>st</sup> solvation shell. An extension to correlate the positions of two different classes of atoms is obvious. The pair distribution function (PDF)  $g_{XY}(r)$  between atom type  $X$  and  $Y$  with population  $N_X$  and  $N_Y$  reads,

$$g_{XY}(r) = \frac{1}{N_X N_Y} \sum_{i=1}^{N_X} \sum_{j=1}^{N_Y} \langle \delta(|r_i - r_j| - r) \rangle \quad (3.19)$$

It effectively counts the number of  $Y$ -type of atom, which are located within a distance of  $r$  around the atom  $X$ , in the form of a density. The cumulative PDF is calculated from Eq. 3.19 as,

$$G_{XY}(r) = \int_0^r g_{XY}(r') 4\pi r'^2 dr' \quad (3.20)$$

Figures 3.5 and 3.6 show the PDF of like atoms and unlike atoms in

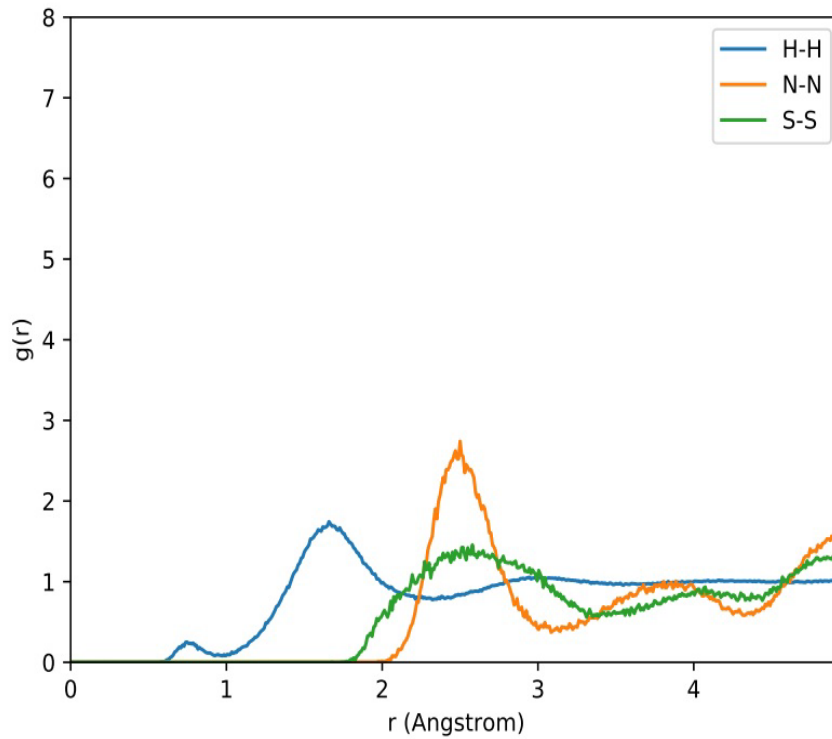


**Figure 3.5:** Pair distribution functions of like atoms in the 100 GPa Abm<sub>2</sub> phase of NH<sub>3</sub>+H<sub>2</sub>S mixture at 2000K.

### Chapter 3

Abm<sub>2</sub> type crystalline NH<sub>3</sub>-H<sub>2</sub>S mixture at 100 GPa and 2000K. The initial peak at  $\sim 0.74\text{\AA}$  and  $1.01\text{\AA}$  in Figures 3.5 and 3.6, respectively, indicates the hydrogen-bond length of short-lived H<sub>2</sub> molecules and typical N-H distances in NH<sub>4</sub><sup>+</sup> motifs.

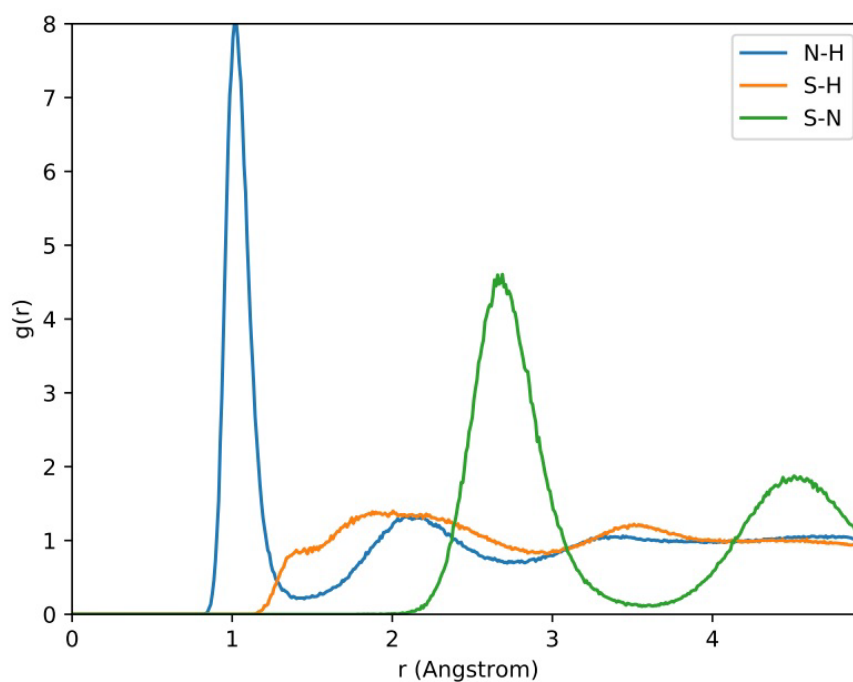


**Figure 3.6:** Pair distribution functions of unlike atoms in the 100 GPa Abm<sub>2</sub> phase of NH<sub>3</sub>+H<sub>2</sub>S mixture at 2000K.

## Reference

- [1] Murnaghan F D 1944 The Compressibility of Media under Extreme Pressures *Proc. Natl. Acad. Sci.* **30** 244–7
- [2] Birch F 1947 Finite Elastic Strain of Cubic Crystals *Phys. Rev.* **71** 809–23
- [3] Vinet P, Smith J R, Ferrante J and Rose J H 1987 Temperature effects on the universal equation of state of solids *Phys. Rev. B* **35** 1945–53
- [4] Demuth T, Jeanvoine Y, Hafner J and Ángyán J G 1999 Polymorphism in silica studied in the local density and generalized-gradient approximations *J. Phys. Condens. Matter* **11** 3833–74
- [5] Kraus D, Vorberger J, Pak A, Hartley N J, Fletcher L B, Frydrych S, Galtier E, Gamboa E J, Gericke D O, Glenzer S H, Granados E, MacDonald M J, MacKinnon A J, McBride E E, Nam I, Neumayer P, Roth M, Saunders A M, Schuster A K, Sun P, van Driel T, Döppner T and Falcone R W 2017 Formation of diamonds in laser-compressed hydrocarbons at planetary interior conditions *Nat. Astron.* **1** 606–11
- [6] Dutta R and Mandal N 2012 Structure, elasticity and stability of reidite (ZrSiO<sub>4</sub>) under hydrostatic pressure: A density functional study *Mater. Chem. Phys.* **135** 322–9
- [7] Errandonea D and Garg A B 2018 Recent progress on the characterization of the high-pressure behaviour of AVO<sub>4</sub> orthovanadates *Prog. Mater. Sci.* **97** 123–69
- [8] Parisi F, Sciascia L, Princivalle F and Merli M 2012 The pressure-induced ringwoodite to Mg-perovskite and periclase post-spinel phase transition: a Bader’s topological analysis of the ab initio electron densities *Phys. Chem. Miner.* **39** 103–13
- [9] Hermann A, Ashcroft N W and Hoffmann R 2012 High pressure ices *Proc. Natl. Acad. Sci.* **109** 745–50
- [10] Naden Robinson V and Hermann A 2020 Plastic and superionic phases in ammonia-water mixtures at high pressures and temperatures *J. Phys. Condens. Matter* **32**
- [11] Chatterji T, McIntyre G J and Lindgard P A 2009 Antiferromagnetic phase transition and spin correlations in NiO *Phys. Rev. B - Condens. Matter Mater. Phys.* **79** 1–4
- [12] Lin J-F and Tsuchiya T 2008 Spin transition of iron in the Earth’s lower mantle *Phys. Earth Planet. Inter.* **170** 248–59
- [13] Tsuchiya T, Wentzcovitch R M, da Silva C R S and de Gironcoli S 2006 Spin Transition in Magnesiowustite in Earth’s Lower Mantle *Phys. Rev. Lett.* **96** 198501
- [14] Blöchl P E, Jepsen O and Andersen O K 1994 Improved tetrahedron method for Brillouin-zone integrations *Phys. Rev. B* **49** 16223–33
- [15] Das P K, Mandal N and Arya A 2017 Effects of cation ordering on the elastic and electronic properties of Mg-Fe silicate phases at high pressures *J. Appl. Phys.* **122**

### Chapter 3

- [16] Liu C, Gao H, Hermann A, Wang Y, Miao M, Pickard C J, Needs R J, Wang H T, Xing D and Sun J 2020 Plastic and Superionic Helium Ammonia Compounds under High Pressure and High Temperature *Phys. Rev. X* **10** 21007
- [17] Beckstein O, Klepeis J E, Hart G L W and Pankratov O First-principles elastic constants and electronic structure of Pt<sub>2</sub>Si and PtSi
- [18] Gupta F, Pasturel A and Brillant G 2010 Diffusion of oxygen in uranium dioxide: A first-principles investigation *Phys. Rev. B - Condens. Matter Mater. Phys.*
- [19] Savrasov S Y 1992 Linear response calculations of lattice dynamics using muffin-tin basis sets *Phys. Rev. Lett.* **69** 2819–22
- [20] Savrasov S Y 1996 Linear-response theory and lattice dynamics: A muffin-tin-orbital approach *Phys. Rev. B* **54** 16470–86
- [21] Alfè D 2009 PHON: A program to calculate phonons using the small displacement method *Comput. Phys. Commun.* **180** 2622–33
- [22] Baroni S, Giannozzi P and Testa A 1987 Green's-function approach to linear response in solids *Phys. Rev. Lett.* **58** 1861–4
- [23] Giannozzi P, de Gironcoli S, Pavone P and Baroni S 1991 Ab initio calculation of phonon dispersions in semiconductors *Phys. Rev. B* **43** 7231–42
- [24] Gonze X, Allan D C and Teter M P 1992 Dielectric tensor, effective charges, and phonons in  $\alpha$ -quartz by variational density-functional perturbation theory *Phys. Rev. Lett.* **68** 3603–6
- [25] Yosida K 1965 Ergodic Theory and Diffusion Theory BT - Functional Analysis ed K Yosida (Berlin, Heidelberg: Springer Berlin Heidelberg) pp 379–411
- [26] Henkelman G, Uberuaga B P and Jónsson H 2000 A climbing image nudged elastic band method for finding saddle points and minimum energy paths *J. Chem. Phys.* **113** 9901–4
- [27] Sheppard D, Xiao P, Chemelewski W, Johnson D D and Henkelman G 2012 A generalized solid-state nudged elastic band method *J. Chem. Phys.* **136** 74103

## **Silicates-I: $U_{1-x}Th_xSiO_4$ solid solution**

---

*Introductory notes*

*Computational methods*

*Structural parameters*

*Characteristics of the phase transition*

*Polyhedral geometry and distortion*

*U/ThO<sub>8</sub> polyhedral distortions*

*Highlights of the results*



## 4.1 Introductory notes

Uranium (U) and thorium (Th) are the most crucial radionuclides in governing a range of processes in the interior of terrestrial planets. However, their modes of occurrence in crystalline phases, especially at high pressure, in terrestrial planetary bodies that contain silicates as the major constituent are yet to be fully explored. Many geophysicists have demonstrated potential high-pressure Mg-Fe silicate phases are capable of housing nominal amount of water[1,2] to hypothesize the deep-mantle water reservoir in the Earth[3,4]. But, their lattice structures lack efficiency in hosting these radionuclides owing to their large ionic radii and contrasting valence configurations. This poses a major problem in respect of the residence of U and Th in crustal and mantle mineral phases on geological time scales (million years). Zircon ( $ZrSiO_4$ ) has been found to be a unique naturally occurring silicate phase, which can

## **Chapter 4**

substantially house these radionuclides[5–7]. Due to its long-term chemical stability and mechanical durability zircon is considered as the most competent accessory material for straight disposal of spent nuclear fuel (SNF) and immobilization of vitrified nuclear waste in underground repositories[8,9]. Zircon structured U-bearing phase, called coffinite ( $\text{USiO}_4$ ) is a natural phase, and also crystallizes as an alteration product of SNF under low temperature silica-rich condition[10]. Its Th-homologue, called Thorite ( $\text{ThSiO}_4$ ) occurs in the Earth's crust. These two phases are economically viable ores for extraction of nuclear materials and are prospective phases to find immense utility at the front-end of the nuclear fuel cycle. Further, precipitation of coffinite from uranium dioxide ( $\text{UO}_2$ ) under reducing condition[11] can be used to control U(IV) concentration in direct environment and thus serve as viable metallic waste-form towards the back-end of nuclear fuel cycle[12,13]. They undergo pressure dependent structural transition from zircon- (Space Group:  $I4_1/amd$ ) to reidite- or scheelite- type phase (Space Group:  $I4_1/a$ )[14–16]. The accommodation of U and Th in these two phases, their mutual substitution and fluctuations in thermodynamic parameters can largely affect the bonding characteristics and local polyhedral structure around U/Th and induce significant distortion in these coordination polyhedra. It is thus worthwhile to study the local geometrical distortions of U/Th coordination polyhedra, and their effects on the observable physical properties of these phases. In addition, understanding the transformation behaviour of zircon-type  $\text{U}_{1-x}\text{Th}_x\text{SiO}_4$  to reidite-type phase under elevated hydrostatic pressure regime is critical to



explore their applicability in nuclear industries as well as fundamental science issues, such as geochronology[17,18].

Earlier and recent experimental studies focused on the techniques of synthesizing coffinite and the thermochemical problems encountered therein[19–25]. Similar experimental studies were also carried out for synthesizing thorite[26,27]. Barring the experimental investigation of Bauer et al.[15], Zhang et al.[14] and the computational study of Bose et al.[16], a detailed analysis of the crystal chemistry of coffinite and thorite in high pressure environments is left unattended. Zhang et al.[14] reported an irreversible zircon to reidite type phase transition of USiO<sub>4</sub> at 14~17 GPa and inferred the possibility of a pressure-induced electron transfer (U<sup>4+</sup> to U<sup>5+</sup>). Bauer et al.[15] revisited this transition through high-pressure experiments and established it to be thermodynamically reversible. They identified that this transition is driven by softening of a silent vibrational raman mode. The presence of impurity in the form of UO<sub>2</sub> in coffinite samples used by the former[14] might hinder the reversibility of the phase transition, which was observed in pure samples of the later[15]. Based on a lattice dynamical study, Bose et al.[16] predicted such a transition in ThSiO<sub>4</sub> at a pressure > 3 GPa. A parallel line of computational study dealt with temperature dependent phase transition of thorite to huttonite (monoclinic), but without accounting the effect of pressure[28]. The same transition was studied employing several different experimental techniques by Estevenon et al.[27], Finch et al.[29] and Mazeina et al.[30]. All these earlier studies showed the phase transition of pure phases, either USiO<sub>4</sub> or ThSiO<sub>4</sub>. However, these two phases have a strong tendency to

## *Chapter 4*

form a solid solution, as reported from natural samples [19, 31–34] and chemical synthesis [22, 24, 35] in zircon-type phase, as initially hypothesized by Goldschmidt [36]. But, none of the studies have so far provided any insight into the phase transition of U-Th solid solutions from experiments or theoretical calculations, and thus it is worthwhile to revisit the phase transition behaviour. Substitution of Th in  $\text{USiO}_4$  phase or vice-versa can cause significant geometric distortions in coordination polyhedra of their unit cells, which in turn manifest themselves through convoluted behavior of various physical properties. Such geometric distortions can also be a consequence of variations in thermodynamic environment. Existing literature presents two geometrical methods in quantifying such distortions. Robinson et al.[37] proposed that the degree of distortion of coordination polyhedra in terms of quadratic elongation ( $\lambda$ ) and angular variance ( $\sigma_\theta^2$ ). Alternatively, Makovicky et al.[38] expressed the distortions considering the volume ratio of polyhedra and their circumscribed sphere for their real and ideal geometry, keeping the number of coordinated atoms fixed. However, both the approaches adhere to some limitations in terms of their applicability. Robinson's[37] consideration provides with excellent numerical estimates for two cases of regular, convex and uniform polyhedra (tetrahedra ( $Z= 4$ ), octahedra ( $Z= 6$ )) and can be generalized to cube, dodecahedron ( $Z= 8$ ) and icosahedron ( $Z= 12$ ). Later studies[38] improved the analysis by incorporating distortion of an additional set of four polyhedra with  $Z= 12$  as cuboctahedra, anticuboctahedra, icosahedra and maximum-volume hexagonal prism. These methods, however, fail to deal with the distortions of polyhedra, which display strongly irregular

and/or non-uniform geometry. To overcome this hurdle, Mursic et al.[39] provided an alternative approach to quantify the distortions of ZrO<sub>8</sub>-triangular dodecahedra or snub-disphenoids in zircon (ZrSiO<sub>4</sub>). He treated the ZrO<sub>8</sub>-polyhedron as two interpenetrating ZrO<sub>4</sub>-tetrahedra, constructed by four edge sharing and four corner sharing oxygen respectively. Based on this formulation, Marques et al.[40] calculated the geometry of ZrO<sub>8</sub>-snub-disphenoid in zircon and reidite phases. However, his calculations suffer from a major shortcoming as ZrO<sub>8</sub>-polyhedra in the reidite phase lack edge sharing O atoms. Furthermore, configuring a dodecahedron in terms of two tetrahedra leads to a volume incompatibility. To meet this gap, it demands an entirely new approach to quantify the longitudinal and angular distortion of 8-coordinated snub-disphenoids without manipulating their original geometry.

Using density functional theory (DFT) calculations this chapter explores the mechanism of zircon- to reidite-type phase transformations under hydrostatic pressure conditions in coffinite, and thorite and their solid solutions (U<sub>1-x</sub>Th<sub>x</sub>SiO<sub>4</sub>, where, x=0.25, 0.50, 0.75), accounting the effects of local polyhedral geometry. The present study develops a novel approach to numerically estimate the polyhedral (AO<sub>8</sub>, A: U, Th) distortions. The observed nonlinear variation of phase transition pressures with U:Th ratio is then correlated with the distortions of U/Th coordination polyhedra for the two participating phases.

## **4.2 Computational methods**

The atomistic calculations have been performed within the framework of density functional theory (DFT) as implemented in Quantum ESPRESSO

## Chapter 4

suite[41–43]. Spin-polarized simulations were performed using projector augmented-wave (PAW) method[44]. The exchange-correlation effects of the electrons were treated using PBE-GGA, as parametrized by Perdew et al.[45]. For U, Th, Si, O atoms the following orbitals were treated as valence states: U ( $6s^27s^26p^66d^{1.5}5f^{2.5}$ ), Th ( $6s^27s^26p^66d^{1.5}f^1$ ), Si ( $3s^23p^2$ ), O ( $2s^22p^2$ ). The core cut-off radii for them are 2.1 a.u., 2.1 a.u., 1.9 a.u. and 1.1 a.u. respectively. The remaining core electrons along with the nuclei were treated by scalar relativistic PAW pseudopotentials incorporating a non-linear core correction[46]. The kinetic energy cut-off for each individual members of the solid solution was kept at 1700 eV. The BFGS (Broyden–Fletcher–Goldfarb–Shanno)[47,48] algorithm was used for geometrical optimization to find the ground state electronic structure under strict convergence criteria. In both cases the convergence threshold for energy and forces were set to  $10^{-8}$  Ry and  $10^{-6}$  Ry/bohr, respectively. For the zircon- and reidite- type phases, the brillouin zones were sampled by  $7 \times 7 \times 8$  and  $7 \times 7 \times 4$  Monkhorst-Pack[49] k-point grid respectively, which gave rise to 50 and 99 irreducible k-points in their brillouin zone.

Hubbard-U factor in terms of strong Coulomb-like Hartree-Fock electrostatic potential is introduced to the system to handle  $d$  and  $f$  electrons of uranium and thorium. This computational study aimed to estimate the factor  $U$  self-consistently. A set of simulations for the  $U_{0.5}Th_{0.5}SiO_4$  configuration were performed with  $U$  varying from 1 to 5 eV, for both uranium and thorium. But no changes were observed in the orbital occupancy. Secondly, the calculations underestimated the lattice constants, which are

incommensurate with experimental data. Thus, the Hubbard-U was not taken into account in the rest simulations.

### 4.3 Structural parameters

The tetragonal unit cells of coffinite ( $USiO_4$ ), thorite ( $ThSiO_4$ ) and compositionally varying members ( $U_{1-x}Th_xSiO_4$ ) contain 24 atoms in their conventional cell, both in zircon- and reidite-type phases. Both have 4 formula units per conventional cell. The former phase crystallizes in Laue group  $4/mmm$  with  $I4_1/amd$  space group, whereas the later crystallizes in Laue group  $4/m$ , but with different space group ( $I4_1/a$ ). The positions of Si and U/Th atoms

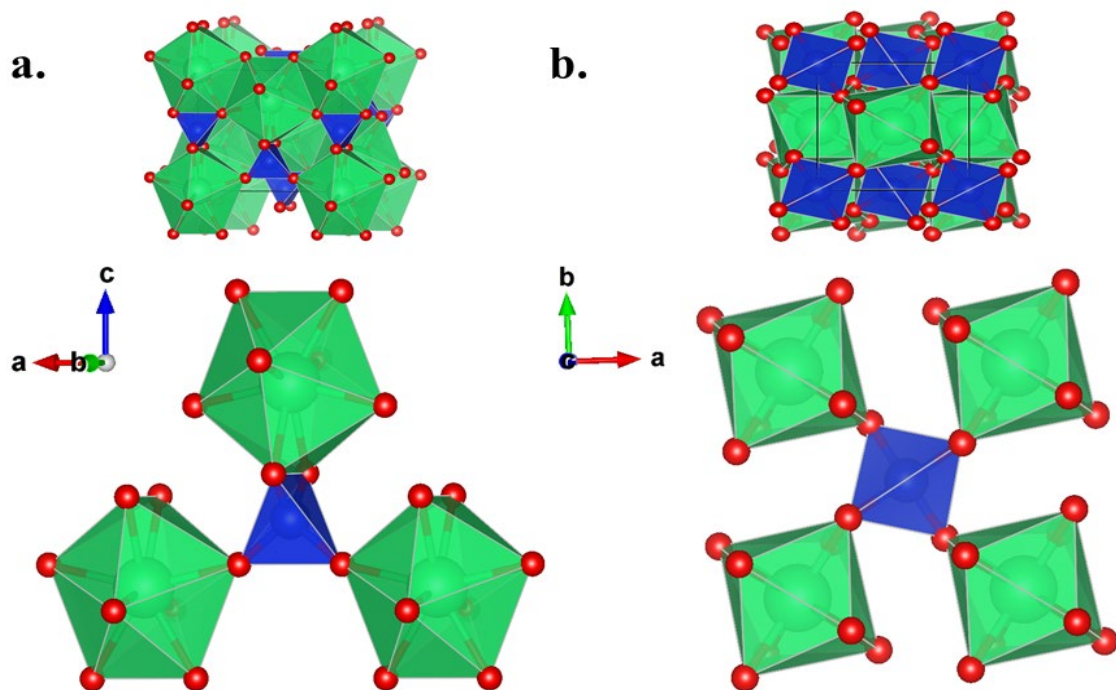


**Figure 4.1:** The unit cells of  $ThSiO_4$  and the connection and alignment of the Th-dodecahedra with respect to Si-tetrahedra in **a.** zircon type phase and **b.** reidite type phase. Green polyhedras are Th-polyhedras and blue polyhedras are Si-tetrahedras. Red spheres are Oxygen atoms. The reidite structure is comparatively open with a hollow tunnel parallel to crystallographic c-axis.

## Chapter 4

are fixed by symmetry; they are located at  $(0, 1/4, 3/8)$  and  $(0, 3/4, 1/8)$  on the 4b and 4a Wyckoff sites, respectively. The 16h Wyckoff sites  $(0, u, v)$  are occupied by the O-atoms, where  $u$  and  $v$  are the internal parameters. Here we restrict our discussion on the crystal structure of zircon ( $\text{ZrSiO}_4$ ) which has been extensively studied [16, 39, 50, 51]. In contrary, our attention focuses upon the different structures of  $\text{U}_{1-x}\text{Th}_x\text{SiO}_4$  solid solution, especially on their high-pressure polymorphs which are virtually unexplored. They have a chain of alternating edge sharing  $\text{SiO}_4$  tetrahedra and (U/Th)- $\text{O}_8$  triangular dodecahedra extending parallel to the  $c$  crystallographic axis in their zircon-type phases (Figure 4.1a). On the other hand, the reidite type contains the actinide polyhedra and the  $\text{SiO}_4$  tetrahedra in a zig-zag manner along the  $c$ -axis (Figure 4.1b).

During the zircon- to reidite-type transition, the mode of sharing between  $\text{SiO}_4$  and U/Th $\text{O}_8$  polyhedra undergoes a dramatic modification (Figure 4.1a-b). The reidite-type structure consists of two intercalated diamond lattice sites, one occupied with U and/or Th and the other with Si. They are coordinated with eight and four oxygen atoms, forming U/Th $\text{O}_8$ -dodecahedra and  $\text{SiO}_4$ -tetrahedra, respectively. However, the two polymorphs show striking dissimilarities in the array of U/Th $\text{O}_8$ -dodecahedra and their nearest neighbour Si-tetrahedra. In zircon phase, we find both edge and corner sharing between the two types of cationic polyhedra, forming a compact tetragonal cell. In contrast, their high-pressure phase (reidite-type) display only corner sharing between neighbouring actinide polyhedra and  $\text{SiO}_4$  tetrahedra (Figure 4.1). The calculated values of lattice parameters,  $c/a$  ratios and unit-cell

volumes are presented in Table-4.1 and compared with previous theoretical and experimental studies. For coffinite, we obtain  $a = 7.0303 \text{ \AA}$  and  $c = 6.2872 \text{ \AA}$ , showing an excellent agreement (within 0.5% to 0.65%) with the reported values from computational study of Bauer et al.[15] and experimental studies[15,21–23]. For the thorite end member also, our results ( $a = 7.1839 \text{ \AA}$

**Table 4.1:** Optimized lattice parameters, c/a ratios, volumes of unit cells and bulk moduli for U<sub>1-x</sub>Th<sub>x</sub>SiO<sub>4</sub> solid solutions in both ambient pressure zircon phase and its high pressure polymorphic phase viz reidite.

Phase (Sp. Gr.)	x	a (Å)	c (Å)	c/a	Volume (Å <sup>3</sup> )	Bulk Modulus (GPa)	Transition Pressure (GPa)
<b>Zircon (I4<sub>1</sub>/amd)</b>	0.00	7.0303	6.2872	0.8942	310.75	181.30	-
		7.0135 <sup>[21]</sup>	6.2669 <sup>[21]</sup>		-	-	
		6.981 <sup>[19]</sup>	6.250 <sup>[19]</sup>		-	-	
		6.9862 <sup>[15]</sup>	6.2610 <sup>[15]</sup>		305.58 <sup>[15]</sup>	181 <sup>[15]</sup>	
		6.9842 <sup>[22]</sup>	6.2606 <sup>[22]</sup>		305.38 <sup>[22]</sup>	-	
		6.9904 <sup>[24]</sup>	6.2610 <sup>[24]</sup>		305.94 <sup>[24]</sup>	-	
		6.9936 <sup>[14]</sup>	6.2614 <sup>[14]</sup>		-	188 <sup>[14]</sup>	
	0.25	7.0758	6.2997	0.8904	315.41	174.49	-
		7.0105 <sup>[22]</sup>	6.2680 <sup>[22]</sup>		308.06 <sup>[22]</sup>	-	
		7.007 <sup>[19]</sup>	6.275 <sup>[19]</sup>		-	-	
	0.50	7.1181	6.3180	0.8876	320.11	167.57	-
		7.039 <sup>[19]</sup>	6.294 <sup>[19]</sup>		-	-	
	0.75	7.1553	6.3320	0.8849	324.19	173.60	-
		7.0949 <sup>[22]</sup>	6.3194 <sup>[22]</sup>		318.10 <sup>[22]</sup>	-	
		7.071 <sup>[19]</sup>	6.314 <sup>[19]</sup>		-	-	
	1.00	7.1839	6.3511	0.8841	327.75	178.20	-
		7.1816 <sup>[22]</sup>	6.2946 <sup>[22]</sup>		324.66 <sup>[22]</sup>	-	
		7.1568 <sup>[24]</sup>	6.3152 <sup>[24]</sup>		323.46 <sup>[24]</sup>	-	
		7.133 <sup>[28]</sup>	6.319 <sup>[28]</sup>		-	-	
		7.1439 <sup>[27]</sup>	6.3183 <sup>[27]</sup>		322.46 <sup>[27]</sup>	-	
7.129 <sup>[30]</sup>		6.319 <sup>[30]</sup>	321.15 <sup>[30]</sup>		-		
7.128 <sup>[19]</sup>		6.314 <sup>[19]</sup>	-		-		
7.1328 <sup>[52]</sup>	6.3188 <sup>[52]</sup>	321.48 <sup>[52]</sup>	-				
<b>Reidite (I4<sub>1</sub>/a)</b>	0.00	4.9794	11.2318	2.2557	278.49	239.05	8.52
		4.9502 <sup>[15]</sup>	11.0750 <sup>[15]</sup>		271.39 <sup>[15]</sup>	212 <sup>[15]</sup>	15 <sup>[15]</sup>
		4.8654 <sup>[14]</sup>	11.0316 <sup>[14]</sup>		261.14 <sup>[14]</sup>	274 <sup>[14]</sup>	14-17 <sup>[14]</sup>
	0.25	4.9915	11.3389	2.2717	282.51	233.60	7.67
	0.50	5.0053	11.4308	2.2837	286.18	230.00	6.82
0.75	5.0157	11.5241	2.2976	289.92	227.30	7.92	
1.00	5.0251	11.6072	2.3099	293.10	225.64	8.68	

## Chapter 4

and  $c = 6.3511 \text{ \AA}$ ) hold a good match with the experimental data[22], showing a negligible difference (0.02%). They are also in consistent with the theoretical results of Shein et al.[28] and other experimental results [19,22,24,27,30,52]. The present calculations for the reidite-type phase of coffinite yield cell parameters:  $a = 4.9794 \text{ \AA}$  and  $c = 11.2318 \text{ \AA}$ , closely tracking ( $\sim 0.58\%$ ) experimental results of synchrotron powder diffraction by Bauer et al.[15]. We predict for the first time the lattice parameters of the high-pressure polymorph of Thorite:  $a = 5.0251 \text{ \AA}$ ,  $c = 11.6072 \text{ \AA}$ .

Considering the overestimation of GGA formalism, the results presented above suggest that the calculated cell parameters for U-Th solid solution phases and their high pressure polymorphs would remain valid, even the results could not be verified due to lack of experimental data. Figure 4.2 shows the variation of unit cell volumes and  $c/a$  ratio normalized for members of each phases with respect to the corresponding values of coffinite and its high-pressure reidite polymorph, respectively. Due to their homologous topology, the incorporation of Th by substituting U enforces a linear increase in volume for both the phases, consistent with the Vegard's law. These increments of volumes are expected as the atomic radius of Th (0.24 nm) is a little larger than that of U (0.23 nm). In particular, the small difference between there atomic radii is chemically desirable aiding to the tolerance of the crystal structure for mixing ions of different sizes in each site and the genesis of the silicate solid solution. On another note, substitution between U and Th preserves the composite electrical neutrality of the crystalline aggregate and is commensurate with the local charge balance through their coordination environment in their



crystallographic site. Having said that, the manner of facilitating the volume expansion is markedly distinct for different phases appearing as obvious from the variation of  $c/a$  ratio (Figure 4.2). The reidite-type phase undergoes a

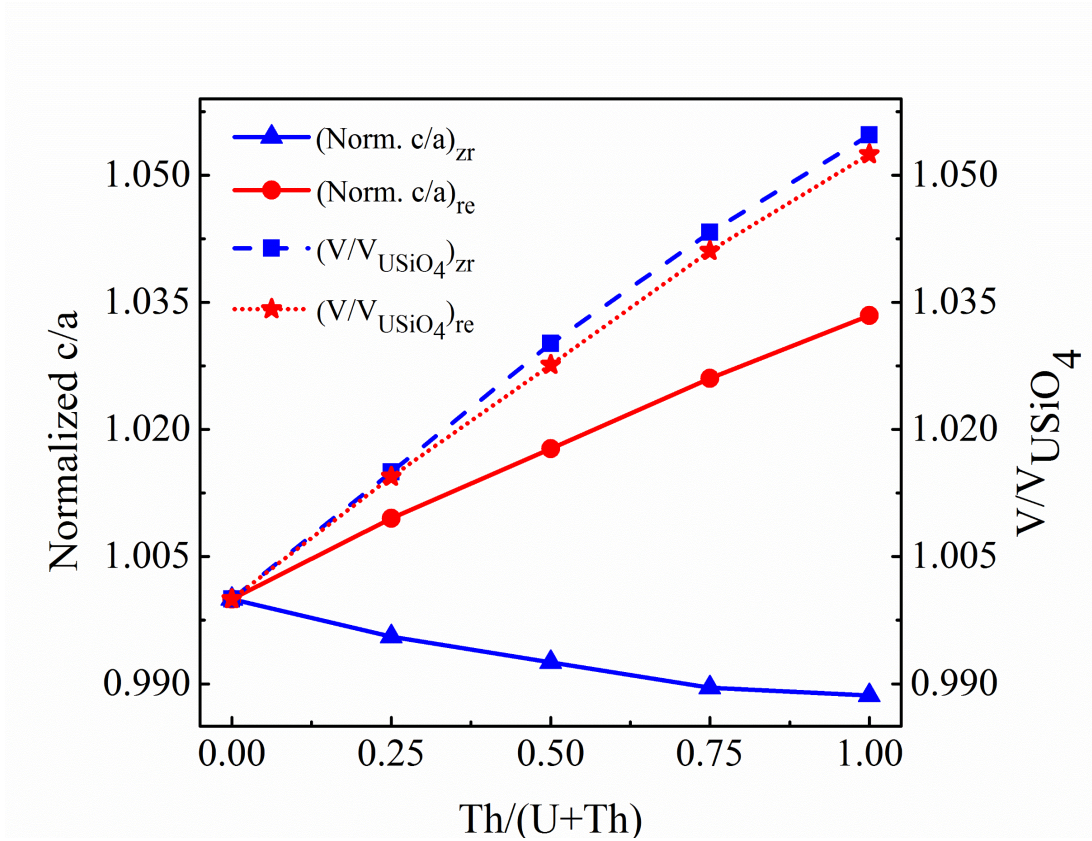


**Figure 4.2:** Variation of  $c/a$  ratio and unit cell volume of  $U_{1-x}Th_xSiO_4$  in both zircon and reidite type phases, where  $x = Th/(U+Th)$ . For a better comparison all the  $c/a$  ratios and volumes have been normalized with respect to the corresponding values of  $USiO_4$  member of the corresponding phase. Notice the distinct nature of undergoing volume change in different phases:  $c/a$  increment in reidite and opposite in zircon.

monotonic gain in  $c/a$  whereas the zircon-type phase exhibits a completely antipodal behaviour. This result provide reinforcement to the finding of Dutta et. al.[50] who showed that the reidite demonstrates a greater compressibility along  $c$ -axis compared to  $a$ -axis and vice versa in zircon phases. Our analysis confirms that the increment along  $a(c)$  is more administrative in volume change in zircon (reidite) -type phase.

## Chapter 4

### 4.4 Characteristics of the phase transition

I have theoretically investigated the effect of hydrostatic pressure on the unit-cell volumes of  $U_{1-x}Th_xSiO_4$  solid solutions in both zircon- and reidite-type phases as a function of U/Th ratio. To obtain the critical hydrostatic pressure for zircon- to reidite-type structural transformation, I have used the formalism of enthalpy crossover of the two phases for a given U/Th ratio of the solid solution. The entire exercise has been performed with the ground state enthalpies of the structures at  $T = 0$  K. The pressure-homologue rule[53] suggests that the phase with larger cations undergoes structural transition at lower pressures, as compared to those with smaller cations. According to this rule, the transition pressure ( $p_t$ ) for  $ThSiO_4$  should be lower than that of  $USiO_4$ . However, the results predict that  $p_t$  for the end-member phases hardly differs from one another. The calculations also reveal an atypical variation of  $p_t$  with the radionuclide U and Th concentration (Figure 4.3). The calculated transition pressure 8.52 GPa for the U-endmember (Table 4.1) decreases to 7.67 GPa as 25 at% of U is replaced by Th. The transition pressure then drops to attain a minimum value of 6.82 GPa when Th and U occur in equal concentration. Further increment of Th reverses the trend of transition pressure variation to reach a value of 8.68 GPa for  $ThSiO_4$  phase, which is comparable to that for  $USiO_4$  phase. The pressure transmitting media chosen in experiments by Zhang et al.[14] and Bauer et al.[15] are (16/3/1) methanol/ethanol/water mixture and neon, respectively. Methanol/ethanol/water mixture exhibits signs of nonhydrostacticity at 10-11 GPa, whereas neon does the same at 15 GPa [54]. Close to these pressure ranges and beyond it, the media lose their ideal fluid

behavior, and start to support shear stress in developing non-hydrostaticity.

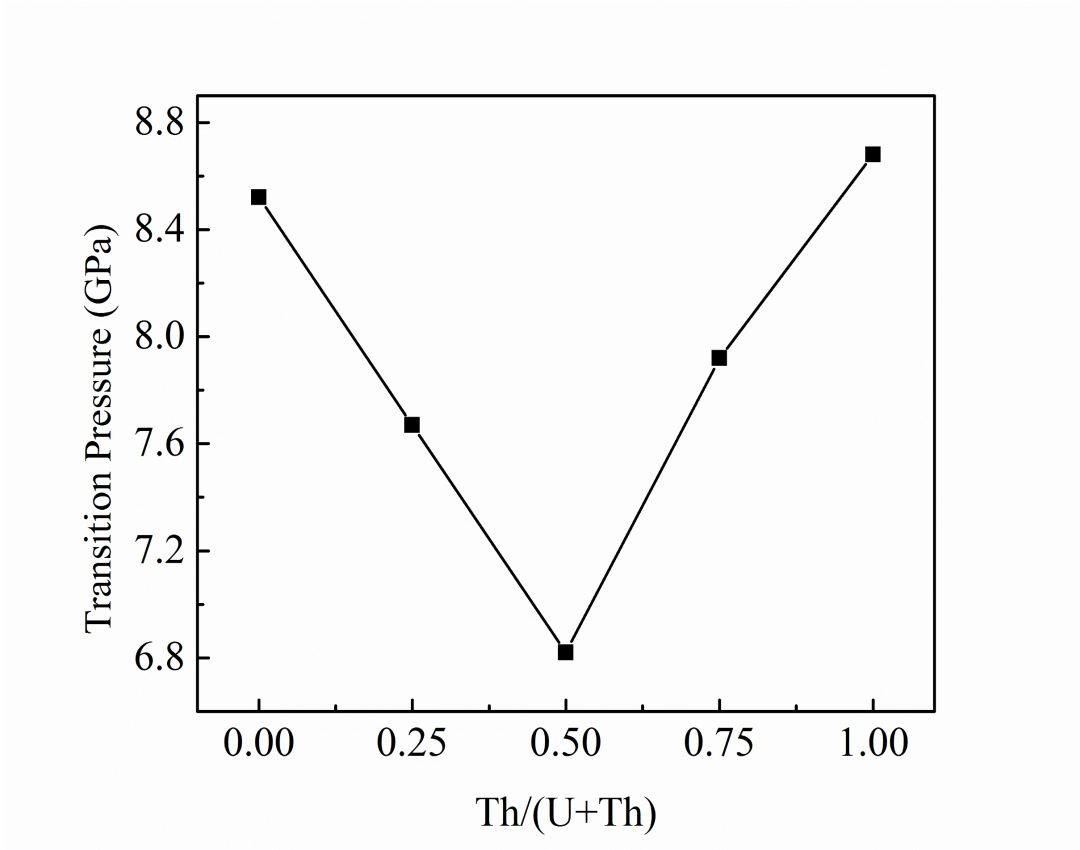


**Figure 4.3:** Variation of Zircon→reidite type transition pressure of  $U_{1-x}Th_xSiO_4$ ,  $x = Th/(U+Th)$ . The transition pressure for end members of this stoichiometric spectrum are almost equal ( $\sim 8.6$  GPa). The lines are guide to the eye. The transition pressure attains a minimum when the concentrations of U and Th are equal.

This non-hydrostatic response might be the reason behind the apparent disagreement between results of Zhang et al.[14] and Bauer et al.[15]. My theoretical value of the transition pressure differs from the experimental results of Bauer et al.[15] and Zhang et al.[14] mainly due to two reasons. All the calculations are performed at  $T = 0$  K, whereas their experiments were carried out at room temperatures ( $T > 0$  K). The non-zero temperature condition can lead to a significant increase of the transition pressure, as predicted from the positive Clapeyron-slope for a similar phase transition in pure  $ZrSiO_4$ . The coffinite sample used by Zhang et al. for in-situ X-ray

## Chapter 4

diffraction and IR measurements contained 5-10 wt% of  $\text{UO}_2$  mixed with coffinite. The presence of such impurity might also influence the transition pressure to become different from our calculated value for pure  $\text{USiO}_4$ . It is noteworthy that the zircon-reidite phase transition pressure of pure  $\text{ZrSiO}_4$  obtained from DFT calculations differs substantially from static pressure and shock-wave compression experiments. Timms et al. [55] have provided a detailed discussion on this issue. Experimental observations suggest that this transition is kinetically sluggish. Hence, the difference in experimental and theoretical results can be a consequence of the kinetic effects and the associated barrier with it[40]. Coffinite and its high-pressure polymorph are isomorphic to zircon and reidite phases, respectively. I thus consider similar effects to be responsible for the underestimation of transition pressure in my theoretical calculations. However, the calculated  $p_t$  for  $\text{ThSiO}_4$  is consistent with the result obtained from the force field study of Bose et al.[16], who predicted  $p_t > 3$  GPa.

Fitting the E-V curve of coffinite with the third order Birch-Murnaghan equation of states yields a bulk modulus of 181.3 GPa, holding an excellent agreement with previous experimental values; 188 GPa[14] and 181 GPa[15]. To the best of my knowledge, the bulk moduli of the Th-end member and other intermediate members of reidite type phases are not reported elsewhere. The theoretical results presented in Table-4.1 show a monotonic decrease in the bulk moduli of the reidite-type phases with increasing Th content. The zircon-type phases display distinctly different variations of their bulk moduli with U/Th concentrations. Their endmembers have comparable values of the bulk moduli (181.3 GPa for  $\text{USiO}_4$  and 178.2 for  $\text{ThSiO}_4$ ). Any departure from the

pure phases reduces the values, where it attains a minimum (167.57 GPa) at Th at% = U at%. In order to validate my theoretical calculations, we compared the value of bulk modulus obtained for the reidite-type phase of  $USiO_4$  (239.05 GPa) with the available experimental data and found a fairly good agreement with the results of Bauer et al.[15].

The phase transitions we discussed above involve volume collapses ( $\Delta V$ ), which are constrained within 10.38% to 10.57% (Table 4.1).  $\Delta V$  is minimum for coffinite, and maximum for thorite. Bauer et al.[15] had reported a volume collapse of 11.18% for coffinite from experiments, which matches with our theoretical prediction. I have investigated the variation of compressibility for

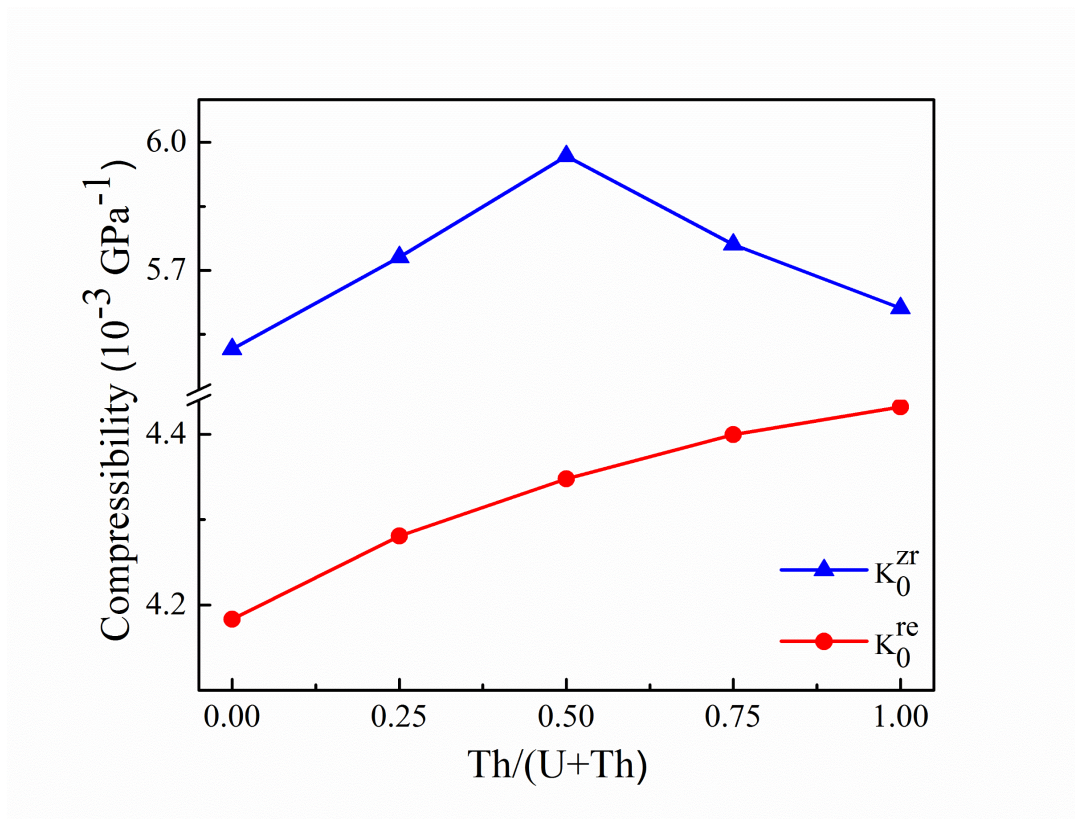


**Figure 4.4:** Compressibilities of  $U_{1-x}Th_xSiO_4$ ,  $x = Th/(U+Th)$  in both phases. Note the existence of a maximum value of compressibility in  $U_{0.5}Th_{0.5}SiO_4$ .

both phases with different Th concentrations (Figure 4.4). The compositional

## Chapter 4

mid-member of the zircon-type phase has the highest compressibility ( $5.97 \times 10^{-3} \text{ GPa}^{-1}$ ), implying that  $\text{U}_{0.50}\text{Th}_{0.50}\text{SiO}_4$  is the most pressure sensitive in the solid solution spectrum. Based on this finding, we can extrapolate that the zircon-type phase of this composition will behave as the most compressible phase, and thereby undergoes structural transition at the lowest hydrostatic pressure in the solid solution series (Figure 4.3). The compressibility of reidite-type phases is always lower than the zircon type for any given U/Th concentration. However, their compressibility increases monotonically with increasing Th content (Figure 4.4).

### 4.5 Polyhedral geometry and distortion

Both the zircon- and the reidite-type phases house U/Th atoms in 8-fold coordination with O atoms, forming a distorted polyhedral structure, called *triangular dodecahedra*, which is mathematically described as snub-disphenoid. An ideal snub-disphenoid has 8 vertices (i.e. the locations of O atoms here) and 12 equilateral triangles as its enclosing surfaces. The lines between two adjacent O- atoms form 18 edges of the snub-disphenoid. It is noteworthy that all the vertices are not equivalent; four of them form the edge by assembling with four nearest neighbours, whereas the rest four with five nearest neighbours (Figure 4.5). We designate the two non-equivalent sets of four O atoms as  $\text{O}_4$ -s and  $\text{O}_5$ -s. In addition, another remarkable feature concerns heterogeneity in the type of oxygen atoms in those  $\text{U/ThO}_8$  polyhedra. In case of zircon-type phase, the U/Th polyhedra share an edge with the Si-tetrahedra; the resulting edge contains two  $\text{O}_4$  atoms at its extremities, in

contrary to a point sharing with Si-tetrahedra, where the position is occupied by O<sub>5</sub> atom. The reidite-type phase, on the other hand, lacks edge sharing, and does not have any constraint in respect of the preference of O-atom in different geometrical sites, as observed in the zircon-type phase. This phase accommodates the shared O-atoms as either O<sub>4</sub> or O<sub>5</sub>.

A snub-disphenoid contains a unique point (X in Figure 4.5), equidistant from the four vertices that are connected to four nearest neighbor vertices occupied by O<sub>4</sub> atoms. Let the distance between X and O<sub>4</sub> be  $l_4$ . Similarly, X is also equidistant from the remaining four vertices connected to five nearest neighbor vertices occupied by O<sub>5</sub> atoms. Consider their length as  $l_5$ . The two lengths are characteristically unequal ( $l_4 \neq l_5$ ). These types of atomic configurations are distinguished based on a purely geometrical consideration, which is necessary to form the edges of snub-disphenoid, not to be confused with an electronic correspondence to bond formation. To quantify the longitudinal and angular distortions,  $l_4, l_5$  and the angles formed by adjacent vertices at X, are considered in the cases of ideal snub-disphenoids isovolumetric with our calculated ones.

### **4.5.1 Theoretical framework for polyhedral distortion**

Consider an ideal snub-disphenoid of unit edge length, as illustrated in Figure 4.5. The solutions to the coordinates of vertices are available in Wolfram Math library. This analysis, however, develops independently a theoretical scheme to obtain a geometrical solution. The theoretical treatment involves solving a set of four simultaneous quadratic equations for p,q,r and s; obtained

## Chapter 4

from equating the algebraic expression of each edge lengths to 1. In total, we have 8 equations, albeit 4 of them being redundant for solving; but these provide an aid to verify the solutions. The solutions for  $p$ ,  $q$ ,  $r$  and  $s$  obtained from our calculations follow:

$$p \approx 0.64458, q \approx 0.57837,$$

$$r \approx 0.98949 \text{ and } s \approx 1.56786.$$

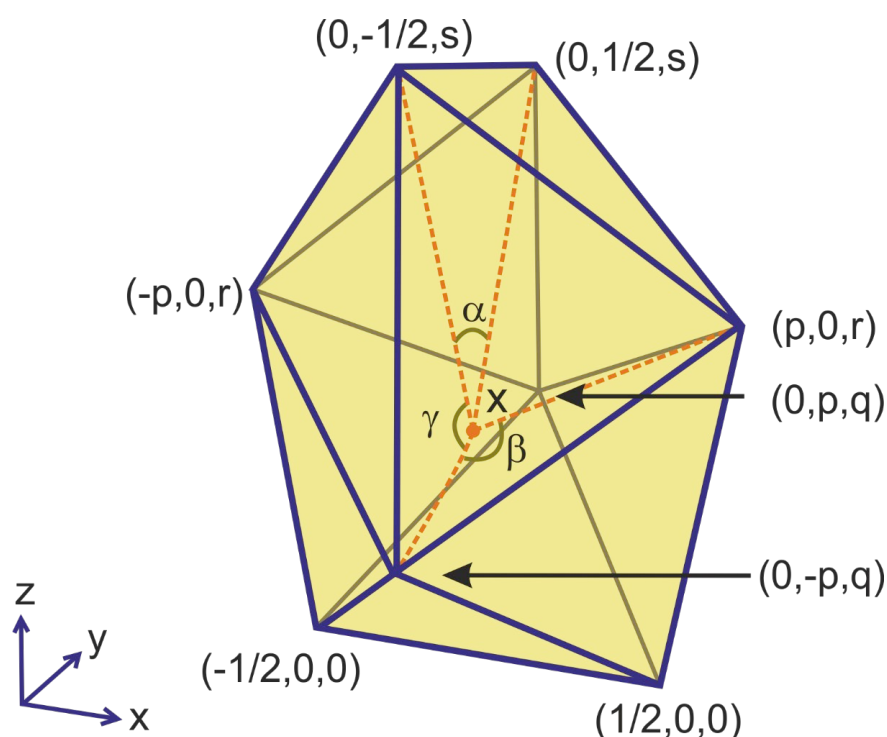


**Figure 4.5:** Distribution of coordinates of vertices of an ideal snub-disphenoid of unit edge length. The origin lies at the midpoint of the bottom edge, as evident from the chosen coordinates of the vertices. The red point ( $X$ ) inside is the special point as discussed above. The vertices with  $p$  and  $q$  in their coordinates are the position of  $O_5$  and the rest are the position of  $O_4$ . The different type of bond angles that can occur with different multiplicities are also shown as  $\alpha$ ,  $\beta$  and  $\gamma$ .

To find the coordinate of  $X$ , required to calculate the ideal bond length, the theoretical treatment adopts the Nelder-Mead optimization scheme, which evaluates the coordinates of the centre treating the sum of distances of the vertices from  $X$  to converge to a global minimum. Using this operation we obtain the coordinates of  $X$  as  $(0, 0, \sim 0.78393)$ , and  $l_4 \approx 0.929809$  and  $l_5 \approx$



0.676568. An introspection of this analysis provides a further insight into the polyhedral geometry. the z-coordinate of X is  $s/2$  and/or  $(p+r)/2$ . The problem of finding the coordinates of vertices and of the special point for an ideal snub-disphenoid with edge length  $a$ , then reduces to a scaling problem. The prescription is to multiply  $p, q, r, s$  and the coordinate of the special point by the factor,  $a$ . The ideal edge length of a snub-disphenoid can be calculated from its volume via the relation

$$a \approx \left( \frac{V}{0.8594937} \right)^{\frac{1}{3}} \quad (4.1)$$

The same approach can be followed to find different sets of  $l_4$  and  $l_5$  for ideal snub-disphenoids of varying volumes. Strikingly, the  $l_4$  to  $l_5$  ratio remains a constant,  $L (\approx 1.374302)$ , irrespective of the ideal snub-disphenoid's volume. A similar ratio can be found for distorted U or Th snub-disphenoids, expressed as  $l_U$  and  $l_{Th}$ , respectively. The deviation of  $l_U$  and  $l_{Th}$  from  $L$  can be treated as a measure of distortion of the polyhedra under study. We can define the following factors,

$$\delta_U = (l_U - L)^2 \quad \text{and}$$

$$\delta_{Th} = (l_{Th} - L)^2 \quad (4.2)$$

to quantify longitudinal distortions of U and Th-polyhedra, respectively.

Now we will deal with an analysis of the polyhedral angles. It is necessary to clarify in the beginning that only those angles formed by any two adjacent vertices at X should be treated as bond angles, so that the edges of the snub-disphenoid lies opposite to the angle under consideration. Since the

## Chapter 4

vertices are of two kinds, the adjacent vertices may or may not be of the same kind. Their contrasting configurations can give rise to three geometrically and numerically distinct angles with multiplicity of 2, 4 and 12 respectively:  $O_4 - X - O_4(\alpha)$ ,  $O_5 - X - O_5(\beta)$  and  $O_4 - X - O_5(\gamma)$ . For ideal cases, we find that  $\alpha = 65.061^\circ$ ,  $\beta = 95.297^\circ$  and  $\gamma = 75.158^\circ$  from the laws of cosines. Therefore, we can consider three different sample angular variances  $\sigma_\alpha^2$ ,  $\sigma_\beta^2$  and  $\sigma_\gamma^2$  or their sum  $\sigma^2$ , and express them as,

$$\sigma_\alpha^2 = \sum_{i=1}^2 (\alpha_i - 65.061)^2$$

$$\sigma_\beta^2 = \frac{1}{3} \sum_{j=1}^4 (\beta_j - 95.297)^2$$

$$\sigma_\gamma^2 = \frac{1}{11} \sum_{k=1}^{12} (\gamma_k - 75.158)^2$$

And, finally 
$$\sigma^2 = \sigma_\alpha^2 + \sigma_\beta^2 + \sigma_\gamma^2 \quad (4.3)$$

which will serve as the measure of the total angular distortion.

## 4.6 U/ThO<sub>8</sub> polyhedral distortions

An ideal regular polyhedron always contains a unique point inside, equidistant from the vertices. This point represents the position of a cation in the polyhedron, whereas the vertices serve as the positions of anions or the central atoms of ligands. For an ideal regular polyhedron, the distance between this unique point and the vertices defines a longitudinally unique bond. Such a regular arrangement gives rise to a unique angle formed at the centre by any two adjacent vertices in an undistorted polyhedron. This angle can be treated as ideal bond angle. Polyhedral distortions are then quantified in terms of the

ideal bond length and bond angles formed at the centre[37]. But it has been observed that, even ideal, but irregular polyhedra can have varying centre to vertex lengths. Thus, different bond lengths and bond angles are found to occur with varying multiplicity. Consequently, the existing methods employed in estimating the polyhedral distortions are untenable. This kind of geometrical complexity occurs in many crystalline phases. For example, actinide centered eight-fold coordination polyhedra with snub-disphenoidal shape can be found in various types of structural symmetry, such as, Monoclinic- Monazite,  $\text{CuTh}_2(\text{PO}_4)_2$ [56]; Trigonal- Dugganite[57]; Orthorhombic- Vitusite and  $\text{CaU}(\text{PO}_4)_2$ [58]; zircon, reidite, wolframite and fergusonite phases; Hexagonal- Rhabdophane group of minerals. An analysis of the geometrical peculiarity of snub-disphenoids thus merits a discussion to obtain new structural insights. In this study, I have dealt with the perplexing geometry of U-Th polyhedra in zircon- and reidite-type phases which display an irregular geometry as well as distorted shapes. Here I developed a novel approach for the geometrical analysis of a non-ideal snub-disphenoid. Two physical parameters are accounted to quantify the distortion. The distortion analysis enables us to interpret the transition from zircon- to reidite-type phases of uranothorite.

The discussion explains how co-ordination geometry is responsible for the evolution of two types of U/Th-O bonds with varying lengths, each with multiplicity 4. In the foregoing description each O atoms will be designated as O<sub>4</sub> and O<sub>5</sub> to express their unique positions (the type of vertices they occupy) in the polyhedra (Figure 4.5). Table-4.2 summarizes the calculated bond lengths, providing their comparison with the available data in literature. The

## Chapter 4

U-O<sub>4</sub> and U-O<sub>5</sub> bond-lengths for coffinite (2.438 and 2.311 Å) are within 0.8% of the values estimated from both the synchrotron powder measurement and **Table-4.2**. Calculated bond lengths of U<sub>1-x</sub>Th<sub>x</sub>SiO<sub>4</sub> in both zircon and reidite phases with varying U and Th percentage. The bracket in the last columns succeeding the data is the multiplicity of that bond.

<i>Phase</i>	<i>x</i>	<i>U-O<sub>4</sub> (Å)</i>	<i>U-O<sub>5</sub> (Å)</i>	<i>Th-O<sub>4</sub> (Å)</i>	<i>Th-O<sub>5</sub> (Å)</i>	<i>Si-O(m) (Å)</i>
<b>Zircon</b>	0.00	2.438 2.418 <sup>[15]</sup> 2.439 <sup>[22]</sup>	2.311 2.310 <sup>[15]</sup> 2.298 <sup>[22]</sup>	-	-	1.647(4)
	0.25	2.440	2.324	2.465	2.347	1.660(2),1.635(2)
	0.50	2.438	2.342	2.469	2.362	1.651(2),1.647(2)
	0.75	2.442	2.357	2.464	2.374	1.655(2),1.647(2)
	1.00	-	-	2.469 2.467 <sup>[22]</sup> 2.47 <sup>[52]</sup>	2.384 2.363 <sup>[22]</sup> 2.37 <sup>[52]</sup>	1.650(4)
<b>Reidite</b>	0.00	2.424 2.4304 <sup>[15]</sup> 2.474 <sup>[16]</sup>	2.344 2.3895 <sup>[15]</sup> 2.328 <sup>[16]</sup>	-	-	1.660(4)
	0.25	2.421	2.349	2.479	2.385	1.665(2),1.656(2)
	0.50	2.412	2.354	2.476	2.391	1.667(2),1.658(2)
	0.75	2.441	2.359	2.483	2.393	1.662(2),1.657(2)
	1.00	-	-	2.487	2.394	1.659(4)

DFT+U study of Bauer et.al[15]. These bond lengths are also in excellent agreement with the EXAFS measurements of Labs et al.[22] (2.439 and 2.298 Å, i.e. within 0.5%).

For the zircon-type ThSiO<sub>4</sub>, the present calculations yield Th-O<sub>5</sub> bond length to be 2.469 Å, which closely tracks the results of Fuchs and Gebert[19] (2.47 Å) and Labs et al.[22] (2.467 Å). The shorter bond length (2.384 Å) slightly differs from the previous results of Fuchs and Gebert[19] and Labs et al.[22]. In zircon type phase the U/Th-O<sub>4</sub> bond lengths are not much sensitive to the stoichiometric exchange between U and Th. But, U/Th-O<sub>5</sub> bond lengths show a monotonic increase on increasing Th-content, and this factor plays the key role in volume expansion while substituting Th in place of U. In case of the high

pressure polymorph of USiO<sub>4</sub>, the longer U-O<sub>4</sub> bond is appreciably closer to the DFT+U result of Bauer et al.[15] and the force-field calculation of Bose et.al[16]. The shorter U-O<sub>5</sub> bond length (2.344 Å) is within 1.8 % of the reported values of the earlier studies mentioned above. In contrast to the zircon type, the reidite type phase show similar variations, albeit little, of both the bonds on stoichiometric exchange between U and Th (Table-4.2). The relatively open unit cell of reidite phases permits them to accommodate Th in place of U as it does not involve any significant changes in the polyhedral volume and the corresponding bond lengths. The SiO<sub>4</sub> tetrahedra, being more rigid than the U-Th polyhedra, do not undergo significant geometrical modifications, leaving Si-O bond lengths virtually intact (1.635 Å to 1.667 Å). This finding is commensurate with the previous studies[15,22]. In Figure 4.2 I have shown an inverse relation of the  $c/a$  ratio with Th content; the relation is opposite for the unit cell volume of zircon type phases.

I emphasize that, as the U/Th-O<sub>5</sub> bonds lie almost parallel to  $a$  and  $b$ -axes their length increments have the most effects on increase of the lattice parameters along  $a$  and  $b$ -axes. On the other hand, the U-O<sub>4</sub> bonds have little influence on the lattice parameter along  $c$ . Such contrasting effects of the two types of bonds explain the inverse relation of  $c/a$  with Th content in zircon-type phases. We can also find that the U/Th-O<sub>4</sub> bond length does not significantly change because the O<sub>4</sub> atoms form the edge, shared by both the U/Th and Si-polyhedra. This edge sharing gives rise to a strong connection between the U/Th or Si atoms and O atoms. In contrast, O<sub>5</sub> atoms form corner sharing between U/Th polyhedra and Si-tetrahedra, and thereby develop,

## Chapter 4

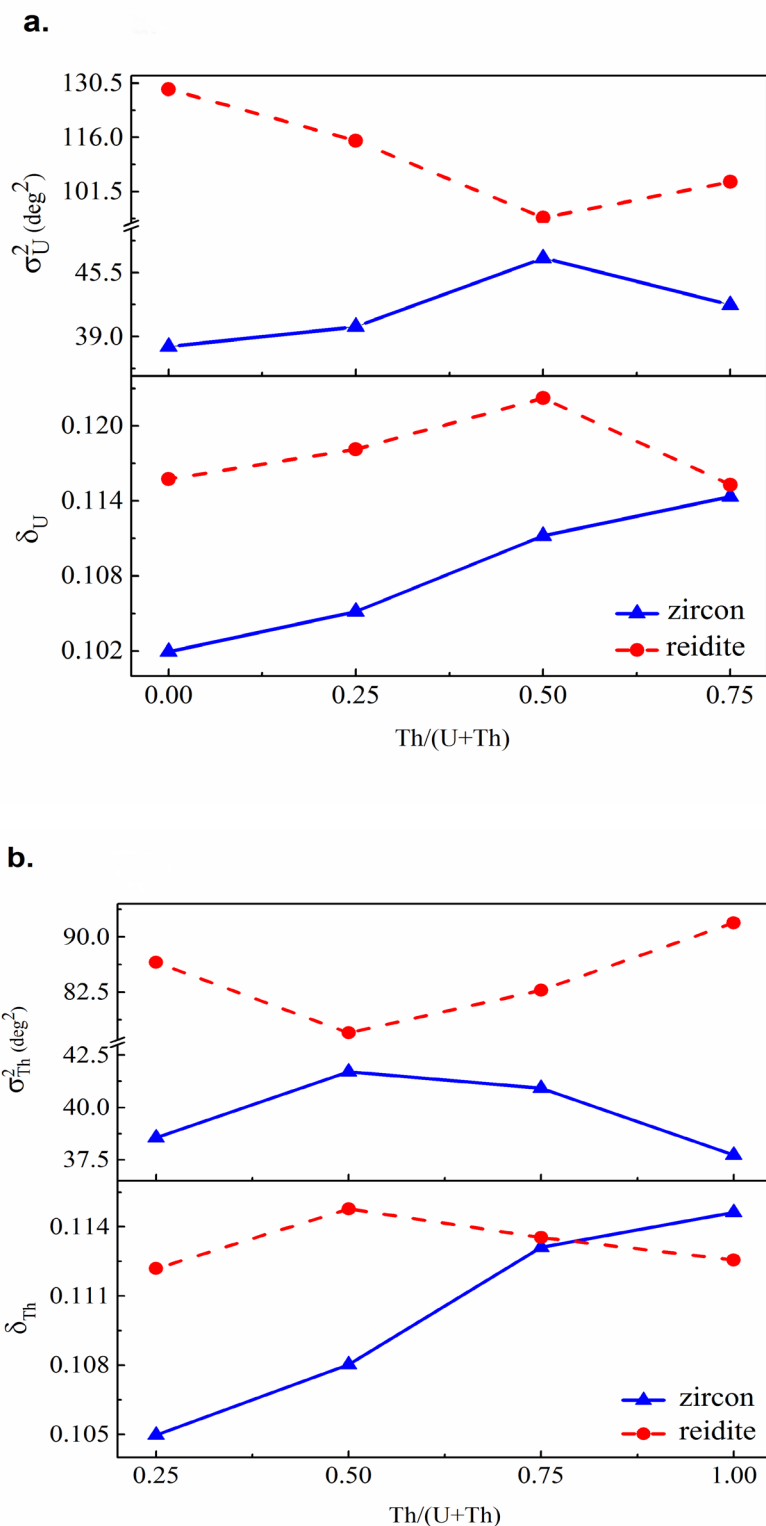
comparatively weaker connections, allowing relatively larger changes in the U/Th-O<sub>5</sub> bond lengths (See Fig. 4.1). The reidite type phases do not show any preferred orientation of the atomic bonds with respect to the unit cell axes. Both the U/Th-O<sub>4</sub> and -O<sub>5</sub> bonds increase their lengths with volume increment, associated with enhancement of  $c/a$  ratios with increasing Th content.

Table-4.3 summarizes the calculated values of  $\delta_U$ ,  $\delta_{Th}$ ,  $\sigma_U^2$  and  $\sigma_{Th}^2$ , as defined in Eqn. 4.2 and 4.3. This analysis confirms that elemental interchange between U and Th has a dramatic effect on the distortion parameters of the polyhedra, which enables us to explain why the phase transition pressure ( $p_t$ ) drops down to a minimum at U/Th = 1 (Figure 4.3). The variations of these parameters with Th concentration in the unit cell is demonstrated in Figure 4.6. The bond length distortions,  $\delta_U$  and  $\delta_{Th}$  for the zircon-type phases hold positive relations with Th concentration. But, for the reidite-type phases, they increase to attain a maximum value at U/Th = 1, and then decline with further increase of Th. Interestingly, the presence of such criticality occurs exactly at U/Th = 1 for both  $\delta_U$  and  $\delta_{Th}$  regressions for the reidite type phases. The

**Table-4.3:** Distortions of bond lengths and bond angles of U and Th snub-disphenoids in compositionally different zircon type structures of U<sub>1-x</sub>Th<sub>x</sub>SiO<sub>4</sub> and in their corresponding reidite phase. The subscript in the name of the parameters in heading refers to actinide atomic species at the point X inside the snub-disphenoid as shown in Fig. 4.5.

Phase	x	$\delta_U$	$\delta_{Th}$	$\sigma_U^2$ (deg <sup>2</sup> )	$\sigma_{Th}^2$ (deg <sup>2</sup> )
Zircon	0	0.10198	-	37.982	-
	0.25	0.10523	0.10497	40.007	38.555
	0.50	0.11110	0.10824	46.984	41.707
	0.75	0.11441	0.11316	42.226	40.923
	1.00	-	0.11468	-	37.732
Reidite	0.00	0.11572	-	128.891	-
	0.25	0.11810	0.11215	115.069	86.555
	0.50	0.12226	0.11475	94.471	76.962
	0.75	0.11523	0.11336	104.038	82.762
	1.00	-	0.11253	-	91.937

corresponding values follow:  $\delta_U = 0.12223$  and  $\delta_{Th} = 0.11478$ . The angular distortion of U-O bonds,  $\sigma_U^2$ , in the reidite-type phase forms a minimum (94.471 deg<sup>2</sup>) at U/Th =1, which exactly coincides with the point of maximum (46.984 deg<sup>2</sup>) in the regression for the zircon type (Figure 4.6a). A similar, although quantitatively different, trend is observed in cases of angular distortion of ThO<sub>8</sub> polyhedra, represented by  $\sigma_{Th}^2$  (Figure 4.6b). The variation  $\sigma_U^2$  and  $\sigma_{Th}^2$  are also characterized by an indicative maximum (minimum) limit in zircon (reidite)-type phases. Evidently, the numerical values of these limits of bond length and angular distortions these phases accommodate, depend entirely on the competing amount of constituent actinides. With elevation in the hydrostatic pressure these zircon type phases have a tendency to reorient and reorganize the polyhedral structures, and to overcome the corresponding difference in distortions. It is evident from Figure 4.6, the difference in  $\sigma_U^2$  and  $\sigma_{Th}^2$  between zircon and reidite type phases becomes minimum when U and Th percentage are equal. Therefore, the zircon to reidite-type phase transition occurs at a minimum hydrostatic pressure (6.82 GPa) for the phase with the unique chemical composition: U<sub>0.5</sub>Th<sub>0.5</sub>SiO<sub>4</sub>. A departure from this unique composition, by either a gain or a loss of Th or U, would widen the gap between  $\sigma_U^2$  and  $\sigma_{Th}^2$ , which acts as a barrier to the structural transition, and requires higher pressures to overcome this barrier. These phase transitions involve a reconstructive mechanism in which the triangular dodecahedra break their bonds and reorganize them into another new dodecahedra in the high-pressure phase. This process proceeds through an intermediate transient cubic phase as demonstrated by Smirnov et al.[59]. This theoretical investigation predicts that



**Figure 4.6:** Variation of polyhedral distortions of **a.** Uranium-snub disphenoid, **b.** Thorium-snub disphenoid in zircon and reidite-type  $U_{1-x}Th_xSiO_4$  with respect to  $x = Th/(U+Th)$  i.e. with normalized Th concentration. Distortions are quantified in terms of bond angle variance ( $\sigma^2$ ) and bond length ratio contrast ( $\delta$ ).



the geometrical difference between the distorted snub-disphenoidal forms in the two states turn to be minimum when  $U/Th = 1$  and facilitates the reconstructive phase transition to occur at the lowest pressure.

Figure 4.7 provides a quantitative description to show how  $\delta_U$  and  $\delta_{Th}$  can vary with hydrostatic stresses in the zircon type phases. Both  $\delta_U$  and  $\delta_{Th}$  hold inverse relations with pressure. However, it is quite interesting to note

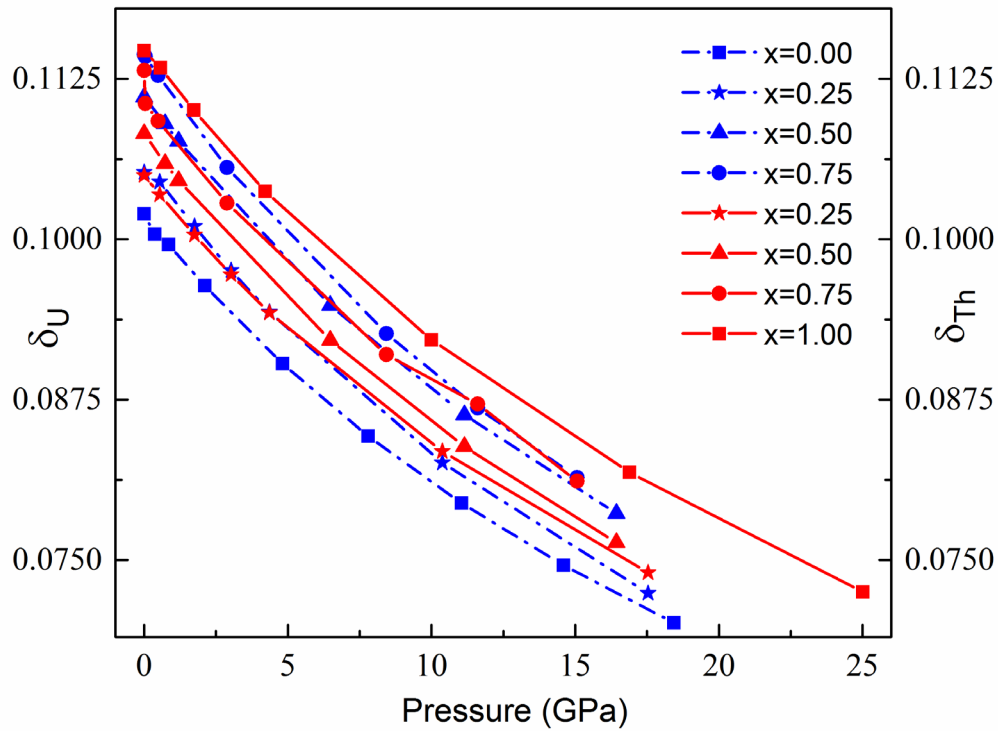


**Figure 4.7:** The pressure dependent variation of  $\delta$  for both U and Th-polyhedra. The blue lines and symbols are for Uranium and the red lines and symbols are for Thorium. The  $x$  in legend stands for  $x = Th/(U+Th)$  like the previous cases. Hence, the square symbols characterize the pure U endmember  $USiO_4$  (red) and pure Th endmember (blue)  $ThSiO_4$  of  $U_{1-x}Th_xSiO_4$  series.

that  $\delta_U$  for  $USiO_4$  is the lowest in ambient condition, and it increases as more and more Th is substituted in place of U, suggesting that the larger element Th partly controls the deformation behaviour of U-polyhedra. In case of Th-polyhedra,  $\delta_{Th}$  is maximum for pure  $ThSiO_4$ , and the degree of distortion is

## Chapter 4

reduced with substitution of Th with U in the solid solution phases. In summary, elemental Th has larger influence on the polyhedral distortion than elemental U. This analysis reveals that pressure-sensitivity of both  $\delta_U$  and  $\delta_{Th}$  drops with increasing pressure. The lower values of  $\delta_U$  and  $\delta_{Th}$  at high pressures suggest that hydrostatic pressures counter to the inherent polyhedral distortions, and facilitate the polyhedra to achieve an ideal structure. At the high pressure regime (beyond 8 GPa) the average pressure derivative for  $\delta_U$ , i.e.  $\frac{\Delta\delta_U}{\Delta P}$  in  $USiO_4$  and  $\delta_{Th}$  in  $ThSiO_4$ , i.e.  $\frac{\Delta\delta_{Th}}{\Delta P}$  are found to be  $1.265 \times 10^{-3} \text{ GPa}^{-1}$  and  $1.324 \times 10^{-3} \text{ GPa}^{-1}$ , respectively.

I have similarly analyzed the polyhedral distortion for the reidite-type phases as a function of hydrostatic pressure. The distortion parameters,  $\delta_U$  and  $\delta_{Th}$  exhibit similar pressure-dependent behavior; however, they vary with pressure at much lower slopes, compared to that observed in zircon phases. According to calculations, an ideal geometry of snub-disphenoid ( $\delta_U = 0$  and  $\delta_{Th} = 0$ ) is possible in reidite type phase at a much higher pressure. Secondly,  $\delta_U$  and  $\delta_{Th}$  for reidite-type phases are not strongly sensitive to Th content in the solid solution. The absence of edge sharing between the U/Th-polyhedra and Si-tetrahedra and the presence of large amount of empty spaces in the conventional unit cell of reidite phases allows the polyhedra to minimize the distortion, and attain a more ideal shape.

Based on the results and discussion presented above, we now offer an outlook of this study. Many materials undergo sequential phase transitions under hydrostatic pressure, e.g., zircon→reidite or reidite→wolframite or

reidite→fergusonite [50,59–64] . In these transitions the AO<sub>8</sub> (A = any cation) polyhedra retain their geometrical shape. Some of the previous studies reported a unique A-O bond length[28]. But our study reveals that the occurrence of such a unique bond length in an AO<sub>8</sub> polyhedron is not possible due to the geometrical constraint of the polyhedron itself. On the other hand, several other studies [15, 22, 40, 51, 52, 58, 59, 62, 64] have reported one short and one longer A-O bond, but without providing any fundamental explanation for such contrasting bond lengths. The present polyhedral analysis provides a concrete mathematical basis of the two types of bonds, and correlates them with the existence of two distinct types of vertices, occupied by O atoms. The bond lengths are observed to demonstrate a unique ratio (A-O<sub>4</sub> / A-O<sub>5</sub> ≈ 1.374302), irrespective of the volumes of the polyhedra in ideal geometry. In addition, my analysis explains why the two types of bonds occur with a multiplicity of four. We believe that revisiting the zircon, reidite/scheelite, wolframite, fergusonite and other structures with similar kind of actinide polyhedra can give rise to newer insights into the dynamics of phase transition in terms of polyhedral distortions.

## **4.7 Highlights of the results**

Using DFT calculations this study provides a comprehensive analysis of the pressure induced zircon- to reidite-type phase transition of U<sub>1-x</sub>Th<sub>x</sub>SiO<sub>4</sub> (x= 0 to 1 in steps of 0.25) solid solution. The analysis shows that the phase transition pressure varies nonlinearly with increasing Th content in the solid solution to attain a minimum value of 6.82 GPa for x = 0.5. The calculations presented

## Chapter 4

here also offer an estimate of the compressibility of solid solution phases in both ambient and high-pressure conditions. The compressibility of zircon type  $U_{0.5}Th_{0.5}SiO_4$  phase is found to be maximum ( $5.97 \times 10^{-3} \text{ GPa}^{-1}$ ), implying it as the most pressure sensitive (soft) phase. This work theoretically predicts the structural parameters of the reidite-type polymorphs of the solid solutions, and also enumerates their mechanical properties.

The present study provides a new interpretation of the phase transition pressure ( $p_t$ ) of  $U_{1-x}Th_xSiO_4$ , accounting the effects of U/ThO<sub>8</sub> polyhedral distortion in the cell structures, and also develops a novel approach to the analysis of the polyhedral distortions of triangular dodecahedra (snub-disphenoids). The following two parameters ( $\delta$  and  $\sigma^2$ ) have been defined to express the longitudinal and angular distortions of highly irregular U/ThO<sub>8</sub>-triangular dodecahedra. The distortion analysis brings out two kinds of geometrically distinct vertices of the triangular dodecahedra, occupied by oxygen atoms, which explains the occurrence of two types of U/Th-O bonds (U/Th-O<sub>4</sub> and U/Th-O<sub>5</sub>) with contrasting lengths. The bond length ratio (U-O<sub>4</sub>/U-O<sub>5</sub> and Th-O<sub>4</sub>/Th-O<sub>5</sub>) remains constant ( $\sim 1.374302$ ), irrespective of the triangular dodecahedral volume. It is worthwhile to note that this theoretical framework to quantify the polyhedral distortions of U/Th-snub disphenoids is based entirely on geometrical considerations. The distortions parameters,  $\delta$  and  $\sigma^2$  are independent to the elements occupying the snub-disphenoid space. Also, they are defined without any attribute to external parameters. Thus, we expect that the parameters:  $\delta$  and  $\sigma^2$  can be used to calculate the distortion of similar AB<sub>8</sub>-type snub-disphenoid in other crystalline phases. The calculations

### ***U<sub>x</sub>Th<sub>1-x</sub>SiO<sub>4</sub> solid solution***

indicate that the difference in angular distortions ( $\sigma_U^2$  and  $\sigma_{Th}^2$ ) between the zircon- and reidite-type phases becomes minimum when U and Th occur equally in the solid solution. This study also confirms the highest compressibility of the zircon type phase for U<sub>0.5</sub>Th<sub>0.5</sub>SiO<sub>4</sub>. The concurrence of minima of transition pressure and the difference in  $\sigma^2$  indicates that the polyhedral distortion plays a critical role in dictating the zircon- to reidite-type transition.

## Chapter 4

### References:

- [1] Hae R, Ohtani E, Kubo T, Koyama T and Utada H 2006 Hydrogen diffusivity in wadsleyite and water distribution in the mantle transition zone *Earth Planet. Sci. Lett.* **243** 141–8
- [2] Zhao C and Yoshino T 2016 Electrical conductivity of mantle clinopyroxene as a function of water content and its implication on electrical structure of uppermost mantle *Earth Planet. Sci. Lett.* **447** 1–9
- [3] Huang X, Xu Y and Karato S 2005 Water content in the transition zone from electrical conductivity of wadsleyite and ringwoodite *Nature* **434** 746–9
- [4] Yoshino T, Matsuzaki T, Shatskiy A and Katsura T 2009 The effect of water on the electrical conductivity of olivine aggregates and its implications for the electrical structure of the upper mantle *Earth Planet. Sci. Lett.* **288** 291–300
- [5] Lee J K W, Williams I S and Ellis D J 1997 Pb, U and Th diffusion in natural zircon *Nature* **390** 159–62
- [6] Reiners P W 2005 Zircon (U-Th)/He thermochronometry *Rev. Mineral. Geochemistry* **58** 151–79
- [7] Kirkland C L, Smithies R H, Taylor R J M, Evans N and McDonald B 2015 Zircon Th/U ratios in magmatic environs *Lithos* **212–215** 397–414
- [8] Ewing R C and Lutze W 1995 Zircon: A host-phase for the disposal of weapons plutonium *J. Mater. Res.* **10** 243–6
- [9] Ewing R C 2002 Nuclear waste forms for actinides *Proc. Natl. Acad. Sci.* **96** 3432–9
- [10] Janeczek J and Ewing R C 1992 Dissolution and alteration of uraninite under reducing conditions *J. Nucl. Mater.* **190** 157–73
- [11] Amme M, Renker B, Schmid B, Feth M P, Bertagnolli H and Döbelin W 2002 Raman microspectrometric identification of corrosion products formed on UO<sub>2</sub> nuclear fuel during leaching experiments *J. Nucl. Mater.* **306** 202–12
- [12] Stieff L R, Stern T W and Sherwood A M 1955 Preliminary Description of Coffinite—a New Uranium Mineral *Science (80- )*. **121** 608–9
- [13] Kamineni D C and Lemire R J 1991 Thorite in fault zones of a granitic pluton, Atikokan, Canada: Implications for nuclear fuel waste disposal *Chem. Geol.* **90** 133–43
- [14] Zhang F X, Pointeau V, Shuller L C, Reaman D M, Lang M, Liu Z, Hu J, Panero W R, Becker U, Poinssot C and Ewing R C 2009 Structural transitions and electron transfer in coffinite, USiO<sub>4</sub>, at high pressure *Am. Mineral.* **94** 916–20
- [15] Bauer J D, Labs S, Weiss S, Bayarjargal L, Morgenroth W, Milman V, Perlov A, Curtius H, Bosbach D, Zänker H and Winkler B 2014 High-pressure phase transition of coffinite, USiO<sub>4</sub> *J. Phys. Chem. C* **118** 25141–9
- [16] Bose P P, Mittal R and Chaplot S L 2009 Lattice dynamics and high pressure phase

- stability of zircon structured natural silicates *Phys. Rev. B - Condens. Matter Mater. Phys.* **79** 174301-1-17431-1–8
- [17] Cocherie A and Legendre O 2007 Potential minerals for determining U-Th-Pb chemical age using electron microprobe *Lithos* **93** 288–309
- [18] von Blackenburg F 1992 Combined high-precision chronometry and geochemical tracing using accessory minerals: applied to the Central-Alpine Bergell intrusion (central Europe) *Chem. Geol.* **100** 19–40
- [19] Fuchs L H and Gebert E 1958 X-ray studies of synthetic coffinite, thorite and uranothorites *Am. Mineral.* **43** 243–8
- [20] Fuchs L H and Hoekstra H R 1959 The preparation and properties of uranium(IV) silicates *Am. Mineral.* **44** 1057–63
- [21] Pointeau V, Deditius A P, Miserque F, Renock D, Becker U, Zhang J, Clavier N, Dacheux N, Poinssot C and Ewing R C 2009 Synthesis and characterization of coffinite *J. Nucl. Mater.* **393** 449–58
- [22] Labs S, Hennig C, Weiss S, Curtius H, Zänker H and Bosbach D 2014 Synthesis of coffinite, USiO<sub>4</sub>, and structural investigations of U<sub>x</sub>Th<sub>(1-x)</sub>SiO<sub>4</sub> solid solutions *Environ. Sci. Technol.* **48** 854–60
- [23] Guo X, Szenknect S, Mesbah A, Labs S, Clavier N, Poinssot C, Ushakov S V., Curtius H, Bosbach D, Ewing R C, Burns P C, Dacheux N and Navrotsky A 2015 Thermodynamics of formation of coffinite, USiO<sub>4</sub> *Proc. Natl. Acad. Sci.* **112** 6551–5
- [24] Guo X, Szenknect S, Mesbah A, Clavier N, Poinssot C, Wu D, Xu H, Dacheux N, Ewing R C and Navrotsky A 2016 Energetics of a uranothorite (Th<sub>1-x</sub>U<sub>x</sub>SiO<sub>4</sub>) solid solution *Chem. Mater.* **28** 7117–24
- [25] Mesbah A, Szenknect S, Clavier N, Lozano-Rodriguez J, Poinssot C, Den Auwer C, Ewing R C and Dacheux N 2015 Coffinite, USiO<sub>4</sub>, Is Abundant in Nature: So Why Is It so Difficult to Synthesize? *Inorg. Chem.* **54** 6687–96
- [26] Frondel C and Collette R L 1957 Hydrothermal synthesis of zircon, thorite and huttonite *Am. Mineral.* **42** 759–65
- [27] Estevenon P, Welcomme E, Szenknect S, Mesbah A, Moisy P, Poinssot C and Dacheux N 2018 Multiparametric Study of the Synthesis of ThSiO<sub>4</sub> under Hydrothermal Conditions *Inorg. Chem.* **57** 9393–402
- [28] Shein I R, Shein K I and Ivanovskii A L 2006 Thorite versus huttonite: Stability, electronic properties and X-ray emission spectra from first-principle calculations *Phys. Chem. Miner.* **33** 545
- [29] Finch C B, Harris L A and Clark G W 1964 The thorite→huttonite phase transformation as determined by growth of synthetic thorite and huttonite single crystals *Am. Mineral.* **49** 782–5
- [30] Mazeina L, Ushakov S V., Navrotsky A and Boatner L A 2005 Formation enthalpy of ThSiO<sub>4</sub> and enthalpy of the thorite → huttonite phase transition *Geochim. Cosmochim. Acta* **69** 4675–83

## Chapter 4

- [31] Pointer C M, Ashworth J R and Ixer R A 1988 The zircon-thorite mineral group in metasomatized granite, Ririwai, Nigeria 2. Geochemistry and metastable solid solution of thorite and coffinite *Mineral. Petrol.* **39** 21–37
- [32] Pointer C M, Ashworth J R and Ixer R A 1988 The zircon-thorite mineral group in metasomatized granite, Ririwai, Nigeria 1. Geochemistry and metastable solid solution of thorite and coffinite *Mineral. Petrol.* **38** 245–62
- [33] Ifill R O, Cooper W C and Clark A H 1996 Mineralogical and process controls on the oxidative acid-leaching of radioactive phases in Elliot Lake, Ontario, uranium ores: II - Brannerite and allied titaniferous assemblages *CIM Bull.* **89** 93–103
- [34] Förster H J 2006 Composition and origin of intermediate solid solutions in the system thorite-xenotime-zircon-coffinite *Lithos* **88** 35–55
- [35] Clavier N, Szenknect S, Costin D T, Mesbah A, Poinssot C and Dacheux N 2014 From thorite to coffinite: A spectroscopic study of  $\text{Th}_{1-x}\text{U}_x\text{SiO}_4$  solid solutions *Spectrochim. Acta - Part A Mol. Biomol. Spectrosc.* **118** 302–7
- [36] Anon 1956 Geochemistry. By the late V. M. Goldschmidt. Edited by Alex Muir, Clarendon Press, 1954. *Q. J. R. Meteorol. Soc.* **82** 547
- [37] Robinson K 1971 Quadratic Elongation: A Quantative Measure of Distortion in Coordination Polyhedra *Science (80-. )*. **172** 567–70
- [38] Makovicky E and Balić-Žunić T 1998 New Measure of Distortion for Coordination Polyhedra *Acta Crystallogr. Sect. B Struct. Sci.* **54** 766–73
- [39] Mursic Z, Vogt T and Frey F 1992 High-temperature neutron powder diffraction study of  $\text{ZrSiO}_4$  up to 1900 K *Acta Crystallogr. Sect. B* **48** 584–90
- [40] Marqués M, Flórez M, Recio J M, Gerward L and Olsen J S 2006 Structure and stability of  $\text{ZrSiO}_4$  under hydrostatic pressure *Phys. Rev. B - Condens. Matter Mater. Phys.* **74** 1–9
- [41] Giannozzi P, Baroni S, Bonini N, Calandra M, Car R, Cavazzoni C, Ceresoli D, Chiarotti G L, Cococcioni M, Dabo I, Dal Corso A, De Gironcoli S, Fabris S, Fratesi G, Gebauer R, Gerstmann U, Gougoussis C, Kokalj A, Lazzeri M, Martin-Samos L, Marzari N, Mauri F, Mazzarello R, Paolini S, Pasquarello A, Paulatto L, Sbraccia C, Scandolo S, Sclauzero G, Seitsonen A P, Smogunov A, Umari P and Wentzcovitch R M 2009 QUANTUM ESPRESSO: A modular and open-source software project for quantum simulations of materials *J. Phys. Condens. Matter* **21**
- [42] Giannozzi P, Andreussi O, Brumme T, Bunau O, Nardelli Buongiorno M and Calandra M 2017 Advanced capabilities for materials modelling with Quantum ESPRESSO *J. Phys. Condens. Matter* **29**
- [43] Baroni S, De Gironcoli S, Corso A D and Giannozzi P 2001 Phonons and related crystal properties from density-functional perturbation theory *Rev. Mod. Phys.* **73** 515–62
- [44] Blöchl P E 1994 Projector augmented-wave method *Phys. Rev. B* **50** 17953–79
- [45] Perdew J P, Jackson K A, Pederson M R, Singh D J and Fiollhais C 1992 Atoms, molecules, solids and surfaces: Applications of the GGA for exchange correlation *Phys. Rev. B* **46**



- [46] Dal Corso A 2014 Pseudopotentials periodic table: From H to Pu *Comput. Mater. Sci.* **95** 337–50
- [47] Broyden C G 1967 Quasi-Newton Methods and their Application to Function Minimisation *Math. Comput.* **21** 368
- [48] Shanno D F 1970 Conditioning of Quasi-Newton Methods for Function Minimization *Math. Comput.* **24** 647
- [49] Hendrik J. Monkhorst 1976 Special points fro Brillouin-zone integretions *Phys. Rev. B* **13** 5188–92
- [50] Dutta R and Mandal N 2012 Structure, elasticity and stability of reidite (ZrSiO<sub>4</sub>) under hydrostatic pressure: A density functional study *Mater. Chem. Phys.* **135** 322–9
- [51] Rignanese G-M, Gonze X and Pasquarello A 2001 First-principles study of structural, electronic, dynamical, and dielectric properties of zircon *Phys. Rev. B* **63** 104305
- [52] Ewing R C ; T M 1978 The Crystal Structures of the ThSiO<sub>4</sub> Polymorphs: Huttonite and Thorite *Acta Crystallogr. Sect. B* **34** 1074–9
- [53] Zhong X, Hermann A, Wang Y and Ma Y 2016 Monoclinic high-pressure polymorph of AlOOH predicted from first principles *Phys. Rev. B* **94** 1–8
- [54] Klotz S, Chervin J C, Munsch P and Le Marchand G 2009 Hydrostatic limits of 11 pressure transmitting media *J. Phys. D. Appl. Phys.* **42**
- [55] Timms N E, Erickson T M, Pearce M A, Cavosie A J, Schmieder M, Tohver E, Reddy S M, Zanetti M R, Nemchin A A and Wittmann A 2017 A pressure-temperature phase diagram for zircon at extreme conditions *Earth-Science Rev.* **165** 185–202
- [56] Louër M, Brochu R, Louër D, Arsalane S and Ziyad M 1995 Structure determination of CuTh<sub>2</sub>(PO<sub>4</sub>)<sub>3</sub> *Acta Crystallogr. Sect. B* **51** 908–13
- [57] Yu H, Young J, Wu H, Zhang W, Rondinelli J M and Halasyamani P S 2016 Electronic, Crystal Chemistry, and Nonlinear Optical Property Relationships in the Dugganite A3B3CD2O14 Family *J. Am. Chem. Soc.* **138** 4984–9
- [58] Dusausoy Y, Ghermani N-E, Podor R and Cuney M 1996 Low-temperature ordered phase of CaU(PO<sub>4</sub>)<sub>2</sub>: synthesis and crystal structure *Eur. J. Mineral.* **8** 667–74
- [59] Smirnov M B, Mirgorodsky A P, Kazimirov V Y and Guinebretière R 2008 Bond-switching mechanism for the zircon-scheelite phase transition *Phys. Rev. B* **78** 94109
- [60] Errandonea D, Pellicer-Porres J, Manjón F J, Segura A, Ferrer-Roca C, Kumar R S, Tschauer O, Rodríguez-Hernández P, López-Solano J, Radescu S, Mujica A, Muñoz A and Aquilanti G 2005 High-pressure structural study of the scheelite tungstates CaWO<sub>4</sub> and SrWO<sub>4</sub> *Phys. Rev. B - Condens. Matter Mater. Phys.* **72** 1–14
- [61] Zhang C C, Zhang Z M, Dai R C, Wang Z P, Zhang J W and Ding Z J 2010 High-pressure raman and luminescence study on the phase transition of GdVO<sub>4</sub>:Eu<sup>3+</sup>-microcrystals *J. Phys. Chem. C* **114** 18279–82

## **Chapter 4**

- [62] Errandonea D, Kumar R, López-Solano J, Rodríguez-Hernández P, Muñoz A, Rabie M G and Sáez Puche R 2011 Experimental and theoretical study of structural properties and phase transitions in  $YAsO_4$  and  $YCrO_4$  *Phys. Rev. B* **83** 134109
- [63] Panchal V, Garg N, Poswal H K, Errandonea D, Rodríguez-Hernández P, Muñoz A and Cavalli E 2017 High-pressure behavior of  $CaMoO_4$  *Phys. Rev. Mater.* **1** 043605
- [64] Errandonea D and Garg A B 2018 Recent progress on the characterization of the high-pressure behaviour of  $AVO_4$  orthovanadates *Prog. Mater. Sci.* **97** 123–69
- [65] Errandonea D, Kumar R S, Achary S N and Tyagi A K 2011 In situ high-pressure synchrotron x-ray diffraction study of  $CeVO_4$  and  $TbVO_4$  up to 50 GPa *Phys. Rev. B* **84** 224121

## **Silicates-II: Titanite (CaTiSiO<sub>5</sub>)**

---

*Introduction*

*Computational approach*

*Structural analysis*

*Elastic constants tensor*

*Negative elasticity*

*Electronic and optical property*

*Concluding notes*



## 5.1 Introduction

Titanite is a multifunctional nesosilicate phase[1], well known as a versatile host for rare earth elements (REE)[2–5], and also widely used as U-Pb geochronometer for dating geological events[6]. This crystalline phase, rich in TiO<sub>2</sub> content, is a demanding material owing to its applications for developing strategic matrices for nuclear waste disposal, which is currently a challenging and intriguing field of research[2,4]. Various properties of single-crystal titanite have been investigated in ambient and high-pressure environments with high-end laboratory techniques, such as DAC (diamond anvil cell) and multi anvil experiments[7–13]. Salje et al.[14] showed the softening of shear modulus through annealing in a radiation damaged titanite sample. Their estimate of the bulk modulus is found to be much lower than that of Angel et al.[15]. However, the literature lacks any reliable experimental

## Chapter 5

or theoretical data for the 2<sup>nd</sup> order elastic constants of titanite, which are the pre-requisite mechanical parameters in order to explore the viability of this crystalline phase in extreme industrial applications. My present study provides an account of the structural morphology and the physical properties of titanite phases ( $P2_1/c$  and  $C2/c$ ) at elevated pressures, and offers an insight into the structural dependence of their elastic properties. The structural analysis evaluates the relative rotation of different atomic bonds and subsequent changes in the alignment of their corresponding polyhedra under imposed strains.

Elasticity is a remarkable macroscopic mechanical property of solids, which can be used to study a wide range of atomic scale phenomena, such as lattice instability, spin transitions, lattice dynamics and phonon instability[16–18]. An enormous volume of the existing literature deals with the elasticity of crystalline phases, but mostly as positive quantities[19–23]. Despite a number of existing continuum models[24–27], the elasticity as a negative quantity is still an enigma because the underlying atomic scale physics for such an unusual mechanical behaviour has remained unexplored. Experimental studies suggest that crystalline materials of low as well as high symmetry structures may have negative elastic constants, implying that the negative elasticity is not a direct consequence of the crystal symmetry[28,29]. Although the reports on the negative elastic constants are scanty, experimental investigations performed on high symmetry cubic phases confirm the existence of this exceptional mechanical behaviour of solids[28–31]. The first principles calculations in this chapter predict the negative component ( $C_{36}$ ) of the elastic

constant tensor ( $C_{ij}$ ) of  $C2/c$  titanite, which, to the best of my knowledge, is reported for the first time. The present thesis aims to provide an atomic level basis of such negative elastic behaviour, taking into account the rotational bond kinematics under a given strain to the crystal.

A recent study by Malcherek and Fischer[32] has compared the phonon dispersions of  $P2_1/c$  and  $C2/c$  phases of titanite ( $\text{CaTiSiO}_5$ ) and mayalite ( $\text{CaSnSiO}_5$ ), showing negative acoustic branches in  $C2/c$  titanite phase along the direction [001]. They have proposed that  $P2_1/c$  titanite can be obtained from  $C2/c$  phase by destabilizing a continuous phonon mode along [001] by lowering the temperature. However, high pressure behaviour of  $P2_1/c$  titanite is still absent in the literature. Secondly, despite a great demand of titanite for its electronic and optical properties in materials engineering, there have not been in-depth theoretical and experimental studies to assess these properties. A line of the present study predicts titanite as a semi-conductor with an electronic band gap of 3.2 eV. The problem motivates me also to investigate the anisotropic optical behaviour of this silicate phase on a frequency range 0-60 eV. Interestingly, the findings provide a new insight into the applicability of titanite as UV-shield materials.

## **5.2 Computational approach**

First principle calculations were performed within the framework of DFT using the VASP5.3[33]. PAW potentials[34] provided with VASP explicitly treat [3p4s], [3d4s], [3s3p] and [2s2p] orbitals for Ca, Ti, Si and O as valence states with the core radii 1.746, 1.323, 1.312 and 0.82 Å, respectively. The calculations considered the revised GGA (RPBE) scheme for the exchange-

## Chapter 5

correlation effects[35]. To account for the electron correlation of Ti *d* electrons we performed GGA+U (on-site correction for Coloumb interaction) calculations by incorporating the Hubbard-type term in the density functional following the method proposed by Dudarev et al.[36]. Therefore, Coulomb repulsion is considered explicitly using  $U_{effective} = U - J$ , where  $J = 0$ . The U value is calculated self consistently with varying values ranging from 2 to 8 eV. U is chosen to be 4 eV as we get the optimum value of band gap with it. All the simulations were carried out on 32 atom cell for both the titanite phases. The kinetic energy cut-off was set at 1000 eV. The conjugate gradient algorithm was employed to perform geometrical optimization in finding the ground state electronic structure under the strict electronic and ionic convergence criteria of  $10^{-6}$  eV and  $10^{-3}$  eV/atom, respectively. The sampling of the brillouin zones was implemented by 3x2x3 and 4x4x3 Monkhorst–Pack[37,38] k-point grids, which gave rise to 10 and 21 irreducible k-points. I used Phonopy[39] for lattice dynamical calculation with 2x2x2 supercell. The force constants were calculated using DFPT without constraining their symmetry and they were interpolated using 17x17x17 q-mesh for the full dispersion curve. Such dense q-mesh was required to increase the accuracy of the phonon dispersion.

### 5.3 Structural analysis

Titanite ( $CaTiSiO_5$ ) crystallizes with monoclinic symmetry (space group:  $P2_1/c$ ; No. 14) (Figure 5.1a) at ambient condition[9,40,41]. This phase undergoes structural transitions with increasing pressure as well as temperature. Under ambient pressure it transforms into another monoclinic phase with space group  $A2/a$  at a temperature of  $\sim 500$  K[11,41–43]. Kunz et



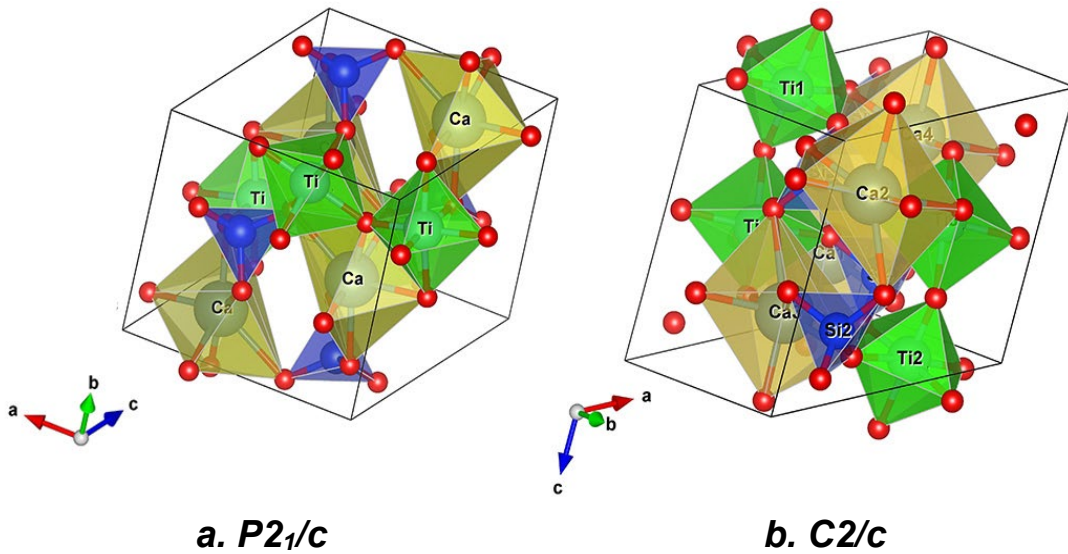


**Figure 5.1:** Monoclinic crystal structures of titanite phases: (a)  $P2_1/c$ , (b)  $C2/c$ .  $\text{TiO}_6$  octahedra share their corner oxygen atom, forming alternate chains along  $a$ -axis in  $P2_1/c$ , whereas along the  $c$  axis in  $C2/c$ . The two sides of  $\text{TiO}_6$  octahedron are shared by edges of two distorted  $\text{CaO}_7$  polyhedra.

al.[44] predicted the same transition with pressure at 6.9 GPa from DAC experiments. Some workers have also reported another phase transition of titanite, i.e.,  $P2_1/c$  to  $C2/c$  (Figure 5.1b) phase at 487 K[11,12,42]. The same transition is reported at a hydrostatic pressure of  $\sim 3.5$  GPa[10], and it is inferred to be analogous to the 825 K transition by Kunz et al.[45] from a powder diffraction study. Using lattice dynamics this computational study predicts that  $P2_1/c$  to  $C2/c$  transition to occur within 5 GPa. Figure 5.2 shows the phonon dispersion curves for  $P2_1/c$  phase at 0 and 5 GPa along the high symmetry points G–Z–B–D–G–A. The optical modes shifts towards higher frequency regions, whereas the acoustic modes soften to some negative values with increasing pressure. The phonon dispersion at 0 GPa suggest that the  $P2_1/c$  phase to be dynamically stable, but it develops a negative acoustic branch along G–A at 5 GPa, implying that the  $P2_1/c$  phase becomes

## Chapter 5

dynamically unstable at 5 GPa. The phonon dispersion analysis is in agreement with previous finding of  $P2_1/c$  to  $C2/c$  transition at  $\sim 3.5$  GPa[10].

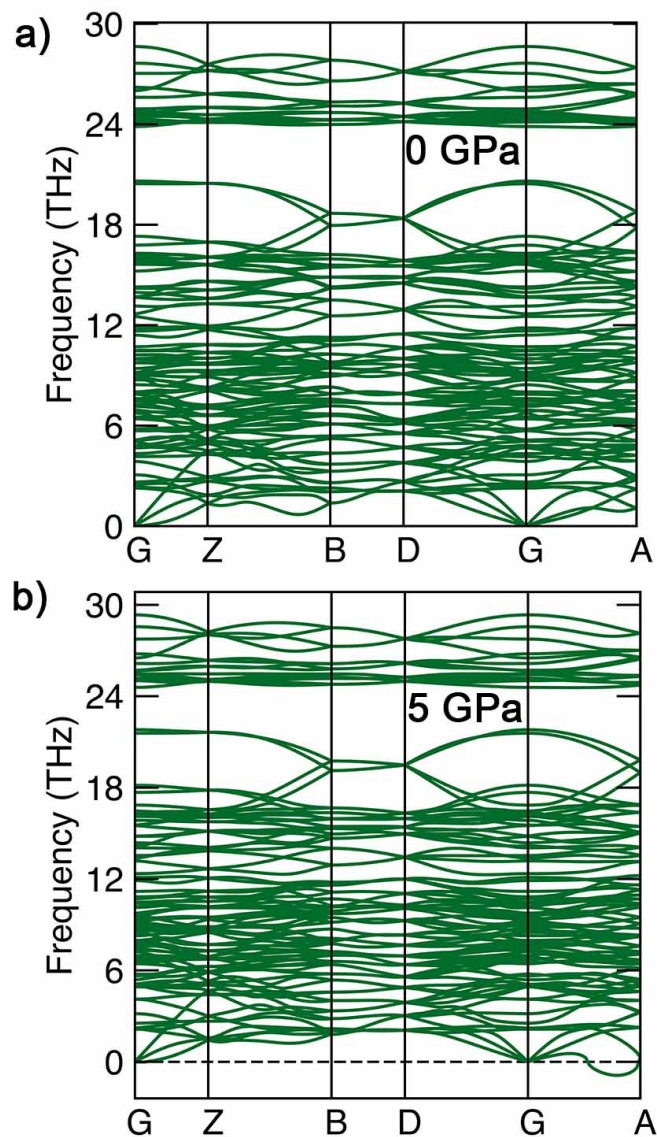


**Figure 5.2:** Phonon dispersion curves for  $P2_1/c$  titanite phase at (a) 0 GPa and (b) 5 GPa.

Ca, Ti, Si and O atoms occupy the  $4e$  wyckoff sites in the lattice structure of the monoclinic phase ( $P2_1/c$ ). Si atoms occur in a four-fold coordination with O atoms to constitute  $SiO_4$  tetrahedra, which act as a building block of the titanite structure. Ti and Ca atoms occur in six- and seven-fold coordination with O atoms, where the  $TiO_6$  octahedra form corner-linked

## Titanite ( $\text{CaTiSiO}_5$ )

chains along the  $a$  axis (Figure 5.1a). These octahedra are tilted in opposite directions alternately along the chains, sharing their edges with  $\text{CaO}_7$  polyhedra arranged in chains parallel to [101].  $\text{SiO}_4$  tetrahedra share their corners with both  $\text{TiO}_6$  and  $\text{CaO}_7$  polyhedra [12,41,46]. A detailed description of the crystal structure can be found in Speer and Gibbs' work [41]. The Ti atoms are slightly off-centred in the polyhedra arranged along the  $a$  axis at room temperature, which results in an anti-ferroelectric distortion pattern, but without any net inherent ferroelectric moment. However, the tetrahedral geometry remains unaffected even in the presence of any external electric field applied along  $a$  direction. Zhang et al. predicted that switching of Ti displacements is not possible in strong electric fields (at least 35 kV/cm) along the  $a$  direction in a temperature range of 0 to 500 K [11].

**Table 5.1:** Pressure (GPa) dependent variation of structural parameters ( $a$ ,  $b$ ,  $c$  in Å,  $\beta$  in degree), average bond length (Å) and polyhedral volumes (Å<sup>3</sup>) of titanite.

	$P$	$a$	$b$	$c$	$\beta$	$\text{Ca-O}$	$\text{Ti-O}$	$\text{Si-O}$	$\text{CaO}_7$	$\text{TiO}_8$	$\text{SiO}_4$
<b>P2<sub>1</sub>/c</b>	0	6.75771	8.83485	7.25632	114.4897	2.6989	2.0695	1.6655	21.412	10.582	2.335
		7.069*	8.722*	6.566*	113.86*						
		6.5723#	8.8425#	7.3115#	114.495#						
	1	6.72548	8.82113	7.22032	114.3361	2.6847	2.065	1.6628	21.087	10.507	2.327
	2	6.69496	8.80710	7.18687	114.1886	2.6744	2.061	1.6601	20.783	10.436	2.319
	3	6.66578	8.79334	7.15516	114.0512	2.6638	2.0568	1.6575	20.492	10.369	2.310
	4	6.63853	8.77969	7.12526	113.9189	2.6543	2.0525	1.6549	20.219	10.308	2.302
5	6.61207	8.76615	7.09678	113.7922	2.6456	2.0483	1.6526	19.956	10.249	2.295	
<b>C2/c</b>	0	6.76014	8.83809	7.20586	114.2951	2.6262	2.0643	1.6633	21.288	10.516	2.333
		6.7629#	8.8495#	7.2289#	114.250#						
	1	6.72733	8.82342	7.18123	114.1776	2.6254	2.0602	1.6609	20.994	10.456	2.325
	2	6.69641	8.80871	7.15696	114.0673	2.6240	2.0562	1.6586	20.711	10.398	2.317
	3	6.66645	8.79471	7.13312	113.9549	2.6229	2.0521	1.6563	20.438	10.343	2.309
	4	6.63910	8.78017	7.11025	113.8518	2.6211	2.0483	1.6541	20.182	10.289	2.302
	5	6.61300	8.76644	7.08770	113.7521	2.6191	2.0445	1.6519	19.937	10.237	2.295

\*[41]

#[32]

## Chapter 5

Table 5.1 presents the pressure dependent variations of the structural parameters of both titanite phases ( $P2_1/c$  and  $C2/c$ ) in the pressure ( $p$ ) range 0 to 5 GPa. The cell volume of  $P2_1/c$  phase reduces by  $\sim 4.53\%$  at  $p = 5$  GPa, whereas the lattice parameters,  $a$ ,  $b$  and  $c$ , reduce by  $\sim 2.15\%$ ,  $0.77\%$ ,  $2.19\%$  respectively, implying that the  $P2_1/c$  phase has the lowest compressibility along the  $b$  axis. The  $C2/c$  phase shows similar pressure dependent changes in  $a$ ,  $b$  and  $c$  ( $\sim 2.17\%$ ,  $0.81\%$  and  $1.64\%$ , respectively). However, the  $c$  axis of  $C2/c$  phase shows remarkably higher incompressibility than  $P2_1/c$  phase. I also evaluated polyhedral volumes as a function of  $p$ .  $CaO_7$  polyhedra undergo large modifications of their volume with increasing  $p$ , whereas  $SiO_4$  tetrahedra show much smaller pressure-induced modifications for both the titanite phases. In case of  $P2_1/c$  phase, Ca–O bond lengths ( $CaO_7$  polyhedra) reduce by  $\sim 1.97\%$  ( $\sim 10.06\%$ ) at  $p = 5$  GPa, which is significantly low in the  $C2/c$  phase,  $\sim 0.27\%$  ( $\sim 6.34\%$ ).

### 5.4 Elastic constant tensor

The first principles calculations were performed to evaluate the second order elastic constant tensors ( $C_{ij}$ ) of single crystals for both the titanite phases ( $P2_1/c$  and  $C2/c$ ) under hydrostatic pressures up-to 5 GPa. The elastic constant tensor ( $C_{ij}$ ) consists of 13 independent components:  $C_{11}$ ,  $C_{22}$ ,  $C_{33}$ ,  $C_{44}$ ,  $C_{55}$ ,  $C_{66}$ ,  $C_{12}$ ,  $C_{12}$ ,  $C_{23}$ ,  $C_{16}$ ,  $C_{26}$ ,  $C_{36}$  and  $C_{45}$ . Figure 5.3 presents their calculated values as a function of  $p$ , which, to the best of my knowledge, is completely a new theoretical data set. Unfortunately, no experimental data are available to validate these findings. The  $P2_1/c$  phase shows increasing magnitudes of the

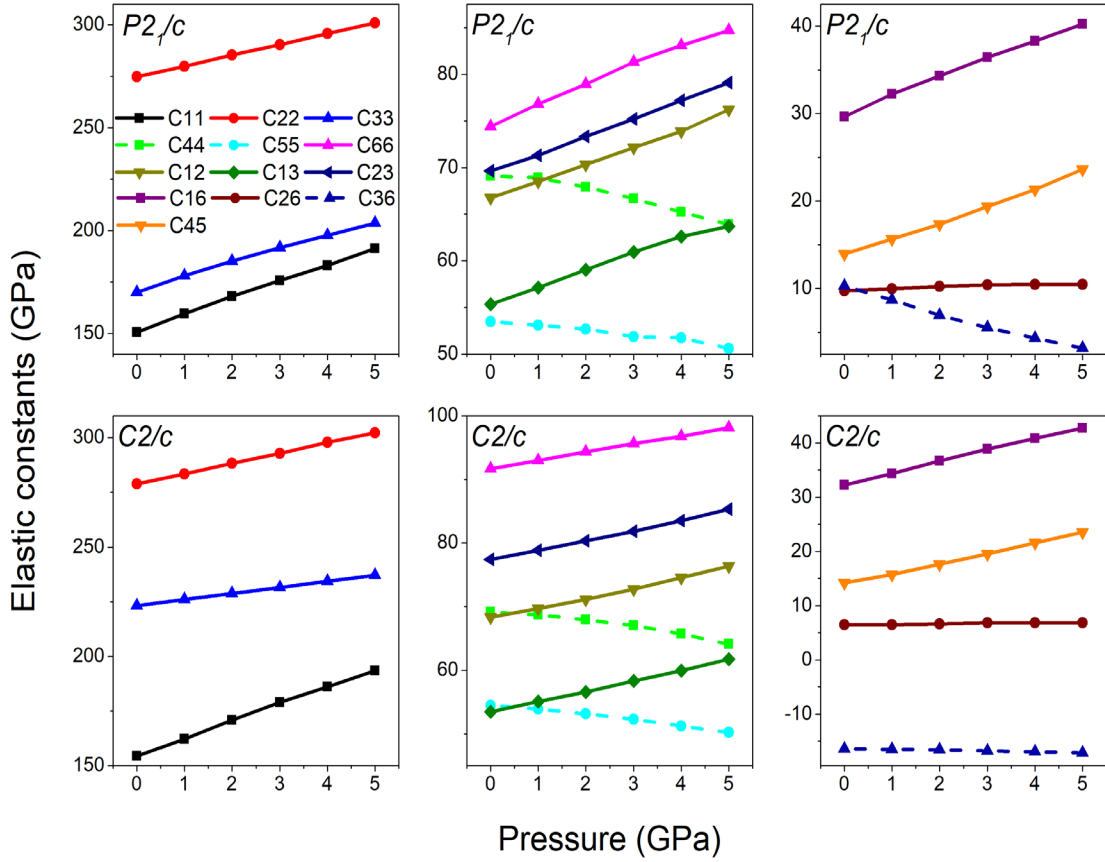


**Figure 5.3:** Calculated plots of the 2<sup>nd</sup> order single-crystal elastic constants of both  $P2_1/c$  (upper panel) and  $C2/c$  (lower panel) titanite phases as a function of hydrostatic pressure. Notice the negative pressure gradients of  $C_{44}$ ,  $C_{55}$  and  $C_{36}$  for both the phases (dashed lines). It is also noteworthy that  $C_{36}$  for  $C2/c$  phase exhibits negative values, where the negativity increases with increasing pressure.

three compressional elastic constants:  $C_{11}$ ,  $C_{22}$  and  $C_{33}$  with  $p$ , where  $C_{11}$  and  $C_{33}$  are nearly equal in the entire range of pressure considered for our calculations, but  $C_{22}$  is always significantly higher than both  $C_{11}$  and  $C_{33}$ . These compressional elastic constants are sensitive to  $p$ , shown by their large pressure derivatives ( $C'_{11}= 8.16$ ,  $C'_{22}=5.21$  and  $C'_{33}= 6.75$ ). The other elastic constants:  $C_{66}$ ,  $C_{12}$ ,  $C_{13}$ ,  $C_{23}$ ,  $C_{16}$ ,  $C_{26}$  and  $C_{45}$  hold positive relations with  $p$  for both the phases. Among them, the elastic constants:  $C_{66}$  and  $C_{16}$  have the steepest gradients, where the pressure derivative of  $C_{16}$  ( $C'_{16}= 2.11$ ) is slightly higher than that of  $C_{66}$  ( $C'_{66}= 2.06$ ). The other four constants:  $C_{12}$ ,  $C_{13}$ ,  $C_{23}$  and

## Chapter 5

$C_{45}$  have lower pressure derivatives ( $C'_{12}= 1.89$ ,  $C'_{13}= 1.67$ ,  $C'_{23}= 1.89$  and  $C'_{45}= 1.94$ ).  $C_{26}$  is almost unaffected by pressure ( $C'_{26}= 0.15$ ).  $C_{13}$  is the most soft elastic constant of  $P2_1/c$  titanite phase, implying that the crystal would exhibit least resistance to the deformation along the  $a$  direction under a longitudinal strain applied in the  $c$  direction.

The  $C2/c$  phase shows similar pressure dependent variations of the compressional elastic constants with  $p$  ( $C'_{11}= 7.79$ ,  $C'_{22}= 4.69$  and  $C'_{33}= 2.78$ ).  $C_{33}$  shows less pressure dependent variations in  $C2/c$  than  $P2_1/c$  titanite phase as the  $c$  axis is less compressible in  $C2/c$  (Table 5.1). Among the other elastic constants:  $C_{66}$ ,  $C_{12}$ ,  $C_{13}$ ,  $C_{23}$ ,  $C_{16}$ ,  $C_{26}$  and  $C_{45}$ ,  $C_{16}$  appears to be the most pressure sensitive constant ( $C'_{16}= 2.11$ , whereas  $C'_{45}= 1.87$ ,  $C'_{13}= 1.67$ ,  $C'_{12}= 1.59$ ,  $C'_{23}= 1.58$  and  $C'_{66}= 1.29$ ). In contrast,  $C_{26}$  is virtually pressure independent elastic constant ( $C'_{26}= 0.08$ ), as in the  $P2_1/c$  phase. The elastic constant tensor shows a large difference between  $C_{16}$  (32.2 GPa) and  $C_{26}$  (6.47 GPa), suggesting that the crystal would have contrasting stiffness in the  $a$  and  $b$  directions under a strain applied on the  $ab$  plane. It means that the titanite phase has the highest degree of anisotropy preferentially on the (001) plane.

The present calculations lead to a novel finding on the elastic behaviour of titanite. Among its 13 elastic constants, the three elastic constants:  $C_{44}$ ,  $C_{55}$  and  $C_{36}$  show remarkably negative pressure gradients for both titanite phases. The crystals can, thus, undergo shear softening at elevated hydrostatic pressures, implying that the phase has a tendency to become mechanically unstable at higher  $p$ . In case of  $P2_1/c$  phase, we obtain the steepest negative gradients for  $C_{36}$  ( $C'_{36}= -1.43$ ), whereas the lowest for  $C_{55}$  ( $C'_{55}= -0.56$ ).  $C_{44}$  also

## *Titanite (CaTiSiO<sub>5</sub>)*

has high negative pressure derivatives ( $C'_{44} = -1.03$ ). The pressure derivatives of these constants for  $C2/c$  phase are:  $C'_{44} = -0.99$ ,  $C'_{55} = -0.85$  and  $C'_{36} = -0.14$ . It is noteworthy that  $C_{36}$  is a negative elastic constant (-16.41 GPa at static condition), and its magnitude decreases with increasing  $p$ .

Let us now focus upon the physical implications of pressure induced shear softening behaviour of titanite phases. The pressure dependent acoustic mode softening is consistent with softening of  $C_{44}$  as its softening has indirect influence on the structural instability[21]. On the other hand, it should be noted that an elastic constant of a crystal can be positive if the energy of its strained state is higher than its relaxed state. The elastic constants can be calculated from the energy of a strained crystal by expanding it in a Taylor series expansion of input strain ( $\delta$ ) as,

$$E(V, \delta) = E(V_0, 0) + V_0 \left( \sum_{i=1}^6 \tau_i \delta_i + \frac{1}{2} \sum_{i=1}^6 \sum_{j=1}^6 C_{ij} \delta_i \delta_j + O(\delta^3) \right) \quad (5.1)$$

where  $E(V, \delta)$  and  $E(V_0, 0)$  are the energies corresponding to the strained and unstrained state of the crystal, respectively. Assuming the initial stress,  $\delta_i = 0$  in the unstrained crystal, we can extrapolate the following relation from Eqn. (1),

$$C_{ij} \propto \frac{\Delta E}{V_0} \quad (5.2)$$

$\Delta E$  is the energy difference between the strained and unstrained states, given by

$$\Delta E = E(V, \delta) - E(V_0, 0) \quad (5.3)$$

Now, let's consider  $(C_{ij})_{p1}$  and  $(C_{ij})_{p2}$  are the two values of given elastic

## Chapter 5

constant at pressure  $p_1$  and  $p_2$ , respectively, where  $p_1 < p_2$ . Using eqn. (2)

we can write

$$\frac{(C_{ij})_{p_1}}{(C_{ij})_{p_2}} = \frac{\Delta E_{p_1} (V_0)_{p_2}}{\Delta E_{p_2} (V_0)_{p_1}} \quad (5.4)$$

As  $(V_0)_{p_1} > (V_0)_{p_2}$  for  $p_1 < p_2$ , the negative pressure gradient of  $C_{ij}$ , i.e.,

$(C_{ij})_{p_1} > (C_{ij})_{p_2}$  demands,  $\Delta E_{p_1} > \Delta E_{p_2}$ . From eqn. (3),

$$E_{p_1}(V_{p_1}, \delta) - E((V_0)_{p_1}, 0) > E_{p_2}(V_{p_2}, \delta) - E((V_0)_{p_2}, 0)$$

which simplifies to

$$E((V_0)_{p_2}, 0) - E((V_0)_{p_1}, 0) > E_{p_2}(V_{p_2}, \delta) - E_{p_1}(V_{p_1}, \delta)$$

$$\Rightarrow \Delta E(V_0, 0)_{p_2-p_1} > \Delta E_{\delta}(V_{\delta}, \delta)_{p_2-p_1} \quad (5.5)$$

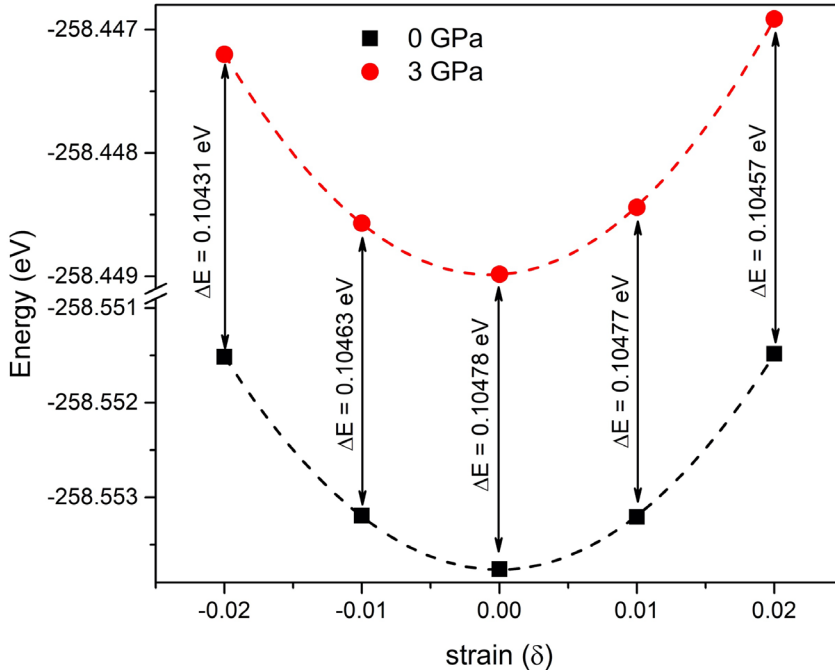


**Figure 5.4:** Variations of energy with strains ( $\pm 2\%$ ) applied to the unstrained titanite crystal ( $P2_1/c$  titanite) at  $p = 0$  (black) and 3 (red) GPa. This particular strain  $[e = \{\delta^2/(1-\delta^2); 0; 0; 2\delta; 0; 0\}]$  was used to calculate  $C_{44}$ . The solid symbols denote the calculated values and the dotted lines represent 2<sup>nd</sup> order best-fit.  $p =$  hydrostatic pressure.



The above equation indicates that the energy differences ( $\Delta E(V_0, 0)_{p_2-p_1}$ ) due to the pressure difference ( $p_2 - p_1$ ) for the unstrained crystals must be higher than the strain ( $\delta$ ) induced energy difference ( $\Delta E_\delta(V_\delta, \delta)_{p_2-p_1}$ ). This is the necessary and sufficient condition for an elastic constant to attain a negative pressure gradient. Figure 5.4 shows strain–energy curves which are used to calculate  $C_{44}$  at 0 and 3 GPa for  $P2_1/c$  titanite phase. The energy difference,  $\Delta E(V_0, 0)_{p_2-p_1}$  for the unstrained titanite crystal is 0.10478 eV, which is higher than any  $\Delta E_\delta(V_\delta, \delta)_{p_2-p_1}$  of strained crystal for any nonzero value of  $\delta$ .

## 5.5 Negative elasticity

An elastic constant can be negative, only when  $\Delta E$  (Eq. 5.3) becomes negative. It can be asserted that a strained state of titanite crystal has lower energy than its relaxed state, which indicates the system is losing some energy by acquiring strain, tending to attain a different energy minimum. It suggests that the ground state structure is already internally strained (distorted), which is also observed by Marcherek and Fischer[32]. On the other hand, an elastic constant denotes a ratio between the resistive stresses developed in a body and the applied strain. The mechanical action can yield a negative value of the elastic constant when a compressive stress (negative quantity) is produced under extensional strain (positive quantity) or vice-versa. However, this is not a usual mechanical behaviour of solids. Consider an alternative approach to demonstrate the physical implication of negative elasticity. An isotropic body (which shows positive elasticity) under a uniaxial compression undergoes an expansion in directions perpendicular to the compression. In other words, the

## Chapter 5

body compressed in a particular direction develops contractional strain (negative) in the applied compression direction, and extensional strain (positive) across it. But, a crystal with negative elasticity can develop contractional strain both along and across the compression direction. I face similar scenario in titanite. The application of positive strains yielded negative stresses in  $C2/c$  titanite. Such negative elasticity was first experimentally reported by Boppart et al.[28] in 1980 from sound velocity measurements, and later by Schärer and Wachter[30] from the Brillouin scattering of  $\text{Sm}_x\text{La}_{1-x}\text{S}$ . Both these studies obtained negative values of  $C_{12}$  in cubic phases at room temperature. However, they did not provide any specific atomic scale mechanism to explain this uncommon elastic behaviour. In fact, their results suggest the crystal symmetry is not a key factor to the negative elasticity. In this study we take into account the bond kinematics during crystal deformation to address this mechanical problem.

$C_{36}$  was calculated by applying shear strain  $\varepsilon_{12}$  in the monoclinic structure of titanite. The stress components along  $a$ ,  $b$  and  $c$  directions were obtained as a function of input shear strain to find  $C_{36}$ . We take the stress component  $\sigma_{33}$  corresponding to the applied shear strain,  $\varepsilon_{12}$ . According to this study, the shear strain  $C_{12}$  develops compressive stresses:  $\sigma_{11}$ ,  $\sigma_{22}$  and  $\sigma_{33}$  along the three crystallographic directions [100], [010] and [001], respectively. It is noteworthy that the crystal gives rise to the negative elastic constants essentially under shear deformation. The role of shear strain in lattice scale modifications thus appears to be a key in theorizing the mechanical behaviour of titanite. A bond dynamic model is proposed to demonstrate how the lattice

collapse by bond rotation can lead to such negative elasticity. This model allows us to suggest the bond kinematics as a driving factor for structural contraction perpendicular to the compression direction. The rotational kinematics is evidently manifested in the relative structural rearrangement of the constituent neighbouring polyhedra, which can be quantified by the angular relations between two neighbouring polyhedra. The structure can accommodate the compressive stress entirely by the rotational motion of rigid bonds. Evidently, this rotational kinematics involves complex dynamics of the rigid bonds which are supposed to be tangled in a network. They can intricately influence one another in their rotational motion. This mode of rotation-dominated bond kinematics seems to restrict structural expansion perpendicular to the direction of applied compression, as in the case of positive elasticity. In contrary, it results in contraction perpendicular to the compression direction, satisfying the condition required for negative elasticity.

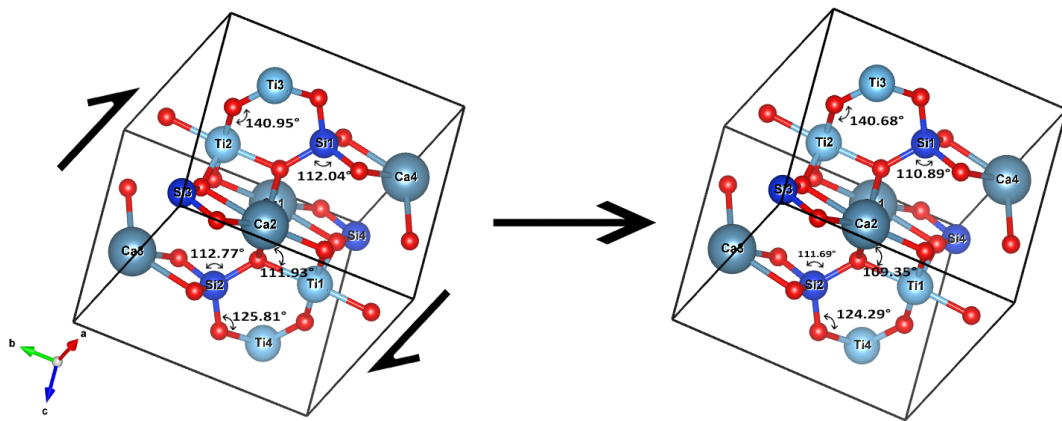


**Figure 5.5:** Changes of different bond angles in the lattice structure ( $C2/c$  phase) subjected to shear strain  $\epsilon_{12}$  at ambient pressure ( $p = 0$  GPa). This particular strain is associated with  $C_{36}$ .

It follows from this discussion that the rotational bond kinematics is the key factor in controlling the negative elasticity in titanite crystals.

## Chapter 5

To support the theoretical interpretation, I performed an analysis of bond angles in the unstrained and strained states of the lattice configuration of the actual crystal structure of  $C2/c$  titanite (Figure 5.5). For a given Lagrangian strain ( $\pm 2\%$ ), the Ca–O–Si bond angle is found to change from its initial value of  $95.18^\circ$  to  $97.35^\circ$ , implying a bond rotation by  $2.17^\circ$ . Similarly, Ca–O–Ti and Ti–O–Si bond angles are reduced from  $111.93^\circ$  to  $109.35^\circ$  and  $125.81^\circ$  to  $124.29^\circ$ , respectively. These two bonds thus undergo substantial rotations,  $2.58^\circ$  and  $1.52^\circ$ , respectively. These observations confirm that the given shear strain is accommodated dominantly by reorienting the angular disposition of cationic polyhedra. In case of the elastic constants,  $C_{36}$ , the applied shear strain (on  $ab$  plane in the  $a$ -direction) affects the O–O distance to a small extent, as measured on that shear plane. For a variation of the shear strain between  $-0.02$  and  $0.02$ , the O–O distance undergoes negligibly small changes ( $2.737 \text{ \AA}$  to  $2.723 \text{ \AA}$ ). On contrary, the O–Si–O angles in  $SiO_4$ -tetrahedra, measured on planes subparallel to the  $ab$ -plane are found to reduce from  $112.035^\circ$  to  $110.891^\circ$ . The neighbouring Ti-polyhedra also undergo an angular rearrangement, while the bridging bond angle of Ti–O–Ti between the tetrahedra varies from  $140.958^\circ$  to  $140.682^\circ$ . Our analysis clearly reveals that, in contrary to the natural behaviour of crystals to resist the strain, the deformation appears to be facilitated by the crystal itself. This antipodal mechanical behaviour of the crystal is a reflection of the negative elastic constants. Our analysis of the strain-induced bond angle modifications in titanite strongly supports the bond rotation as a mechanism to determine the negative elasticity of a crystal. Thus, the bond stretching and bond rotation are

recognized as two competing mechanisms in deciding the positive versus negative elasticity of crystalline solids. The dominance of bond stretching over bond rotation would result in a positive elastic behaviour, as commonly described in solid mechanics. However, the opposite bond dynamics, i.e., restricted bond stretching will favour the negative elasticity, as in the case of titanite phase. It is noteworthy that the negative elastic constant ( $C_{36}$ ) of  $C2/c$  titanite increases its magnitudes with increasing pressure (Figure 5.3). This pressure-induced enhancement of the negative behaviour warrants our interpretation. Increasing pressures generally strengthen atomic bonds in a crystal and restrict their stretching during deformation under a deviatoric stress field. At elevated pressures the crystal thus prefers to accommodate the strain mainly by bond rotation and facilitate its negative elastic behaviour.

To explain the rotational bond dynamics responsible for the negative  $C_{36}$ , I have also calculated the valence charge density on the three principal crystallographic planes: (100), (010), and (001) (Figure 5.6). The charge

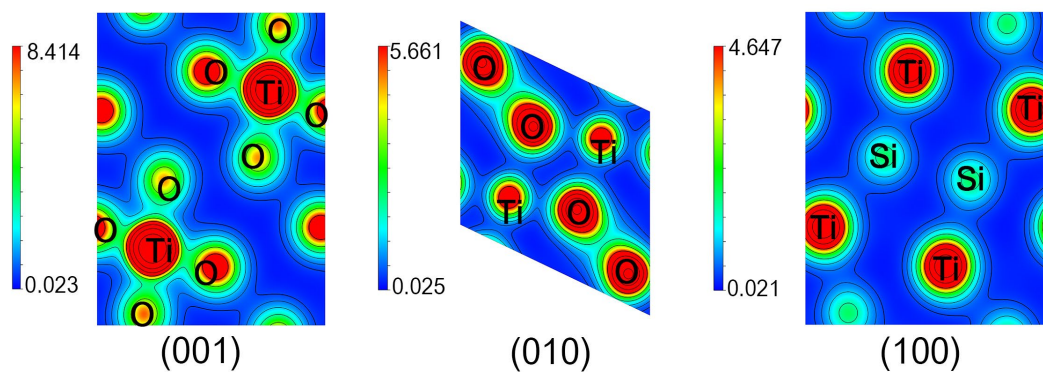


**Figure 5.6:** Valence charge density of the  $C2/c$  titanite phase on the three crystallographic planes: (001), (010) and (100). It is noteworthy that the charge density on (001) displays strong covalent bonding between Ti and O. Moreover, this crystallographic plane shows a much higher degree of anisotropy in charge distribution than the other two planes.

distribution clearly reveals the anisotropic nature of titanite. In the (001)

## Chapter 5

plane, Ti–O shows strong covalent bonding with a maximum accumulated charge of  $8.4148 e/\text{\AA}^3$ , which is the highest among all other planes. Such a large accumulation of the electronic charge gives rise to high bond strength between Ti and O atoms, which favours the bond rotation kinematics to dominate over bond stretching/shortening under a given shear strain  $C_{12}$ . The shear strain is eventually accommodated by local rotation of the atom clusters (Ti–O) present in this plane, resulting in a contraction of the whole structure, a condition for  $C_{36}$  to attain a negative value. Furthermore, the strong Ti–O covalent bond produces large resistance to applied strain  $C_{22}$  in the crystal. The charge density plot then allows us to explain why  $C_{22}$  turns out to be the numerically largest component of the elastic constant tensor  $C_{ij}$  of titanite (Figure 5.3).

### 5.5.1 Elastic moduli

The calculated elastic constants are used also to test the mechanical stability of the monoclinic titanite phase utilizing the following stability criteria [31],

$$\begin{aligned} C_{11} > 0, C_{22} > 0, C_{33} > 0, C_{44} > 0, C_{55} > 0, C_{66} > 0, \\ [C_{11} + C_{22} + C_{33} + 2(C_{12} + C_{13} + C_{23})] > 0 \\ (C_{33}C_{66} - C_{36}^2) > 0, (C_{44}C_{55} - C_{45}^2) > 0, (C_{22} + C_{33} - 2C_{23}) > 0. \end{aligned}$$

The analysis reveals that the negative elastic constant does not affect the mechanical stability of the phase, even at high pressures. According to the standard equations used in the theory of elasticity, the elastic constants ( $C_{ij}$ ) are the fundamental quantities to determine the elastic moduli of a crystal. The negative values of the elastic constant can thus influence the bulk mechanical properties. The bulk ( $B$ ), shear ( $G$ ) and Young's ( $E$ ) moduli of both titanite phases were evaluated as a function of pressure, considering both the

positive and negative elastic constants (Figure 5.7). The calculations yield very low shear modulus for both titanite phases, similar to the results of Salje et al.[14] who obtained  $G \sim 46\text{--}52$  GPa for undamaged titanite. The calculated  $G$

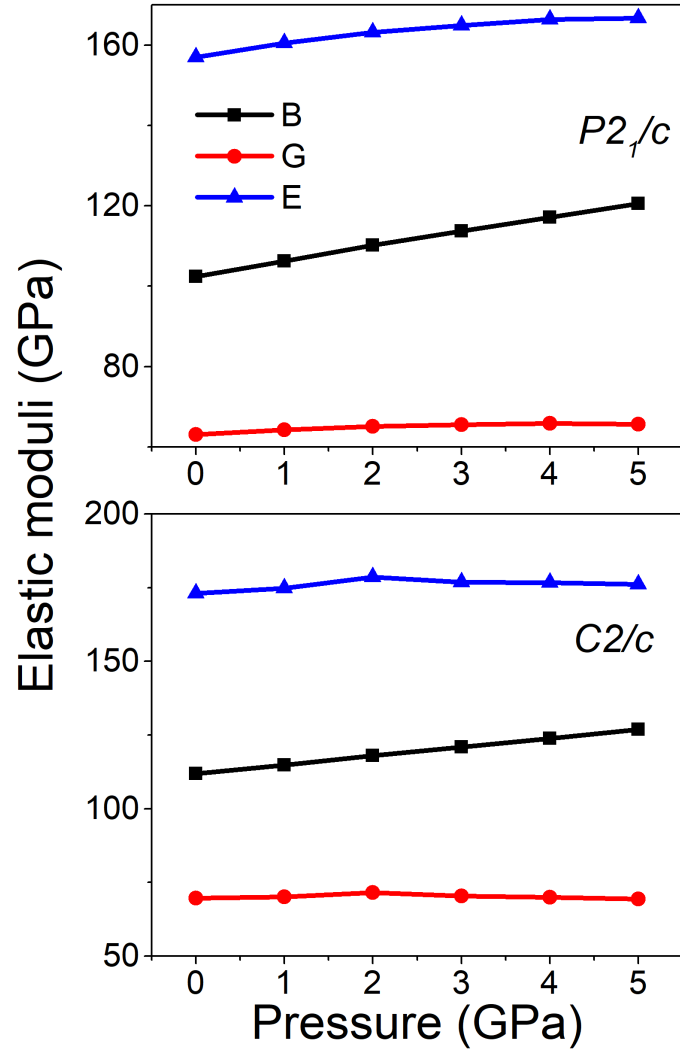


**Figure 5.7:** Variation of the elastic moduli: bulk moduli ( $B$ ), shear moduli ( $G$ ) and Young's moduli ( $E$ ) of the titanite phases with hydrostatic pressures (0 to 5 GPa).  $B$  is found to be the most sensitive with pressure.

values at static condition ( $T = 0$ ) is, however, slightly higher ( $\sim 63$  GPa) than theirs.  $B$  (102 GPa at static condition) of the  $P2_1/c$  phase is found to be the most pressure sensitive elastic modulus, where  $B' = 3.63$  in the pressure range 0 to 5 GPa. In contrast,  $E$  and  $G$  are relatively much less sensitive to pressure ( $E' = 1.9$  and  $G' = 0.52$ ).  $C2/c$  phase shows similar pressure dependent

## Chapter 5

behaviour of  $B$  and  $E$  ( $B' = 2.98$ ,  $E' = 0.59$ ), whereas  $G$  is less sensitive to pressure ( $G' = 0.06$ ). The static shear and bulk modulus are slightly higher than those of  $P2_1/c$  phase (69 and 112 GPa, respectively). The high values of bulk modulus indicate the titanite phase can be used as a hard material, despite its directional negative single crystal elasticity. The present theoretical results also predict titanite as an example of perfectly anisotropic crystal with universal anisotropy index[47] of 0.69. A 3D Young's modulus surface, which is also a measure of minimum thermal conductivity, is constructed for  $C2/c$

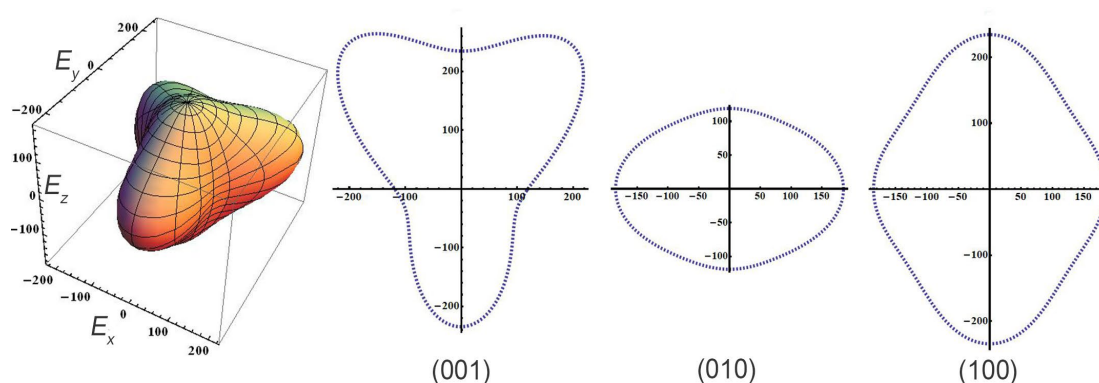


**Figure 5.8:** Graphical representations of 3D Young's modulus surface and its projections on the three mutually perpendicular planes: (001), (010) and (100) for  $C2/c$  titanite. The anisotropy is clearly visible on (001) and it conforms to the valence charge density (See Figure 5.4 and Figure 5.6).

titanite to show the degree of elastic anisotropy. Figure 5.8 shows its projections on the principal crystallographic planes for  $C2/c$  titanite. This 3D surface of  $E$  vividly reveals strongly anisotropic mechanical behaviour of titanite even under static condition, with  $E_1 = 119.48$ ,  $E_2 = 234.29$  and  $E_3 = 186.17$  GPa, where  $E_1$ ,  $E_2$  and  $E_3$  are the Young's modulus in the  $a$ ,  $b$  and  $c$  direction, respectively. The average Young's modulus ( $E = 173.11$ ) is close to  $E_3$ , implying that the (001) plane plays the most crucial role in determining the bulk mechanical behaviour of titanite.



In this study I considered the ratios of  $E_1$ ,  $E_2$  and  $E_3$  to express as a measure of the degree of anisotropy on the three principal crystallographic planes: (001), (010) and (100), where  $E_2/E_1 = 1.96$ ,  $E_3/E_1 = 1.56$ , and  $E_2/E_3 = 1.17$ , respectively. The calculated ratios suggest the highest anisotropy on (001) and the lowest on (100), which is consistent with the valence charge density (Figure 6). The charge distributions show much stronger directionality on (001) than the other two planes, resulting in the highest degree of anisotropy in Young's modulus on this plane.

## 5.6 Electronic and optical properties

The electronic density of states determines both intraband and interband transition, which influence the optical properties of materials. The spin polarized electronic density of states for  $P2_1/c$  titanite is presented in Figure 5.9. Fermi level is set to zero of the energy scale. The electronic energy gap ( $E_g$ ) is found to be 3.2 eV, which indicates titanite can be used as semiconductor. The valence band is characterized by  $O-p$ ,  $Ca-s$  and  $Ca-p$  states. The top of the valence band, i.e., closer to Fermi energy, is mainly dominated by  $O-p$  states. However,  $Ti-d$  states are the principal contributor of the bottom of the conduction band. Some hybridization between  $O-p$  and  $Ti-d$  also can be observed in the conduction band.

Using the electronic structure technique, the frequency dependent real ( $\epsilon_1$ ) and imaginary ( $\epsilon_2$ ) part of the complex dielectric function of  $P2_1/c$  titanite (Figure 5.10) were calculated. These calculations provide a new set of findings on the optical properties of this silicate phase. The dielectric function is

## Chapter 5

resolved into three polarization direction [100], [010] and [001], i.e., parallel to

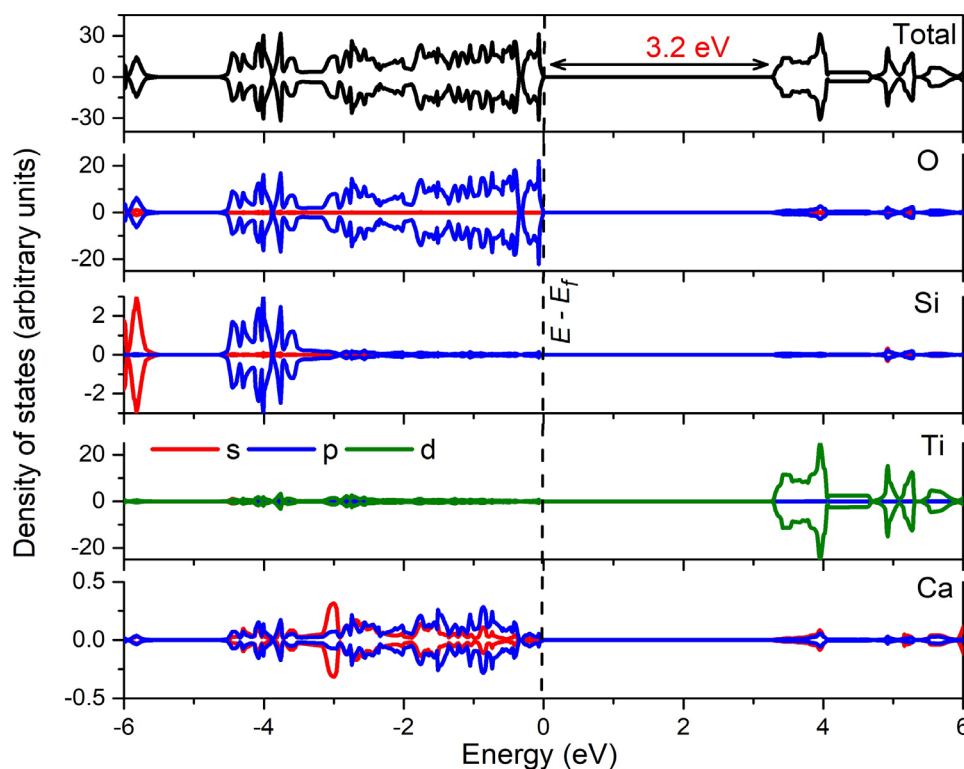


**Figure 5.9:** Spin polarised orbital projected electronic density of states for  $P2_1/c$  titanite phase.

$a$ ,  $b$  and  $c$ -axis, respectively, as titanite belongs to highly anisotropic monoclinic

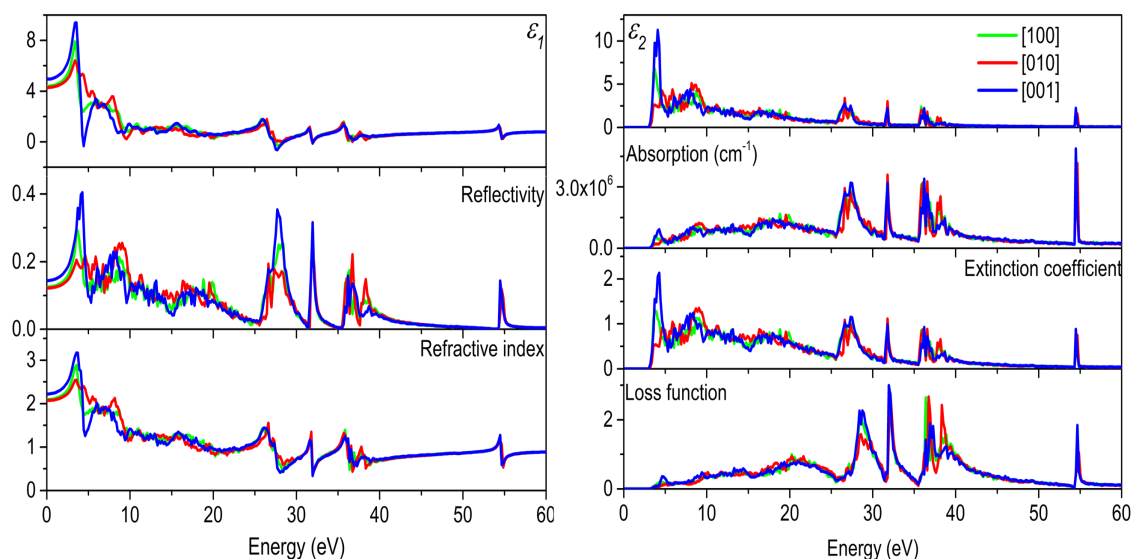


**Figure 5.10:** Polarization dependent optical properties of  $P2_1/c$  titanite phase as a function of energy.

## *Titanite (CaTiSiO<sub>5</sub>)*

crystal class. We obtain the static dielectric constant (i.e., at  $\omega = 0$ ) values as 4.38, 4.29 and 4.94, corresponding to  $a$ -,  $b$ - and  $c$ -axis respectively. Their highest peak values, 8.04, 6.43 and 9.47 occur at  $\sim 3.36$  eV. The real part of the dielectric function is strongly anisotropic.  $\epsilon_1$  shows a sharp decrease as we move from 3.36 eV to a higher frequency region and  $\epsilon_1$  parallel to  $c$  attains a negative value at  $\sim 4.36$  eV, which indicates that most of the incident photon along  $c$  will be reflected at this point. The result suggests that we can use this metallic behaviour of titanite for shielding purpose in a specific frequency region. The energy loss of a fast traversing electron can be described by the electron loss function. The peaks in the loss function are used to characterize the plasmon resonance. These plasmon frequency peaks corresponds to the transition from metallic property ( $\epsilon_1 < 0$ ) to dielectric property ( $\epsilon_1 > 0$ ). The peaks of the loss function occur exactly at a point where  $\epsilon_1$  switches negative to positive ( $\sim 4.36$  eV). Several peaks occur in the range between 26 to 40 eV. Specially, these high frequency peaks in the loss function depict an excellent dielectric property of titanite. A decent knowledge of refractive index of a material can help us to judge it for its potential optical applications. The calculated refractive indices of titanite (2.09, 2.07 and 2.21 for  $a$ ,  $b$  and  $c$ , respectively) are fairly in agreement with previously reported values [40].

The complex part  $\epsilon_2$  is linked with the photon absorption. The optical absorption edge is found at  $\sim 3.2$  eV for all the directions, suggesting the threshold for direct optical transition from valence band to conduction band at the Gamma point, which is consistent with the electronic band gap (Figure 5.9). The highest peak on  $\epsilon_2$  that occurs at 4.8 eV has a value of 11.3, which justifies

## Chapter 5

the reddish brown color of titanite. This peak corresponds to the hybridization between  $Ti-d$  and  $O-p$  states (Figure 5.9). Several peaks in the high frequency regions correspond to intra-band transition depending upon the energy of incident photon. The calculated absorption spectra have a spread from  $\sim 3.2$  eV to 60 eV. The same spread is also visible in reflectivity spectra with a maximum of 0.4 at 4.26 eV. For a better understanding, I have plotted absorption, reflectivity and refractive index spectra, covering the IR, visible and UV ranges

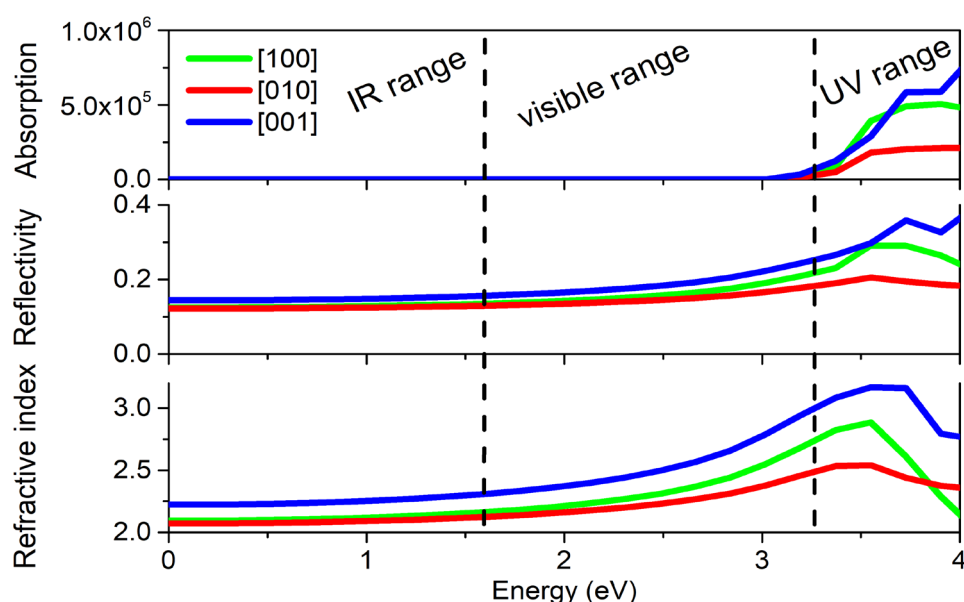


**Figure 5.11:** Anisotropic absorption, reflectivity and refractive index of  $P2_1/c$  titanite in infrared (IR), visible and ultraviolet (UV) spectra.

(Figure 5.11). The absorption and reflectivity increase rapidly as incident photon frequency crosses the visible spectrum range, especially in the [001] direction. These anisotropic optical properties are consistent with our previous findings. Extinction coefficient, which is a measure of the capability of light absorption of a material, also shows similar behaviour. Our calculated extinction coefficient has a peak at 4.26 eV and has a spread up-to 60 eV. These results indicate that titanite will behave like an opaque material in the UV

region due to its high absorption and reflectivity, whereas transparent in the visible range (up-to ~3.2 eV).

## 5.7 Concluding notes

To conclude the principal outcomes of this study, this chapter of the thesis presents a completely new set of theoretical data on the mechanical properties of monoclinic titanite phase. The theoretical calculations reveal unusual negative values of the elastic constant:  $C_{36}$  for  $C2/c$  phase and negative pressure gradients of the shear elastic constants,  $C_{44}$ ,  $C_{55}$  and  $C_{36}$  for both the titanite phase:  $P2_1/c$  and  $C2/c$ . A novel atomic scale mechanism is proposed to demonstrate the cause of negative elasticity in titanite; the rotational bond kinematics, driven by valence charge accumulation on (001) plane leads to structural collapse in a direction orthogonal to the applied shear strain, resulting in the negative elastic behaviour. Based on strain–energy calculations at varying pressures, the calculations allow us to constrain the necessary conditions leading to the negative pressure gradients of the shear elastic constants. The lattice dynamical analysis confirms the structural phase transition from  $P2_1/c$  to  $C2/c$  in titanite within 5 GPa.

The present calculations suggest that wide bandgap ( $E_g = 3.2$  eV) titanite shows an exceptionally strong opacity in the UV region. Based on this fact, I propose titanite as a potential shield material for UV radiation. This crystalline phase can also be used for developing optical filter/polarizer. Its transparent property in the low-frequency region provides an excellent scope for designing various optoelectronic devices.

## Chapter 5

### References:

- [1] W.A. Deer, R.A. Howie, J. Zussman, *Rock Forming Minerals, Volume 1A: Orthosilicates*, Geol. Soc. 1 (1982) 919.
- [2] E.R. Vance, D.K. Agrawal, *Incorporation of radionuclides in crystalline titanates*, Nucl. Chem. Waste Manag. 3 (1982) 229–234.
- [3] P.J. Hayward, F.E. Doern, E.V. Cecchetto, S. Mitchell, *Leaching studies of natural and synthetic titanite, a potential host for wastes from the reprocessing of Canadian nuclear fuel*, Can. Mineral. 21 (1983) 611–623.
- [4] Y. Pan, M.E. Fleet, N. MacRae, *Late alteration in titanite (CaTiSiO<sub>5</sub>): Redistribution and remobilization of rare earth elements and implications for U/Pb and Th/Pb geochronology and nuclear waste disposal*, Geochim. Cosmochim. Acta. 57 (1993) 355–367.
- [5] R. Rao, T. Sakuntala, P. Sengupta, G.K. Dey, K. Sharma, G.P. Kothiyal, *High pressure behavior of sphene glass ceramics*, Board of Research in Nuclear Sciences, India, 2008.
- [6] B.R. Frost, K.R. Chamberlain, J.C. Schumacher, *Sphene (titanite): phase relations and role as a geochronometer*, Chem. Geol. 172 (2001) 131–148.
- [7] S. Rath, *Comparative Pressure-Dependent Structural Studies of Titanite (CaTiOSiO<sub>4</sub>) and Malayaite (CaSnOSiO<sub>4</sub>)*, 2002.
- [8] D.H. Lindsley, D. Hausermann, *High-pressure phase transition in titanite (CaTiOSiO<sub>4</sub>)*, 81 (1996) 1527–1530.
- [9] C.L. Hollabaugh, W.G. College, *The crystal structure of an Al-rich titanite from Grisons, Switzerland*, 69 (1984) 725–732.
- [10] R.J. Angel, M. Kunz, R. Miletich, A.B. Woodland, M. Koch, D. Xirouchakis, *High-pressure phase transition in CaTiOSiO<sub>4</sub> titanite*, Phase Transitions. 68 (1999) 533–543.
- [11] M. Zhang, E.K.H. Salje, U. Bismayer, H.G. Unruh, B. Wruck, C. Schmidt, *Phase transition(s) in titanite CaTiSiO<sub>5</sub>: An infrared spectroscopic, dielectric response and heat capacity study*, Phys. Chem. Miner. 22 (1995) 41–49.
- [12] M. Taylor, G.E. Brown, *High-temperature structural study of the P2<sub>1</sub>/a e A2/a phase transition in synthetic titanite, CaTiSiO<sub>5</sub>*, Am. Mineral. 61 (1976) 435–447.
- [13] M.J. Gutmann, K. Refson, M. V. Zimmermann, I.P. Swainson, A. Dabkowski, H. Dabkowska, *Room temperature single-crystal diffuse scattering and ab initio lattice dynamics in CaTiSiO<sub>5</sub>*, J. Phys. Condens. Matter. 25 (2013).
- [14] E.K.H. Salje, D.J. Safarik, J.C. Lashley, L.A. Groat, U. Bismayer, *Elastic softening of metamict titanite CaTiSiO<sub>5</sub>: Radiation damage and annealing*, Am. Mineral. 96 (2011) 1254–1261.
- [15] R.J. Angel, M. Kunz, R. Miletich, A.B. Woodland, M. Koch, R.L. Knoche, *Effect of isovalent Si, Ti substitution on the bulk moduli of Ca(Ti<sub>(1-x)</sub>Si<sub>(x)</sub>)SiO<sub>5</sub> titanites*, Am. Mineral. 84 (1999) 282–287.
- [16] S. Fu, J. Yang, J.F. Lin, *Abnormal Elasticity of Single-Crystal Magnesiosiderite*

- across the Spin Transition in Earth's Lower Mantle, *Phys. Rev. Lett.* 118 (2017) 1–6.
- [17] S. Speziale, T.S. Duffy, R.J. Angel, Single-crystal elasticity of fayalite to 12 GPa, *J. Geophys. Res. B Solid Earth.* 109 (2004) 1–15.
- [18] R.J. Angel, J.M. Jackson, H.J. Reichmann, S. Speziale, Elasticity measurements on minerals: a review, *Eur. J. Mineral.* 21 (2009) 525–550.
- [19] R.A. Casali, N.E. Christensen, Elastic constants and deformations potential of ZnS and ZnSe under pressure, *Solid State Commun.* 108 (1998) 793–798.
- [20] B.B. Karki, M.C. Warren, L. Stixrude, G.J. Ackland, J. Crain, Ab initio studies of high-pressure structural transformations in silica, *Phys. Rev. B.* 55 (1997) 3465–3471.
- [21] P.K. Das, N. Mandal, A. Arya, Effects of Fe substitution on B3-B1 phase transition and structural, vibrational, and electronic properties of ZnS from DFT calculations, *J. Appl. Phys.* 121 (2017) 085101.
- [22] P.K. Das, N. Mandal, A. Arya, Effects of cation ordering on the elastic and electronic properties of Mg-Fe silicate phases at high pressures, *J. Appl. Phys.* 122 (2017) 225107.
- [23] P.K. Das, A. Chowdhury, N. Mandal, A. Arya, First-principles characterisation of the pressure-dependent elastic anisotropy of SnO<sub>2</sub> polymorphs, *Philos. Mag.* 96 (2016) 1861–1882.
- [24] G.W. Milton, A. V Cherkaev, Which Elasticity Tensors are Realizable?, *J. Eng. Mater. Technol.* 117 (1995) 483–493.
- [25] J.N. Grima, R. Gatt, A. Alderson, K.E. Evans, On the origin of auxetic behaviour in the silicate  $\alpha$ -cristobalite, *J. Mater. Chem.* 15 (2005) 4003–4005.
- [26] J.W. Jiang, H.S. Park, Negative poisson's ratio in single-layer black phosphorus, *Nat. Commun.* 5 (2014) 1–7.
- [27] L. Yu, Q. Yan, A. Ruzsinszky, Negative Poisson's ratio in 1T-type crystalline two-dimensional transition metal dichalcogenides, *Nat. Commun.* 8 (2017) 1–8.
- [28] H. Boppart, A. Treindl, P. Wachter, S. Roth, First observation of a negative elastic constant in intermediate valent TmSe, *Solid State Commun.* 35 (1980) 483–486.
- [29] Y.C. Zhou, C. Zhao, F. Wang, Y.J. Sun, L.Y. Zheng, X.H. Wang, Theoretical prediction and experimental investigation on the thermal and mechanical properties of bulk  $\beta$ -Yb<sub>2</sub>Si<sub>2</sub>O<sub>7</sub>, *J. Am. Ceram. Soc.* 96 (2013) 3891–3900.
- [30] U. Schärer, P. Wachter, Negative elastic constants in intermediate valent Sm<sub>x</sub>La<sub>1-x</sub>S, *Solid State Commun.* 96 (1995) 497–501.
- [31] Z.J. Wu, E.J. Zhao, H.P. Xiang, X.F. Hao, X.J. Liu, J. Meng, Crystal structures and elastic properties of superhard IrN<sub>2</sub> and IrN<sub>3</sub> from first principles, *Phys. Rev. B - Condens. Matter Mater. Phys.* 76 (2007) 1–15.
- [32] T. Malcherek, M. Fischer, Phase transitions of titanite CaTiSiO<sub>5</sub> from density functional perturbation theory, *Phys. Rev. Mater.* 2 (2018) 1–13.

## Chapter 5

- [33] G. Kresse, J. Furthmüller, Efficient iterative schemes for ab initio total-energy calculations using a plane-wave basis set, *Phys. Rev. B.* 54 (1996) 11169–11186.
- [34] G. Kresse, D. Joubert, From ultrasoft pseudopotentials to the projector augmented-wave method, *Phys. Rev. B.* 59 (1999) 1758–1775.
- [35] B. Hammer, L.B. Hansen, J.K. Nørskov, Improved adsorption energetics within density-functional theory using revised Perdew-Burke-Ernzerhof functionals, *Phys. Rev. B - Condens. Matter Mater. Phys.* 59 (1999) 7413–7421.
- [36] S.L. Dudarev, G.A. Botton, S.Y. Savrasov, C.J. Humphreys, A.P. Sutton, Electron-energy-loss spectra and the structural stability of nickel oxide: An LSDA+U study, *Phys. Rev. B.* 57 (1998) 1505–1509.
- [37] J.D. Pack, H.J. Monkhorst, ‘special points for Brillouin-zone integrations’, *Phys. Rev. B.* 16 (1976) 1748–1749.
- [38] J.D. Pack, H.J. Monkhorst, ‘special points for Brillouin-zone integrations’-a reply, *Phys. Rev. B.* 16 (1977) 1748–1749.
- [39] A. Togo, I. Tanaka, First principles phonon calculations in materials science, *Scr. Mater.* 108 (2015) 1–5.
- [40] C.R. Robbins, Synthetic CaTiSiO<sub>5</sub> and its germanium analogue (CaTiGeO<sub>5</sub>), *Mater. Res. Bull.* 3 (1968) 693–698.
- [41] J.A. Speer, G. V Gibbs, The crystal structure of synthetic titanite, CaTiOSiO<sub>4</sub>, and the domain textures of natural titanites, *Am. Mineral.* 61 (1976) 238–247.
- [42] S. Ghose, Y. Ito, D.M. Hatch, Paraelectric-antiferroelectric phase transition in titanite, CaTiSiO<sub>5</sub>, *Phys. Chem. Miner.* 17 (1991) 591–603.
- [43] E. Salje, C. Schmidt, U. Bismayer, Structural phase transition in titanite, CaTiSiO<sub>5</sub>: A ramanspectroscopic study, *Phys. Chem. Miner.* 19 (1993) 502–506.
- [44] M. Kunz, D. Xirouchakis, D.H. Lindsley, D. Hausermann, High-pressure phase transition in titanite (CaTiOSiO<sub>4</sub>), *Am. Mineral.* 81 (1996) 1527–1530.
- [45] M. Kunz, T. Arlt, J. Stolz, In situ powder diffraction study of titanite (CaTiOSiO<sub>4</sub>) at high pressure and high temperature, *Am. Mineral.* 85 (2000) 1465–1473.
- [46] S. Ghose, Y. Ito, D.M. Hatch, Paraelectric-antiferroelectric phase transition in titanite, CaTiSiO<sub>5</sub>, *Phys. Chem. Miner.* 17 (1991) 591–603.
- [47] S.I. Ranganathan, M. Ostoja-Starzewski, Universal elastic anisotropy index, *Phys. Rev. Lett.* 101 (2008) 3–6.



## Dense hydroxide Brucite [Mg(OH)<sub>2</sub>]

---

*Overture*

*Computational methodology*

*Crystal structure and equation of state*

*Proton transport mechanisms*

*Proton diffusion coefficients*

*Electrical conductivity*

*Highlights of the outcomes*



## 6.1 Overture

The presence of small elements and water have significant effect on the mineralogical structure, composition and dynamics[1,2] of the Earth's mantle which in turn effects the melting temperature[3,4], elastic properties[5–13], electrical conductivity[14–19], viscosity, diffusion of atoms[20–27] in minerals. It is widely accepted that the carrier of hydrogen into deep earth are a batch of hydrous minerals such as dense hydrous mineral silicates (DHMSs)[28], nominally anhydrous minerals (NAMs)[4,29] and  $\delta$ -AlOOH[30,31]. However, apart from phase D most of the hydrous minerals are reported to decompose at high pressures corresponding to the cold subducting slabs [32–35]. Electrical conductivities of DHMSs are observed to increase with pressure suggesting a higher mobility of H atoms. This observation indicates that pressure may act as an ally to enhance movement of protons in crystalline minerals. Though rare in the mantle of the earth, brucite is an archetype hydrous and layered mineral

## Chapter 6

of the MgO-SiO<sub>2</sub>-H<sub>2</sub>O ternary system (MSH), which is most rich in its ability to potentially host water and water-derived species in the mantle[36,37]. In ambient condition brucite assumes a trigonal crystalline structure (space group:  $P\bar{3}m1$ ) where Mg<sup>2+</sup> and OH<sup>-</sup> are arranged in layer. Pressure induced proton frustration in trigonal Brucite have been investigated by Raugei et al. [38] and Mookherjee and Strixwood[39]. The former experimental study has showed that under elevated pressure H moves in the *ab* plane and localize separately at three equivalent positions contrary to one in low pressure condition. However, at around 1 GPa brucite undergoes a structural transition to a lesser symmetric trigonal structure (space group:  $P\bar{3}$ )[40] leading to a change of dynamical positional disorder of proton to a static one[41]. The layered structure of  $P\bar{3}m1$  brucite have motivated several researchers to study the diffusion of proton, resulting electrical conductivities[37,42] and it's dehydration properties[43] whereas the proton diffusion in  $P\bar{3}$  brucite remains unexplored. Static DFT calculation and novel structure searching method have demonstrated that  $P\bar{3}$  brucite has a larger p-T stability field compared to its low pressure predecessor and around 19 GPa it transforms to a new tetragonal  $P4_12_12$  phase[41]. Nevertheless, this new phase is yet to be experimentally verified. They have also reported that  $P\bar{3}$  brucite decomposes into MgO + H<sub>2</sub>O (liquid) and MgO + ice VII mixtures at high p- high T and high p-low T conditions respectively. But barring the ex-situ geophysical survey of Kirby et al. [44] and subduction zone thermal models of Bina et al. [45], the presence of ice VII phase in the deep interior of the earth remains highly debated. In brucite, high pressure x-ray diffraction study of Fei et al. [46] reveals a smooth

## ***Brucite [Mg(OH)<sub>2</sub>]***

diffraction pattern, however in the same paper the authors deduced that at room temperature brucite would decompose into periclase and water at 27 GPa. The apparently contradictory results indicates that the decomposition is associated with a high kinetic barrier and brucite is likely to be stable at even higher pressures. Pressure induced enhancement of proton transport in  $P\bar{3}m1$  brucite have been reported by Guo and Yoshino[37] but limited to 13 GPa corresponding to the upper mantle regime. Recently, Shaack et al. [47] has demonstrated that in  $P\bar{3}$  brucite nuclear quantum effects play a major role in the mobility of H and it reaches a maximum at 67 GPa in room temperature. Still, an exhaustive account of the H-diffusion in brucite at high pressure and temperature and its implication for the deep earth is still lacking in literature. On the other hand, electrical conductivities of DHMS and nominally anhydrous minerals (NAMs) like olivine and its high-pressure polymorph ringwoodite and wadsleyite cannot account for the high conductivity zones in lower mantle. To explain this difference, there should be some other mineral or mineral aggregate which can notably account for this. It is important to note that the  $P\bar{3}$  brucite structure consists of hollow 2-D well parallel to the ab-plane which are devoid of Mg and O atoms. This channel can offer significant free space for the H to move and thereby enhance the electrical conductivity of the mantle.

This study uses Ab-initio Molecular Dynamics to systematically explore the diffusion of H in  $P\bar{3}$  brucite in the range 10-80 GPa and 1250-2000K. The diffusion co-efficient of H is calculated in the chosen p-T conditions which reveal an anomalous relation of the diffusion coefficients with pressure along the isotherms. The reasons for the differences in diffusivities of H are

## ***Chapter 6***

elucidated. The results demonstrate that the onset temperature of H-diffusion in brucite is largely influenced by the confining pressure. This study also deals with the anisotropy in H diffusion in brucite. Finally, the proton induced electrical conductivity is calculated and compared with deep mantle electrical conductivity to find how far the presence of brucite can affect it.

### **6.2 Computational methodology**

Static, density-functional theory calculations were performed to obtain structures of  $P\bar{3}$  brucite at desired pressures up to 80 GPa using the Vienna ab initio simulation package (VASP)[48,49]. The local structural relaxations calculations were performed using the generalized gradient approximation of the Perdew-Becke-Ernzhoff [50] formalism to model electronic exchange-correlation effects, together with projector-augmented wave (PAW) [51] implementation. The PAW-GGA potentials are used to describe the ionic core of H, O and Mg where their valence electronic configurations were  $1s^1$ ,  $2s^22p^4$  and  $3s^23p^0$ , respectively, with core cut-off radii of 1.1, 1.52 and 2.0 Å. The simulations employ an appropriate regular gamma centric  $5 \times 5 \times 5$  grid of Monkhorst-Pack[52] k points to sample the electron density in the reciprocal space and a kinetic energy cut-off of 625 eV along with a cut-off of 610 eV for the augmented part. These parameters ensured that the precision of the energy calculation is typical on the order of 1meV/atom in energy and better than 0.5 GPa in pressure.

To capture the effect of temperature on the motion of atoms, I have performed ab-initio molecular dynamics simulations (AIMD) as implemented

## *Brucite [Mg(OH)<sub>2</sub>]*

in VASP. The isokinetic NVT ensembles are chosen at a given temperature,  $T$ , keeping a fixed volume,  $V$ , and the number of atoms,  $N$ , in the simulation box. The simulations were performed at volumes corresponding to the desired pressure. The ionic temperatures during the simulations were kept steady employing a Noose-Hoover thermostat[53,54]. Each AIMD simulation was for 8000-10000 timesteps with each timestep being equal to 1 fs, resulting to a total simulation time ranging from 8 to 10 ps. AIMD simulation are typically sensitive of the size of the system under study. To account for this size effect, all the AIMD simulations were carried out on a 2x2x3 supercell containing 180 atoms, obtained from the fully relaxed conventional unit cells from the static DFT calculations. The fixed gamma point was used to sample the reciprocal space of the supercells. The constraint imposed by fixed volume along with increasing temperatures affect the resultant pressure. This study considers the thermal pressure correction and, observed them to be within 1.5-2.7% of the target pressure. The images of the crystal structures are rendered using VESTA and the images of the trajectories of H-atoms are extracted from Visual Molecular Dynamics (VMD) suite.

### **6.3 Crystal structure and equation of state**

The crystal structure of  $P\bar{3}$  brucite consists of  $Mg^{2+}$  cations and  $OH^-$  anions arranged in layers, assuming an overall trigonal structure. The protons are located in channels in between the edge sharing  $MgO_6$  octahedra (Figure 6.1). The transition from  $P\bar{3}m1$  to  $P\bar{3}$  brucite, the latter being a maximal

## Chapter 6

subgroup of the former, is characterised by the reduction of mirror planes owing to the spatial disorder of proton distribution. In the lattice structure the

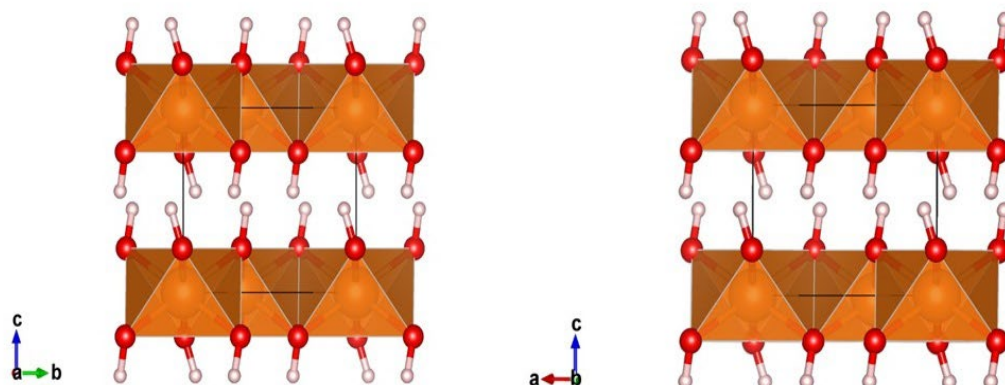


**Figure 6.1:** Crystal structure of  $P\bar{3}$  brucite as seen from perpendicular to a-axis (left) and b-axis (right). The brown polyhedra are  $MgO_6$  octahedra. Red and Pink spheres are O and H atoms, respectively. Note the 2D channel parallel to ab-plane.

Mg atoms occupy two distinct crystallographic positions: Wyckoff site 1a (0, 0, 0) and 2d ( $1/3, 2/3, z_{Mg}$ ), whereas the O and H atoms occupy general Wyckoff site 6g and 6i respectively. The most interesting characteristics of the  $P\bar{3}$  phase is the occurrence of two different H-H distances[39], where both of them decrease on increasing pressure up to a certain threshold value, beyond which one of them starts to stretch as a consequence of increasing O-H---O angle. Under ambient conditions, the lattice parameters are calculated as  $a = b = 5.48529 \text{ \AA}$ ,  $c = 4.79506 \text{ \AA}$  and  $\alpha = \beta = 90^\circ$ ,  $\gamma = 120^\circ$ ; these calculated values are in close agreement with previous findings [39,41]. The weak interaction between  $MgO_6$  layers is responsible for higher compressibility of this phase along its c-axis. The 2<sup>nd</sup> order Birch-Murnaghan equation of state fit (Figure 6.2) yields a bulk modulus of  $46.25 (\pm 1.7) \text{ GPa}$  with a pressure derivative of



5.03, which agree well with the DFT results of Hermann and Mukherjee [41].

The calculated equilibrium volume per formula unit for this phase, 42.02 Å<sup>3</sup> is

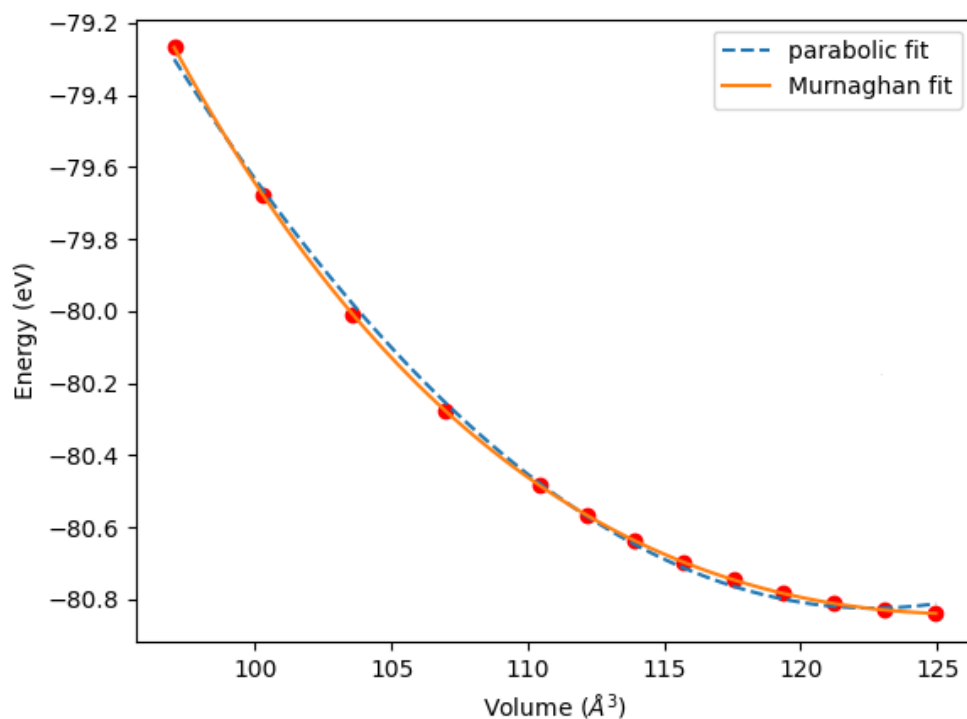


**Figure 6.2:** Second order Birch-Murnaghan equation of state of P $\bar{3}$  brucite.

also consistent with their finding.

## 6.4 Proton transport mechanisms

Pressure induced proton frustration and its effect on the mobility of H in P $\bar{3}$ m1 brucite has been previously studied both computationally[38] and experimentally [39,55,56]. Quench experiments are also performed to elucidate the phase stability of P $\bar{3}$ m1 brucite[40]. Despite those previous studies, the migratory behaviour of H in high pressure P $\bar{3}$  phase and its effects on the electrical conductivities in deep earth remains almost unattended. I have

## Chapter 6

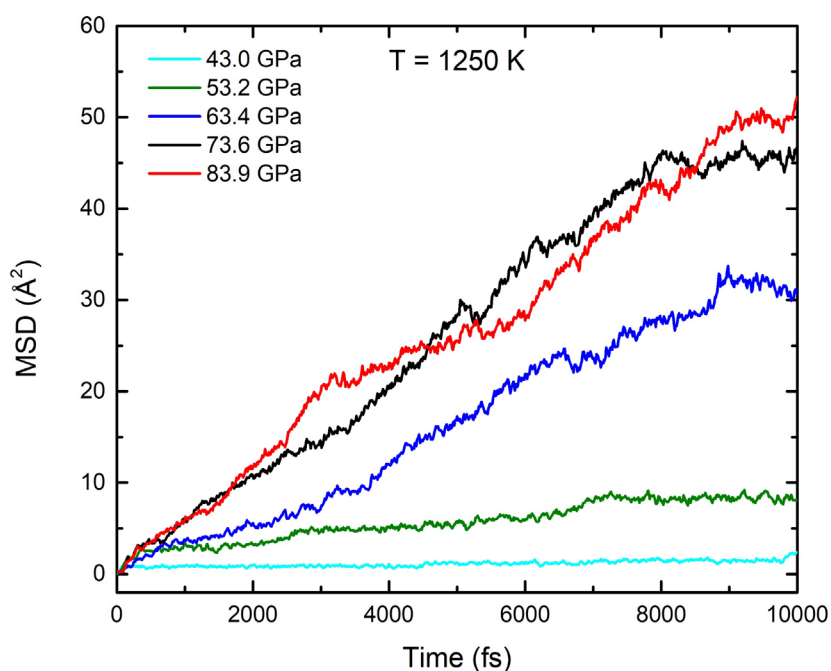


**Figure 6.3:** Mean squared displacements of H-atom at 1250K. Note that a reasonable proton diffusion is not observed until the pressure rose to a value near 43GPa at this temperature.

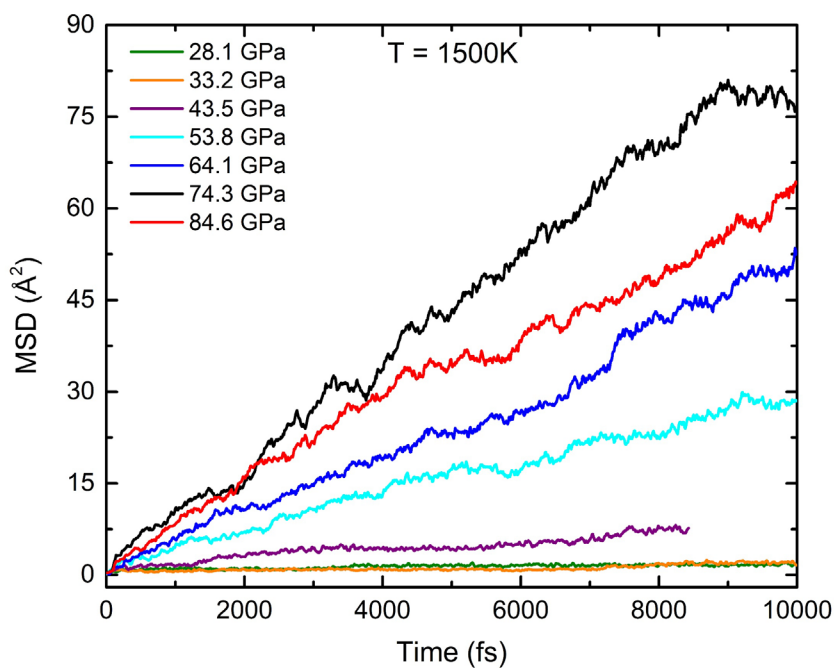


**Figure 6.4:** MSD of hydrogen at 1500K. The maximum mobility of H is observed at 74.3 GPa.

performed AIMD simulations to investigate the kinematic behaviour of proton

in  $P\bar{3}$  brucite at pressures corresponding to lower and upper mantle. The diffusion constants are calculated from the slope of the mean squared displacement (MSD) vs time curve. It is important to emphasise here that the calculated MSD demonstrates different line segments of varying slope (Figure 6.3-6.8). In order to minimize the error, the final slope was calculated as an average of the slopes of the MSD in several non-intersecting time intervals. Figure 6.3 shows our calculated MSD of hydrogen atoms at several pressures at the temperature of 1250K, where no notable movement of protons were observed below 43 GPa, which decreases to 28 GPa when the temperature is increased to 1500K (Figure 6.4).

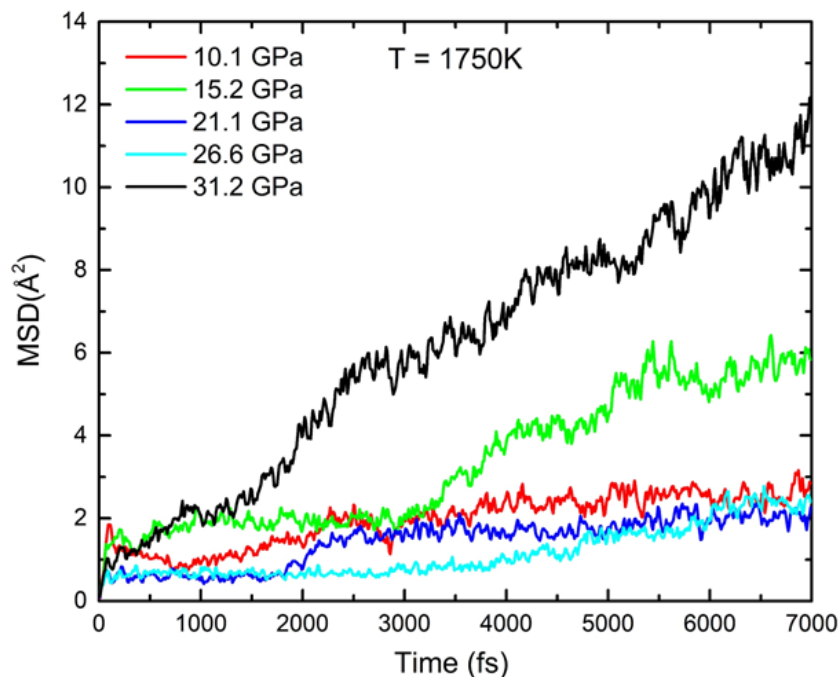


**Figure 6.5:** MSD of H atoms at 1750K and up to pressure of 31.2 GPa.

The onset pressure for proton mobility decreases further to 10.1 and 13.4 GPa when the temperatures are set to 1750K and 2000K, respectively (Figure

## Chapter 6

6.5, 6.6 and 6.7). However, irrespective of the temperature to which crystalline brucite is subjected to, the maximum movement of H-atoms are observed in the

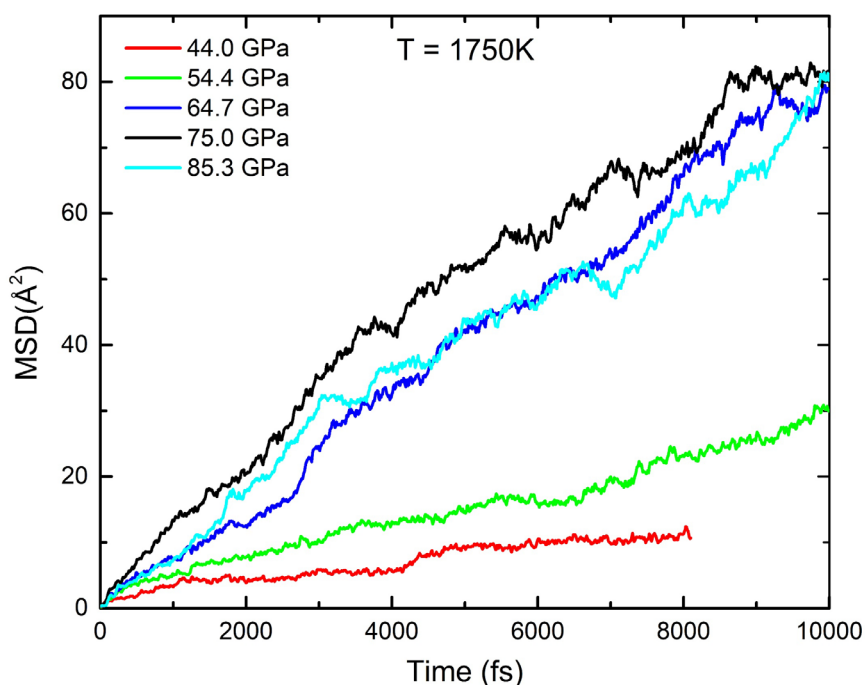


**Figure 6.6:** MSD of H atoms at 1750K and high pressures. Note the peak MSD at 75.0 GPa.

range 73.6-75.6 GPa. Thus, the MSD's of hydrogen are observed to display an anomalous correlation with confining pressure, decreasing in magnitude upon further increment in pressure. The disorder in proton distribution in  $P\bar{3}$  brucite can be categorized into two distinct non-exclusive type: a. dynamic disorder, in which each hydrogen jumps from one to another of the three symmetrically equivalent sites; b. static disorder, in which each hydrogen atom is stationary, in any of the three symmetrically equivalent position[39]. With increasing pressure this disorder changes from a dominantly dynamic one to a dominantly static one. The  $\text{OH}^-$  interlayer distances are observed to be much more sensitive to pressure compared to the intralayer  $\text{OH}^-$  distances. At elevated pressure the

interactions between OH<sup>-</sup> becomes much stronger and results to the reversal of proton disorder in the hydrogen sublattice. At the same time it brings the

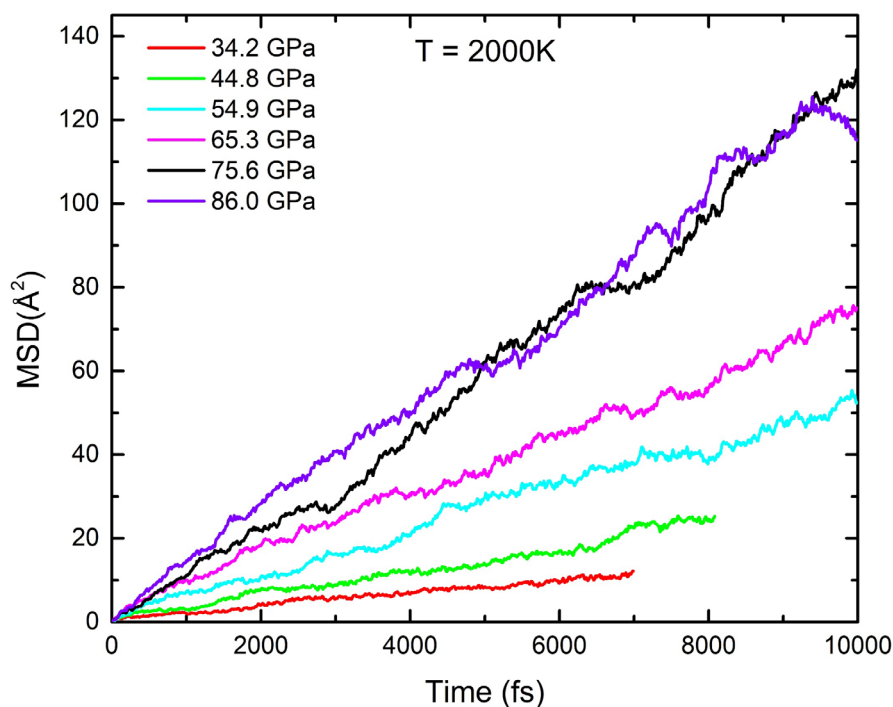


**Figure 6.7:** MSD of H atoms in brucite at 2000K. For brevity only the MSD's above 30 GPa are shown here.

interlayer H-atoms close to each other to form H-bonds, which are short-lived and very weak [38] aiding the protons to hop between O atoms among Mg(OH)<sub>2</sub> layer facing each other.

The proton diffusion mechanism in brucite is a complicated process, influenced by Nuclear Quantum Effects [47], that involves two stages: 1) the dissociation of a covalent O-H bond to form another distinct O-H bond, and 2) the reorientation i.e., the jump of proton from one of the three equivalent 6i sites in order to move from an initial O to the nearest one. Pressure has

## ***Chapter 6***

antipodal effect on these two stages. Rising pressure enhances the Nuclear Quantum Effect and increases the dissociation of O-H bonds. On the other hand, the reorientation process is mostly controlled by temperature where pressure is likely to be inclined to localize the proton in a certain orientation, making this motion unfavourable. The dissociation of O-H bonds creates a quasi 2-D proton layer between adjacent MgO layers. At lower pressures two quasi 2-D layers of H atoms are formed near each Mg-O layer and proton move back and forth between them and also throughout the layers. However, at elevated temperature and at pressure between 73-76 GPa these two layers merge and become indistinguishable. We argue that our MSD's at pressures below 75 GPa represent characteristic back and forth movement of proton between two such layers as well as thermally activated motion of proton in each of these layers. At 73-76 GPa the formation of the one indistinguishable layer, populated with large number of mobile protons, enhances the protonic movement. Below the onset pressure at each temperature only the reorientation occurs and resulting in a back-and-forth motion of H atoms leading to negligible net movement. Although these AIMD calculations do not take into account the NQE on an explicit term, the results are in good agreement with that of Schaack et al.[47]

### **6.5 Proton diffusion coefficients**

I have systematically calculated the diffusion coefficient of H ( $D_H$ ) at various pressure and temperature conditions. Table 6.1 lists our calculated  $D_H$ .

## *Brucite [Mg(OH)<sub>2</sub>]*

As the temperature increases the diffusion coefficients also increase. Notably at each temperature we found  $D_H$  to assume maximum value in the pressure

**Table 6.1:** Calculated diffusion coefficients of H in brucite at temperature 1250-2000K and pressures 10-85 GPa. The pressure includes the thermal correction as well.

Temperature (K)	Pressure (GPa)	Diffusion Coefficient $D_H(m^2/s)$
1250	42.95	1.7011E-10
	53.16	1.3363E-09
	63.37	6.2678E-09
	73.59	9.6683E-09
	83.82	9.4072E-09
1500	28.13	4.20345E-10
	33.19	5.65935E-10
	43.51	1.69786E-09
	53.76	4.55502E-09
	64.02	7.56022E-09
	74.28	1.47315E-08
	84.57	1.07429E-08
1750	10.04	6.79615E-10
	15.26	1.71247E-09
	21.32	4.40833E-09
	26.61	8.18315E-10
	31.20	2.50285E-09
	44.0	2.01455E-09
	54.35	4.85519E-09
	64.64	1.39001E-08

## Chapter 6

	74.96	1.45728E-08
	85.28	1.32427E-08
<b>2000</b>	13.4	3.3315E-09
	18.7	5.74253E-10
	23.9	4.42703E-10
	29.09	7.94527E-10
	34.22	2.26957E-09
	44.6	6.13043E-09
	54.93	7.61753E-09
	65.27	1.09825E-08
	75.6	2.34688E-08
	85.99	2.28415E-08

range 73-76 GPa pressure. Figure 6.8 shows the variation of  $D_H$  with reference to the mantle pressure conditions and different zones in mantle. Several NAMs and transition zone silicates are experimentally observed to host H in their crystalline lattice as substitutional point defects. Olivine aggregates which are dominant species in Earth's lower mantle house nominal amount of water and at higher temperature the H atoms are found to diffuse through the lattice. Discontinuities in seismic wave velocities establishes that olivine undergoes a transition to wadsleyite at 14 GPa and further to Ringwoodite at 24 GPa. Similar to their low-pressure counterpart these transition zone silicates also demonstrate H-mobility at elevated temperatures. Nevertheless, their calculated  $D_H$  are one to two order lower than what we have observed in case of brucite. The reason behind these differences in  $D_H$  can be attributed to their distinctive crystal structure and the different class of mechanisms at play



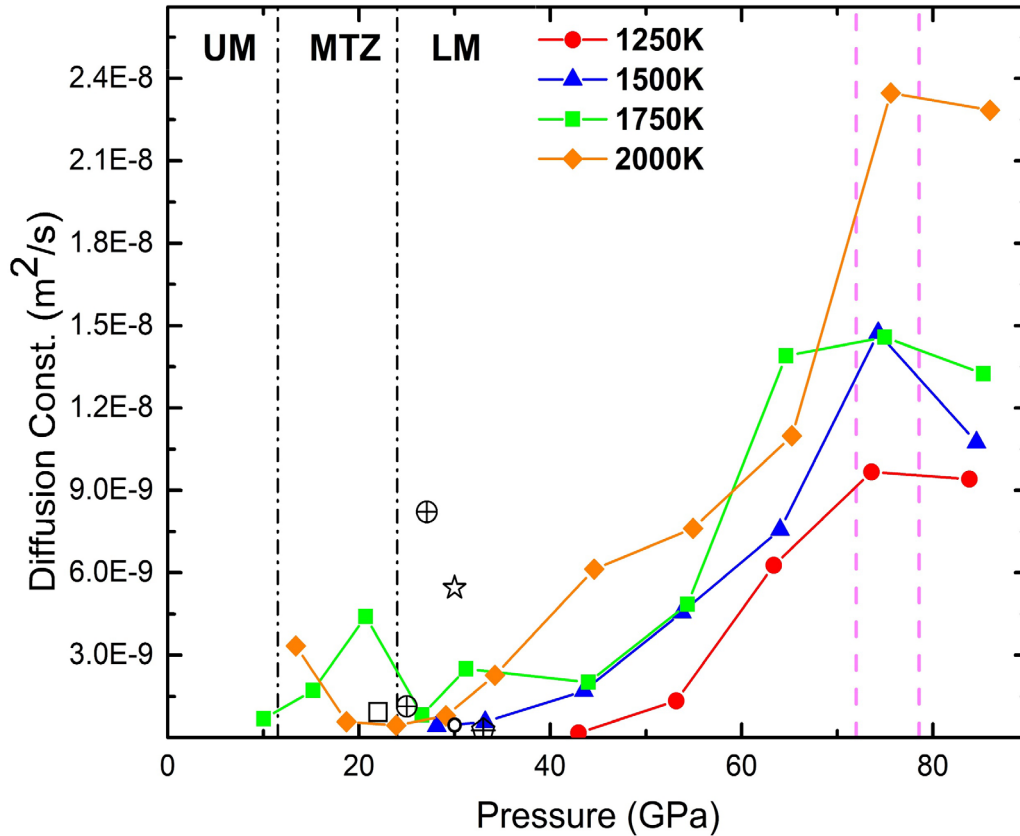


**Figure 6.8:** Proton diffusion co-efficient at various p-T condition. LM- Lower Mantle, UM- Upper Mantle, MTZ- Mantle Transition zone. The black dash-dotted vertical lines at 11 and 24 GPa represents the boundary between LM and MTZ and between MTZ and UM respectively. The zone between the magenta vertical lines represents the high-pressure zone where maximum H-diffusion occurs. For comparison the data of H-diffusion in transition zone silicates i.e., in ringwoodite and wadsleyite after Caracas and Panero [27] are also included. Ringwoodite: circle with + sign-  $Mg^{2+} \rightarrow 2H^+$  at 2000K and 2500K, star-  $Si^{4+} \rightarrow Mg^{2+} + 2H^+$  at 2500K, open circle- both  $Mg^{2+} \rightarrow 2H^+$  and  $Si^{4+} \rightarrow Mg^{2+} + 2H^+$  at 2500K, pentagon -  $Si^{4+} \rightarrow 4H^+$  at 2500K; wadsleyite: open square-  $Mg^{2+} \rightarrow 2H^+$  at 2000K. Note the characteristic large proton diffusion coefficient in brucite at high pressures.

to promote the H-diffusion process. Olivine and Ringwoodite belong to the category of nesosilicates whereas wadsleyite is a sorosilicate. All the former minerals are characterised by the presence of Mg/Fe octahedra and Si-tetrahedra forming a network like structure. In those silicates H must diffuse through asymmetric channels formed by the cationic polyhedra. In contrast brucite is a layered hydroxide mineral which offers an unhindered motion of protons through the layer between  $MgO_6$ -octahedra. In addition to that, the H-

## ***Chapter 6***

diffusion mechanism in both classes of minerals have remarkable differences. In silicates a net diffusion of H is realised only when an H atom jumps from one substitutional vacancy to the next one. This whole process is thermally controlled and relies on simultaneous creation-annihilation of vacancies together with probabilistic hopping of H through those vacancies. In contrast, the H-diffusion in brucite is initiated and largely regulated by the pressure induced amorphization of the H-sublattice. This pressure induced amorphization creates a pool of mobile H atoms between adjacent  $\text{MgO}_6$  layers, depleted of any Mg or O atom to restrict H-mobility. The combined effect of the structure and mechanism of H-diffusion gives rise to a diffusional free energy barrier ranging from 1.66 eV to 3.14 eV for H in ringwoodite and wadsleyite [27] respectively. In contrast, the dissociative and rotational free energy barriers for H in brucite are in the order of 0.01-0.11 eV and 0.03-0.10 eV at room temperature [47], which are expected to drop to even lower values when the temperature rises. Clearly, this higher migration barrier in silicates makes H-diffusion in them kinetically restricted, energetically less favoured and demands relatively higher temperature to initialize as compared to brucite. The apparent free flow of protons and lower migration barrier are thus responsible for the observed high  $D_{\text{H}}$  in brucite phase.

The initial high value of  $D_{\text{H}}$  observed in 2000K isotherm in the low-pressure regime can be attributed to the incongruent melting of brucite. Figure 6.9 and 6.10 shows the variations of MSD's of Mg and O atoms at several pressures along 2000K isotherm. At low pressure of  $\sim 13$  GPa both the MSD's of Mg and O atoms shoot upwards, together with the MSD of H atom (Figure

6.7), indicating that the entire crystalline structure undergoes a melting at this pressure and temperature.

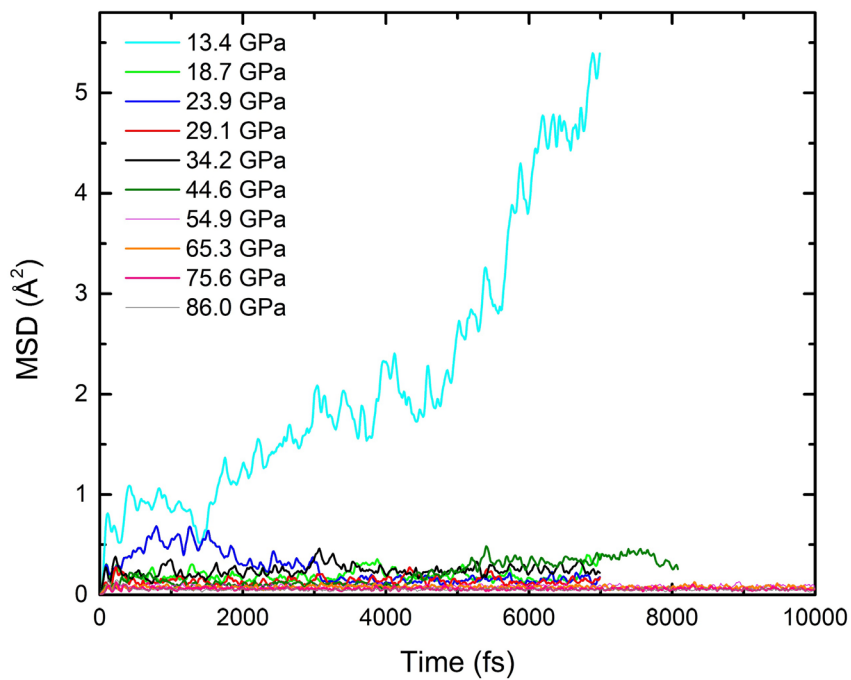


**Figure 6.9:** MSD of Mg atoms at different pressures while the temperature was kept fixed at 2000K. Note the large MSD of Mg atoms at 13.4 GPa indicating the melting of brucite.

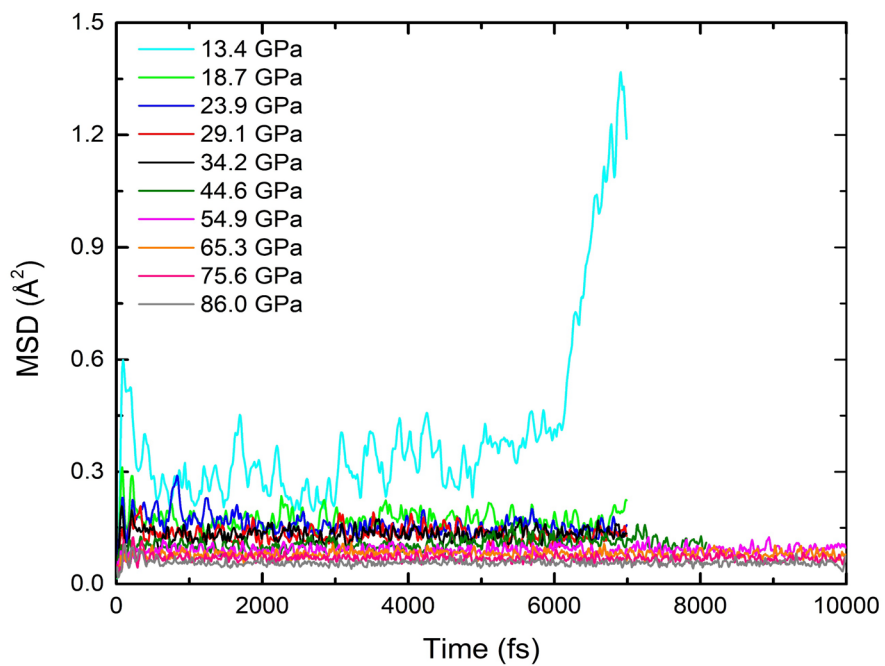


**Figure 6.10:** MSD of O atoms in brucite at 2000K. The O atom displays a qualitatively similar increment in MSD as the Mg atoms at 13.4 GPa.

## Chapter 6

However, at higher pressures the melting point of brucite drops, and the H atoms only occur in a mobile state. Figure 6.11 illustrates the MSD of the comparatively heavy atoms at 1250K. It is important to note that at 1250K

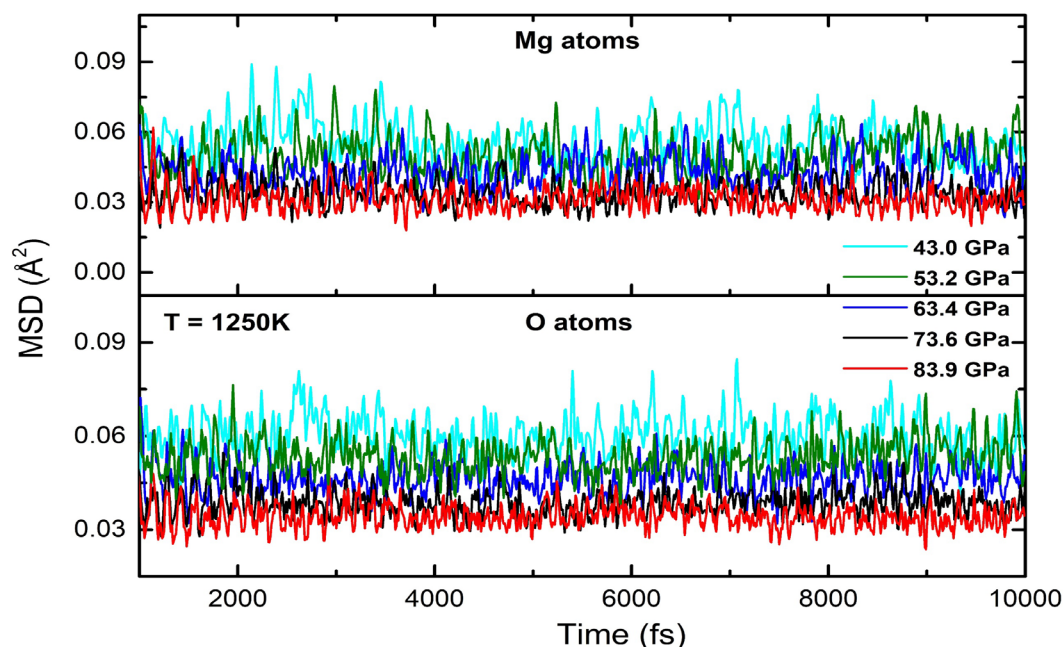


**Figure 6.11:** MSD's of Mg and O atoms at 1250K. The relatively low MSD's suggest the vibrational movement of Mg and O atoms.

both the MSD of Mg and O atoms oscillates around some small value indicating the stretching and shortening of Mg-O bonds as the Mg and O atoms execute thermally activated vibrational motions.

### 6.5.1 Anisotropy in proton diffusion

The proton diffusion in brucite is highly anisotropic in nature. Figure 6.12 demonstrates that movements of almost all of the H-atoms are restricted within the planes parallel to crystallographic *ab*-plane, with hardly any out of plane motion observed. The  $\text{MgO}_6$ -polyhedral network here act as a barrier to restrict motions of H-atoms parallel to *c*-axis. I have calculated the axis decomposed diffusion coefficient along the three axes viz.  $D_{[100]}$ ,  $D_{[010]}$  and  $D_{[001]}$ .

## *Brucite [Mg(OH)<sub>2</sub>]*

Further, they are normalized with respect to  $D_H$  at corresponding p-T conditions as  $d^*_{[100]} = D_{[100]}/D_H$ ,  $d^*_{[010]} = D_{[010]}/D_H$  and  $d^*_{[001]} = D_{[001]}/D_H$ , respectively.  $d^*_{[001]}$  is found to be negligible in magnitude, asserting that proton

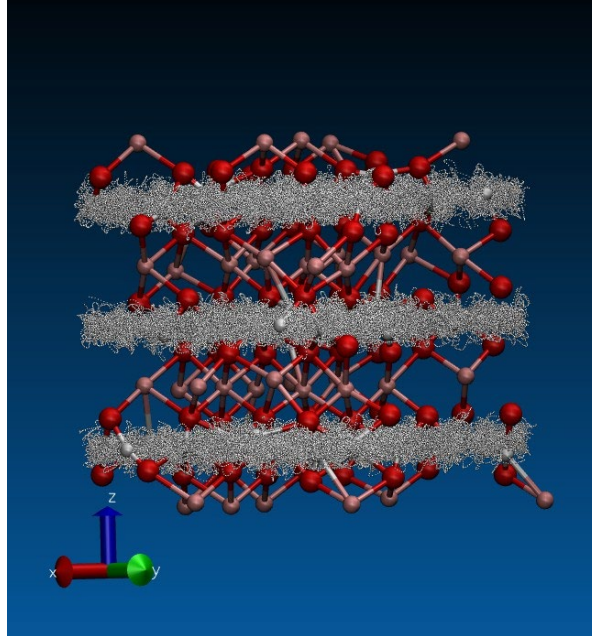


**Figure 6.12:** Trajectories of the hydrogen atom (white) in the quasi 2-D layer between MgO<sub>6</sub> octahedra. Red and pink spheres are Mg and O atom respectively. Note that none of the trajectories of the H atom crossed the MgO<sub>6</sub> layer.

diffusion along c-axis contributes almost null. The plot of  $d^*_{[100]}/d^*_{[010]}$  ratio as a function of pressure in the range 30-90 GPa shows no obvious correlation between the  $d^*_{[100]}/d^*_{[010]}$  ratio with pressure-temperature (Figure 6.13). Comparable values of  $d_{[100]}$  and  $d_{[010]}$  are only obtained at some specific p-T eg. 40GPa-1500K, 70 GPa-1250K, 80 GPa-1500K and 80 GPa-1750K. At those p-T points the movements of H along the  $a$ - and  $b$ -axis are similar in nature.  $d^*_{[100]}/d^*_{[010]}$  at 2000K exhibits maximum anisotropy in diffusion on and above 70 GPa, indicating that protons are much more prone to move along the  $a$ -axis rather than  $b$ -axis. Fig 6.1 shows that the distribution of H-atoms in between MgO<sub>6</sub> layers are identical when viewed along  $a$ - or  $b$ -axis. When the pressure

## Chapter 6

induced proton disorder and amorphization of the H-sublattice set in, both  $a$ - and  $b$ -direction becomes relatively less indistinguishable in terms of proton

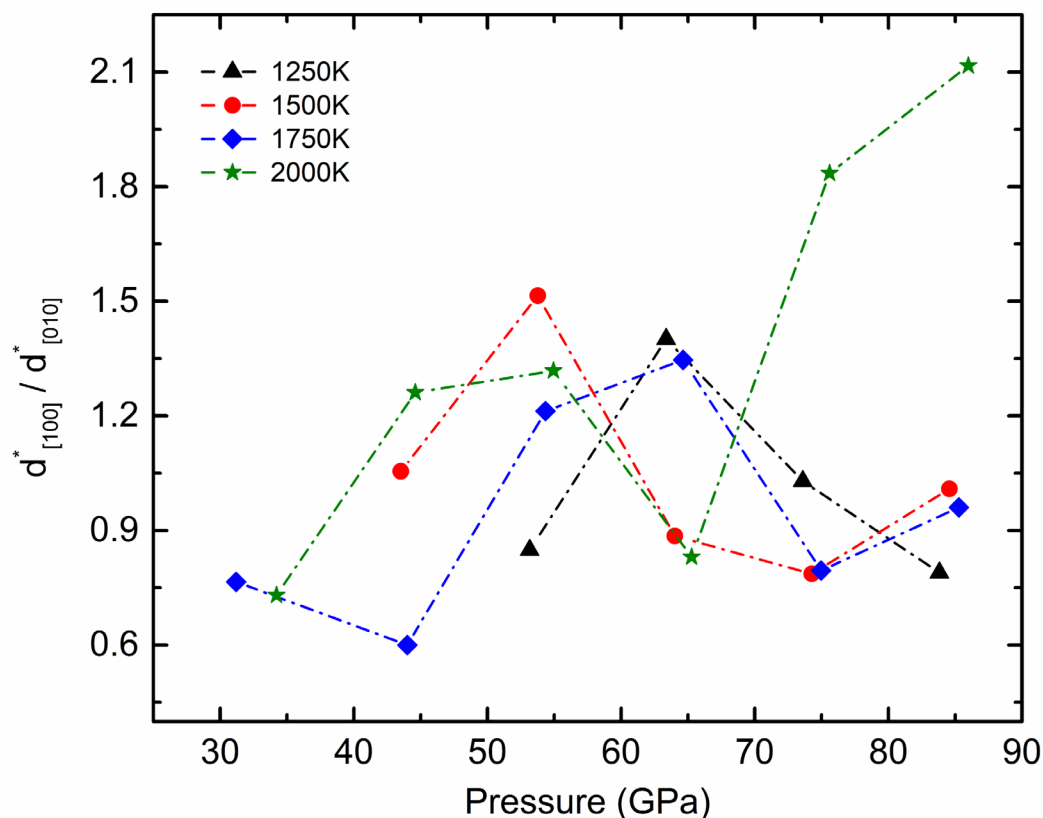


**Figure 6.13:** Anisotropic character of proton diffusion in brucite.

mobility. The H-atom diffusion parallel to  $ab$ -plane thus becomes asymmetric in nature without showing any preferred directional dependence.

### 6.6 Electrical conductivity

The increased proton diffusion in brucite results in an increment in electrical conductivity ( $\sigma$ ) as both the temperature and pressure are raised (Figure 6.14). Electrical conductivity of dry and wet  $P\bar{3}m1$  brucite have been experimentally calculated by Gasc et al. [42] but up to the pressure of 2 GPa only. At these pressures the wet sample is found to show an electrical conductivity in the range  $10^{-2}$  to  $10^{-3}$  S/m at 1173K, which is reasonably low

than our calculations. Guo and Yoshino [37] did a similar study on the same crystalline brucite and observed a maximum conductivity of 32 S/m at pressure 11-13 GPa. This value is comparable to the calculated electrical conductivity at

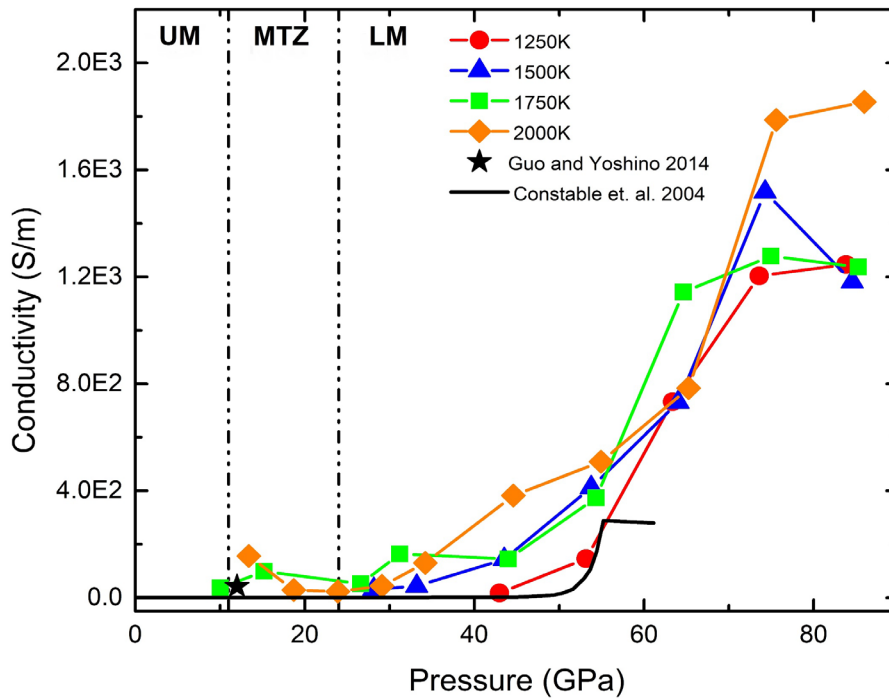


**Figure 6.14:** Electrical conductivity of  $P\bar{3}$  brucite. The black star represents conductivity of  $P\bar{3}m1$  brucite at 11-13 GPa [ref. 37].

p-T points of 28GPa-1500K, 10GPa-1750K and 18.7 GPa-2000K respectively. Even much higher values of  $\sigma$  are observed experimentally in DHMS phase A, phase D and the super-hydrous phase B by Guo and Yoshino [57]. Phase A features a  $\sigma$  of 55 S/m at 10 GPa in the temperature range 500-900K, phase D on the other hand shows an electrical conductivity of 1342 S/m at 22 GPa in the same temperature range. I have obtained comparable values of the electrical conductivities in  $P\bar{3}$  brucite but only in the pressure range 50-60 GPa and between temperature 1500-2000K. This asserts that such high

## *Chapter 6*

conductivities are not unusual. In fact, the removal of the mirror plane and lowering of symmetry in pressure induced  $P\bar{3}m1$  to  $P\bar{3}$  transition in brucite allows more space for H to diffuse rapidly. At pressures higher than 60 GPa, our calculated values of  $\sigma$  surpass the conductivities of DHMS phases. Although the diffusion of H is characterised by a maximum value in the range 73-76 GPa, for 1250k and 2000K we observed that the maximum  $\sigma$  is attained beyond this pressure range despite the fall of diffusion coefficients. For the other two temperatures the trend of the variation of  $\sigma$  is similar to what we observed for  $D_H$  at those temperatures.

Figure 6.14 compares the calculated  $\sigma$  values with mantle electrical conductivity using magnetic satellite measurements by Constable and Constable[58]. At low pressure regime our  $\sigma$  values are in good agreement with their data. Their observation shows a seemingly rapid increment of  $\sigma$  at around 50 GPa, however this study is limited to 60 GPa in pressure. The calculated  $\sigma$  also demonstrates a rapid increment in similar range of pressure although they don't converge to a fixed value as the pressure is increased further. Our observation together with the identification of high  $\sigma$  in DHMS by Guo and Yoshino [57] indicates the presence of proton disordered brucite in lower and upper mantle region of the earth. The mean electrical conductivity of the mantle ranges from  $10^{-4}$  to  $10^3$  S/m[59] which is lower than our calculated conductivities of brucite beyond 60 GPa corresponding to the upper mantle. Thus, this study infers that the amount of brucite in shallow mantle could be moderate to high but reasonably small in lower mantle and brucite could occur as independent pockets at those depths.



## 6.7 Highlights of the outcomes

This chapter have systematically investigated the proton diffusion behaviour in  $P\bar{3}$  brucite at high pressure and high temperature regime. The study reveals an anomalous behaviour of hydrogen diffusion where the diffusion constants increase up to a certain pressure and then exhibit maxima in 73-76 GPa pressure range across all the isotherms. At this pressure range two separate layers of protons between  $MgO_6$  octahedral sheets emerge and coalesce with each other. This coalition of proton layers generates high number of free protons. At high temperature the hydrogen sublattice amorphized leaving the Mg and O atoms static in their lattice sites. The degree of amorphization increases with increasing temperature and thus yields highly mobile protons. Beyond this pressure, the coalition of proton layers becomes ineffective and thereby reduces the diffusion constant. The arrangement of H in layered structure of  $P\bar{3}$  brucite is identical along crystallographic a- and b-axis. The calculated anisotropy in proton migration thus reveals no axial preference but indicates towards the random thermal motion of protons, other than the fact that no net diffusion of proton is observed along c-axis, which was present in  $P\bar{3}m1$  brucite[37].

AIMD calculations are used to evaluate the apparent contribution of the protonic conductivities to the electrical conductivities of brucite under varied hydro-thermal conditions. While the diffusion constants are observed to increase steadily with temperature, the electrical conductivities offer a complex variation. For 1500K and 1750K, the maximum of conductivity coincides with the same p-T points where the diffusion constant shows maxima, whereas for

## ***Chapter 6***

1250K and 2000K the conductivities are observed to increase further with temperature. At pressures corresponding to upper mantle the conductivity features very high values comparable to several DHMS phase. Comparison with geomagnetic data [58,59] allows us to conclude that apart from predominant constituents of the mantle such as silicates and oxides, brucite can also be present in the earth's mantle in small amount.

**References**

- [1] Hirschmann M and Kohlstedt D 2012 Water in Earth's mantle *Phys. Today* **65** 40–5
- [2] Williams Q and Hemley R J 2001 Hydrogen in the Deep Earth *Annu. Rev. Earth Planet. Sci.* **29** 365–418
- [3] Inoue T 1994 Effect of water on melting phase relations and melt composition in the system Mg<sub>2</sub>SiO<sub>4</sub>-MgSiO<sub>3</sub>-H<sub>2</sub>O up to 15 GPa *Phys. Earth Planet. Inter.* **85** 237–63
- [4] Hirschmann M M 2006 Water, melting, and the deep Earth H<sub>2</sub>O cycle *Annu. Rev. Earth Planet. Sci.* **34** 629–53
- [5] Komabayashi T and Omori S 2006 Internally consistent thermodynamic data set for dense hydrous magnesium silicates up to 35 GPa, 1600 °C: Implications for water circulation in the Earth's deep mantle *Phys. Earth Planet. Inter.* **156** 89–107
- [6] Panero W R 2010 First principles determination of the structure and elasticity of hydrous ringwoodite *J. Geophys. Res. Solid Earth* **115**
- [7] Tsuchiya J and Tsuchiya T 2009 First principles investigation of the structural and elastic properties of hydrous wadsleyite under pressure *J. Geophys. Res. Solid Earth* **114** 1–13
- [8] Jacobsen S D, Jiang F, Mao Z, Duffy T S, Smyth J R, Holl C M and Frost D J 2008 Effects of hydration on the elastic properties of olivine *Geophys. Res. Lett.* **35**
- [9] Panero W R, Smyth J R, Pigott J S, Liu Z and Frost D J 2013 Hydrous ringwoodite to 5 K and 35 GPa: Multiple hydrogen bonding sites resolved with FTIR spectroscopy *Am. Mineral.* **98** 637–42
- [10] Jung H, Katayama I, Jiang Z, Hiraga T and Karato S 2006 Effect of water and stress on the lattice-preferred orientation of olivine *Tectonophysics* **421** 1–22
- [11] Karato S 1995 Effects of Water on Seismic Wave Velocities in the Upper Mantle *Proc. Japan Acad. Ser. B Phys. Biol. Sci.* **71** 61–6
- [12] Klepepe A K, Jephcoat A P, Olijnyk H, Slesinger A E, Kohn S C and Wood B J 2001 Raman spectroscopic study of hydrous wadsleyite ( $\beta$ -Mg<sub>2</sub>SiO<sub>4</sub>) to 50 GPa *Phys. Chem. Miner.* **28** 232–41
- [13] Caracas R 2015 The influence of hydrogen on the seismic properties of solid iron *Geophys. Res. Lett.* **4** 3780–5
- [14] Karato S 1990 The role of hydrogen in the electrical conductivity of the upper mantle *Nature* **347** 272–3
- [15] Wang D, Mookherjee M, Xu Y and Karato S I 2006 The effect of water on the

## Chapter 6

- electrical conductivity of olivine *Nature* **443** 977–80
- [16] Fuji-Ta K, Katsura T, Matsuzaki T and Ichiki M 2007 Electrical conductivity measurements of brucite under crustal pressure and temperature conditions *Earth, Planets Sp.* **59** 645–8
- [17] Ichiki M, Baba K, Obayashi M and Utada H 2006 Water content and geotherm in the upper mantle above the stagnant slab: Interpretation of electrical conductivity and seismic P-wave velocity models *Phys. Earth Planet. Inter.* **155** 1–15
- [18] Zhao C and Yoshino T 2016 Electrical conductivity of mantle clinopyroxene as a function of water content and its implication on electrical structure of uppermost mantle *Earth Planet. Sci. Lett.* **447** 1–9
- [19] Novella D, Jacobsen B, Weber P K, Tyburczy J A, Ryerson F J and Du Frane W L 2017 Hydrogen self-diffusion in single crystal olivine and electrical conductivity of the Earth's mantle *Sci. Rep.* **7** 1–10
- [20] Farver J R 2010 Oxygen and Hydrogen Diffusion in Minerals *Rev. Mineral. Geochemistry* **72** 447–507
- [21] Zhang Y and Ni H 2010 Diffusion of H, C, and O Components in Silicate Melts *Rev. Mineral. Geochemistry* **72** 171–225
- [22] Demouchy S and Mackwell S 2006 Mechanisms of hydrogen incorporation and diffusion in iron-bearing olivine *Phys. Chem. Miner.* **33** 347–55
- [23] Delon R, Demouchy S, Marrocchi Y, Bouhifd M A, Barou F, Cordier P, Addad A and Burnard P G 2018 Helium incorporation and diffusion in polycrystalline olivine *Chem. Geol.* **488** 105–24
- [24] Demouchy S, Thoraval C, Bolfan-Casanova N and Manthilake G 2016 Diffusivity of hydrogen in iron-bearing olivine at 3 GPa *Phys. Earth Planet. Inter.* **260** 1–13
- [25] Denis C M M, Demouchy S and Alard O 2018 Heterogeneous hydrogen distribution in orthopyroxene from veined mantle peridotite (San Carlos, Arizona): Impact of melt-rock interactions *Lithos* **302–303** 298–311
- [26] Hae R, Ohtani E, Kubo T, Koyama T and Utada H 2006 Hydrogen diffusivity in wadsleyite and water distribution in the mantle transition zone *Earth Planet. Sci. Lett.* **243** 141–8
- [27] Caracas R and Panero W R 2017 Hydrogen mobility in transition zone silicates *Prog. Earth Planet. Sci.* **4**
- [28] Tsuchiya J 2013 Geophysical Research Letters - 2013 - Tsuchiya - First principles prediction of a new high-pressure phase of dense hydrous.pdf 4570–3
- [29] Demouchy S, Shcheka S, Denis C M M and Thoraval C 2017 Subsolidus hydrogen partitioning between nominally anhydrous minerals in garnet-bearing peridotite *Am. Mineral.* **102** 1822–31

- [30] Zhong X, Hermann A, Wang Y and Ma Y 2016 Monoclinic high-pressure polymorph of AlOOH predicted from first principles *Phys. Rev. B* **94** 1–8
- [31] Litasov K D, Kagi H, Shatskiy A, Ohtani E, Lakshtanov D L, Bass J D and Ito E 2007 High hydrogen solubility in Al-rich stishovite and water transport in the lower mantle *Earth Planet. Sci. Lett.* **262** 620–34
- [32] Liu L 1987 Effects of H<sub>2</sub>O on the phase behaviour of the forsterite-enstatite system at high pressures and temperatures and implications for the Earth *Phys. Earth Planet. Inter.* **49** 142–67
- [33] Shieh S R, Mao H K, Hemley R J and Ming L C 1998 Decomposition of phase D in the lower mantle and the fate of dense hydrous silicates in subducting slabs *Earth Planet. Sci. Lett.* **159** 13–23
- [34] Frost D J 1999 The stability of dense hydrous magnesium silicates in Earth's transition zone and lower mantle *Mantle Petrol. F. Obs. High Press. Exp. A Tribut. to Fr. R. (Joe) Boyd. Geochemical Soc.* 283–96
- [35] Nishi M, Irifune T, Tsuchiya J, Tange Y, Nishihara Y, Fujino K and Higo Y 2014 Stability of hydrous silicate at high pressures and water transport to the deep lower mantle *Nat. Geosci.* **7** 224–7
- [36] Guo X, Yoshino T, Okuchi T and Tomioka N 2013 H-D interdiffusion in brucite at pressures up to 15 GPa *Am. Mineral.* **98** 1919–29
- [37] Guo X and Yoshino T 2014 Pressure-induced enhancement of proton conduction in brucite *Geophys. Res. Lett.* **41** 813–9
- [38] Raugeri S, Luigi Silvestrelli P and Parrinello M 1999 Pressure-induced frustration and disorder in Mg(OH)<sub>2</sub> and Ca(OH)<sub>2</sub> *Phys. Rev. Lett.* **83** 2262–5
- [39] Mookherjee M and Stixrude L 2006 High-pressure proton disorder in brucite *Am. Mineral.* **91** 127–34
- [40] Duffy T S, Meade C, Fei Y, Mao H and Hemley R J 1995 High-pressure phase transition in brucite, Mg(OH)<sub>2</sub> **80** 222–30
- [41] Hermann A and Mookherjee M 2016 High-pressure phase of brucite stable at Earth's mantle transition zone and lower mantle conditions *Proc. Natl. Acad. Sci. U. S. A.* **113** 13971–6
- [42] Gasc J, Brunet F, Bagdassarov N and Morales-Flórez V 2011 Electrical conductivity of polycrystalline Mg(OH)<sub>2</sub> at 2 GPa: Effect of grain boundary hydration-dehydration *Phys. Chem. Miner.* **38** 543–56
- [43] Guo X, Yoshino T, Chen S, Wu X and Zhang J 2022 Partial dehydration of brucite and its implications for water distribution in the subducting oceanic slab *Geosci. Front.* **13** 101342
- [44] Kirby S H, Stein S, Okal E A and Rubie D C 1996 Metastable mantle phase

## Chapter 6

- transformations and deep earthquakes in subducting oceanic lithosphere *Rev. Geophys.* **34** 261–306
- [45] Bina C R and Navrotsky A 2000 Possible presence of high-pressure ice in cold subducting slabs *Nature* **408** 844–7
- [46] Fei Y and Mao H-K 1993 Static compression of  $\text{Mg}(\text{OH})_2$  to 78 GPa at high temperature and constraints on the equation of state of fluid  $\text{H}_2\text{O}$  *J. Geophys. Res. Solid Earth* **98** 11875–84
- [47] Schaack S, Depondt P, Huppert S and Finocchi F 2020 Quantum driven proton diffusion in brucite-like minerals under high pressure *Sci. Rep.* **10** 1–10
- [48] Kresse G and Furthmüller J 1996 Efficient iterative schemes for ab initio total-energy calculations using a plane-wave basis set *Phys. Rev. B - Condens. Matter Mater. Phys.* **54** 11169–86
- [49] Kresse G and Hafner J 1993 Ab initio molecular dynamics for liquid metals *Phys. Rev. B* **47** 558
- [50] Perdew J P, Burke K and Ernzerhof M 1996 Generalized Gradient Approximation Made Simple *Phys. Rev. Lett.* **77** 3865–8
- [51] Blöchl P E 1994 Projector augmented-wave method *Phys. Rev. B* **50** 17953–79
- [52] Hendrik J. Monkhorst 1976 Special points for Brillouin-zone integrations *Phys. Rev. B* **13** 5188–92
- [53] Nosé S 1984 A unified formulation of the constant temperature molecular dynamics methods *J. Chem. Phys.* **81** 511–9
- [54] Hoover W G 1985 Canonical dynamics: Equilibrium phase-space distributions *Phys. Rev. A* **31** 1695–7
- [55] Catti M, Ferraris G, Hull S and Pavese A 1995 Static compression and H disorder in brucite,  $\text{Mg}(\text{OH})_2$ , to 11 GPa: a powder neutron diffraction study *Phys. Chem. Miner.* **22** 200–6
- [56] Parise J B, Leinenweber K, Weidner D J, Kemin Tan and Von Dreele R B 1994 Pressure-induced H bonding: neutron diffraction study of brucite,  $\text{Mg}(\text{OH})_2$ , to 9.3 GPa *Am. Mineral.* **79** 193–6
- [57] Guo X and Yoshino T 2013 Electrical conductivity of dense hydrous magnesium silicates with implication for conductivity in the stagnant slab *Earth Planet. Sci. Lett.* **369–370** 239–47
- [58] Constable S and Constable C 2004 Observing geomagnetic induction in magnetic satellite measurements and associated implications for mantle conductivity *Geochemistry, Geophys. Geosystems* **5** 1–15
- [59] Civet F, Thébault E, Verhoeven O, Langlais B and Saturnino D 2015 Electrical

***Brucite [Mg(OH)<sub>2</sub>]***

conductivity of the Earth's mantle from the first Swarm magnetic field measurements *Geophys. Res. Lett.* **42** 3338–46





## **Molecular crystalline NH<sub>3</sub>-H<sub>2</sub>S mixture**

---

*Motivation*

*Computational details*

*AIMD Phase Diagram*

*Plastic and superionic phases*

*Diffusivity of H, N and S*

*Analysis of local structures*

*Combined P-T effects on band gap*

*Concluding notes*



## Molecular crystalline $\text{NH}_3\text{-H}_2\text{S}$ mixtures

---

### 7.1 Motivation

Hydrogen bonded linear mixtures of dense molecular crystalline phases have gained major importance in diverse scientific fields of interest. The ‘ice giants’ Uranus and Neptune have gaseous atmospheres, comprised of hydrogen and helium predominantly, featuring characteristically small rocky cores, leaving out a considerably large mantle region. Their vast mantle regions consist mainly of isolated ‘molecular ices’ of water, ammonia and methane and also their mixtures. Observations from astronomical campaigns[1–8] suggest that these compositions are expected in the interior of their moons and also in similar exoplanets like these ice giants. The thermodynamic environment in the mantle region of this ‘ice giants’, dominated by hot-ice layers, are characterized by extreme pressure in the range of several hundred gigapascals and temperatures up to several thousand kelvin rendering access to the exotic regions in the phase diagram of water [9–11], ammonia[12], methane[13–15] and ammonia-water mixtures [16–19]. Under the extreme conditions at the

## *Chapter 7*

deep planetary interiors, these hot ice mixtures of molecular liquids [1,20] are expected to exhibit complicated chemical activities resulting in non-retention of molecular structure, formation of superionic states and potential demixing etc. [21–23]. The physical and chemical behaviour of the hot dense ices thus significantly influence the atmospheric composition, rotational velocities, gravitational moments and the internal quasi-homogeneous or heterogeneous chemical structures of these celestial bodies and their thermodynamic evolution. There have been several experimental studies on the binary molecular ices and hydrocarbons at pressure and temperatures relevant to interiors of the ice giant planets and exoplanets which revealed unusual chemical behaviour with unforeseen reactivity [24,25]. On the other hand, first-principle studies have explored a range of mixtures of molecular ices and their interactions with the two of the most lightest constituents e.g., H and He and predicted a plethora of stable compounds demonstrating exotic physical phenomena like plasticity and superionicity [21,22,26–29]. Hydrogen sulphide ( $\text{H}_2\text{S}$ ), despite identified from planetary atmospheric observations as being existing in Uranus and Neptune [30–32], received less attention. Their composition, miscibility with other molecular ices and physico-chemical properties under extreme environment thus demand a systematic study to expand our understanding of these planets and develop their realistic models. Recently, the first principles study of Li et al. [33] predicted that  $\text{NH}_3$  indeed reacts with  $\text{H}_2\text{S}$  and forms a series of novel binary compounds with varying stoichiometry.

From a material science inspired point of view, H<sub>2</sub>S is one of the simplest compound capable of showing conventional superconductivity above 200K and at an elevated pressure of 155 GPa[34–38]. First principles study of Cui et al. [39] has recently predicted a metastable superconducting CH<sub>4</sub>-SH<sub>3</sub> hydride perovskite phase. It is possible to attain such high-T<sub>C</sub> superconductivity in a cubic CSH<sub>7</sub> phase at 100 GPa and 180K [40]. The most important recent discovery in this line of research was made by Snider et al. [41], who have experimentally achieved room temperature superconductivity in a carbonaceous sulphur hydride for the first time. All these studies motivate further research on dense molecular mixtures of H<sub>2</sub>S. The interaction of H<sub>2</sub>S with molecular ices in elevated pressure regime merits a systematic investigation to find a route towards lowering the pressure required for reaching such superconducting state, which is largely unexplored till now.

In analogy to ammonia water mixtures, Li et al. [33] have computationally predicted a number of molecular crystalline phases of NH<sub>3</sub>-H<sub>2</sub>S mixture. Extensive studies dealt with various NH<sub>3</sub>:H<sub>2</sub>S ratios and revealed that potential mixtures, such as ammonia mono-sulfide (AMS, NH<sub>3</sub>:H<sub>2</sub>S=1:1), ammonia di-sulfide (ADS, NH<sub>3</sub>:H<sub>2</sub>S=1:2), ammonia hemi-sulfide (AHS, NH<sub>3</sub>:H<sub>2</sub>S=2:1) and ammonia quarter-sulfide (AQS) (NH<sub>3</sub>:H<sub>2</sub>S=4:1) can stabilize over a wide range of pressure. All of them undergo pressure induced structural transitions. Among them, AMS shows the most diverse structural evolution. Starting from a tetragonal P4/nmm phase it readily transforms to two consecutive monoclinic Cc and P2<sub>1</sub>/m phases at 11 and 50 GPa, respectively. Upon further compression the P2<sub>1</sub>/m phase undergoes serial phase transitions

## *Chapter 7*

to orthorhombic  $\text{Abm}_2$  and  $\text{Cmma}$  phases at 95 and 125 GPa respectively. Electron-phonon coupling calculations shows that the  $\text{Abm}_2$  and  $\text{Cmma}$  phases demonstrate superconductivity at low temperatures of 21.4K and 49.9 K.

Inspired by AMS's stability over a diverse pressure range and superconducting nature, this phase has been chosen in the present thesis to explore the potential superionic character. I employ AIMD simulation to investigate the high-pressure high-temperature behaviour of the AMS phases starting from the crystalline solid state which is stable at the lowest pressure and then going upward in both pressure and temperature to investigate the physical changes occurring in the system. Compressed ammonia is reported to demonstrate plastic phases[42]; so does water[43,44] and ammonia-water mixture[22,26]. Further increase in temperature of these single or binary molecular ices result in a transformation into superionic[27] states and eventually to a liquid state. The presence of such plastic and superionic phases for ammonia water mixture calls for a similar investigation on ammonia sulfide mixtures. Here, a pressure-temperature phase diagram of AMS is developed with a special emphasis on the dependence of the solid, plastic, superionic and liquid phases on temperature. In particular, it will be intriguing to see whether the melting curve intersects with the isentropes of Uranus and Neptune which would indicate the existence of a partially solid lower mantle in these planets characterized by diffusive proton mediated electrical conductivity. I further calculate the diffusivity of hydrogen as well as of the nitrogen and sulfur and examine the pair distribution functions to analyze whether the liquid phase retains its molecular nature or turns atomic on heating.

## 7.2 Computational details

I have performed Ab-initio molecular dynamics (AIMD) simulation on Ammonia mono sulphide (AMS) mixtures ( $\text{NH}_3\text{:H}_2\text{S} = 1\text{:}1$ ) as implemented in VASP[45,46]. The ground state structures are obtained from Li et al. [33]. In AIMD, the motion of the atoms is governed by Newtonian dynamics, albeit restricted within the crystal. The interatomic forces influencing the atomic motion are computed within the framework of density functional theory (DFT). I chose the projector-augmented wave (PAW)[47] formalism of the DFT to capture electron-ion interactions. The exchange-correlation effect is expressed in the functional form as proposed by Perdew-Burke-Ernzerhof [48] of the generalized gradient approximation type. The calculations employed a kinetic energy cut-off of 600 eV together with a fixed Balderaschi-type k-point to sample the reciprocal space. In the AIMD simulations pressure, temperature and ionic positions were sampled in every ten time steps.

The simulations used isokinetic NVT ensembles at the temperature,  $T$ , at fixed volume,  $V$ , and number of atoms,  $N$ , in the simulation box. The temperature was monitored by a Nose-Hoover type thermostat [49,50]. The volumes chosen for the simulations correspond to the desired pressure. Each simulation was run for 10000-14000 timesteps, with each timestep of 0.5 fs, for supercells of sizes ranging from 180 to 448 atoms. The NVT ensemble, which constrains the volume, affects the actual pressure on the system as the temperature of the AIMD simulations are increased. I thus considered the thermal pressure correction and, found the pressure variation restricted within 2-5% of the target pressure. For each AMS phase, a systematic grid of density-

## **Chapter 7**

temperature points are studied (in 250K steps), encompassing their high pressure-stability range, and beginning from the most stable crystal structure at any given external pressure. The molecular dynamics trajectories of each atomic species are analysed via mean square displacements (MSD) and pair distribution functions (PDF). The PDF's were calculated using the Atomic Simulation Environment package[51]. Eq. 3.14 has been used to calculate the diffusion coefficients from the slope of the MSD versus time plot.

Structures of different high-pressure and -temperature phases at varying timesteps were extracted from the AIMD data. The standard DFT implementation in VASP has been utilized to calculate the density of states of the phases at various pressure-temperature conditions across the entire simulation time. As the supercells considered in the AIMD simulations contain several hundreds of atoms, a gamma centred  $3\times 3\times 3$  Monkhorst-Pack[52] k-point grid together with tetrahedron method [53] was chosen to calculate the density of states and to enumerate the band-gap.

### **7.3 AIMD phase diagram**

The P-T phase diagram for ammonia monosulphide (AMS) mixtures is shown in Figure 7.1 starting from the stable structures between the pressure range 0-160 GPa and covering up to a temperature  $T = 3500\text{K}$ . The  $P4/nmm$  phase at ambient pressure is the only one among the candidate mixtures found to undergo a direct transition from a solid state to liquid state upon heating. For the rest of the AMS mixtures at high pressure, increasing temperature reveals zones of solid phases, plastic or rotating phases followed by superionic



states, and eventually liquid states. This categorization of different states is

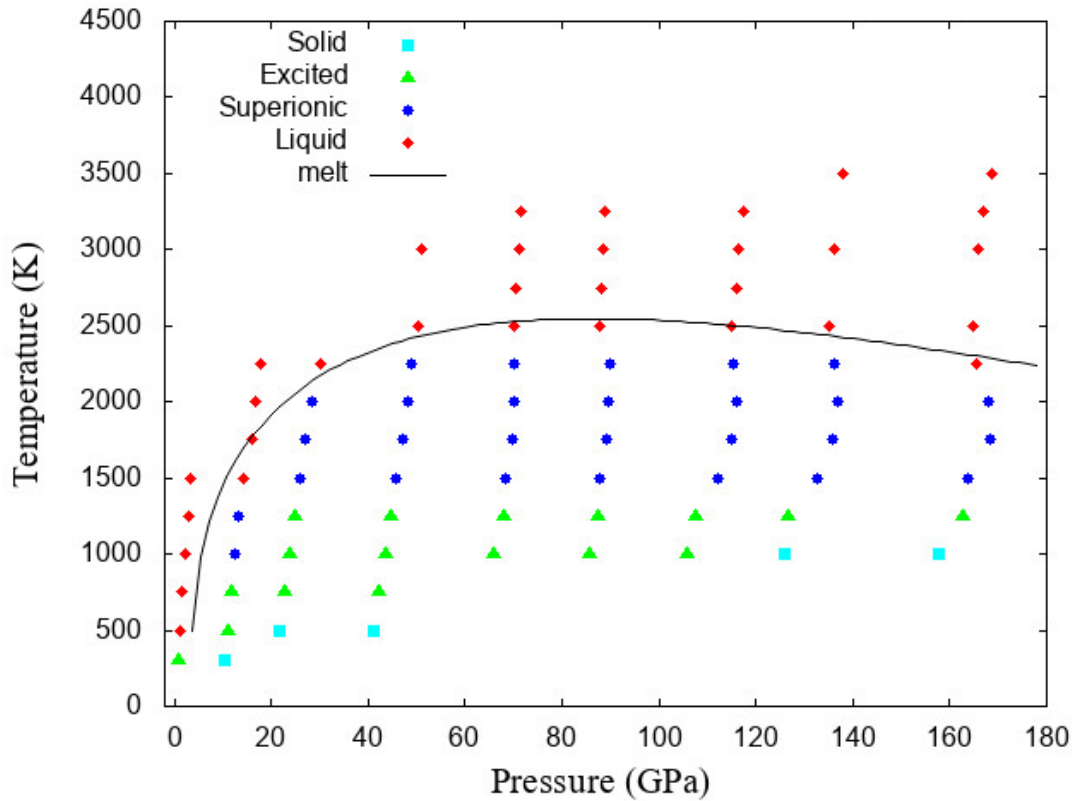


**Figure 7.1:** Pressure-temperature phase diagram of NH<sub>3</sub>+H<sub>2</sub>S (1:1) mixture along with the melting curve. The different symbol represents different states of the molecular crystalline material.

based on the analysis of the MSD of different species as illustrated in Figure 7.2-7.7. The locally excited or the plastic states are characterized by initial growth in their MSD which gradually plateaus to a small finite value as illustrated in Figure 7.2a and 7.3a. Whereas in the superionic states, the heavy atoms (S and N) are stationary at their lattice positions (negligible MSDs) with the highly mobile protons diffusing between the sublattice of heavy atoms (Figure 7.2-Figure 7.5) Correspondingly, the superionic states are associated with a finite proton diffusion coefficients ( $D_H > 0$ ) and non-diffusive heavy atoms i.e.  $D_N = D_S \sim 0$ . Finally, in the liquid state, all atoms are mobile

## Chapter 7

irrespective of their masses and diffuse throughout the entire simulation cell (Figure 7.4 and Figure 7.5c and 7.5d).

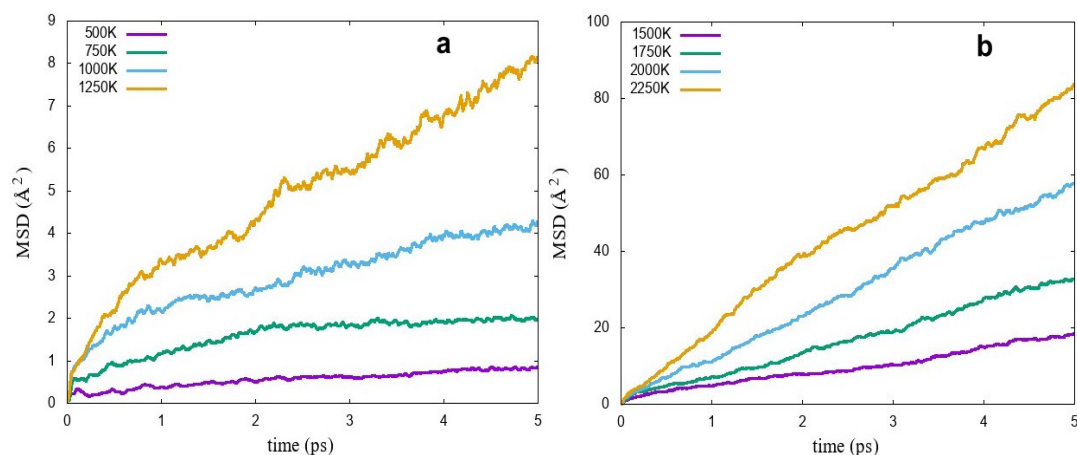


**Figure 7.2:** Mean square displacements of H atoms at different temperatures of the Cc phase around 20 GPa as a function of time.

Our studied AMS phases are stable with respect to decomposition into individual  $\text{NH}_3$  and  $\text{H}_2\text{S}$  or mixtures of  $\text{NH}_3$  and  $\text{H}_3\text{S} + \text{S}$  up to 150 GPa in

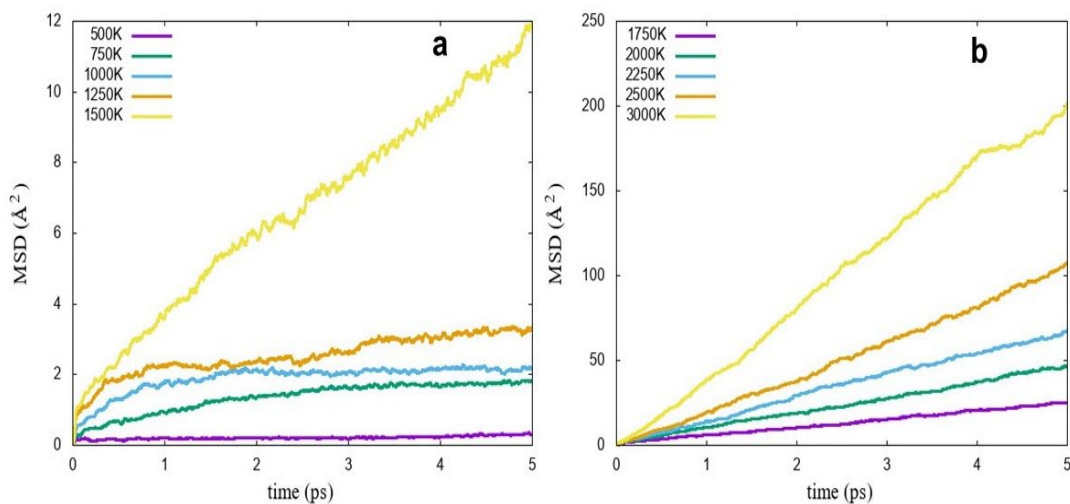


**Figure 7.3:** Mean squared displacements of H atoms for the Cc phase at 40 GPa.

pressure. Beyond 150 GPa, the enthalpy of  $\text{NH}_3$  and  $\text{H}_3\text{S} + \text{S}$  mixture becomes lower than our high-pressure Cmma phase, thus limiting the high-pressure stability of the AMS phase[26]. The ambient pressure P4/nmm phase readily

melts at 500K, however the similar crystalline phase at 10 GPa shows intermediate plastic and superionic states which results in an increment of the

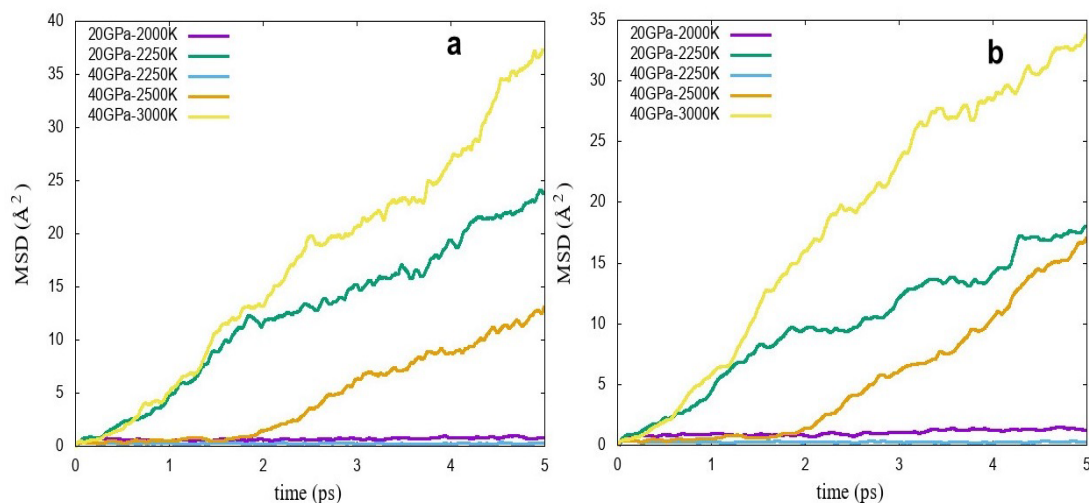


**Figure 7.4:** Mean squared displacements of a. N and b. S atoms in the Cc phase at different pressures and temperatures.

melting point (Figure 7.1). At 20 GPa the Cc phase melts at a temperature between 2000-2250K and at 40 GPa it increases further to 2500K. A melting point convergence is observed at 2500K for the P2<sub>1</sub>/m and Abm<sub>2</sub> phase before it drops to 2250K for the Cmma phase stable at the highest pressure. These type of anomalous variation of melting point is observed in case of elements like Barium, Germanium, and Bismuth, and compounds like KNO<sub>2</sub> and KH<sub>2</sub>AsO<sub>4</sub>. For such materials characterized by falling melting curve at high-pressure regime are better to be fitted with Kechin equation [54] rather than the standard Simon-Glatzel equation[55] which fails to capture the maxima of the melting curve. The black line in Figure 7.1 represents the melting curve of AMS. The calculated melting curve lies close to the ammonia monohydrate (NH<sub>3</sub>:H<sub>2</sub>O = 1:1) and ammonia dihydrate (NH<sub>3</sub>:H<sub>2</sub>O = 1:2) mixtures[22,26] but differs substantially from the ammonia quarterhydrate phase (NH<sub>3</sub>:H<sub>2</sub>O = 4:1)

## Chapter 7

showing much higher melting points. Li. et al. [33] have shown that the partial charges on  $\text{SH}^-$  and  $\text{S}^{2-}$  lies in the range of -0.62 to -0.65, whereas for  $\text{OH}^-$  and  $\text{O}^{2-}$  they are far more negative ranging from -0.68 to -1.3 as calculated by Robinson et al.[17]. Consequently, the binding energies of hydrogen bonded

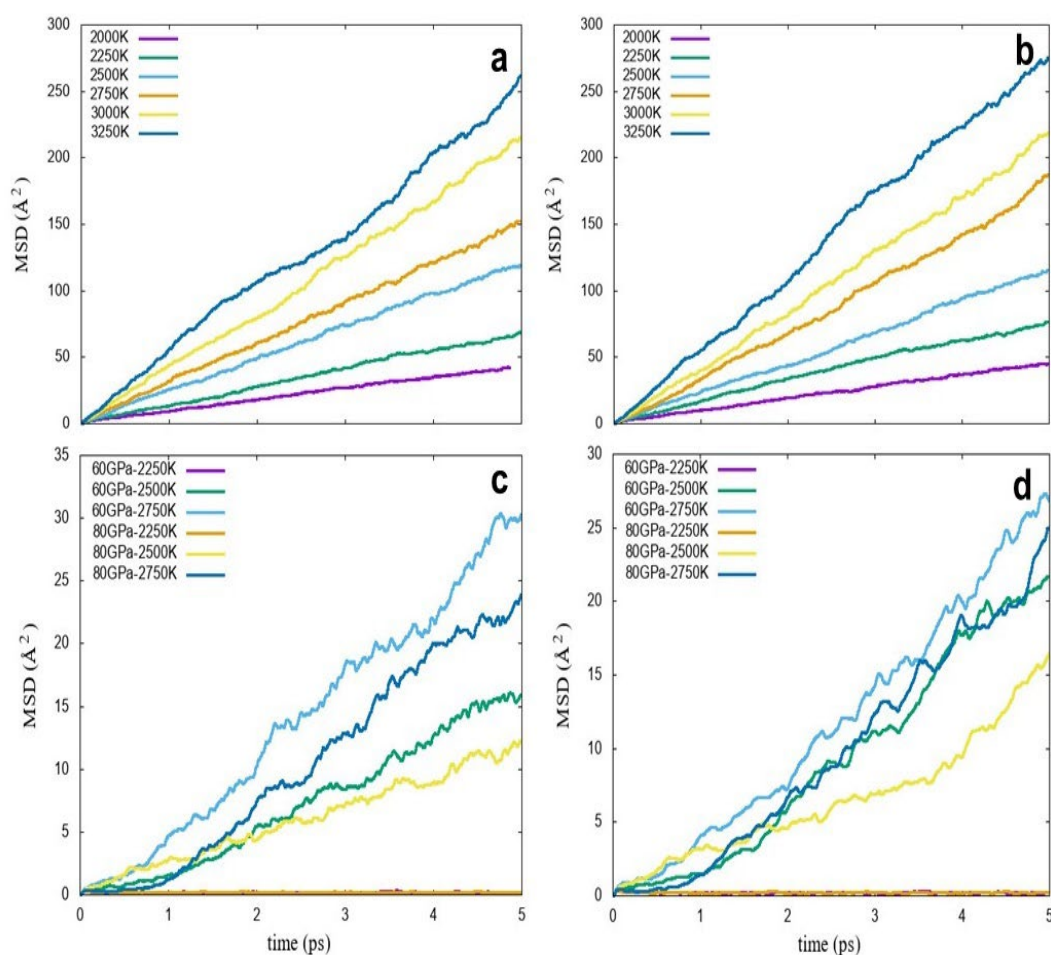


**Figure 7.5:** Mean square displacements of H atoms in  $\text{P2}_1/\text{m}$  phases at a. 60 GPa and b. 80 GPa. The same is shown for c. N and d. S atoms in the bottom panels.

$\text{H}_2\text{S}$ -ammonia dimers and trimers like  $\text{HSH}\cdots\text{NH}_3$ ,  $\text{H}_3\text{NH}\cdots\text{SH}$  and  $\text{H}_3\text{NH}\cdots\text{S}\cdots\text{HNH}_3$  are reasonably lower than those of the water-ammonia dimers and trimers. We can argue that these lower binding energies require a lower temperature for melt generation and thus explain the low melting points of the  $\text{NH}_3\text{-H}_2\text{S}$  phases. It is noteworthy that, the isentropes for Uranus and

Neptune[56] do not intersect with our melting curve, but they follow the melting curve very closely at pressures under 30 GPa, suggesting that the superionic phases of AMS may be present in the shallow mantle region of these ice giant planets. The present simulation shows that around 10 GPa, P4/nmm phase attains superionicity at 1000K, whereas for the other high pressure phases superionic nature does not appear until 1500K. Another important observation is the pressure drop in superionic to liquid transition of the P2<sub>1</sub>/m, Abm<sub>2</sub> and Cmma phases. This indicates that the density of the liquid state of these phases are greater than their solid/superionic counterparts.

## **7.4 Plastic and superionic phases**

At elevated temperature and pressure NH<sub>3</sub> shows a plastic regime in its phase diagram which has been experimentally verified [42]. Although there are no computational or experimental studies on the superionicity of H<sub>2</sub>S, its pressure induced metallization at 96 GPa have been explored experimentally by Sakashita et. al [57]. These plastic phases of molecular crystalline solids represent the states with free rotor molecules as the main constituent which are constrained to their designated spots in the lattice. They occur as intermediate states between solid and the superionic states indicative of the partially amorphized sublattice. But for molecular mixture of ices, the case is not as straightforward as individual ices of water or ammonia etc. since molecular mixtures feature several different chemical and structural motifs as well as basins of proton attractors. Their complicated interaction generates local excitations where the atoms leave their lattice site without yielding a net diffusion. Although the different AMS phases exhibit characteristic

## Chapter 7

orientations of the hydrogen bonded S-H---H-S chains, the remaining chemical motif  $\text{NH}_4^+$  are equipped with configurational proton disorder, which suggests that these phases should develop plasticity.

Indeed similar to ammonia, water[43,44] and ammonia-water mixtures,

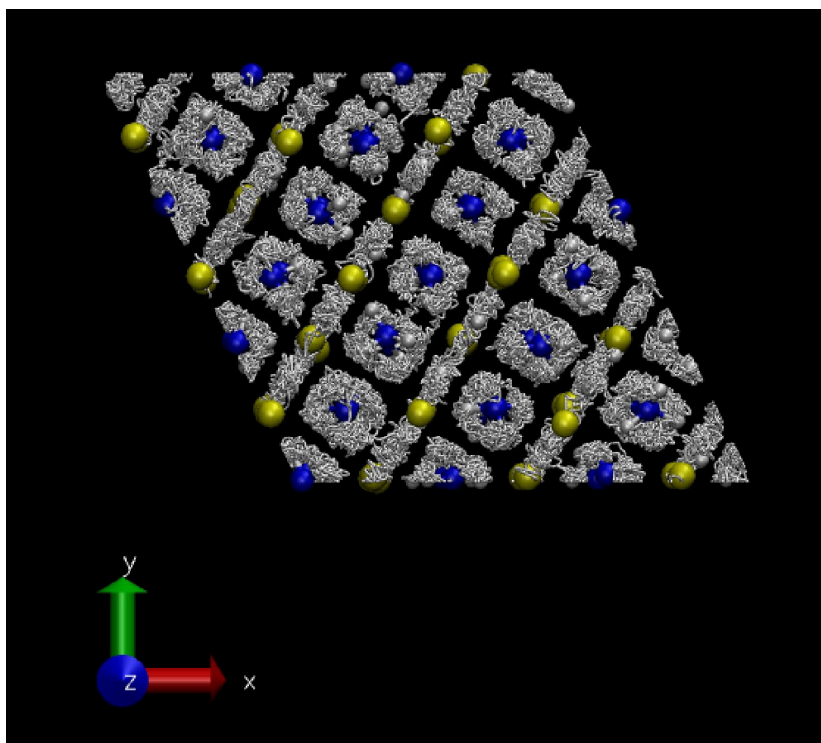


**Figure 7.6:** Trajectories of the H-atoms (white lines) around N atoms (blue) and S atoms (yellow) of the  $\text{Abm}_2$  phase at 100 GPa and 1000K. The disjoint motion of H atoms around N and S atoms represents vibrational and rotational motions representing the plastic states.

this computational investigation reveals that, barring the  $P4/nmm$  phase at ambient pressure, rest of the AMS mixtures undergo a transition from the plastic zone to the superionic region with increasing temperature. Fig 7.6 shows typical molecular dynamics trajectories of proton in the  $\text{Abm}_2$  phase at a pressure of 100 GPa and a temperature of 1000K. The protons are mobile in nature, but they do not diffuse through the entire simulation cell. In contrast to the ammonia hemihydrate AHH phase, where both rotation of  $\text{NH}_4^+$  and occasional proton hopping along the H-bonds from  $\text{NH}_4^+$  to  $\text{O}^{2-}$  ions are

effective, the dominant leading local excitations in this case involve individual rotations of NH<sub>4</sub><sup>+</sup> motifs and oscillatory motion of protons along lines of SH<sup>-</sup> chains. The dynamic equilibrium NH<sub>4</sub><sup>+</sup> + O<sup>2-</sup> ⇌ NH<sub>3</sub> + OH<sup>-</sup> present in case of ammonia hemihydrate is absent here. However, the situation is different for

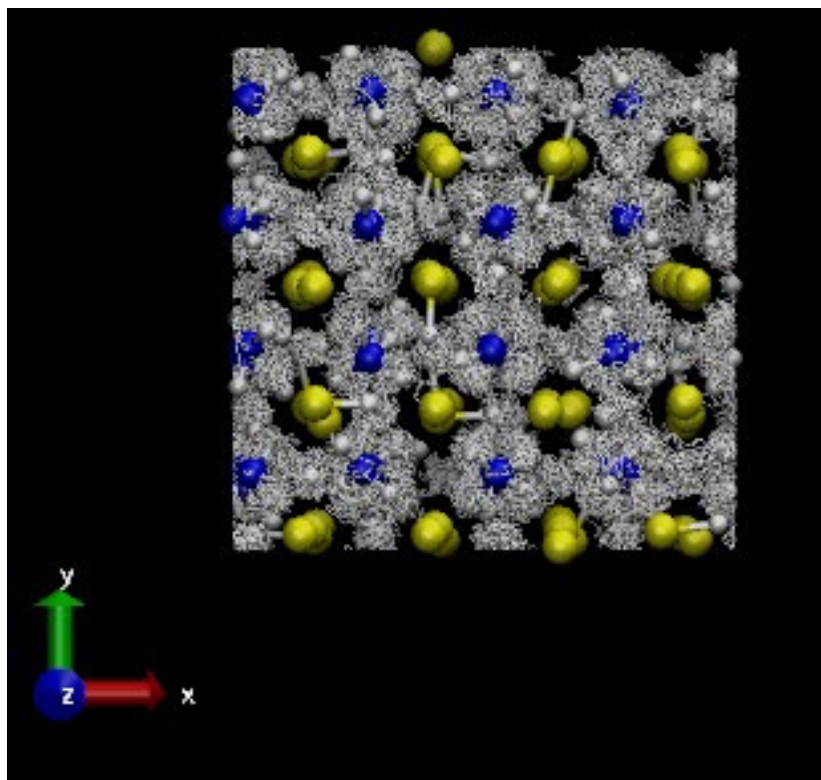


**Figure 7.7:** Trajectories of H atoms in the surroundings of N and S atoms in the Cc phase at 40 GPa and 1000K. The colours carry the usual meaning as in Figure 7.6.

the Cc phase at 40 GPa and 1000K. As Figure 7.7 reveals that the plasticity in this phase is entirely controlled by a dynamic equilibrium of proton exchange between molecular motifs, giving rise to transient S<sup>2-</sup> ions. The proton MSD's shown in Figure 7.2-7.3 rises continuously up to 2 ps and 1 ps for the low temperature Cc phases at 20 GPa and 40 GPa, respectively and finally converges to 2 Å<sup>2</sup>. The distance between the protons in disordered NH<sub>4</sub><sup>+</sup> units are  $d_{HH} \sim 1.63$  Å. Assuming that the local tetrahedral orientation of the NH<sub>4</sub><sup>+</sup> units remain unaltered, the  $H_{MSD}$  thus can approach an approximate value

## Chapter 7

$H_{\text{MSD}} = \frac{3}{4} \times d_{\text{HH}}^2 = 1.993 \text{ \AA}^2$ . This indicates that the regime where  $H_{\text{MSD}}$  converges to a finite value ( $\sim 2 \text{ \AA}^2$ ) does not produce diffusive protons, but causes local excitations resulting in a plastic state.

The superionic states are identified from the MSD plots of every

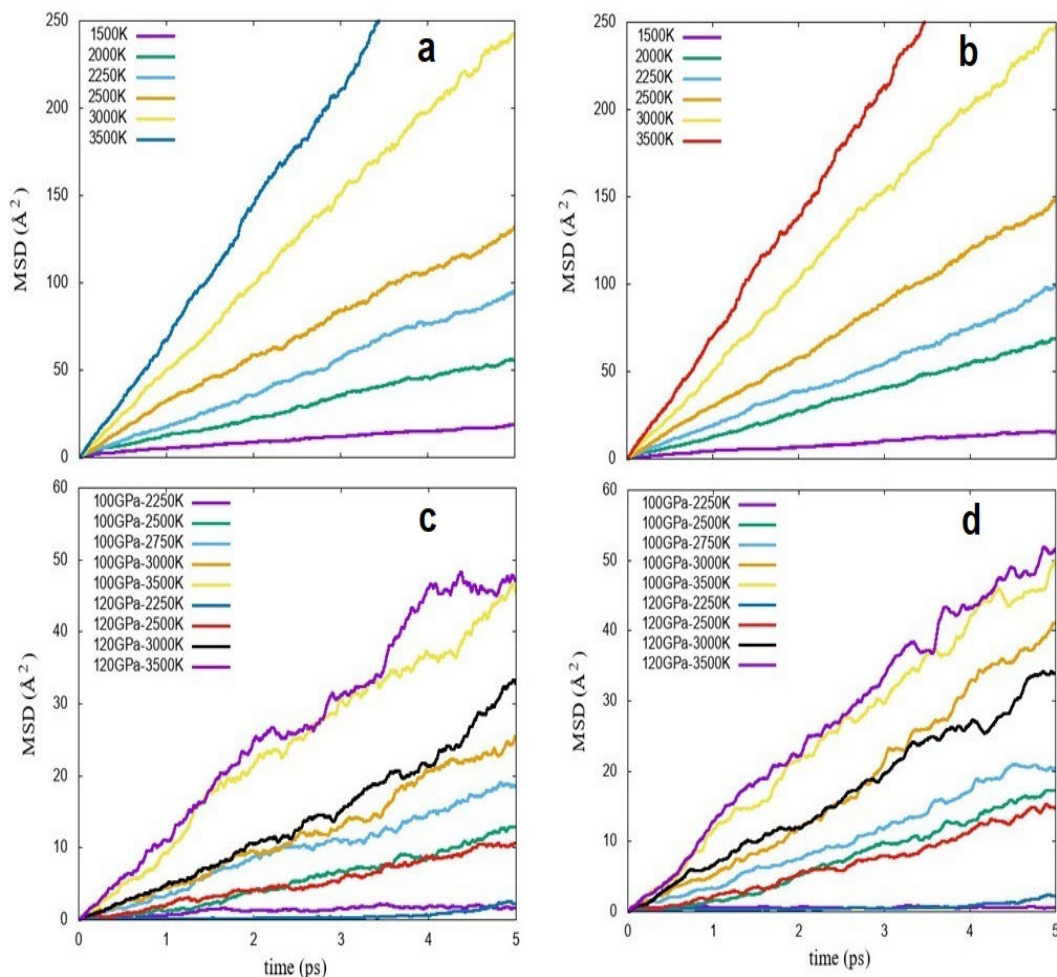


**Figure 7.8:** MSD of H atoms in Abm2 phases at a. 100 GPa and b. 120 GPa. The bottom panel shows the MSD of c. N atoms and d. S atoms in Abm2 phases at different preesure-temperature.

simulation run, based on the following two criteria: 1) the hydrogen atoms are significantly mobile, able enough to leave their lattice sites, and 2) the heavy atoms of N and S are stationary, forming a stable N-S sublattice, as evident from Figure 7.9 for the  $P2_1/m$  phase at 60 GPa and 2250K. A phase is considered to be in a superionic state when the MSD of N and S atoms stays



constant as a function of time at a reasonably small value whereas the MSD of H exhibits rapid increment as the AIMD simulation progresses. Figure 7.2, 7.3, 7.5a-b, 7.8a-b and 7.10a illustrate the typical MSD of protons of the Cc phase at 20 GPa, 40 GPa; P2<sub>1</sub>/m phase at 60 GPa, 80 GPa, Abm<sub>2</sub> phase at 100 GPa, 120 GPa and Cmma phase at 150 GPa respectively in both the plastic and superionic regime. The onset temperature for superionicity in the P4/nmm phase at 10 GPa is observed to be 1000 K which rises to 1500 K at 20 GPa and

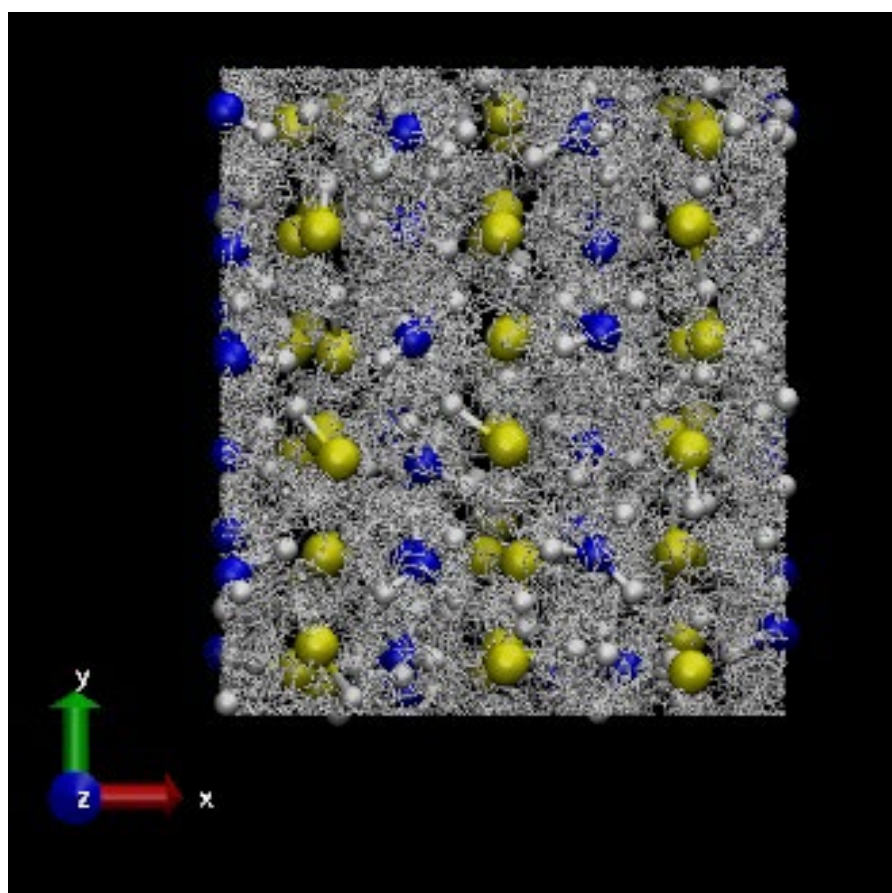


**Figure 7.9:** Trajectories of H atoms (white lines) in the superionic state of the P2<sub>1</sub>/m phase at 60 GPa and 2250 K. The yellow and blue spheres are S and N atoms respectively. Here the trajectories of the H-atoms are distributed across the entire simulation cell as opposed to the plastic states where they revolve around the relatively heavy atoms (Figure. 7.6-7.7).

stays the same for the subsequent high-pressure phases. For pure ammonia [12], water [10] or ammonia-water mixture [26], the superionicity for the high-pressure phases are observed at a temperature of 2000 K and above,

## Chapter 7

pushing their melting curve upwards. The mixing of ammonia and hydrogen sulphide can enforce an enhanced proton transfer between the constituent molecular motifs as eminent in the plastic region. This could lead to a much

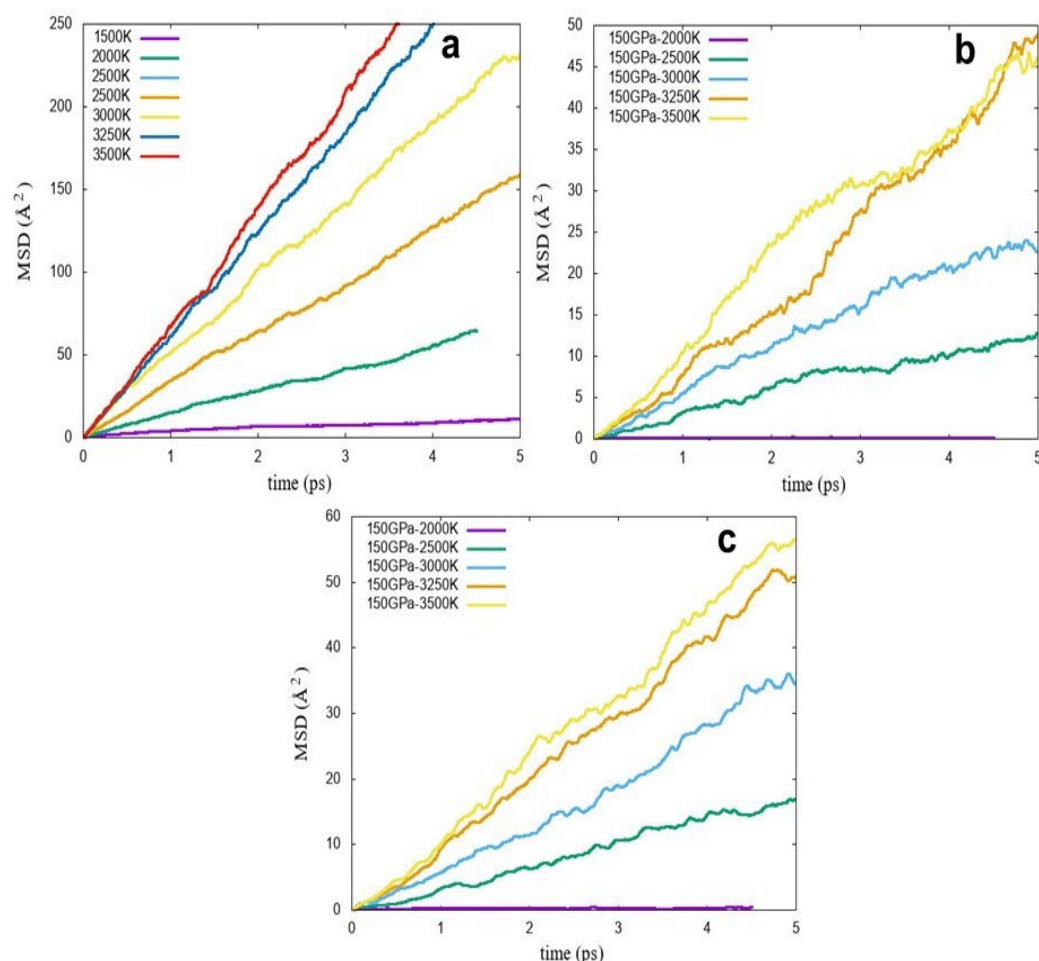


**Figure 7.10:** MSD of the a. H atoms b. N atoms and c. S atoms in the Cmma phase of AMS.

moderate P-T requirement to attain superionic behaviour in AMS phases compared to pure molecular ammonia. In general, the superionic state is spread over a broader temperature regime as the temperature is increased reaching a maximum of 2250K for the intermediate high-pressure phases, before falling down to 2000K for the Cmma phase. It is important to note here that the melting in our simulations were obtained using ‘heat until melting’ method. This method has a drawback as it includes superheating, which

overestimates the melting points. It will be intriguing to determine the accurate melting points via the improved methods like solid-liquid phase coexistence, thermodynamic integration, annealing or the Z-method and to compare the accuracy of our results to have an estimate of the size effects on the melting points of the AMS phases.

## 7.5 Diffusivity of H, N and S

As discussed in the earlier sections, the diffusion of the light constituent element H is observed in both the superionic and the liquid regime whereas the diffusion of the heavy elements N and S are realized only when the system is molten. Eq. 3.14 has been used to calculate the diffusion coefficients from the slope of the linear region of their respective MSD vs time plot (Figure 7.2-7.5, 7.8 and 7.10). For the plastic phases mediated by the rotating molecular motifs the MSD of H increases initially and then oscillate around some mean value where protons are halfway from their maximum displacement. This leads to a finite proton MSD, but with a negligibly small slope, i.e., the diffusion coefficient reduces to zero. The diffusion coefficients of the solid phases are essentially zero. Any diffusion coefficient smaller than  $10^{-9}$  m<sup>2</sup>/s are thus not considered in the present calculation because they entirely owe to rotational or vibrational motions. Table 7.1 lists our calculated proton diffusion coefficients  $D_H$  across the superionic and liquid states of AMS and Figure 7.11 shows the variation of  $D_H$  with respect to increasing pressure. The initial green circle is observed to be higher in magnitude even compared to the other values along the isotherm of 2250K. This is due to the fact that it belongs to the ambient

## Chapter 7

P4/nmm phase which readily melts at a lower temperature of 500K. Thus, a

**Table 7.1:** Proton diffusion coefficients in AMS mixtures under varied pressure and temperature condition.

Temperature (K)	Pressure (GPa)	Proton diffusion coefficient (m <sup>2</sup> /s)
1500	1.63	2.03094E-07
	14.346	1.12363E-08
	25.995	3.63646E-08
	45.785	1.99283E-08
	68.41	1.53756E-08
	87.808	1.67554E-08
	112.315	3.3461E-08
	132.66	2.98279E-08
	163.94	2.02639E-08
1750	16.175	2.8531E-08
	27.079	6.03188E-08
	47.015	4.4796E-08
	69.746	2.47312E-08
	89.264	2.3698E-08
	114.879	2.76627E-08
	168.24	3.02622E-08
2000	16.875	4.01462E-08
	28.419	1.15565E-07
	48.015	9.32954E-08
	70.178	8.02414E-08
	89.425	8.98081E-08
	115.968	1.0599E-07
	137.02	1.38752E-07

	168.06	1.42035E-07
<b>2250</b>	17.677	4.39181E-08
	30.016	1.65147E-07
	49.029	1.31747E-07
	69.94	1.30088E-07
	90.032	1.41287E-07
	115.493	1.93197E-07
	136.26	1.92975E-07
	165.38	1.93013E-07
<b>2500</b>	50.255	2.15019E-07
	69.941	2.46005E-07
	87.911	2.20018E-07
	115.149	2.54116E-07
	135.08	3.01756E-07
	164.67	3.21171E-07
<b>3000</b>	51.097	3.99192E-07
	71.152	4.42337E-07
	88.325	4.30026E-07
	116.543	4.77724E-07
	136.062	4.9045E-07
	166.05	4.55762E-07

three-fold increment of temperature generates incredibly fast protons. Structural motif plays an important role in determining the mobility of the proton. This is reflected in the fact that  $D_H$  for the molten P4/nmm phase at 10 GPa is comparable to the  $D_H$  of the superionic states of the high-pressure phases along the 1500K and 1750K isotherm.  $D_H$  along the higher temperature isotherms easily supersede the value of the former.  $D_H$  is observed to decrease

## Chapter 7

at the high-pressure end of the 3000K isotherm. Since the molecular system at this temperature contains every kind of constituent mobile atoms, this decreasing  $D_H$  indicates that the presence of larger mobile atoms constrains the motion of protons.

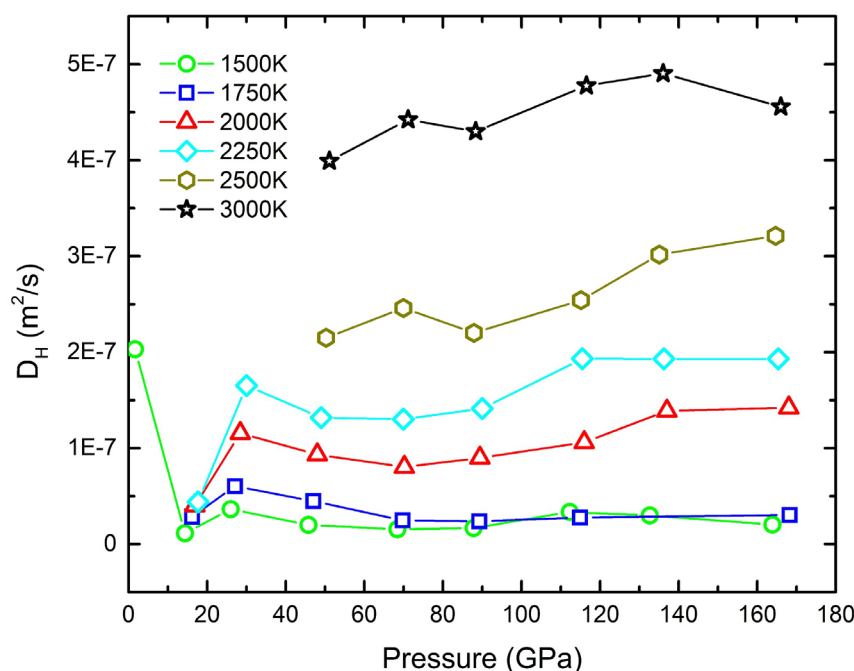


**Figure 7.11:** Diffusion coefficients of H in AMS mixture along different isotherms and at different pressures. Note the high  $D_H$  for 1500K at low pressures where the mixture is in liquid state.

The situation for  $D_N$  and  $D_S$  are a bit different. Figure 7.12 features the diffusion of heavy element N and S in the liquid state at 2500K and 3000K. The  $D_N$  and  $D_S$  for the  $Abm_2$  phases at 100 and 120 GPa (initial pressures for the AIMD simulation) exhibit very less difference in value. The  $P2_1/m$  phases at 60 and 80 GPa on the other hand (initial pressures) shows a very drastic variation. Despite being heavier, the diffusion constants of S atoms are observed to surpass the diffusion coefficients of N atoms at most of the P-T

points, as evident from Figure 7.12. Only the Cmma phase yields similar values

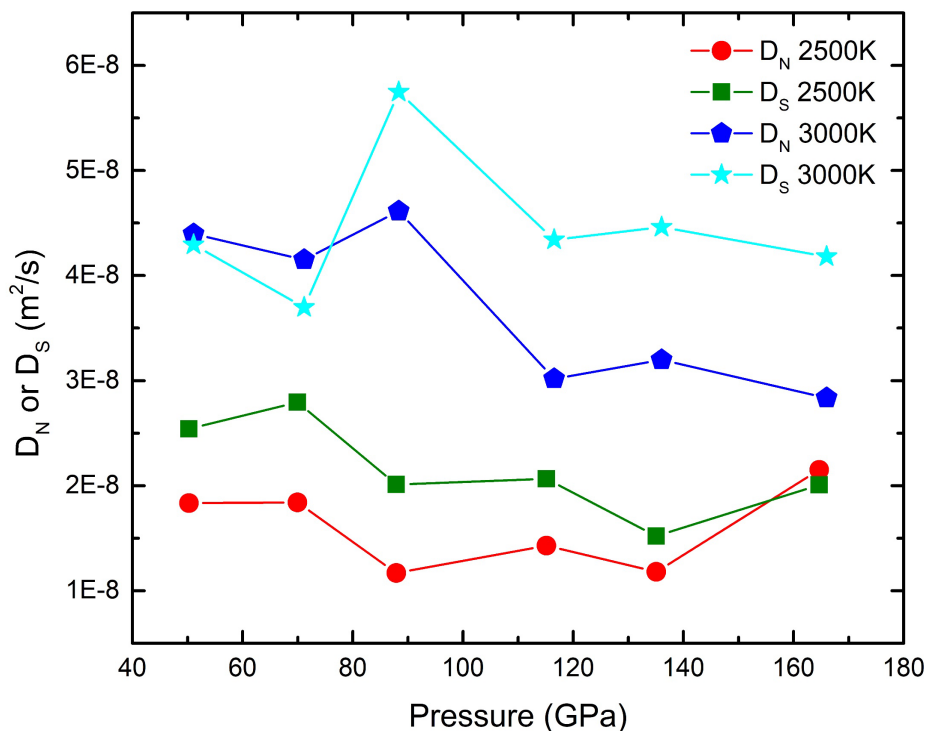


**Figure 7.12:** Diffusion coefficients of nitrogen and sulfur atoms along different isotherm under varying pressure. Note the higher temperature required for the diffusion of nitrogen and sulfur atoms as compared to the hydrogen ones in Fig. 7.11.

of  $D_N$  and  $D_S$  at 2500K.

## 7.6 Analysis of local structures

In the previous section, we have determined and categorized the P-T space of AMS into different regimes viz. solid, plastic, superionic and liquid, by applying a combination visual inspection of the trajectories and MSD's of all the constituent elements. This helped us to identify a selection of intriguing behaviors: variation in hydrogen bonded network enforced by rotating S-H or N-H covalent bonds, the local disassociation of such bonds to generate molecular or purely ionic defects and finally the creation of fully diffusive

## Chapter 7

proton within the stable sublattice of the heavy atoms. We will now analyze the aforementioned behaviors in light of our calculated PDF, which will assert our assignment of different regimes and provide us with a more perceptive microscopic picture of the non-solid regions.

In case of simple systems, the radial distribution function, averaged over all constituents presents information about the atomistic condition of the system under study. However, a multi-component system poses additional complexity. To overcome this hurdle, I have dealt with individual pair distribution functions between like and unlike elements to reveal characteristic details. These are shown in Figure 7.13 and Figure 7.14 for the  $P2_1/m$  phase at 60 GPa and  $Abm_2$  phase at 120 GPa, respectively, at various temperatures. At 1000K, the  $P2_1/m$  phase retains its solid structure. Hence, the PDF is associated with a strong peak at 1.05 Å, which indicates the covalent distance  $d_{NH}$ , while first peak in the S-H PDF is at 1.4 Å implying the hydrogen bonded covalent distance  $d_{S-NH} = 1.4$  Å (Figure 7.13b). The second peak in S-H PDF rises from the second nearest neighboring S-H pairs. When the molecular system enters the superionic domain upon further heating, the second S-H peak widens drastically and moves to a large distance, causing the long-range ordering to die out (Figure 7.13d and 7.14d). This is a consequence of both the rotation of the  $NH_3$  or the  $NH_4^+$  motifs and the proton hopping across the S-H---N bonds. In contrast the peak at  $d_{NH} = 1.05$  Å only broadens and diminishes in amplitude with increasing temperature, indicating that only the hopping away of protons from the  $NH_4^+$  motifs affect them (7.13d and 7.14d). In the liquid state, an exquisite chemistry develops at elevated pressure and



temperature. At 3000K we observed the emergence of a peak at 0.74 Å in the PDF of hydrogen only, which is consistent with the bond length of a typical H<sub>2</sub>

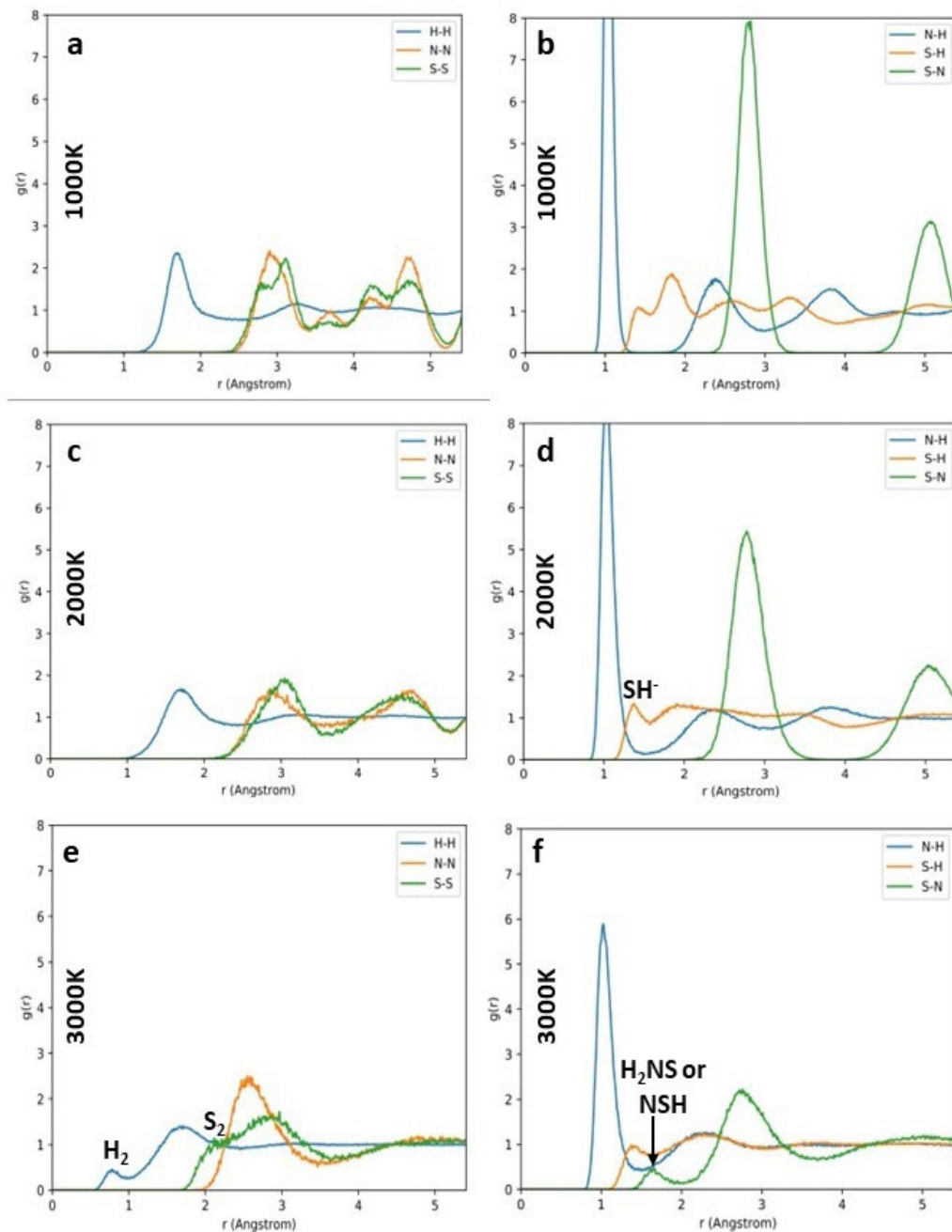


**Figure 7.13:** Pair distribution functions (PDF) of like atoms (left panels) and unlike atoms (right panel) of the P21/m phase at 60 GPa. Different peaks are identified corresponding to the H-N and H-S lengths indicating the formation of different chemical motifs at higher temperatures.

molecule (Figure 7.13e and 7.14e). However, at these high pressures and temperatures pure hydrogen is atomic and molecular hydrogen will be very

## Chapter 7

short-lived, although the existence of other elements may influence the formation of molecular hydrogen and allow it to be present in these hot-ice

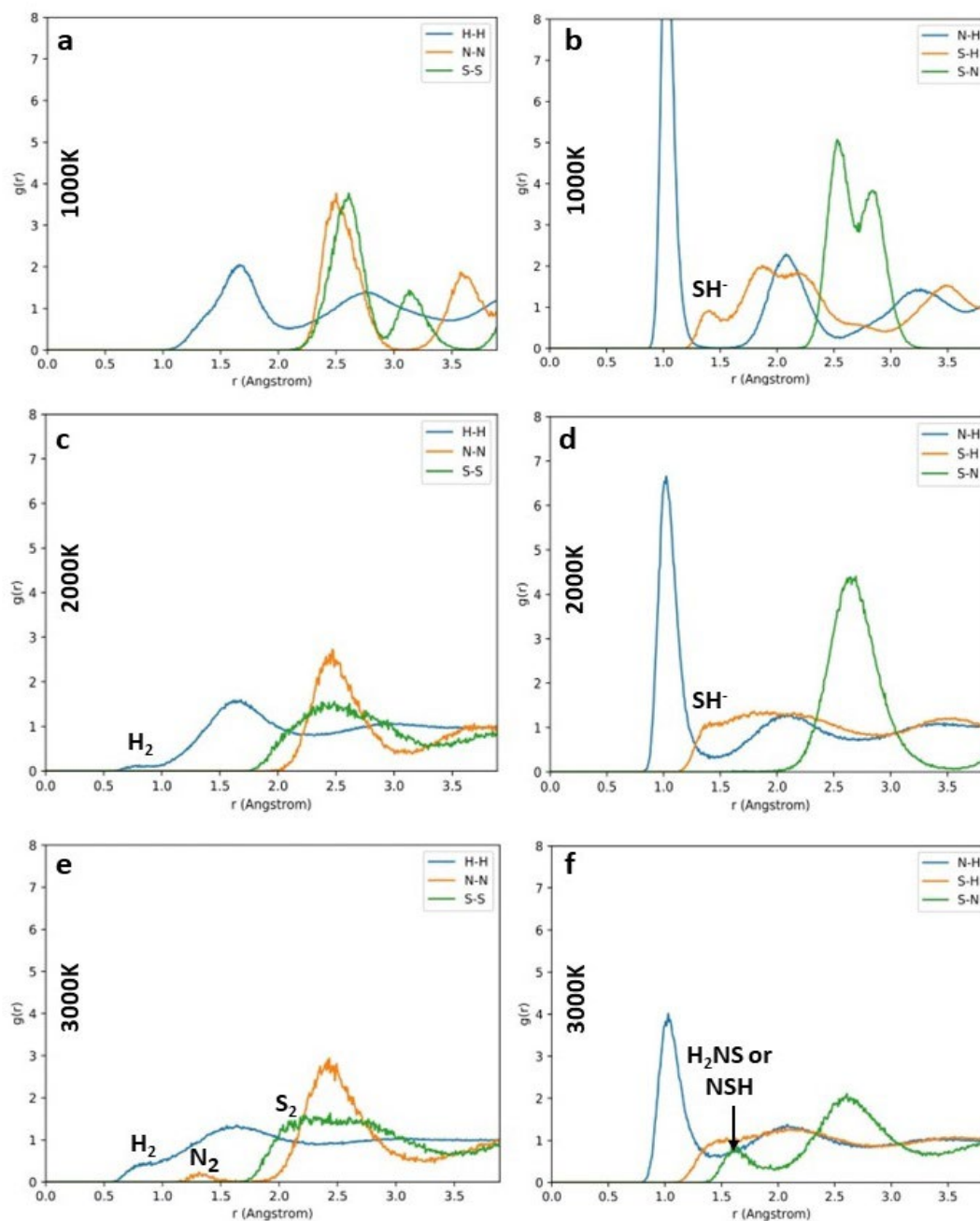


**Figure 7.14:** PDF of like atoms (left panel) and unlike atoms (right panel) in the Abm<sub>2</sub> phase at 100 GPa.

mixtures. It is important to note that the Abm<sub>2</sub> phase at 2000K also sports the formation of H<sub>2</sub> molecule (Figure 7.14c), but the peak in the PDF is very small in magnitude and the lifetime of H<sub>2</sub> molecules could even be very transient.

The characteristic difference between the molten P2<sub>1</sub>/m phase and Abm<sub>2</sub> phase can be attributed to the formation of molecules of heavy atoms present in the system. The former phase only shows the appearance of S<sub>2</sub> molecules, whereas the latter gives rise to both the N<sub>2</sub> and S<sub>2</sub> molecules (Figure 7.13e and 7.14e). The peak at the PDF of S-S bond distances appear at around 2 Å, which is slightly larger than the bond distance of static disulphur (1.9 Å). Although disulphur disintegrates readily when irradiated by sunlight, the dense cloudy atmosphere of the ice-giant planets may act as a shield and hence, aid the formation of S<sub>2</sub> molecules in the mantle of these planets. On the other hand, the peak for N-N PDF is located at 1.4 Å. These N–N bonds are longer than the N–N bonds in static N<sub>2</sub> molecules (1.1 Å) but relatively shorter than single N–N bonds in polymeric nitrogen (1.6 Å). The bond life-time of these species are likely to be very short as the N<sub>2</sub> molecules are in rigorous rotation. Unlike Robinson and Hermann's study [26], this investigation does not find any molecular species like NS, analogous to NO, although NS and NS<sup>+</sup> have been detected in stellar clouds and comets [58,59]. Instead, we can recognize a peak in the S-N PDF at 1.6-1.7 Å, which can be attributed to the S-N bond distances observed in molecular species like H<sub>2</sub>NS, NSH or HNSH[60] and in Dinitrogen sulphide [61]. The relatively smooth and featureless structure of the H-H PDF at high pressure and high temperature (Figure 7.14e) indicates that the total dissociation of H<sub>2</sub> molecules is very likely to happen en route to a plasma.

## **7.7 Combined P-T effects on band gap**

The molecular mixtures, by and large, tend not to have a metallic character unless enforced by an extreme pressure and/or temperature

## *Chapter 7*

condition, which leads to a collapse of their wide band gap.  $\text{H}_2\text{S}$  and  $\text{H}_3\text{S}$  are found to metalize at relatively lower pressures around 100 GPa [35]. This property of  $\text{H}_2\text{S}$  is observed to be carried through their mixture with methane, resulting in a room temperature superconducting material at 250 GPa [41]. Li et al. [33] have reported the evolution of band gap with hydrostatic pressure of the AMS phases. Below 90 GPa, all the phases  $P4/nmm$ ,  $Cc$  and  $P2_1/m$  have wide band gaps ranging from 1 to 3.5 eV. However, the  $Abm_2$  and  $Cmma$  phase are reported to gain pressure induced metallic character beyond 90 GPa. Although the  $Cmma$  phase is metallic over its entire pressure range of stability, the  $Abm_2$  phase undergoes a band gap collapse at 88 GPa, resulting in a semiconductor-metallic transition. Thus, the metallization of  $\text{H}_2\text{S}$  can be expected to occur in its mixture with ammonia at higher temperatures. Barring the  $Cmma$  phase, the present study investigated the combined effect of temperature and pressure on the evolution of the band gap of the rest of the stable AMS phases. Figure 7.15 shows that the metallic character at relatively low pressures does not develop even at higher temperatures considered in this calculation. The relatively high band gap of  $P4/nmm$  phases at 10 GPa and 1000K compared to its low-pressure predecessor is mainly due to the fact that at 0 GPa and 1000K, the  $P4/nmm$  phase is already molten whereas at 10 GPa it demonstrates superionic nature. In Figure 7.15, we can find that the collapse of the band gap is the most pronounced in case of the  $Cc$  phase at 20 GPa, as indicated by the steeper slope. In the superionic regime, the  $Cc$  phase at 20 GPa features a band-gap lower than 1 eV together with the high-pressure  $Cc$  phase at 40 GPa and  $P2_1/m$  phase. The  $P2_1/m$  phase at 80 GPa has the

lowest band gaps of them all, however the band gap of this phase is less sensitive to the rise in temperature as evident from its seemingly flat variation

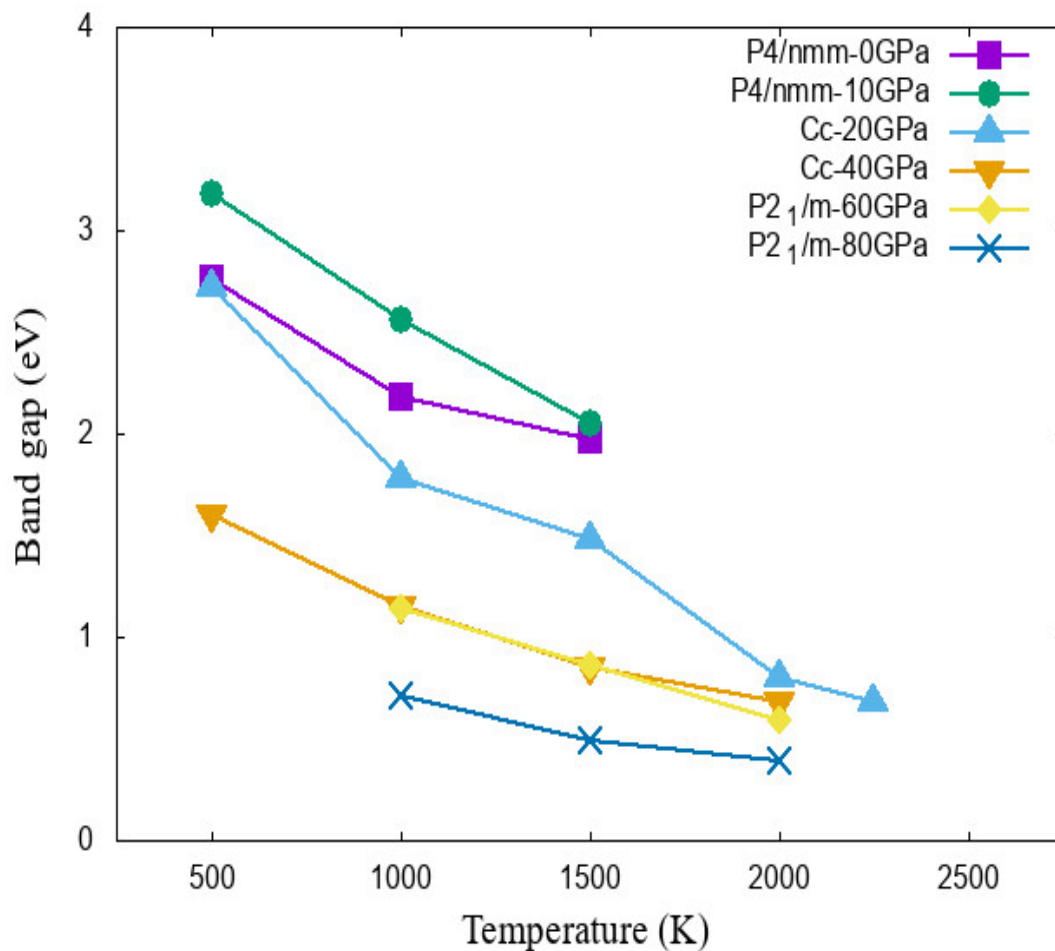


**Figure 7.15:** Variation of band gaps of different AMS phases at different pressures in response to elevated temperatures.

with temperature. This analysis suggests that the metallization of the Cc phase at 20 GPa can be obtained at a very high temperature, albeit lower than the temperature required for metallization of the other high-pressure AMS phases.

## 7.8 Concluding notes

In summary, this chapter presents crucial results from AIMD simulations at pressures and temperatures anticipated in the mantle regions of the ice giant Uranus and Neptune with new finding on the phase diagram of

## *Chapter 7*

1:1 molecular mixture of  $\text{NH}_3$  and  $\text{H}_2\text{S}$  Ammonia monosulphide and the evolution of their electronic properties. The simulations provide a wide range of intriguing physical and chemical properties of the mixtures. This study also demonstrates similar transitions of their states on heating, as observed in case of pure molecular ammonia, but somewhat different from that in case of  $\text{H}_2\text{S}$ . In ambient pressure, solid AMS melts fully to form molecular liquid without any intermediate plastic or superionic state. But, on and above a pressure of 10 GPa, a regime of plastic or locally excited states appear, which is triggered by the rotation of different molecular motifs. These local molecular motifs are found to be chemically and structurally different from the motifs in the constituent individual molecular ices. This is a consequence of the chemical complexity in the AMS mixture. Further increase in temperature results in a plastic to superionic transition where highly mobile protons diffuse through the heavy atom sublattice. This superionic region covers a major portion of the P-T phase diagram. The lowering of the onset temperature required for the superionic behavior compared to that of the ice of pure ammonia is attributed to the complex chemical interaction and dynamic equilibrium between different motifs existing in the AMS mixture. The melting curve is obtained via direct heating of the superionic states and is found to lie below the melting curve of pure ammonia. Although  $\text{H}_2\text{S}$  being a minor component of the ice giant interiors, a comparison with the isentropes of Uranus and Neptune indicates that in the shallow mantle region of these planets  $\text{H}_2\text{S}$  can be bound with ammonia and the AMS mixture can exist there.

This chapter has evaluated the diffusion coefficients of protons in both

superionic and liquid states while those of the N and S atoms in liquid states only. The proton diffusivity is found to increase with temperature but holds a non-linear relation with pressure. Sulphur, although heavier in mass, diffuses faster than nitrogen in the liquid state. This difference in diffusional behaviour is attributed to the superior strength of the N-H bond, compared to the S-H bond. The PDF analysis of the high temperature regime reveals that heating favours the existence of molecular species rather than the ionic ones. It is reported that in the superionic and the liquid regimes, just near the melting points the mixture mostly contains short-lived molecular motifs of both like and unlike atoms. However, at much higher temperatures the formation of H<sub>2</sub> molecules is indicated.

This study also provides an account of the effect of temperature on the band gap of the AMS phases. The Abm<sub>2</sub> and Cmma mixture remain metallic in the whole temperature range. The rest of the phases are characterized by a closure of the band gap with increasing temperature. Among these phases, the band gap of Cc phase at 20 GPa favours the heating the most. To achieve metallic character of these phases, further increment of temperature is required, which could possibly turn the mixture atomic from molecular.

## Chapter 7

### References

- [1] Hubbard W B and Macfarlane J J 1980 Structure and Evolution of Uranus and Neptune *J. Geophys. Res.* **85**
- [2] Hubbard, W.B. Nellis, W.J. Mitchell, A.C. Holmes, N.C., Limaye, S.S. McCandless P C 1991 Interior Structure of Neptune: Comparison with Uranus *Science (80- )*. **253** 648–51
- [3] Ross M 1981 The ice layer in Uranus and Neptune-diamonds in the sky? 435–6
- [4] Sekine Y, Genda H, Sugita S, Kadono T and Matsui T 2011 Replacement and late formation of atmospheric N<sub>2</sub> on undifferentiated Titan by impacts *Nat. Geosci.* **4** 359–62
- [5] Noack L, Snellen I and Rauer H 2017 Water in Extrasolar Planets and Implications for Habitability *Space Sci. Rev.* **212** 877–98
- [6] Rauer H, Catala C, Aerts C, Appourchaux T, Benz W, Brandeker A, Christensen-Dalsgaard J, Deleuil M, Gizon L, Goupil M J, Güdel M, Janot-Pacheco E, Mas-Hesse M, Pagano I, Piotto G, Pollacco D, Santos, Smith A, Suárez J C, Szabó R, Udry S, Adibekyan V, Alibert Y, Almenara J M, Amaro-Seoane P, Eiff M A V, Asplund M, Antonello E, Barnes S, Baudin F, Belkacem K, Bergemann M, Bihain G, Birch A C, Bonfils X, Boisse I, Bonomo A S, Borsa F, Brandão I M, Brocato E, Brun S, Burleigh M, Burston R, Cabrera J, Cassisi S, Chaplin W, Charpinet S, Chiappini C, Church R P, Csizmadia S, Cunha M, Damasso M, Davies M B, Deeg H J, Díaz R F, Dreizler S, Dreyer C, Eggenberger P, Ehrenreich D, Eigmüller P, Erikson A, Farmer R, Feltzing S, de Oliveira Fialho F, Figueira P, Forveille T, Fridlund M, García R A, Giommi P, Giuffrida G, Godolt M, da Silva J G, Granzer T, Grenfell J L, Grottsch-Noels A, Günther E, Haswell C A, Hatzes A P, Hébrard G, Hekker S, Helled R, Heng K, Jenkins J M, Johansen A, Khodachenko M L, Kislyakova K G, Kley W, Kolb U, Krivova N, Kupka F, Lammer H, Lanza A F, Lebreton Y, Magrin D, Marcos-Arenal P, Marrese P M, Marques J P, Martins J, et al 2014 *The PLATO 2.0 mission* vol 38
- [7] Helled R, Anderson J D, Podolak M and Schubert G 2011 Interior models of Uranus and Neptune *Astrophys. J.* **726**
- [8] Arridge C S, Achilleos N, Agarwal J, Agnor C B, Ambrosi R, André N, Badman S V., Baines K, Banfield D, Barthélémy M, Bisi M M, Blum J, Bocanegra-Bahamon T, Bonfond B, Bracken C, Brandt P, Briand C, Briois C, Brooks S, Castillo-Rogez J, Cavalié T, Christophe B, Coates A J, Collinson G, Cooper J F, Costa-Sitja M, Courtin R, Daglis I A, De Pater I, Desai M, Dirx D, Dougherty M K, Ebert R W, Filacchione G, Fletcher L N, Fortney J, Gerth I, Grassi D, Grodent D, Grün E, Gustin J, Hedman M, Helled R, Henri P, Hess S, Hillier J K, Hofstadter M H, Holme R, Horanyi M, Hospodarsky G, Hsu S, Irwin P, Jackman C M, Karatekin O, Kempf S, Khalisi E, Konstantinidis K, Krüger H, Kurth W S, Labrianidis C, Lainey V, Lamy L L, Laneuville M, Lucchesi D, Luntzer A, MacArthur J, Maier A, Masters A, McKenna-Lawlor S, Melin H, Milillo A, Moragas-Klostermeyer G, Morschhauser A, Moses J I, Mousis O, Nettelmann N, Neubauer F M, Nordheim T, Noyelles B,



- Orton G S, Owens M, Peron R, Plainaki C, Postberg F, Rambaux N, Retherford K, Reynaud S, Roussos E, Russell C T, Rymer A M, Sallantin R, Sánchez-Lavega A, Santolik O, Saur J, Sayanagi K M, Schenk P, Schubert J, Sergis N, et al 2014 The science case for an orbital mission to Uranus: Exploring the origins and evolution of ice giant planets *Planet. Space Sci.* **104** 122–40
- [9] Hermann A, Ashcroft N W and Hoffmann R 2012 High pressure ices *Proc. Natl. Acad. Sci.* **109** 745–50
- [10] French M, Mattsson T R, Nettelmann N and Redmer R 2009 Equation of state and phase diagram of water at ultrahigh pressures as in planetary interiors *Phys. Rev. B - Condens. Matter Mater. Phys.* **79** 1–11
- [11] Marques M, Ackland G J and Loveday J S 2009 Nature and stability of ice X *High Press. Res.* **29** 208–11
- [12] Bethkenhagen M, French M and Redmer R 2013 Equation of state and phase diagram of ammonia at high pressures from ab initio simulations *J. Chem. Phys.* **138**
- [13] Spanu L, Donadio D, Hohl D and Galli G 2009 Theoretical investigation of methane under pressure *J. Chem. Phys.* **130**
- [14] Nakahata I, Matsui N, Akahama Y and Kawamura H 1999 Structural studies of solid methane at high pressures *Chem. Phys. Lett.* **302** 359–62
- [15] Benedetti L R, Nguyen J H, Caldwell W A, Liu H, Kruger M and Jeanloz R 1999 Dissociation of CH<sub>4</sub> at high pressures and temperatures: Diamond formation in giant planet interiors? *Science (80-. )*. **286** 100–2
- [16] Fortes A D and Choukroun M 2010 Phase behaviour of ices and hydrates *Space Sci. Rev.* **153** 185–218
- [17] Naden Robinson V, Marqués M, Wang Y, Ma Y and Hermann A 2018 Novel phases in ammonia-water mixtures under pressure *J. Chem. Phys.* **149**
- [18] Naden Robinson V, Wang Y, Ma Y and Hermann A 2017 Stabilization of ammonia-rich hydrate inside icy planets *Proc. Natl. Acad. Sci.* **114** 9003–8
- [19] Loveday J S and Nelmes R J 2004 The ammonia hydrates - Model mixed-hydrogen-bonded systems *High Press. Res.* **24** 45–55
- [20] Chau R, Hamel S and Nellis W J 2011 Chemical processes in the deep interior of Uranus *Nat. Commun.* **2** 203–5
- [21] Cavazzoni C, Chiarotti G L, Scandolo S, Tosatti E, Bernasconi M and Parrinello M 1999 Superionic and metallic states of water and ammonia at giant planet conditions *Science (80-. )*. **283** 44–6
- [22] Bethkenhagen M, Cebulla D, Redmer R and Hamel S 2015 Superionic Phases of the 1:1 Water-Ammonia Mixture *J. Phys. Chem. A* **119** 10582–8
- [23] Bethkenhagen M, Meyer E R, Hamel S, Nettelmann N, French M, Scheibe L,

## Chapter 7

- Ticknor C, Collins L A, Kress J D, Fortney J J and Redmer R 2017 Planetary Ices and the Linear Mixing Approximation *Astrophys. J.* **848** 67
- [24] Pruteanu C G, Ackland G J, Poon W C K and Loveday J S 2017 When immiscible becomes miscible-Methane in water at high pressures *Sci. Adv.* **3** 1–6
- [25] Kraus D, Vorberger J, Pak A, Hartley N J, Fletcher L B, Frydrych S, Galtier E, Gamboa E J, Gericke D O, Glenzer S H, Granados E, MacDonald M J, MacKinnon A J, McBride E E, Nam I, Neumayer P, Roth M, Saunders A M, Schuster A K, Sun P, van Driel T, Döppner T and Falcone R W 2017 Formation of diamonds in laser-compressed hydrocarbons at planetary interior conditions *Nat. Astron.* **1** 606–11
- [26] Naden Robinson V and Hermann A 2020 Plastic and superionic phases in ammonia-water mixtures at high pressures and temperatures *J. Phys. Condens. Matter* **32**
- [27] Xu W, Robinson V N, Zhang X, Zhang H C, Donnelly M E, Dalladay-Simpson P, Hermann A, Liu X Di and Gregoryanz E 2021 Ionic Phases of Ammonia-Rich Hydrate at High Densities *Phys. Rev. Lett.* **126** 15702
- [28] Liu Z, Botana J, Hermann A, Valdez S, Zurek E, Yan D, Lin H Q and Miao M S 2018 Reactivity of He with ionic compounds under high pressure *Nat. Commun.* **9** 1–10
- [29] Song X, Yin K, Wang Y, Hermann A, Liu H, Lv J, Li Q, Chen C and Ma Y 2019 Exotic Hydrogen Bonding in Compressed Ammonia Hydrides *J. Phys. Chem. Lett.* **10** 2761–6
- [30] Irwin P G J, Toledo D, Garland R, Teanby N A, Fletcher L N, Orton G S and Bézard B 2019 Probable detection of hydrogen sulphide (H<sub>2</sub>S) in Neptune’s atmosphere *Icarus* **321** 550–63
- [31] de Pater I, Romani P N and Atreya S K 1991 Possible microwave absorption by H<sub>2</sub>S gas in Uranus’ and Neptune’s atmospheres *Icarus* **91** 220–33
- [32] Irwin P G J, Toledo D, Garland R, Teanby N A, Fletcher L N, Orton G A and Bézard B 2018 Detection of hydrogen sulfide above the clouds in Uranus’s atmosphere *Nat. Astron.* **2** 420–7
- [33] Li X, Lowe A, Conway L, Miao M and Hermann A 2021 First principles study of dense and metallic nitric sulfur hydrides *Commun. Chem.* **4** 1–10
- [34] Li Y, Hao J, Liu H, Li Y and Ma Y 2014 The metallization and superconductivity of dense hydrogen sulfide *J. Chem. Phys.* **140**
- [35] Li Y, Wang L, Liu H, Zhang Y, Hao J, Pickard C J, Nelson J R, Needs R J, Li W, Huang Y, Errea I, Calandra M, Mauri F and Ma Y 2016 Dissociation products and structures of solid H<sub>2</sub>S at strong compression *Phys. Rev. B* **93** 020103
- [36] Duan D, Liu Y, Tian F, Li D, Huang X, Zhao Z, Yu H, Liu B, Tian W and Cui T 2014 Pressure-induced metallization of dense (H<sub>2</sub>S)<sub>2</sub>H<sub>2</sub> with high-T c superconductivity *Sci. Rep.* **4** 30–2

- [37] Errea I, Calandra M, Pickard C J, Nelson J, Needs R J, Li Y, Liu H, Zhang Y, Ma Y and Mauri F 2015 High-pressure hydrogen sulfide from first principles: A strongly anharmonic phonon-mediated superconductor *Phys. Rev. Lett.* **114** 1–5
- [38] Errea I, Calandra M, Pickard C J, Nelson J R, Needs R J, Li Y, Liu H, Zhang Y, Ma Y and Mauri F 2016 Quantum hydrogen-bond symmetrization in the superconducting hydrogen sulfide system *Nature* **532** 81–4
- [39] Cui W, Bi T, Shi J, Li Y, Liu H, Zurek E and Hemley R J 2020 Route to high-T<sub>c</sub> superconductivity via CH<sub>4</sub>-intercalated H<sub>3</sub>S hydride perovskites *Phys. Rev. B* **101** 1–5
- [40] Sun Y, Tian Y, Jiang B, Li X, Li H, Iitaka T, Zhong X and Xie Y 2020 Computational discovery of a dynamically stable cubic SH<sub>3</sub>-like high-temperature superconductor at 100 GPa via CH<sub>4</sub> intercalation *Phys. Rev. B* **101** 1–7
- [41] Snider E, Dasenbrock-Gammon N, McBride R, Debessai M, Vindana H, Vencatasamy K, Lawler K V., Salamat A and Dias R P 2020 Room-temperature superconductivity in a carbonaceous sulfur hydride *Nature* **586** 373–7
- [42] Ninet S, Datchi F and Saitta A M 2012 Proton Disorder and Superionicity in Hot Dense Ammonia Ice *Phys. Rev. Lett.* **108** 165702
- [43] Aragoñes J L and Vega C 2009 Plastic crystal phases of simple water models *J. Chem. Phys.* **130** 244504
- [44] Takii Y, Koga K and Tanaka H 2008 A plastic phase of water from computer simulation *J. Chem. Phys.* **128** 204501
- [45] Kresse G and Furthmüller J 1996 Efficient iterative schemes for ab initio total-energy calculations using a plane-wave basis set *Phys. Rev. B - Condens. Matter Mater. Phys.* **54** 11169–86
- [46] Kresse G and Hafner J 1993 Ab initio molecular dynamics for liquid metals *Phys. Rev. B* **47** 558
- [47] Blöchl P E 1994 Projector augmented-wave method *Phys. Rev. B* **50** 17953–79
- [48] Perdew J P, Burke K and Ernzerhof M 1996 Generalized Gradient Approximation Made Simple *Phys. Rev. Lett.* **77** 3865–8
- [49] Nosé S 1984 A unified formulation of the constant temperature molecular dynamics methods *J. Chem. Phys.* **81** 511–9
- [50] Hoover W G 1985 Canonical dynamics: Equilibrium phase-space distributions *Phys. Rev. A* **31** 1695–7
- [51] Hjorth Larsen A, Jørgen Mortensen J, Blomqvist J, Castelli I E, Christensen R, Dułak M, Friis J, Groves M N, Hammer B, Hargus C, Hermes E D, Jennings P C, Bjerre Jensen P, Kermode J, Kitchin J R, Leonhard Kolsbjerg E, Kubal J, Kaasbjerg K, Lysgaard S, Bergmann Maronsson J, Maxson T, Olsen T, Pastewka L, Peterson A, Rostgaard C, Schiøtz J, Schütt O, Strange M, Thygesen K S, Vegge T, Vilhelmsen

## Chapter 7

- L, Walter M, Zeng Z and Jacobsen K W 2017 The atomic simulation environment—a Python library for working with atoms *J. Phys. Condens. Matter* **29** 273002
- [52] Monkhorst H J and Pack J D 1976 Special points for Brillouin-zone integrations\* *Phys. Rev. B* **13** 5188–92
- [53] Blöchl P E, Jepsen O and Andersen O K 1994 Improved tetrahedron method for Brillouin-zone integrations *Phys. Rev. B* **49** 16223–33
- [54] Kechin V V. 1995 Thermodynamically based melting-curve equation *J. Phys. Condens. Matter* **7** 531–5
- [55] Simon F and Glatzel G 1929 Bemerkungen zur Schmelzdruckkurve *Zeitschrift für Anorg. und Allg. Chemie* **178** 309–16
- [56] Redmer R, Mattsson T R, Nettelmann N and French M 2011 The phase diagram of water and the magnetic fields of Uranus and Neptune *Icarus* **211** 798–803
- [57] Sakashita M, Yamawaki H, Fujihisa H, Aoki K, Sasaki S and Shimizu H 1997 Pressure-Induced Molecular Dissociation and Metallization in Hydrogen-Bonded H<sub>2</sub>S Solid *Phys. Rev. Lett.* **79** 1082–5
- [58] Canaves M V, De Almeida A A, Boice D C and Sanzovo G C 2002 Nitrogen Sulfide In Comets Hyakutake (C/1996 B2) And Hale–Bopp (C/1995 O1) *Earth. Moon. Planets* **90** 335–47
- [59] Cernicharo J, Lefloch B, Agúndez M, Bailleux S, Margulès L, Roueff E, Bachiller R, Marcelino N, Tercero B, Vastel C and Caux E 2018 Discovery of the Ubiquitous Cation NS<sup>+</sup> in Space Confirmed by Laboratory Spectroscopy *Astrophys. J.* **853** L22
- [60] Pereira P S S, Macedo L G M and Pimentel A S 2010 New insight into the formation of Nitrogen sulfide: A quantum chemical study *J. Phys. Chem. A* **114** 509–15
- [61] Davy R D and Schaefer H F 1991 Dinitrogen Sulfide (N<sub>2</sub>S) and Its Protonated Isomers *J. Am. Chem. Soc.* **113** 1917–22

## Summary and conclusions

---

*U<sub>1-x</sub>Th<sub>x</sub>SiO<sub>4</sub>: Phase transition & mechanical property*

*Effect of polyhedral distortion on phase transition*

*Elastic property of titanite*

*Electronic and optical property of titanite*

*H diffusion in brucite under high pressure*

*Electrical conductivity of brucite*

*Plastic, superionic and melting behaviour of AMS*

*Local structure and band-gap of AMS*

*Future scope*



### 8.1 $U_{1-x}Th_xSiO_4$ : Phase transition & mechanical property

Zircon type natural silicates are considered to be both industrially and geologically demanding. From a material science point of view their mechanical stability and endurance to corrosion and extreme thermodynamic environment make them ideal candidate for nuclear waste immobilization and disposal of spent nuclear fuel. From the geological perspective, zircon type silicates often host radionuclides like U, Th, Pu etc. as substitutional defects in place of zirconium atom. U-Th-Pb radiogenic geochronology is thus extensively used in geological studies to quantitatively explore the ages of rocks and geological events. The present thesis is focused upon the atomistic phenomena involved in the zircon- to reidite-type high-pressure phase transition of pure uranium and thorium endmember coffinite ( $USiO_4$ ) and thorite ( $ThSiO_4$ ) as well as the series of uranothorite solid solutions ( $U_{1-x}Th_xSiO_4$ ;  $x = 0$  to 1, in steps of 0.25). The effect of increasing hydrostatic pressure on the phase transition and mechanical properties are concluded below.

## Chapter 8

- Using the enthalpy crossover method, the first-principles calculations suggest the pressure-dependent zircon- to reidite-type structural transition to take place at 8.52 GPa for the U-end member (coffinite), which is comparable to that (8.68 GPa) for the Th-end member (thorite). According to the pressure homologue rule, the substitution of U by Th should lower the transition pressure ( $P_T$ ). The present thesis, however, reports a non-linear relation of  $P_T$  with Th content in the phase, showing a minimum value (6.82 GPa) for the composition with equal U and Th proportions ( $U_{0.5}Th_{0.5}SiO_4$ ).
- The bulk moduli of the zircon-type uranothorite also features a similar nonlinear trend with the U/Th ratio, attaining a minimum of 167.6 GPa in the solid-solution series at U/Th = 1, where the values for the end-members: coffinite and thorite are 181.3 GPa and 178.2 GPa, respectively. In contrast, the bulk moduli of the reidite-type phases decrease monotonically (from 239 GPa to 225.6 GPa) with increasing Th content, but always lying above the values for the zircon-type counterpart.
- Consequently, their compressibility shows contrasting variations with the Th content; the zircon-type phases yield a maximum compressibility for  $U_{0.5}Th_{0.5}SiO_4$ , whereas the reidite-type continuously increases its compressibility. This finding establishes the zircon-type  $U_{0.5}Th_{0.5}SiO_4$  as the most compressible solid solution phase that explains the lowest  $P_T$ .
- The U-Th interchange results in a drastic change in the mode of volume expansion for the zircon- and reidite-type phases, where the crystallographic  $c/a$  ratio in the later phase undergoes a steady gain with increasing Th content, where the other phase shows a completely opposite relation. The reidite-type



phase thus gives rise to higher compressibility along the  $c$ -axis than the  $a$ -axis, as opposed to that for the zircon-type phase.

## **8.2 Effect of polyhedral distortion on phase transition**

The uranothorite phases display their lattice structures consisting of highly irregular U/ThO<sub>8</sub> triangular dodecahedra, and the distortions of these dodecahedra significantly influence their zircon to reidite-type transition pressure. The present thesis theoretically derives two novel parameters in quantifying these distortions. Their analysis leads to the following major findings.

- In U/ThO<sub>8</sub> polyhedra the radionuclides occupy the central positions, and the O atoms occupy two distinct types of vertices with multiplicity 4, resulting in two different U/Th-O bond lengths. In their undistorted state, the ratio of these two bond lengths assumes a fixed value of  $\sim 1.374302$ . On the other hand, each of two adjacent O atoms forms three geometrically different angles at the U/Th position, with multiplicity 2, 4 and 12 respectively. The undistorted configuration has these angles as  $65.061^\circ$ ,  $95.297^\circ$  and  $75.158^\circ$ . This thesis provides an analysis of the U/ThO<sub>8</sub> polyhedral distortions using two new parameters:  $\delta$  and  $\sigma^2$  to quantify the distortions of bond lengths and angles, respectively. This analysis also explains the two distinct types of U/Th-O bonds with contrasting lengths.
- $\sigma_U^2$  and  $\sigma_{Th}^2$  for zircon- and reidite-type phases assume a minimum difference for the intermediate chemical composition (U<sub>0.5</sub>Th<sub>0.5</sub>SiO<sub>4</sub>), 47.487 and 35.261 in deg<sup>2</sup> for UO<sub>8</sub> and ThO<sub>8</sub> polyhedra, respectively. Interestingly, the

## Chapter 8

transition pressure ( $P_T$ ) is reduced to a minimum at the point of this minimum difference in angular distortion. The present thesis offers the following explanation. The zircon- to reidite-type transition is reconstructive, where U/Th-O bonds completely dissociate and reorganize to form new polyhedra in the high-pressure phase. The minimum difference in polyhedral distortion enables this transition to take place at the lowest pressure when U/Th = 1.

### 8.3 Elastic property of titanite

Using first-principles calculations this thesis presents a detailed analysis of the mechanical properties of titanite ( $\text{CaTiSiO}_5$ ), a naturally occurring nesosilicate, extensively utilized to manufacture a range of opto-electronic devices. Titanite undergoes a structural transition from  $P2_1/c$  to  $C2/c$  structure under 5 GPa. The major elastic properties of this phase are highlighted below:

- The 13 elastic constants of titanite (monoclinic) are sensitive to hydrostatic pressure. In the  $P2_1/c$  phase  $C_{44}$ ,  $C_{55}$  and  $C_{36}$  shows an inverse relation with pressure, implying its negative pressure gradient, whereas the rest hold positive relations. The compressional elastic constants  $C_{11}$ ,  $C_{22}$  and  $C_{33}$  have the highest values of their pressure derivatives ( $C'_{11}= 8.16$ ,  $C'_{22}=5.21$  and  $C'_{33}= 6.75$ ). In contrast, the other shear elastic constants are less sensitive to pressure, where  $C_{13}$  is the softest constant with the lowest pressure derivative ( $C'_{13}= 1.67$ ).
- The present calculations reveal negative elasticity of the  $C2/c$  phase, which is explained here. The shear elastic constant  $C_{36}$  assumes negative

## ***Summary and conclusions***

values and the negativity increases with pressure. The other elastic constants show qualitatively similar pressure dependent variations, as found in its low-pressure polymorph. This study proposes a rotational bond kinematics approach to theorize the origin of such negative elasticity, taking into consideration of the changes in bond angles under shear strains ( $\epsilon_{12}$ ). On application of  $\epsilon_{12}$ , the bond angle Ca-O-Si increases by  $2.17^\circ$  while the Ca-O-Ti and Ti-O-Si bond angles reduce by  $2.58^\circ$  and  $1.52^\circ$ . These estimates imply that the bond rotation accommodates the shear strain by reorienting the angular disposition of cationic polyhedra. For the other elastic constants, the crystal, on the other hand, resists the strain, except  $C_{36}$  that favours the shear deformation.

## **8.4 Electronic and optical properties of titanite**

- Spin-polarized calculation of density of states of  $P2_1/c$  titanite yields a band-gap of 3.2 eV, implying that this phase can be used as a wide band-gap semiconductor.
- The real ( $\epsilon_1$ ) and imaginary ( $\epsilon_2$ ) parts of the frequency dependent complex dielectric function of  $P2_1/c$  titanite indicate that titanite is optically anisotropic with the static dielectric constant along crystallographic  $a$ -,  $b$ - and  $c$ -axis as 4.38, 4.29 and 4.94. The anisotropic character is stronger for the real part, compared to the imaginary part.  $\epsilon_1$  assumes a negative value along  $c$ -axis at 4.36 eV. Titanite can be thus used as a shielding material at preferred optical frequencies. The complex part of the dielectric function ( $\epsilon_2$ ) is related to photon

## Chapter 8

absorption, and the absorption edges lie close to 3.2 eV for all crystallographic directions.

- The absorption, refractive index and reflectivity are calculated across the infra-red, visible and ultraviolet region along with the loss function and extinction coefficient. The calculated refractive indices of optically anisotropic titanite are 2.09, 2.07 and 2.21 along the *a*-, *b*- and *c*-axis, respectively. The extinction coefficient peaks at 4.26 eV and its shoulder is spread up to 60 eV. The titanite phase is thus transparent in the visible range, but opaque in the UV region. Based on this finding, the thesis proposes titanite as a potential UV shielding material.

### 8.5 H-diffusion in brucite under high pressure

Transition zone silicates and dense hydrous mineral silicate phases are observed to house nominal to moderate amount of hydrogen and water and aids the recycling of water into the earth's mantle. This doctoral work used ab-initio molecular dynamics (AIMD) simulations to study the mobility of hydrogen in brucite [Mg(OH)<sub>2</sub>], which is an outstanding hydroxide phase in Earth's subduction zones. The simulations reveal that the mechanism of hydrogen diffusion in brucite markedly different from those in silicates. P $\bar{3}$  brucite has a layered structure, with H atoms located between two adjoining MgO<sub>6</sub>-octahedral layers. The layered structure acts as an ideal passage to facilitate the mobility of H atoms. The major outcomes of this study on the hydrogen diffusion in brucite are the following:

## *Summary and conclusions*

- For a given temperature, this phase shows a sharp transition in the mobility of H atoms at a threshold hydrostatic pressure. The MSD of H-atoms steadily increases with increasing pressure up to 73-76 GPa but drops with further pressure elevation. This finding suggest that the hydrogen diffusivity becomes most effective at an optimum pressure.
- In the brucite phase the H mobility is onset only when a critical hydrostatic pressure is attained. Such pressure induced mobility results from dynamic disordering of H atoms in the lattice sites between the MgO<sub>6</sub> octahedral layers. The onset pressure drops with increasing temperature, e.g., 43.0 GPa at 1250K, which steadily reduces to 28.0 GPa at 1500K, 13.4 GPa at 1750K and 10.4 GPa at 2000K.
- The maximum estimated diffusion coefficient is 2.34688E-08 m<sup>2</sup>/s for a pressure of 75.6 GPa and a temperature of 2000K.
- In silicates the diffusion of H involves hopping of H atoms between substitutional and interstitial defects, whereas the diffusion in brucite phase at elevated pressure and temperature takes place in such manner so that the process results in amorphization of the H-sublattice, but without disturbing the Mg- and O-sublattice structures. This amorphization gives rise to a pool of highly mobile H-atoms that can readily diffuse along the channel.
- The diffusion of H atoms in P $\bar{3}$  brucite is highly anisotropic, with almost no diffusion along the *c*-axis. This directional diffusivity is explained in the following way. The MgO<sub>6</sub> octahedra form a sheet perpendicular to the *c*-axis, and act as an effective barrier to restrict the interlayer motion of H-atoms, and facilitate their intralayer motion. The ratio of normalized diffusion constants

## Chapter 8

along  $a$ - and  $b$ -axis [ $d^*_{[100]}/d^*_{[010]}$ ] has been evaluated as function of pressure and temperature. This study finds no steady correlation of  $d^*_{[100]}/d^*_{[010]}$  with pressure, which is perhaps a consequence of the isotropic configurational arrangements of H atoms on the  $ab$ -plane.

### 8.6 Electrical conductivity of brucite

- Using the Nernst-Einstein equation, the thesis provides a new insight for the apparent contribution of the protonic conductivity in brucite at elevated pressures (10 - 86 GPa) and temperatures (1250-2000K). The electrical conductivity for different isotherms attains peak values at different pressures above 70 GPa. At 1250K and 2000K the phase gains maximum conductivity of  $1.25\text{E}+03$  S/m and  $1.85\text{E}+03$  S/m at 83.8 GPa and 85.99 GPa, respectively. However, the peak values ( $1.52\text{E}+03$  S/m and  $1.28\text{E}+03$  S/m) of conductivity at 1500K and 1750K occur at relatively lower pressures, 74.28 and 74.96 GPa, respectively.
- The calculated values of conductivity are validated with magnetic satellite data, which show good agreement at low pressures. However, this validation is limited up to 45 GPa as the ex-situ magnetic studies are unavailable above this pressure range. The conductivity estimates suggest that brucite can be a potential mineral phase in the lower mantle and the mantle transition zone. Secondly, brucite can occur as segregated patches between dominant constituent silicates and oxides in the upper mantle and explain the origin of high electrical conductivity therein.

## **8.7 Plastic, superionic and melting behaviour of AMS**

Atmospheric observations indicate that the ice giant planets contain several light elements, such as C, N, S and O, in addition to H and He, and that their amounts exceed the solar abundance ratios. Hot dense molecular ices of ammonia, water, methane are suggested to be major constituents of these planetary bodies. A part of this thesis sheds light upon the miscibility and high-pressure high-temperature behaviour of molecular crystalline mixture (in 1:1 ratio) of ammonia and hydrogen sulphide viz. ammonia monosulphide (AMS). The key outcomes of this study are concluded below.

- The thesis develops the total phase diagram of AMS, where the ambient pressure  $P4/nmm$  phase directly transforms from the solid to liquid state at a temperature of 500K. On the other hand, the high pressure phases:  $P4/nmm$  (10 GPa),  $Cc$  (20-50GPa),  $P2_1/m$  (50-90 GPa),  $Abm_2$  phase (100-130 GPa) and  $Cmma$  (150 GPa) show a transformation of solid to plastic or rotational states with increasing temperature. The plastic states are characterized by an MSD of H atoms, which increases initially, but approach a plateau of small values, implying a non-diffusive state of H. The small value of MSD, converged at around  $2 \text{ \AA}^2$ , indicates the rotation of  $\text{NH}_3$  molecules or  $\text{NH}_4^+$  motifs. Further increase of temperature results in a transformation to superionic states, where the H-sublattice melts totally, giving rise to highly diffusive protons. The  $P4/nmm$  phase at 10 GPa attains the superionic state at 1000K, whereas the rest of the high-pressure phases reach a similar state at 1500K. Heating of the superionic states eventually leads to a molecular liquid state.

## **Chapter 8**

- The melting point of AMS initially increases steeply from 500K to 2250K and then converges to 2500K at higher pressure before falling again to 2250K at 166 GPa. The melting points at different pressure are fitted with the Kechin equation to find the melting curve.
- The diffusion coefficients of H increase with temperature in the superionic regime. In the liquid regime, all the constituent atoms are mobile. This study evaluates the diffusion constants of particularly, N and S in the liquid state, and reveals that their motion hinders the mobility of H atoms. In some of the high-pressure phases, comparable values of proton diffusion coefficients are thus obtained from the superionic and liquid regimes. Sulphur, in spite of being heavier than nitrogen, is found to diffuse more rapidly in the liquid state. The contrasting mobility originates from the superior strength of the N-H bonds, as compared to the S-H bonds.

### **8.8 Local structure and band-gap of AMS**

- Analysis of the pair distribution functions (PDF) is utilized to identify the formation of short- or long-lived molecular motifs in the elevated thermodynamic conditions. This study reports that heating facilitates the existence of molecular species than ionic ones. In the liquid regime, the H-H PDF peaks at 0.74 Å, which is equal to the typical bond-length in H<sub>2</sub> molecules. However, at this condition hydrogen is atomic in nature and the life-time of H<sub>2</sub> molecule could be very less. In the low temperature regime, the N-H and S-H PDF's show peaks at 1.04 Å and 1.4 Å, where the former length is the typical N-H bond length in ammonia and the latter is the S---NH distance. This asserts



## *Summary and conclusions*

that the states of the phases are still solid. Upon entering the superionic domain, the S---NH peak widens and spreads out suggesting rapid movement of hydrogen. The loss of structure of the H-H PDF indicates that in the superionic regime H-sublattice has undergone complete melting. The S-N PDF shows characteristic peaks at 1.6-1.7 Å on and above 3000K. These peaks are most likely to occur because of the formation of molecular species like HSNH or H<sub>2</sub>NS.

- The high-pressure phases: Abm<sub>2</sub> and Cmma are metallic in their ground state. The present thesis predicts varying band gaps for the rest of the phases at pressures up to 90 GPa and different temperatures. For the Cc phase at 20 GPa the band gap drops from a value of 2.79 eV at 500K to 0.8 at 2000K. For the P2<sub>1</sub>/m phase at 60 and 80 GPa, the band gap is obtained to be 1.139 eV and 0.711 eV at 1000K. When the temperature is raised to 2000K their band gap reduces to 0.59 eV and 0.39 eV respectively. Among the phases, Cc phase at 20 GPa shows the steepest decrease in band-gap with temperature. This study finally concludes that temperature induced metallization is possible in AMS mixture. However, this metallization can only be achieved in AMS liquid at extremely high temperatures, far exceeding the conditions of the solid or superionic states.

## **8.9 Future Scope**

Silicate phases are the building blocks of the heterogeneously stratified interior of the Earth. These phases constitute up to 80% of the crust and mantle region. Understanding the physico-chemical properties of these silicates under extreme thermodynamic and ultra-chemical environment thus carries

## ***Chapter 8***

profound importance from the perspective of earth sciences. Simultaneously, the knowledge of such properties can further be valuable to explore their prospective utility in several industrial fronts. This present thesis deals with two such significant silicate phases: uranothorite and sphene/titanite. These studies thus pave the way for the future scope to investigate several other silicates, like ring silicates and phyllosilicates. An advancement of this research by doping of other heavy radionuclides in zircon structure and transition metals in titanite and in other silicates to tune their much-solicited physical properties will thus have substantial implications in materials engineering as well as from the perspective of geosciences. Nuclear waste immobilization is a challenging aspect for the nuclear energy sector. Recognizing potential silicates for environment friendly disposal of spent nuclear fuel is very important to avoid hazardous incidents. A future line of the present effort would target at the applicability of silicate phases, e.g., pyrochlore and beryl, as potential host for nuclear wastes.

The recycling of water and other light elements into the deep interior of earth have always eluded the scientific community and they have found dense hydrous mineral silicates as potential host of water. This thesis suggests brucite, a proton-rich hydroxide mineral phase as a potential material for hydrogen recycling into the mantle region of the Earth. The layered structure of brucite has significantly vacant 2-D channel between cationic octahedral layers. It would be a challenging move to address the following questions. 1. How can the trigonal brucite house other small and light elements, e.g., helium and carbon? 2. If it is capable to do so, how much can the concentration of light

## *Summary and conclusions*

elements influence the stability and mechanical properties of brucite under high pressure? 3. How does the mobility of H change depending on the presence of other light elements? 4. Can the other light elements also diffuse through the sublattice of Mg and O in significant quantities?

It has been predicted earlier that the ammonia monosulphide mixture shows superconductivity at high pressures. A line of this thesis dealt with a study of ammonia monosulphide ( $\text{NH}_3:\text{H}_2\text{S} = 1:1$ ) in the context of ice giant planets, e.g., Uranus and Neptune, with an objective to explore the superionic behaviour of this mixture in the ultra-high pressure temperature regime. The findings can be further utilized to devise practical procedures in lowering the pressure required for attaining superconductivity. There is a scope of establishing phase diagrams for the molecular crystalline ammonia hemisulphide ( $\text{NH}_3:\text{H}_2\text{S} = 2:1$ ), ammonia disulphide ( $\text{NH}_3:\text{H}_2\text{S} = 1:2$ ) and ammonia quartersulphide ( $\text{NH}_3:\text{H}_2\text{S} = 1:4$ ) to predict their stability fields. In particular, it will be worthwhile to explore the miscibility and stability of the ternary molecular mixtures of hot ices like  $\text{H}_2\text{O}$ ,  $\text{NH}_3$ ,  $\text{CH}_4$  and  $\text{H}_2\text{S}$  under the pressure temperature conditions as expected in the interiors of the ice giant planets.

In this thesis the hydrostatic pressure and temperature of investigation are limited up to a pressure of 170 GPa and a temperature of 3500K. The interior of our planet earth features a much higher temperature and pressure reaching  $6100^\circ\text{C}$  and 364 GPa at the centre of the core. On the other hand, the pressure inside the gas giant planets (Jupiter and Saturn), ice giant planets

## ***Chapter 8***

(Uranus and Neptune) and other extra-terrestrial planets can reach up to several terapascals. An effort to study the interior composition of such planets including the Earth thus can reveal exotic physics and chemistry of atomic and molecular motifs. A line of this study can be extended to evaluate the housing and alloying of small elements like H, Si, O and S with iron at the condition of the inner core boundary of the earth.

The current thesis is focussed mainly on the bulk static and kinematic behaviour of atomic and molecular crystalline solids under elevated pressure and temperature. Solid state diffusion is observed to govern several chemical reactions and micro structural changes. However, diffusion can also occur along line and surface defects which comprise of grain boundaries, dislocations etc. These diffusion along linear, planar and surface defects is remarkably faster than the diffusion in bulk lattice and they induce dramatic variation in the surface properties. The thesis thus opens a potential future opportunity of undertaking atomic scale simulations to explore the surface behavior.

## **List of publications:**

---

1. **Mondal S. K.**, Das P. K., Mandal N., Arya A. ‘A novel approach to the structural distortions of U/Th snub-disphenoids and their control on zircon → reidite type phase transitions of  $U_{1-x}Th_xSiO_4$ ’ 2020 J. Phys.: Condens. Matter 32 145401 DOI 10.1088/1361-648X/ab60e4
2. Das P. K., **Mondal S. K.**, Mandal N. ‘First principles prediction of exceptional mechanical and electronic behaviour of Titanite ( $CaTiSiO_5$ )’ 2021 Materialia 15 100964 DOI 10.1016/j.mtla.2020.100964

## **Submitted for publication:**

1. **Mondal S. K.**, Das P. K., Mandal N., Arya A., ‘High pressure-temperature induced anomalous proton diffusion in  $P\bar{3}$  brucite: Implication for high electrical conductivity in deep mantle of the earth’ submitted to Journal of Chemical Physics

## **Under preparation:**

1. **Mondal S. K.**, Mandal N., Hermann A., ‘Novel ammonia-hydrogen sulphide (1:1) mixtures under extreme conditions: Implications for Ice-giant planets’

## **Publication outside the scope of this thesis:**

1. Das P. K., **Mondal S. K.**, Mandal N., Arya A., ‘p-T dependent structural transformations of Zn-monochalcogenides to switch their semiconductor – metal transition: A DFT study’ under review in Physica B: Condensed Matter

